

The geology of the Windfall gold deposit, Québec, Canada

by

Brandon G. Choquette

A thesis submitted in partial fulfillment  
of the requirements for the degree of  
Master of Science in Geology

The Faculty of Graduate Studies  
Laurentian University  
Sudbury, Ontario, Canada

© Brandon G. Choquette

**THESIS DEFENCE COMMITTEE/COMITÉ DE SOUTENANCE DE THÈSE**  
**Laurentian University/Université Laurentienne**  
Faculty of Graduate Studies/Faculté des études supérieures

Title of Thesis Titre de la thèse	The geology of the Windfall gold deposit, Québec, Canada		
Name of Candidate Nom du candidat	Choquette, Brandon		
Degree Diplôme	Master of Science		
Department/Program Département/Programme	Geology	Date of Defence Date de la soutenance	April 21, 2021

**APPROVED/APPROUVÉ**

Thesis Examiners/Examineurs de thèse:

Dr. Daniel Kontak  
(Supervisor/Directeur(trice) de thèse)

Dr. Jacob Hanley  
(Committee member/Membre du comité)

Dr. Reuben Padilla  
(Committee member/Membre du comité)

Dr. Jean-Luc Pilotte  
(External Examiner/Examineur externe)

Approved for the Faculty of Graduate Studies  
Approuvé pour la Faculté des études supérieures  
Dr. Lace Marie Brogden  
Madame Lace Marie Brogden  
Acting Dean, Faculty of Graduate Studies  
Doyenne intérimaire, Faculté des études supérieures

**ACCESSIBILITY CLAUSE AND PERMISSION TO USE**

I, **Brandon Choquette**, hereby grant to Laurentian University and/or its agents the non-exclusive license to archive and make accessible my thesis, dissertation, or project report in whole or in part in all forms of media, now or for the duration of my copyright ownership. I retain all other ownership rights to the copyright of the thesis, dissertation or project report. I also reserve the right to use in future works (such as articles or books) all or part of this thesis, dissertation, or project report. I further agree that permission for copying of this thesis in any manner, in whole or in part, for scholarly purposes may be granted by the professor or professors who supervised my thesis work or, in their absence, by the Head of the Department in which my thesis work was done. It is understood that any copying or publication or use of this thesis or parts thereof for financial gain shall not be allowed without my written permission. It is also understood that this copy is being made available in this form by the authority of the copyright owner solely for the purpose of private study and research and may not be copied or reproduced except as permitted by the copyright laws without written authority from the copyright owner.

## **Abstract**

The Windfall deposit is an advanced-stage exploration gold project owned and operated by Osisko Mining Inc. and is located in the northeastern portion of the Abitibi greenstone belt, Québec, Canada. This is the first deposit-scale study and as such aims to provide an understanding of its geological setting and the evolution with a focus on the origin of gold mineralization. The study integrates several aspects, including: 1) geological mapping; 2) characterization of the various host rock lithologies and their alteration; 3) results of new age dating; and 4) characterization of the different vein types, their mineralogy and chemical and textural nature of the gold mineralization. The overall conclusion of the study suggests that the gold deposit formed ca. 2.7 Ga due to a magmatic-hydrothermal fluid exsolved from an underlying magma now represented by a swarm of felsic dike rocks spatially associated with the ore body.

## Co-authorship Statement

This thesis manuscript is the result of several collaborative projects in which co-authors provided supervision, access to various scientific works and discussion, hence they are listed as co- authors for chapters 2 and 3.

As first author of these chapters, I collected samples, took photographs, and documented geological observations and relationships from drill core, surface and underground exposures at the Windfall deposit. In addition, I made petrographic observations, prepared samples for geochemical analysis (*e.g.*, geochemistry, cathodoluminescence, fluid inclusion, oxygen-sulfur-carbon isotopic analysis), processed fluid inclusions and lithochemical data. Both chapters are co-authored by my supervisor Dr. D.J. Kontak who has provided extensive scientific guidance and feedback during many of our geological discussions. The third chapter is co-authored by Dr. M. Fayek and R. Sharpe who completed the lab work for the SIMS O and S isotopes. This chapter is also co- authored by É.C. Lavoie who completed the work for the LA-ICP-MS elemental maps of pyrite.

## **Acknowledgements**

I would foremost like to acknowledge my thesis supervisor Dr. Dan Kontak who provided me with this amazing opportunity to study a unique ore deposit setting. This project would not have been possible without his support and experience.

I would also like to acknowledge the assistance of many colleagues from the Osisko Mining exploration team at the Windfall gold deposit. I extend my gratitude to Mathieu Savard, Louis Grenier and Isabelle Roy who have accommodated me at the Windfall site and provided me with the freedom and an amazing opportunity to document and study the Windfall gold system. I would also like to thank Julien Avar, Alex Brodeur-Grenier, Édouard Côté-Lavoie and Louis-Mathieu Tremblay who have shared their experiences and knowledge of the deposit through many meaningful geological discussions over the past few years.

Finally, I would like to acknowledge my wife Fanny Roy who offered her support, her time, and has been patient and understanding over the past few years during the completion of this thesis.

## Table of Contents

Abstract .....	iii
Co-authorship Statement.....	iv
Acknowledgements.....	v
Table of Contents .....	vi
List of Figures .....	xiii
List of Tables .....	xvi
List of Appendices .....	xvii
Chapter 1: Introduction .....	1
1.1 Research problem and thesis objectives.....	1
1.2 Structure of thesis.....	1
Chapter 2: Geological and geochemical features of the Archean Windfall gold system with a preliminary classification.....	2
Abstract .....	2
2.1 Introduction .....	3
2.2 Regional geological setting .....	5
2.2.1 Abitibi greenstone belt.....	5
2.2.2 Urban-Barry greenstone belt .....	6
2.3 Methods.....	7
2.3.1 Previous geological studies .....	7

2.3.2 Field work and sampling .....	8
2.3.3 Handheld XRF analysis .....	8
2.3.4 Petrography.....	9
2.3.5 Whole-rock litho geochemistry .....	9
2.3.6 Multi-element ore geochemistry.....	11
2.3.7 EMPA analyses.....	11
2.3.8 U-Pb zircon dating.....	12
2.4 Results .....	13
2.4.1 Geology of the Windfall gold deposit .....	13
2.4.1.1 Volcanic rocks .....	13
2.4.1.2 Synvolcanic sedimentary horizons .....	14
2.4.1.3 Mafic intrusive rocks .....	14
2.4.1.4 Windfall intrusive complex.....	14
2.4.1.4.1 Pre-mineral QFP with small angular quartz eyes ± volcanic fragments.....	15
2.4.1.4.2 Pre-mineral fragmental QFP .....	15
2.4.1.4.3 Pre-mineral QFP with large quartz eyes .....	16
2.4.1.4.4 Post-mineral Red Dog intrusion - QFP with large quartz eyes and hematite alteration .....	16
2.4.1.4.5 Post-mineral fine grained QFP with hematite alteration.....	17
2.4.1.5 Post-mineral diorite.....	17

2.4.2 Lithogeochemistry of rock units .....	18
2.4.3 Alteration types.....	20
2.4.3.1 Proximal-type alteration.....	21
2.4.3.2 Distal-type alteration.....	21
2.4.3.3 Background alteration.....	22
2.4.3.4 Post-mineral alteration .....	22
2.4.4 Alteration geochemistry .....	23
2.4.4.1 Alteration indices .....	23
2.4.4.2 Pearce-element ratios diagrams .....	24
2.4.4.3 Mass balance.....	24
2.4.5 Vein types .....	25
2.4.5.1 Pre-mineral veins .....	26
2.4.5.2 Syn-mineral veins .....	26
2.4.5.3 Post-mineral veins.....	27
2.4.6 Structural Features .....	29
2.4.6.1 D <sub>1</sub> event: regional scale folding.....	29
2.4.6.2 D <sub>2</sub> event: N-ENE structures .....	29
2.4.6.2.1 D <sub>2a</sub> event: pre- to syn-mineral N-ENE structures .....	30
2.4.6.2.2 D <sub>2b</sub> event: post-mineralization ENE structures - the Mazères deformation zone .....	31

2.4.6.3 D3 event: late brittle faults.....	31
2.4.6.4 D4 event: late tilting.....	32
2.4.7 Gold mineralization, vein geometries, ore petrography and relative timing of the Au event.....	32
2.4.7.1 Types of Au ore .....	32
2.4.7.1.1 Vein-type mineralization .....	33
2.4.7.1.2 Replacement-type mineralization .....	34
2.4.7.1.3 High-grade gold .....	34
2.4.7.2 Ore petrography .....	35
2.4.7.3 Geochemistry of gold mineralized samples .....	35
2.4.7.4 Relative timing of gold mineralization .....	36
2.4.8 U-Pb Geochronology .....	37
2.5 Discussion .....	38
2.5.1 Timing and nature of magmatism and Au mineralization.....	38
2.5.2 Structural and hydrothermal evolution of the Windfall Gold Deposit .....	40
2.5.3 Early ca. 2698 Ma Au mineralization in the Abitibi greenstone belt .....	42
2.5.4 Nature of mineralization and elemental signature .....	44
2.5.5 Proposed geological classification of the Windfall gold deposit .....	45
2.6 Conclusions .....	48
2.7 References .....	50

2.8 Figures .....	58
2.9 Tables .....	84
Chapter 3: A fluid chemical study of the Archean Windfall gold deposit, Quebec, Canada:	
Evidence for fluid mixing in an intrusion-related gold system.....	89
Abstract .....	90
3.1 Introduction .....	92
3.2 Geology of the Windfall gold deposit.....	94
3.2.1 Rock types and timing constraints.....	95
3.2.2 Alteration Types .....	97
3.2.3 Vein types and mineralization styles .....	98
3.2.4 Deformation history.....	99
3.2.5 Ore zones geometries.....	100
3.3 Methods.....	102
3.3.1 Previous geological studies and research .....	102
3.3.2 Petrography, mineral identification and mineral chemistry .....	102
3.3.3 LA-ICP-MS pyrite mapping and binary plots .....	103
3.3.4 Cathodoluminescence.....	104
3.3.5 Fluid inclusions petrography and microthermometry .....	105
3.3.6 Carbon isotopes of FI extracts .....	106
3.3.7 SIMS in situ oxygen isotopes .....	107

3.3.8 SIMS in situ sulfur isotopes of pyrite.....	108
3.4 Results.....	108
3.4.1 Ore petrography and mineral identification.....	108
3.4.2 Cathodoluminescence of quartz.....	109
3.4.3 Fluid inclusions petrography and inclusion types .....	110
3.4.4 Microthermometric measurements and PTX calculations.....	112
3.4.5 Stable isotopes .....	115
3.4.5.1 $\delta^{18}\text{O}$ values for magmatic and hydrothermal quartz .....	115
3.4.5.2 $\delta^{13}\text{C}$ of fluid inclusion extracts .....	115
3.4.5.3 $\delta^{34}\text{S}$ of pyrite.....	116
3.4.6 LA-ICP-MS mapping and $\delta^{34}\text{S}$ of pyrite.....	116
3.5 Discussion.....	118
3.5.1 Cathodoluminescence observations.....	118
3.5.2 Implications of O and S isotope data for fluid reservoirs.....	121
3.5.2.1 Oxygen isotopic data.....	121
3.5.2.2 Sulfur isotopic data .....	124
3.5.3 Implications of fluid inclusions .....	126
3.5.3.1 Fluid inclusion types, timing of entrapment and post-entrapment changes.....	126
3.5.3.2 PTX conditions for vein fluids.....	129
3.5.3.3 Origin and implications of the aqueous and carbonic fluids.....	131

3.5.4 Implications of pyrite mapping for primary and secondary gold enrichment .....	135
3.5.5 A working model for Windfall gold deposit .....	138
3.6 Conclusions .....	142
3.7 References .....	143
3.8 Figures .....	156
3.9 Tables .....	178

## List of Figures

Figure 2.1. Geological map of the Urban-Barry greenstone belt and stratigraphic column.....	58
Figure 2.2. Surface and cross-section geology maps of the WGD.....	59
Figure 2.3. Photographs of synvolcanic rock types.....	60
Figure 2.4. Photographs of intrusive rock types.....	61
Figure 2.5. Photomicrographs of QFP intrusions from the WIC.....	62
Figure 2.6. Geochemical data plots: Pearce (1996) and Jensen (1976) plots for volcanic rocks, and Y versus Zr and TiO <sub>2</sub> versus Zr plots for volcanic and intrusive rocks.....	63
Figure 2.7. Major and trace element geochemistry plots for the WIC.....	64
Figure 2.8. Photographs of alteration types.....	65
Figure 2.9. Geochemical data of volcanic and intrusive rock types plotted in Alteration Box plots and Pearce element ratio diagrams.....	66
Figure 2.10. Mass balance plots for pre-mineral large quartz eye QFP dike.....	67
Figure 2.11. Photographs of pre-mineral and post-mineral veins.....	69
Figure 2.12. Photographs of syn-mineral veins.....	71
Figure 2.13. Geological map of the WGD and stereoplots for foliation and mineralized veins in each zone.....	73

Figure 2.14. Photographs of pre- to syn- and post-mineral deformation associated to D <sub>2</sub> deformation event.....	74
Figure 2.15. Underground geology map of the Lynx bulk zone and photographs of mineralization types observed.....	76
Figure 2.16. Photomicrographs of syn-mineral veins.....	78
Figure 2.17. Geochemical plots of high-grade gold samples and EMPA analysis of gold grains.	80
Figure 2.18. Photograph of the post-mineral intrusion cross-cutting gold mineralization as observed in surface exposure and drill core.....	81
Figure 2.19. Concordia plots for U-Pb zircon analyses of a felsic volcanic, pre- and a post-mineral QFP intrusions.....	82
Figure 2.20. Paragenesis summarizing the sequence of events for the WGD.....	83
Figure 3.1. Geological map of the Urban-Barry greenstone belt.....	156
Figure 3.2. Surface and cross-sections of the WGD.....	157
Figure 3.3. Photographs of volcanic and intrusive rocks in the WGD.....	159
Figure 3.4. Photographs of pre-mineral and post-mineral veins.....	161
Figure 3.5. Photographs of replacement-type mineralization.....	163
Figure 3.6. Photographs of vein-type mineralization.....	164
Figure 3.7. Paragenesis summarizing the sequence of events for the WGD.....	165
Figure 3.8. Photomicrographs of ore mineralogy from syn-mineral veins and replacements.....	166

Figure 3.9. Photomicrographs of different pyrite types.....	168
Figure 3.10. Cathodoluminescence images of select quartz types and Results of SIMS $\delta^{18}\text{O}$ of quartz analyses .....	169
Figure 3.11. Photomicrographs of fluid inclusion types.....	170
Figure 3.12. Bar, binary and isochore plots for fluid inclusion microthermometry data.....	171
Figure 3.13. Reflected light images of zoned pyrite with results of SIMS $\delta^{34}\text{S}$ of pyrite.....	172
Figure 3.14. LA-ICP-MS trace element map and binary plots of pyrite from syn-mineral vein and replacements.....	173
Figure 3.15. LA-ICP-MS trace element map and binary plots of pyrite from syn-mineral vein and replacements.....	174
Figure 3.16. LA-ICP-MS trace element map and binary plots of pyrite from syn-mineral vein and replacements.....	175
Figure 3.17. Quartz-water fractionation diagram calculated from SIMS $\delta^{18}\text{O}$ of quartz.....	176

### List of Tables

Table 2.1. Average compositions of least altered phases of the WIC used for calculations of crystallization pressure.....	84
Table 2.2. Average major and trace element geochemistry from progressively altered large quartz eye QFP intrusion from the WGD.....	85
Table 2.3. Calculated gains and losses from progressively altered large quartz eye QFP intrusions.....	86
Table 2.4. Trace element geochemistry from gold mineralized sample that grade > 10 g/t Au...	87
Table 2.5. Summary of U-Pb zircon geochronology.....	88
Table 3.1. Microthermometry data for carbonic fluid inclusions (type 1a) .....	178
Table 3.2. Microthermometry data for aqueous-carbonic fluid inclusions (type 1b) .....	180
Table 3.3. Microthermometry data for aqueous fluid inclusions (type 2) .....	180
Table 3.4. Data from $\delta^{18}\text{O}$ isotope analyses of quartz.....	181
Table 3.5. Data from $\delta^{13}\text{C}$ isotope analyses of fluid inclusion extracts.....	183
Table 3.6. Data from $\delta^{34}\text{S}$ isotope analyses of pyrite .....	184

## **List of Appendices**

- Appendice A: Trace element geochemistry for QFP dikes of the WIC..... (separate file)
- Appendice B: Mass Balance table..... (separate file)
- Appendice C: U-Pb geochronology table for QFP dikes..... (separate file)
- Appendice D: LA-ICP-MS operating conditions for geochronology at Geotop..... (separate file)
- Appendice E: O-C-S tables for isotope data ..... (separate file)
- Appendice F: Fluid inclusion tables ..... (separate file)

## **Chapter 1: Introduction**

### **1.1 Research problem and thesis objectives**

The Windfall gold deposit located in the Urban-Barry greenstone belt is a recently explored Archean age lode-gold deposit that is coeval with calc-alkaline felsic magmatism dated ca. 2698 Ma (U-Pb zircon). Over the past few years (i.e., 2014 to present), the deposit has been extensively explored mainly by diamond drilling (i.e., >1 million metres) and underground exploration which began in 2018. This work has established a spatial and temporal association between felsic magmatism and high-grade gold mineralization (measured and indicated resource of 6.023 Mt at 9.6 g/t Au and an inferred resource of 16.401 Mt at 8.0 g/t Au; Richard et al., 2021) and thus demonstrates its potential to be interpreted as a possible Archean intrusion-related gold deposit. This thesis aims to document and interpret the geology of the Windfall gold deposit through the integration of comprehensive field work and complementary laboratory studies to assess the genesis of the deposit and develop an ore-deposit model.

### **1.2 Structure of thesis**

This thesis is written as three separate chapters. Chapter 1 provides an introduction to the thesis and outlines the research problem, objectives, and structure of the thesis. Chapter 2 is written as a manuscript for submission to a scientific journal and is entitled: “*Geological and geochemical features of the Archean Windfall gold system with a preliminary classification*”. Chapter 3 is written as a manuscript for submission to a scientific journal and is entitled: “*A fluid chemical study of the Archean Windfall gold deposit, Quebec, Canada*”.

## **Chapter 2: Geological and geochemical features of the Archean Windfall gold system with a preliminary classification**

Brandon Choquette<sup>1</sup>, Daniel J. Kontak<sup>1</sup>

<sup>1</sup>*Mineral Exploration Research Centre, Harquail School of Earth Sciences, Laurentian University, Sudbury, Ontario, P3E 2C6*

### **Abstract**

The Windfall gold deposit (WGD) is an Archean greenstone belt-hosted gold deposit located in the Urban-Barry greenstone belt of the Abitibi Subprovince, Québec (Canada). Extensive drilling (~1,300,000 m since 2016) has defined a measured and indicated resource of 6.023 Mt at 9.6 g/t Au (1.86 Moz) and an inferred resource of 16.401 Mt at 8.0 g/t Au (4.24 Moz). Gold mineralization is hosted in a package of bi-modal 2705 Ma volcanic rocks that record greenschist facies metamorphism and folding related to a D<sub>1</sub> event that formed an open, ENE-trending fold plunging about 35° NE. This stratigraphy is intruded by several generations of ENE-trending calc-alkaline granodiorite quartz-feldspar porphyry dikes (QFP) that are separated into two groups: 1) pre-mineral QFP (2698 ± 3 Ma) which hosts the Au mineralization and associated hydrothermal alteration; and 2) post-mineral QFP (2697.6 ± 0.4 Ma) which truncates the former, as observed in drill core. The early dikes are coeval with and overprinted by D<sub>2</sub> faults and a penetrative schistosity that locally intensify to shear zones.

Gold mineralized zones are localized to deformation zones and form thin, subvertical and elongate lensoids plunging moderately towards the ENE. These zones are further subdivided into areas: 1) spatially associated with contacts between pre-mineral QFP dikes and volcanic rocks; and 2) where strong chemical contrasts between Fe-Mg rich lithologies and felsic rocks. Two styles of Au mineralization occur: 1) grey to colorless quartz veins and stockworks with

subordinate carbonate-pyrite-tourmaline; and 2) pervasive- to patchy sericite-carbonate  $\pm$  silica  $\pm$  tourmaline  $\pm$  fuchsite alteration with disseminated pyrite-tourmaline. Pyrite dominates with traces of arsenopyrite, sphalerite, chalcopyrite, tennantite-tetrahedrite, galena, native gold, electrum and locally minor Sb-rich and complex telluride phases with the associated gold occurring as free gold and as inclusions in pyrite. Gold was emplaced during two distinct events: 1) a main one (+6 Moz) between the pre- and post-mineral QFP dikes; and 2) a later stage remobilization event.

The spatial and temporal association of the QFP intrusions and Au at the WGD suggests an intrusion-related model which has important implications for both local and regional exploration in this and similar Archean greenstone terranes.

## **2.1 Introduction**

The geology and nature of gold deposits are known to vary considerably, in particular with regards to the host rocks, styles of mineralization, nature of alteration, degree of deformation and depth of formation, which collectively are used to define deposit settings or types (e.g., Poulsen et al., 2000; Goldfarb et al., 2005; Robert et al., 2007). In regards to major gold deposit types, the intrusion-related class which includes: 1) oxidized Phanerozoic Cu-Au and Au only intrusion-hosted deposits (e.g., stockwork, skarns; e.g., Sillitoe, 2010) that relate to arc-type magmatism and generally restricted to the Phanerozoic, although exceptions are known (e.g., Archean Côte Gold; Katz et al., 2017, 2021); 2) the reduced-intrusion related (RIR) that are characterized by a Te-Bi-W-As elemental association and associated to post-collisional extensional magmatism of mainly Phanerozoic age (e.g., Thompson et al., 1999; Hart, 2007); and 3) Archean oxidized Au (Te-Ag) deposits centred on intermediate- to felsic intrusions, also

known as the syenite-associated deposits (e.g., Young-Davidson, Macassa, Upper Beaver, Lac Bachelor, Beattie; see Robert, 2001; Monecke et al., 2017) which are most prominent in the Archean Abitibi greenstone belt (AGB). Defining the type of gold deposit and its attributes is critical to both the development of exploration models, our understanding of metallogeny of gold systems, but also, and most importantly, how a deposit is modeled for ore reserves and mining (e.g., Robert et al. 2005, 2007; Goldfarb and Groves 2015). It is these aspects of gold deposits which this study addresses, specifically the recently explored Windfall gold deposit (WGD) of Osisko Mining Inc. which has a measured and indicated resource of 6.023 Mt at 9.6 g/t Au (1.86 Moz) and an inferred resource of 16.401 Mt at 8.0 g/t Au (4.24 Moz) (Richard et al., 2021). Given the size of this resource and lack of a gold-equivalent significant deposit type in the Urban-Barry greenstone belt (UBGB; Fig. 2.1A, B), the study has metallogenic implications the UBGB and for the entire contiguous AGB.

The WGD lies in the underexplored UBGB, an eastward continuation of the gold endowed AGB (~230 Moz Au; Monecke et al., 2017). Previous discoveries and studies in this belt, such as the Barry gold deposit (Kitney et al., 2011), suggest gold mineralization equates to the classic orogenic or greenstone-hosted quartz-carbonate type (Goldfarb et al. 2005; Dubé and Gosselin, 2007). However, the latter inference is in question given that recent and continued development of the WGD has defined a close spatial and temporal association of gold with a suite of felsic (i.e., granodiorite) intrusions well constrained to ca. 2698 Ma (TIMS U-Pb zircon; see below). Thus, one aspect of this study is to focus on this apparent relationship and better address if it is an intrusion-related versus intrusion-associated deposit.

Here we present the first overview of the geology of the WGD which defines the characteristics of the host rocks, alteration and vein types, mineral paragenesis, structural aspects

and characteristics of gold mineralization. The study is based on an extensive database which includes drill core logs, litho-geochemistry, structural measurements on oriented core, and petrographic study of select samples. A complementary paper (see chapter 3) addresses the fluid-chemical aspects (e.g., fluid inclusion, isotopes, trace-element geochemistry of pyrite) of the deposit and further explores the deposit model presented below.

## **2.2 Regional geological setting**

### **2.2.1 Abitibi greenstone belt**

The AGB, located in the southeastern portion of the Archean Superior Province, is a 300 km by 700 km east-west trending assemblage of supracrustal rocks composed of folded and deformed mafic- to felsic volcanic rocks, sedimentary basins, and series of plutonic suites. The volcano-sedimentary sequences span ca. 120 myr from 2795 to 2670 Ma and, based on lithological, geochemical and geochronology data, is divided into 11 geological assemblages (Ayer et al., 2005), which is further supported by the documented presence of depositional gaps and unconformities (Thurston et al., 2008).

The AGB is host to numerous gold-rich deposit types (see Monecke et al. 2017), the most significant of which includes volcanogenic base-metal  $\pm$  Au massive sulfide (e.g., Horne, Kidd-Creek, LaRonde-Penna), lode gold (e.g., Hollinger, Dome, Sigma-Lamaque), syenite-associated gold (e.g., Young-Davidson, Macassa, Douay) and the recently defined intrusion-related clan (e.g., Côte Gold, Doyon). Of particular note here is the age of the subvolcanic intrusions and volcanic rocks in the Doyon-Bousquet-LaRonde mining camp of ca. 2698 Ma (Mercier-

Langevin 2007; Galley and Lafrance 2014), this being the age of the felsic dikes at the WGD site.

### **2.2.2 Urban-Barry greenstone belt**

The WGD is located in the UBGB, part of the Abitibi Subprovince (Fig. 2.1A, B), and its geology is described by previous workers (Milner, 1939; Joly, 1990; Bandyayera et al., 2002; Bandyayera et al., 2003; Bandyayera et al., 2004a, b; Rhéaume et al., 2004; Rhéaume and Bandyayera, 2006; Kitney et al., 2011). The latter contributions form the basis of what is summarized below.

The UBGB is overall an E-W trending, 6.5 to 20 km wide and 70 km long belt dominated by mixed mafic- to felsic volcanic rocks with lesser clastic sedimentary sequences. This sequence was deformed into open- to tight, variably plunging folds during the 2.71 to 2.66 Ga Kenoran orogeny (Card, 1990). There are several major deformation zones that cut the UBGB with most trending NE. These features are considered as splays (i.e., second-order structures) off the first-order, E-W trending Urban deformation zone (Fig. 2A). The rocks generally record greenschist grade metamorphism (i.e., albite-chlorite-carbonate assemblage), but locally can reach amphibolite facies (amphibole, plagioclase, epidote, biotite, and quartz) within corridors of intense deformation and proximal to large felsic pluton contacts (Joly, 1990).

The belt is divided into five rock formations constrained to 2791 to 2707 Ma (Fig. 2.1C) (Rhéaume and Bandyayera, 2006), including: 1) the Fecteau (2791 Ma), 2) the Lacroix (undated), 3) the Chanceux (2727 Ma), 4) the Macho (2717 Ma) and 5) the Urban (2714 to 2707 Ma) formations. The WGD is hosted in volcanic rocks mapped as part of the Macho Formation which contains two distinct lithostratigraphic sequences: the Rouleau member and the younger

Windfall member ( $2716.9 \pm 2$  Ma). The Rouleau member is comprised of: 1) calc-alkaline to transitional andesite to andesite-basalt lapilli tuffs; 2) tholeiitic basalts; and 3) mudstones. The Windfall member is comprised of: 1) calc-alkaline dacite, rhyodacite and trachyandesite; 2) tholeiitic felsic tuffs and lavas; 3) tholeiitic to transitional andesite porphyries and tuffs; and 4) minor iron formation (Bandyayera 2002, Rhéaume and Bandyayera, 2006). Recent dating of the youngest felsic volcanic unit at the WGD (see below) indicates an age of  $2705 \pm 4.2$  Ma (Azevedo, 2019). This volcano-sedimentary sequence is cut by a series of quartz feldspar porphyry dikes that are constrained by U-Pb zircon dating to  $2697.6 \pm 0.4$  Ma at the WGD site (D. Davis unpublished report to Osisko Mining Inc., 2017 and see below) and  $2697.1 \pm 0.6$  Ma at the nearby Barry gold deposit (Kitney et al., 2011) located about 10 km southwest of the WGD.

## **2.3 Methods**

### **2.3.1 Previous geological studies**

The current study benefits from earlier work that is incorporated into the present synthesis of the deposit geology: 1) various geological studies focusing on the understanding and genesis of the Windfall deposit that previously suggested an intrusion-related model (El-Rassi et al., 2011; Padilla and Savard, 2018), with several other unpublished internal reports by various authors including H. Poulsen (2016) and R. Sillitoe (2017) who also suggested a high-level intrusion-related gold setting; 2) fifteen internal petrographic reports that includes one by C. Leitch (2012; Vancouver Petrographics), thirteen by L. Tremblay (2014 to 2019; IOS Services Géoscientifiques) and one by É.C. Lavoie (2020; Osisko Mining). These reports describe the volcanic and intrusive rocks, as well as the characteristics of alteration and mineralization; 3) U-Pb geochronology on felsic intrusive rocks (Jack Satterly Laboratory, University of Toronto,

ON) and the youngest felsic volcanic unit (Geotop Laboratory, Université du Québec à Montréal, QC) in the deposit area, the methodology of which is provided below; 4) several internal lithogeochemical studies from 2014-2019 using ALS laboratories (Vancouver, BC) most notable by R. Sproule (2017) and V. Pearson (2019) whose work focused on defining the major- and trace-element signatures of the least altered and altered intrusive and volcanic rock units, and alteration geochemistry associated to the gold mineralization. The protocol is provided below and its relevance is apparent in the following discussion; 5) an internal gold department study by R. Padilla (2016; Talisker Exploration Services) which is a resource that characterizes the ore-related minerals by using reflected light microscopy and microprobe analyses; and 6) various structural interpretations of the geologic setting of the Windfall deposit by V. Pearson (2016; 2019).

### **2.3.2 Field work and sampling**

Field studies involved 16 months of work done over three field seasons. During this time, logging of about 70 diamond drill-holes (DDH) totaling 35 000 m of core from throughout the deposit area was done to identify rock types in addition to characterizing the occurrences and styles of alteration and mineralization. This work provided the basis to: 1) construct a paragenesis based on cross-cutting relationships of dike rocks and different vein generations; 2) draft cross-sections, visualize and map 3D geometries using Leapfrog 3D software; and 3) collect 30 samples for further detailed petrographic and lithogeochemical analysis.

### **2.3.3 Handheld XRF analysis**

An Olympus Vanta Handheld X-Ray Fluorescence Analyzer (XRF) previously calibrated with standards was for several years used as part of the logging protocol at WGD to discriminate

rock types, in particular between felsic volcanic and intrusive rocks. Analysis was done on dried core with an acquisition time of 40 seconds which was sufficient to confidently differentiate the various felsic lithologies which are otherwise very similar in hand sample, but differ in their trace-element signatures (e.g.,  $\text{TiO}_2/\text{Zr}$ ,  $\text{Y}/\text{Zr}$ ).

#### **2.3.4 Petrography**

Polished thin sections, mainly from drill core samples, were studied in reflected and transmitted light using an Olympus BX-51 microscope. The focus of this work was on the mineralogy and texture of the various intrusive rocks, in addition to the alteration and ore mineralogy of mineralized zones. This work was supplemented with use of a JEOL 6400 scanning electron microscope (SEM) coupled to a solid-state Oxford-Sight energy dispersive spectrometer (EDS) housed in the Micro-Analytical Centre (MAC), Laurentian University, Sudbury, ON. Operating conditions used were: 20 kV accelerating voltage, a 1 nA beam current, working distance of 15 mm and acquisition times of 5 to 10 seconds. The collected data were processed offline with an integrated calibration and application (INCA) software.

#### **2.3.5 Whole-rock lithochemistry**

The whole-rock geochemistry database for the WGD consists of 19,658 samples that were collected during various periods of exploration from 2014 to 2020. Three different protocols were used, as described below.

First, a total of 38 core samples from volcanic and intrusive rocks were collected by Eagle Hill Corp. (now Osisko Mining Inc.) to: 1) provide a general characterization of rocks in the WGD; and 2) define geochemical signatures for the different rock types. Analysis for major-

and trace elements was done at ALS Minerals (in Vancouver, BC; see <https://www.alsglobal.com>). Samples were first crushed to 70% <2 mm rifle split and then pulverized to 85% < 75 µm. The powders were then analyzed for major elements using X-ray fluorescence (analytical packages ME-XRF05 and ME-XRF-06), whereas trace elements were analyzed using a lithium-borate-fusion (analytical package ME-MS81h).

Second, a total of 19,590 drill core samples collected during drilling activities from 2014 to 2020 by Osisko Mining Inc. and predecessors were used for: 1) monitoring the consistency of core logging; 2) characterizing (i.e., fingerprinting) alteration and mineralization; and 3) generating a robust geochemical database for the rock units. Samples were analyzed at ALS Minerals (in Vancouver, BC) with the same preparation noted above. The prepared powders were used for LOI (500°C using a 1 gram sample) and analyzed for major and trace elements using X-ray fluorescence (analytical packages ME-XRF05 and ME-XRF26; <https://www.alsglobal.com>).

Third, a total of 30 core samples from least altered QFP intrusive rocks were collected during this study to: 1) characterize least-altered rocks; and 2) use the data to assess paleo-tectonic setting and petrogenesis. Samples were analyzed at the Geoscience Laboratories, Sudbury, ON following their pulverizing in an aluminum oxide ball mill to 90 µm. Loss on ignition (LOI-3ST) was analyzed in a 3-step protocol by heating the sample to 105°C, 500°C and 1000°C. Ferrous iron was analyzed using potentiometric titration with a standard permanganate solution (FEO-ION). Major elements were analyzed using the major element XRF method (XRF-M01) and trace elements were prepared with a closed vessel multi-acid digest (SOL-CAIO) and analyzed with an inductively-coupled plasma mass spectrometry (ICP-MS) (IMC-

100). Further details regarding samples preparation and methods of analysis are available at <https://www.mndm.gov.on.ca>.

### **2.3.6 Multi-element ore geochemistry**

The multi-element geochemistry database for the WGD consists of roughly 190,000 samples that were collected from various periods of exploration from 2014 to 2020. A subset of this dataset (n = 247) containing mineralized samples that graded >10 g/t Au were further analyzed for a variety of trace elements. These materials were analyzed at ALS Minerals (Vancouver, BC) after being crushed to 70% at <2 mm, rifle split and then pulverized to 85% < 75 µm. The powders were then dissolved using a four-acid digestion and analyzed with an ICP-MS (analytical package ME-MS61; see <https://www.alsglobal.com>).

### **2.3.7 EMPA analyses**

The aforementioned internal study by R. Padilla (2016) primarily aimed to identify sulfide minerals and their chemistry and the deportment of gold. The petrographic work and mineral chemistry, done at the Lunar and Planetary Science Department of the University of Arizona, USA, used polished thin sections studied in reflected and transmitted light with select samples analyzed using a CAMECA SX-100 microprobe. A total of 358 points were analyzed for 11 elements (S, Fe, Cu, Zn, Ag, Au, Te, Pb, Bi, As, Sb) in pyrite, chalcopyrite, sphalerite, galena, tennantite, arsenopyrite, Bi-Te mineral grains, Ag-Sb-S mineral grains, and native Au/electrum grains. The data are used here for identifying ore related minerals, and to assess the Au:Ag ratio of gold grains (n = 50).

### 2.3.8 U-Pb zircon dating

The results of high-precision U-Pb dating undertaken by Eagle Hill Corp. on two sample sets are particularly relevant to the present study and are therefore reported here. The first set of samples were the felsic intrusive rocks and were analyzed at the Jack Satterly Geochronology Laboratory, University of Toronto, ON, using chemical abrasion (CA) isotope dilution (ID) thermal ionization mass spectrometry (TIMS) following protocol detailed in Krogh (1973) and Mattinson (2005). Results of this initial work on four single zircon grains from each of the two samples gave concordant dates, but had  $^{207}\text{Pb}/^{206}\text{Pb}$  ages outside of error over ranges of 2714-2698 Ma (EAG-15-552) and 2715-2701 Ma (OBM-16-579). Because of this, a second round of analysis was carried out. The latter used polished zircon grains that had been imaged by backscattered electron (BSE) and cathodoluminescence (CL) modes to detect and avoid cores. These grains were removed from their epoxy mount, cleaned and dissolved for U-Pb analysis following the above method.

The second set of samples were analyzed at the Geotop Laboratory, University of Québec in Montréal, by using a high-resolution laser ablation inductively coupled plasma mass spectrometry (HR-LA-ICP-MS). Approximately 10 kg of rhyolite was collected from an underground exposure at the WGD site. The samples were crushed with a jaw crusher and a disc grinder and zircons were separated using a Wifley table, Frantz magnetic separator and heavy liquids. Select zircon grains were handpicked under a binocular microscope and were mounted in resin and polished to 1  $\mu\text{m}$ . The mounted zircons were examined and imaged by a scanning electron microscope (SEM) in BSE and by CL in order to determine the internal structure of the zircon to select areas for analysis. U-Pb-Th analyses were done using a Nu Attom HR-ICP-MS. The zircon standard used for calibration of the  $^{206}\text{Pb}/^{238}\text{U}$  was 91500 (Wiedenbeck et al., 1995).

Data treatment was performed C. Azevedo by using IOLITE (Paton et al., 2011) and ISOPLOT (Ludwig 2012) software for data statistics and calculations. Further information regarding the instrument operating conditions and methodology are provided in the appendix D.

## **2.4 Results**

### **2.4.1 Geology of the Windfall gold deposit**

The WGD is a structurally controlled, gold-bearing quartz and sulfide vein and replacement-type deposit. Gold mineralization overprints a sequence of volcanic rocks which are cut by a pre-mineralization felsic dike complex (Fig. 2.2A-C). In turn, this mineralized package is crosscut by later felsic- and mafic dikes. The volcanic succession is composed of mafic, intermediate and felsic lavas and rare thin clastic sedimentary horizons that are crosscut by mafic to ultramafic sills. The felsic complex, called the Windfall intrusive complex (WIC), is composed of a series of quartz-feldspar porphyritic granodiorite dikes. The gold mineralization is hosted in deformation zones localized spatially to the contacts between certain quartz-feldspar porphyry dikes and the host volcanic rocks. All rock types have been variably deformed, hydrothermally altered and overprinted by deformation and metamorphism.

#### *2.4.1.1 Volcanic rocks*

The volcanic strata strike predominantly N to ENE and dip roughly 45 to 80° towards the E-SE. All rocks record the effect of regional greenschist grade metamorphism and have a variably developed weak to moderate, penetrative schistosity that generally parallels the volcanic strata and strike N with a dip 40° towards the E. Representative rock pictures are presented in Figure 2.3.

The lowermost stratigraphic section consists of volcanic units are basaltic to andesitic in composition, fine-grained to aphanitic and medium- to dark green. Texturally these massive, pillowed, fragmental, and brecciated volcanic flows are locally vesicular or porphyritic with phenocrysts of plagioclase and rare quartz eyes (<1 cm) (Fig. 2.3A, B). Lying above these mafic lava flows are felsic volcanic rocks of dacitic- to rhyolitic composition. These are beige-grey and are massive to fragmental with local porphyritic textures defined by small (1-3 mm) phenocrysts of quartz (2-10%) and locally contain sub-rounded pyrite clasts (Fig. 2.3C-F).

#### *2.4.1.2 Synvolcanic sedimentary horizons*

In the Lynx zone of the deposit (see Fig. 2.2C), locally thin horizons (0.3-1 m) of argillite and mudstone are interbedded within the felsic volcanic sequence. These sedimentary units have a dark grey-green color, are fine-grained, are bedded, and contain laminations of mixed pyrite-pyrrhotite of up to 2% (Fig. 2.3G)

#### *2.4.1.3 Mafic intrusive rocks*

Throughout the deposit, mafic- to ultramafic sills and dikes are observed cutting the mafic and felsic volcanic package (Fig. 2.3H, I). These intrusions are laterally extensive and range from <1 m to >300 m in thickness. The intrusions range from a basaltic to komatiitic composition and are massive, fine-grained rocks with a medium- to dark green color.

#### *2.4.1.4 Windfall intrusive complex*

The Windfall intrusive complex (WIC) was formed during seven distinct phases of felsic magmatism. The complex, observed crosscutting the volcanic strata at high angles, forms dikes

and stocks that are subvertical to the present surface (Fig. 2.2B, C). The dikes are divided into three main groups based on several distinguishing criteria: color, texture, quartz phenocryst size and abundance, and orientation. Representative rock and thin section pictures are presented in Figures 2.4 and 2.5, respectively.

#### *2.4.1.4.1 Pre-mineral QFP with small angular quartz eyes ± volcanic fragments*

These QFP intrusions are the first phase of the WIC, it is light grey, massive to porphyritic with an aphanitic- to fine-grained groundmass. Where it is porphyritic, it has 2-10 % quartz phenocrysts of <2 mm size (Fig. 2.4A). In thin section, it is generally composed of fine-grained quartz and feldspar in the groundmass with altered phenocrysts of plagioclase showing polysynthetic twinning and sub-rounded to irregular quartz phenocrysts; in addition, there is minor sericite, carbonate, and minor chlorite, rutile and apatite. Locally the unit is fragmental with up to 30% sub-angular volcanic rock fragments ( $\leq 1$  cm) of intermediate to felsic compositions. These intrusive bodies strike N to ENE and dip 35 to 90° towards the E-SE.

#### *2.4.1.4.2 Pre-mineral fragmental QFP*

This unit is located along the contacts of the previously mentioned pre-mineral QFP intrusions with small quartz eyes and locally has sharp- to gradational contacts with the pre-mineral QFP with small angular quartz eyes. It is light grey to beige, varies from massive to fragmental with an aphanitic groundmass. Unlike the previous QFP unit, it contains clasts of sub-rounded- to angular fragments of varied origin: 1) felsic- to mafic volcanic rocks; 2) QFP intrusive rocks; 3) tourmaline breccia cementing quartz and tourmaline altered clasts; and 4) quartz-pyrite fragments (Fig. 2.4B to D). This intrusive body strikes N to ENE and dips 35 to 90° towards the E-SE.

#### *2.4.1.4.3 Pre-mineral QFP with large quartz eyes*

These intrusives cut all the previously mentioned rock types. They are light grey to beige, porphyritic with an aphanitic groundmass. The porphyritic texture is due to <1 to 20 % sub-rounded quartz eyes (1-10 mm), variably altered feldspar phenocrysts, as seen both macroscopically and in thin section (Fig. 2.4E-G). In thin section, it is generally composed of fine-grained quartz-feldspar groundmass, altered phenocrysts of plagioclase showing polysynthetic twinning, sub-rounded quartz phenocrysts, sericite, carbonate, with minor chlorite, rutile, and apatite. This rock is subdivided into three groups based on abundance of quartz eyes and cross-cutting relationships: 1) the earliest phase consists of 10-20% sub-rounded blue-quartz eyes; 2) the second phase consists of 1-10% sub-rounded grey- to colorless quartz eyes; and 3) the last phase consists of <1% sub-rounded grey- to colorless quartz eyes. These intrusive bodies strike N to ENE dipping 35 to 90° towards the E-SE.

#### *2.4.1.4.4 Post-mineral Red Dog intrusion - QFP with large quartz eyes and hematite alteration*

The Red Dog intrusion cuts all volcanic and pre-mineral WIC units, but most importantly is observed to cut the gold-mineralized zones and associated areas of alteration. It is distinct with a red-to-orange to locally beige color, a massive- to porphyritic texture with an aphanitic groundmass. Where porphyritic, it contains 1-10% sub-rounded quartz eyes (1-10 mm) (Fig. 2.4H). In thin section, it contains a fine-grained quartz-feldspar groundmass, weakly altered phenocrysts of plagioclase showing polysynthetic twinning, sub-rounded quartz phenocrysts, carbonate, sericite, rutile and apatite. It is variably altered with a weak- to strong development of hematite after plagioclase and locally weak a chlorite and disseminated magnetite alteration. Locally along the margins of the intrusions, a late-stage Au-barren ankerite alteration associated

with late deformation is observed. The intrusion is on average 100 m thick, strikes N and dips 35° to the E.

#### *2.4.1.4.5 Post-mineral fine grained QFP with hematite alteration*

This intrusive phase cuts all volcanic and WIC units, except the Red Dog unit, but most importantly is also seen to cut gold mineralized zones and associated alteration. It has an aphanitic to fine-grained groundmass that is a pale beige to orange-red (Fig. 2.4I). In thin section, it is generally composed of fine-grained quartz and feldspar in the groundmass, in addition to carbonate and minor rutile and apatite, in the matrix with weakly altered phenocrysts of plagioclase showing polysynthetic twinning and, sub-rounded quartz grains. It has variably developed weak- to moderate pervasive hematite alteration of plagioclase and locally disseminated magnetite. As with Red Dog, along the margins of this intrusive unit is late-stage Au-barren ankerite alteration associated with late deformation. It is on average 15 m thick, strikes N and dips 35° to the E.

#### *2.4.1.5 Post-mineral diorite*

This minor diorite unit cuts all previous units in addition to the gold mineralized zones with associated alteration, thus it is the youngest magmatic event observed at the WGD. It is medium- to dark green, fine-grained with a moderate- to strong chlorite-ankerite alteration (Fig. 2.4J, K). These dikes are on average <1 m wide and oriented N-NE and dip shallowly to the E-SE.

## 2.4.2 Lithochemochemistry of rock units

An extensive suite of major- and trace-element analyses for all the rock units was used to classify the rocks, characterize their petrogenetic affinity (e.g., calc-alkaline) and assess the chemistry and extent of alteration present. Thus, plots using relatively immobile elements (i.e., Zr, Nb, Y, Ti, and rare earth elements (REE)) were used for these purposes, in addition to major elements. Based on earlier internal studies at the WGD, it is apparent that binary plots of  $\text{TiO}_2$  and Y versus Zr are the most useful for discriminating lithologies where alteration is developed because these elements show minor mobility during alteration.

The chemistry of the volcanic rocks ( $n = 6984$ ) defines two general groups of sub-alkaline rocks, one basaltic to andesitic and the other dacitic to rhyolitic (Fig. 2.6A, B) with both groups having tholeiitic to transitional affinities (Fig. 2.6C). The mafic- to ultramafic intrusive rocks ( $n = 2057$ ) are sub-alkaline, chemically homogenous and equate to high-Mg tholeiitic basalt to komatiite in composition and also have a tholeiitic affinity (Fig. 2.6A-C). All of the rocks except the rhyolite - the ultramafic, gabbroic and basaltic to andesitic - collectively cluster about a single fractionation trend in  $\text{TiO}_2$  versus Zr plot which is typical for tholeiitic suites (Pearce and Norry, 1979; Fig. 2.6D).

In contrast to the aforementioned suites, the chemistry of the WIC defines a single group of rocks that have a calc-alkaline affinity (Fig. 2.6C). Their composition is simply defined by removing samples that are significantly altered, indicated by the presence of sericite and carbonate, prior to using the classification diagrams. The pre-mineral QFPs define a strong depletion of  $\text{Na}_2\text{O}$  associated with an increase of  $\text{K}_2\text{O}$  due to feldspar destructive sericite alteration (Fig. 2.7A), whereas the post-mineral QFPs record much less of this alteration (Fig.

2.7B). Both the pre-mineral and post-mineral QFPs record carbonate alteration, as indicated by the increases in LOI (Fig. 2.7C). Based on the latter observations, the least altered WIC rocks have been filtered for sericite alteration which indicates that the Na<sub>2</sub>O contents for least altered pre-mineral and post-mineral QFPs are similar (i.e., 3.5-5 wt.% Na<sub>2</sub>O and 4.5-5.5 wt.% Na<sub>2</sub>O, respectively; see insets in Fig 2.7A, B). The remaining samples (n = 2053) were then filtered for LOI to remove the effects of variable carbonate alteration with the least altered WIC rocks having < 3 wt. % LOI. The resulting subset of data (n = 1148) is considered to reflect the least altered rock types for the WIC. Using normative mineral calculations for these least altered rocks (Kelsey, 1965), these data plot in the granodiorite field of a QAP plutonic rock classification (Fig. 2.7D; Le Maitre et al., 1989) and is consistent with a granodiorite classification using the TAS diagram (Fig. 2.7E; Middlemost, 1994).

The WIC rocks are also easily distinguished from the other rock suites, in particular felsic volcanic rocks, using binary plots of Y and TiO<sub>2</sub> versus Zr (Fig. 2.6C, D). For the WIC rocks, all samples overlap in both the extended mantle-normalized spider plot and also chondrite-normalized REE plot (Fig. 2.7F, G). In the former, samples are enriched in the lesser incompatible elements and have steep left-to-right slopes, in addition to positive anomalies for Cs, W, K, Pb, Mo and Sb, and negative anomalies for Nb, Ta, and Ti (Fig. 2.7F). These rocks also have strong negative sloping REE profiles due to LREE enrichment (i.e., [La/Yb]<sub>N</sub> = 26.69), but the HREE have a generally flat slope (Fig. 2.7G). They are also noted to lack an Eu anomaly, either positive or negative.

For the WIC rocks, the crystallization pressure of the felsic intrusions was estimated by using the numerical model presented in Yang et al. (2017, 2021). For this, data were first filtered for least altered equivalents and then filtered to remove sericite alteration by plotting all relevant

data in a Pearce-element ratio (PER) feldspar control diagram (Stanley and Russell, 1989; Stanley and Madeisky, 1996) and removing all data that exceeded 3% from the feldspar control line (see below). Data were then filtered for <3 wt.% LOI as to remove any remaining significant carbonate alteration. The resulting dataset is then averaged to get a single representative least altered chemistry for each rock type (Table 2.1). This data is then inputted in the provided spreadsheet from Yang et al., 2021. The calculations indicate that for the averaged pre-mineral small quartz eye QFP intrusions, the pressure equates to 138 MPa, whereas for the averaged pre-mineral large quartz eye QFP intrusions the pressure equates to 198 MPa. For the averaged post-mineral Red Dog intrusions, the pressure equates to 261 MPa, and for the averaged post-mineral fine-grained QFP intrusions, the pressure equates to 296 MPa. It is noted that the crystallization pressure for each phase of the WIC record a progressive increase from the earliest phase to the latest phases.

### **2.4.3 Alteration types**

Within the WGD four alteration assemblages are observed in the WGD based on drill core logging. Whereas some are developed over a regional scale of kilometers along major structures (e.g., chlorite-ankerite), others are only developed locally at a meter scale (e.g., silicification). The alteration assemblages are sub-divided into four types based on distribution and timing with respect to mineralization: 1) proximal, 2) distal, 3) background, and 4) post-mineral. A detailed summary of each type is presented below with representative rock and thin section pictures presented in Figure 2.8.

#### *2.4.3.1 Proximal-type alteration*

This alteration consists of sericite-ankerite  $\pm$  silica  $\pm$  tourmaline  $\pm$  fuchsite with an average of 1-10 % disseminated pyrite (Fig. 2.8A to D). Where most prevalent, it has a strong correlation with high Au grades and is referred to as replacement-type ore (see below). In drill core, it varies from a few cm to several meters and is heavily influenced by host-rock composition and intensity of deformation. Intermediate- to mafic rocks (e.g., andesite, basalt, gabbro) are bleached to a light grey-green color, have a moderate to strongly developed pervasive sericite-ankerite assemblage with a local pervasive to patchy silicification (Fig. 2.8A, B). More restricted is fuchsite and is seen as a pervasive or spotted alteration when mineralization is hosted in or immediately proximal (i.e., generally <5 m) to the gabbro or ultramafic units (Fig. 2.8C). Felsic rocks (i.e., rhyolite, QFP dikes) are beige to light grey with development of pervasive sericite-ankerite and locally pervasive silicification (Fig. 2.8D).

#### *2.4.3.2 Distal-type alteration*

This alteration consists of a sericite-ankerite  $\pm$  chlorite assemblage with an average of 0.1-5 % disseminated pyrite and minor disseminated tourmaline (<1%) (Fig. 2.8E to G). The alteration halo varies from zones of 1-2 m to zones extending >10 m from significant Au mineralized intervals. The degree of alteration is heavily influenced by host-rock composition and intensity of deformation. Intermediate- to ultramafic rocks are light green-grey to slightly bleached, have moderate to strongly developed sericite-ankerite assemblage that can be pervasive, patchy or fracture controlled with locally weak to moderate pervasive to patchy chlorite alteration (Fig. 2.8E, F). Felsic rocks are beige to light grey with a strong sericite-ankerite-pyrite alteration with local patchy silicification (Fig. 2.8G). This alteration is commonly

associated with low-Au grades. The combination of low-grade Au and the obliteration of primary volcanic and intrusive textures separate it from the background regional metamorphism.

#### *2.4.3.3 Background alteration*

The background mineral assemblage is one typical of greenschist facies metamorphism. It consists of a weak to moderate, pervasive to spotty chlorite, sericite and carbonate with local biotite, amphibole and epidote seen at depth in the deposit (Fig. 2.8H-I). This observation is consistent with the regional scale mineralogy noted by Bandyayera et al. (2001).

#### *2.4.3.4 Post-mineral alteration*

Two post-mineral hydrothermal alterations are observed: 1) post-mineral hematite  $\pm$  magnetite; and 2) ankerite. The timing of the alterations is constrained by cross-cutting relationships, as identified by observations in surface and underground exposures and in drill core.

The hematite alteration is only observed to affect the post-mineral QFP intrusions and is not associated with gold mineralization. This alteration is pervasive and varies from orange to red (Fig. 2.8J) and locally is associated with disseminated magnetite (Fig. 2.8K).

The late ankerite alteration is observed to overprint the entire deposit and is Au-barren. It is commonly observed overprinting post-mineral intrusions and is often concentrated along the geological contacts. The alteration occurs as a weak pervasive to spotty that is pale cream to white in color (Fig. 2.8L). In recently drilled core, this alteration is readily identifiable with a carbonate stain whereas in historic core it is orange-brown due to oxidation.

#### 2.4.4 Alteration geochemistry

The geochemical database for the WGD is used to further assess the types and extent of the different alteration types. In addition, elemental gains and losses (i.e., mass balance) are used to geochemically fingerprint the alteration types. For the latter, altered samples were compared to their least-altered equivalents, as explained below.

##### *2.4.4.1 Alteration indices*

Data are plotted in an alteration index (AI) diagram using the combined Ishikawa AI (AI; Ishikawa et al., 1976) and the chlorite-carbonate-pyrite index (CCPI; Large et al., 2001). The AI is used to quantify the intensity of chlorite and sericite alteration by looking at the principal rock forming elements gained (i.e., MgO + K<sub>2</sub>O, respectively) over the elements that are lost and/or gained (i.e., Na<sub>2</sub>O, CaO, MgO, K<sub>2</sub>O). At the WGD, alteration grades from a distal carbonate ± sericite with local chlorite (i.e., chlorite when in mafic-intermediate rocks) assemblage towards a proximal sericite-ankerite-pyrite ± silica ± tourmaline ± fuchsite assemblage. The AI quantifies the intensity of sericite alteration related to Au mineralization. In contrast, the CCPI measures the increase in MgO and FeO associated with chlorite formation, Mg-Fe carbonate and pyrite. Noted however is the dependence of this index on various parameters not specifically associated with mineralization, such as mafic and felsic protoliths.

The distribution of data for the different rocks types in the combined CCPI-AI alteration box indicate: 1) the mafic-intermediate rocks (basalt, andesite, gabbro) overlap the fields for least altered rocks and alteration having chlorite, Fe-Mg carbonate and pyrite ± sericite (Fig. 2.9A); 2) felsic volcanic rocks (rhyolite, dacite) mostly record sericite alteration and mostly fall outside the field for least altered rocks (Fig. 2.9A); 3) pre-mineral QFP dike rocks are displaced

from the field for least altered rocks (i.e., rhyolites) towards Fe-Mg carbonate and pyrite in addition to sericite alteration (Fig. 2.9B); and 4) in contrast to all of the altered rocks, the post-mineral QFP dike rocks (e.g., Red Dog intrusion) form a tight cluster and fall in the field for least altered rocks (Fig. 2.9B).

#### *2.4.4.2 Pearce-element ratios diagrams*

Pearce elements ratio (PER) diagrams (e.g., Stanley and Russell, 1989; Stanley and Madeisky, 1996) are used here to better define the chemistry of the alteration. Given that it is dominated by sericite and rocks spatially related to the Au mineralization are felsic intrusions, the control lines used are feldspar and muscovite, as monitored by using the molar ratio  $(2Ca+Na+K)/Zr$ . As  $Al_2O_3$  and Zr shows minor mobility during alteration (i.e., see mass balance below), it was treated as a conserved elements. As seen in Figure 2.9C, the pre-mineral QFP data define a trend that reflects formation of sericite as part of the phyllic alteration related to mineralization noted above. In contrast, data for the post-mineral QFP dike rocks (Fig. 2.9D) do not record this alteration and instead are centered on the feldspar control line.

#### *2.4.4.3 Mass balance*

The Grant (1986) isocon method is used to evaluate elemental gains and losses attending progressive alteration of the least altered to most altered samples for the pre-mineral QFP dikes with large quartz eyes. The respective plots are shown in Figure 2.10 and a summation of the main geochemical data and changes are presented in Tables 2.2 and 2.3.

Geochemical data for this one rock type (i.e., QFP) are simply separated into five sample groups that have decreasing  $Na_2O$  concentration from least- to most-altered as to track the

geochemical changes during the progressive feldspar destructive sericite alteration that is intimately associated with gold mineralization (Fig. 2.10A). For this rock type, oxides and elements such as  $\text{TiO}_2$ ,  $\text{Al}_2\text{O}_3$ , and Zr are interpreted to be conserved during alteration and therefore are used to define the isocon (Fig. 2.10B).

The mass and geochemical changes (i.e., gains and losses) noted from least- to most altered for each of the progressively altered samples assessed are summarized in the relevant plots in Figure 2.10C to F based on using five representative samples for each of the five groups noted. The results indicate the following relative to the least altered rock: 1) there is little mass change in any of the samples (i.e.,  $\leq 5\%$ ); 2) there is significant gain for LOI (10 to 175%); 3) for the major elements, there is variable loss of Ca, consistent loss of Na ( $>20$  to 90%), variable gain for K ( $>30$  to 240%); and 3) for the trace elements, the most significant changes are gains for Au, Ag, As, and S, whereas there are variable gains and losses for Ni, Co, Cu, Zn, Pb, Mo and Bi. Also of note is that silica is generally retained, which means that although it is removed from feldspar during hydrolysis and sericite formation, it is retained in the samples as new quartz.

#### **2.4.5 Vein types**

Veins in the WGD are classified according to their timing with respect to the main gold mineralizing event, their mineralogy and also textures. Three groups are recognized and simply referred to as: 1) pre-mineral, 2) syn-mineral, and 3) post-mineral.

#### *2.4.5.1 Pre-mineral veins*

These veins are free of Au mineralization and based on cross-cutting relationships pre-date mineralization. Two veins types are observed: 1) light blue colored quartz, and 2) carbonate-quartz (Fig. 2.11 A to D).

The blue quartz veins (Fig. 2.11A, B) form sheeted or stockwork-type veins <3 cm in thickness. Texturally they are massive, but locally they can have a faint lamination, and are commonly found in the intrusion-dominated parts of the deposit (e.g., Underdog; see Fig. 2.2B), are Au-barren, and are overprinted by the syn-mineral Au-bearing veins (Fig. 2.11B).

The carbonate veins are dominated by carbonate with minor quartz (<5 %) and are texturally massive, but locally well-developed laminated and colloform-crustiform textures are present (Fig. 2.11C). These veins average 0.5 m thickness and locally show intense fold development, are mostly hosted in Fe-rich lithologies, such as andesites, basalts and the gabbro intrusions, and are Au-barren, except where overprinted by later Au-bearing syn-mineral veins which are pyrite bearing (Fig. 2.11D). Carbonate in these veins is a mixture of Ca-Mg-Fe types, based on a lack of reaction with diluted HCl on drill core. Notably, these veins are very similar to other colloform-textured quartz-carbonate veins documented in other Canadian Archean Au deposit settings (e.g., Red Lake (MacGeehan and Hodgson, 1982; Penczak and Mason, 1997), Dome (Holmes, 1948; Stromberg et al., 2018), Martinière (Castonguay, 2019)).

#### *2.4.5.2 Syn-mineral veins*

These veins consist of massive quartz-carbonate-pyrite  $\pm$  tourmaline  $\pm$  visible gold, are the main host for economic Au mineralization, and have grades of 1 to >100 g/t Au. They have auriferous proximal- and distal alteration haloes (Fig. 2.8A to G), are both parallel to and oblique

to the dominant fabric, can be laminated with pyrite, and occur either as veins or stockworks dominated by grey quartz with subordinate carbonate, pyrite and tourmaline (Fig. 2.12A to J). In these veins, quartz is massive, carbonate occurs as patches or fracture fillings, and tourmaline is euhedral disseminations. Carbonate is again interpreted to be a mixture of Ca-Mg-Fe carbonate based on the lack of reaction with dilute HCl. Sulfides occur as disseminations or as bands, vary in abundance (<1 to 80%; Fig. 2.12D), and are dominated by pyrite with minor base-metal sulfides and sulfosalts (<1% of total sulfide) of chalcopyrite, light-colored sphalerite, arsenopyrite, galena, tennantite, and tetrahedrite. Visible gold is common in this vein type (see below).

#### *2.4.5.3 Post-mineral veins*

Veins of this group are observed to crosscut the syn-mineral veins and the post-mineral hematite altered intrusions. They are weakly mineralized commonly with <0.5 g/t Au, but are not of economic significance due to their erratic gold content and thin nature (i.e., generally <0.3 m). Five vein types are recognized: 1) laminated or banded quartz-carbonate-tourmaline ± pyrite; 2) tourmaline ± pyrite; 3) tourmaline breccias; 4) milky white quartz; and 5) smoky quartz.

The laminated quartz-carbonate-tourmaline ± pyrite type (Fig. 2.11E) occur in fractures and faults that cut the syn-mineral economic veins and are parallel or oblique to the dominant fabric. In these veins, quartz is massive, carbonate is massive or occurs as patches, pyrite occurs as disseminations or bands when present, and tourmaline occurs as massive bands in late fractures. They are dominantly Au-barren, but locally can contain low and erratic Au mineralization when pyrite is present (commonly <1 g/t Au, but locally remobilized gold is observed).

The tourmaline ± pyrite type are thin, fracturing fillings ranging from 0.1 to 1 cm in width. They have either a linear or plan geometry or pygmatic appearance (Fig. 2.11F). Gold grades average <0.5 g/t over sample intervals of 30 cm when sulfides are present.

Breccia-type are tourmaline dominated (i.e., matrix) and are only locally observed in the deposit and the low-Au grades (generally <1 g/t Au) are erratic. These veins contain angular fragments of volcanic rocks or earlier colloform-textured carbonate veins that are cemented by massive fine-grained tourmaline (Fig. 2.11G). Disseminated pyrite (<0.5 %) is commonly observed in the tourmaline matrix.

The milky white quartz type are observed cutting all lithologies and are both mineralized and barren, thus they are interpreted to represent one of the latest hydrothermal events (Fig. 2.11H, I). They are dominated by massive white quartz, locally with 1-5 % ankerite and/or disseminated pyrite. Locally they contain small (mm-sized) grains native gold. In these veins, Au grades are irregular due to the nugget effect.

The smoky quartz type (Fig. 2.11J) have no observed cross-cutting relationship to the milky white quartz veins noted above. They are dominated by massive black- to dark grey quartz, locally with 1-5 % carbonate and/or late fracture filling pyrite and brown-colored sphalerite. These veins are observed cross-cutting gold mineralized veins and the penetrative fabric developed in the hanging wall of the Mazères fault (Fig. 2.2). Similar to the previous post-mineral veins, they can contain small (mm-sized) grains of native gold but are not of economic value.

## 2.4.6 Structural Features

The rocks of the WGD area are weakly to locally strongly deformed. Four recognizable deformation events at the deposit scale are recorded that are simply denoted as D<sub>1</sub>-D<sub>4</sub>: 1) early folding of the volcanic stratigraphy; 2) N-ENE trending faults, shear zones and formation of a tectonic fabric; 3) late brittle faulting and shear zones; and 4) late tilting. The ore bearing lenses are hosted in structures related to the second stage of deformation. It is important to note, that the nomenclature of D<sub>1</sub>-D<sub>4</sub> used here is specific to the mapping area of the WGD and has not been interpreted in a regional context.

### *2.4.6.1 D<sub>1</sub> event: regional scale folding*

At a regional scale, the volcanic sequence is folded into open-to-tight structures with shallow to moderate plunges (Bandyayera et al., 2001a) (Fig. 2.1A). For the WGD, the folded volcanic rocks define an open synformal structure with the fold axis trending N60°E and plunging roughly 35° ENE (D<sub>1</sub>). The latter structure (F<sub>1</sub> fold) is defined by the repetition of lithological units in downhole profiles, as interpreted from magnetic airborne surveys. This deformation event (D<sub>1</sub>) does not record an S<sub>1</sub> fabric and is cut by felsic dike rocks of the WIC and zones of deformation and alteration hosting Au mineralization.

### *2.4.6.2 D<sub>2</sub> event: N-ENE structures*

The D<sub>2</sub> deformation is defined by moderately- to steeply-dipping faults, fractures, shear zones, and locally a weak- to strong penetrative foliation (S<sub>2</sub>) that is consistent with the structural observations noted in Bandyayera et al. (2001). This fabric is observed in deformation zones cross cutting the fold axes and limbs of the earlier F<sub>1</sub> fold at the WGD. This deformation is

considered to be broadly synchronous with Au mineralization, as defined by the field relationships discussed below.

#### *2.4.6.2.1 D<sub>2a</sub> event: pre- to syn-mineral N-ENE structures*

The D<sub>2a</sub> structures consist of a series of conjugate fault-shear zones that are observed to overprint both the volcanic and pre-mineral QFP dikes but are not observed to cut the post-mineral dikes. Three dominant orientations are documented: 1) N-striking and dipping moderately to the E; 2) ENE-striking and dipping 80-60° SE; and 3) W-striking and dipping 80-70° N. The N-striking structures have a well-developed fabric throughout the deposit (Fig. 2.13) and are defined by a weak- to strong S<sub>2</sub> foliation and locally a stretching of fragments (Fig. 2.14A-D). In contrast, the ENE- and W-striking structures are defined by fractures and faults with less fabric development. The expression of these structures is locally dependent on host-rock composition, hence in mafic-intermediate volcanic domains the fabric is defined by a well-developed schistosity, whereas in felsic-dominant domains the fabric forms high-strain zones with a poorly developed fabric, as seen in drill core and underground exposures.

The ENE- and W-striking structures are the most important and are aligned subparallel to the pre-mineral QFP dikes and the main ore lenses. The syn-mineral veins and replacement zones are mostly contained within these deformation corridors (Fig. 2.14A-D) that are concentrated in high-strain zones localized to areas of rheological anisotropies centered on contacts between deformed subvertical QFP intrusions and their host volcanic rocks. The syn-mineral veins are commonly observed to parallel or cut oblique to the S<sub>2</sub> schistosity and are locally transposed by the later (Fig. 2.14A-D). Locally where the fabric is poorly developed, syn-mineral veins occur in brittle fractures (Fig. 2.14E).

#### *2.4.6.2.2 D<sub>2b</sub> event: post-mineralization ENE structures - the Mazères deformation zone*

At the WGD, the Mazères deformation zone (MDZ) is a 175 m wide intense shear zone having an ENE orientation that is observed to crosscut the WGD. The MDZ consists of a series of sub-parallel planar features oriented 060° dipping 60-80°SE (Fig. 2.2). This MDZ is interpreted to be a second-order structure to that of the larger E-W striking, first-order Urban deformation zone (Fig. 2.1). The MDZ has a reverse movement with a sinistral displacement based on geological maps and observed drag folding kinematics seen in the immediate footwall rocks. It is traced along strike for 20 km and marks the boundary between two different geological domains. The WGD is hosted in the footwall rocks of this structure, whereas the hanging wall is characterized by a package of Au-barren mafic- to intermediate volcanic rocks hosting minor ultramafic and felsic intrusions. This latter package of rocks records an intense flattening fabric, as evidenced by the presence of well-developed schistosity, in addition to the boudinaging and folding of quartz-carbonate veins, and of zones of intense alteration (Fig. 2.14F to I). The structure truncates and deforms the deposit and associated mineralization, as observed on geological maps and in drill core. Within 50 m laterally of its footwall, drag folding (F<sub>2</sub> fold) and stretching of the rocks, the S<sub>2</sub> fabric, and of the mineralized vein system is observed to parallel the reverse fault, shear-zone structure (Figs. 2.2A, C and 2.13).

#### *2.4.6.3 D<sub>3</sub> event: late brittle faults*

The rock units, shear zones and Au-mineralized vein system in the WGD are cut and displaced by a series late brittle faults and shear zones (D<sub>3</sub>). These structures, recognized in drill core and underground exposures, correspond to zones of intense fracturing, tectonic breccia, fault gouge, and locally strong-fabric development. The most significant of these are the Roméo

and Windfall faults (Fig. 2.2). The Roméo fault a brittle deformation corridor 100 m wide that consists of a series of parallel planar features. Movement along the structure is sinistral reverse oblique-slip with a relative displacement of 300 m, as defined by offsets of traceable lithological units (i.e., volcanic-volcanic contacts and QFP intrusions). The Windfall fault is a regional-scale feature with sinistral strike-slip movement but an unknown dip-slip orientation. The fault cuts the SW extremity of the WGD and displaces the mineralized system. It is characterized by thick intervals (30-50 m) of broken drill core and zone of tectonic breccia and cohesive fault gouge that are up to 1 m thick. The continuity of mineralized system or volcanic stratigraphy has not yet been identified in the footwall zone, but is interpreted to have a movement on a km scale.

#### *2.4.6.4 D4 event: late tilting*

The rock units, shear zones and Au-mineralized vein system in the WGD are tilted 55° from an inferred original vertical orientation to its present-day inclined orientation. The primary volcanic-volcanic contacts, pre- and post-mineral intrusions, D<sub>2</sub> structures, the Au-mineralized vein system, and the Windfall fault (D<sub>3</sub>) all plunge roughly 35° ENE.

### **2.4.7 Gold mineralization, vein geometries, ore petrography and relative timing of the Au event**

#### *2.4.7.1 Types of Au ore*

Gold mineralization occurs in series of stacked subvertical to moderately-dipping zones having lensoid geometries with true widths averaging 1 to 10 m and generally oriented N-ENE and plunging about 35° ENE. As noted, these lenses are controlled by high-strain zones often spatially associated to contacts between competent subvertical pre-mineral QFP dikes and

volcanic rocks. In addition, the Au zones are also controlled locally by strong chemical contrasts along the contacts between Fe-Mg-rich gabbro sills and enveloping felsic volcanic rocks.

Deformation zones hosting Au ore are characterized by a planar fabric defined by weakly to locally strongly foliated rocks or by fractures and faults related to pre- to syn-mineral D<sub>2a</sub> structures. The two-dominant styles of mineralization are vein- and replacement type, but there are also numerous visible gold-bearing veins.

#### *2.4.7.1.1 Vein-type mineralization*

This type is dominant in brittle felsic domains (i.e., Lynx zone; Fig. 2.2C) and corresponds to the syn-mineral vein group noted above is characterized by grey- to translucent quartz with varying amounts of carbonate, tourmaline, and pyrite (Fig. 2.12A to J). The veins crosscut weak- to moderately-foliated pyritized and sericitized wall rocks. The Au grades, which are highest in vein-type mineralization, range from 1 to >100 g/t; visible gold is common.

These veins form complex arrays that resemble a Riedel shear-fracture pattern (Riedel, 1929). The geometry and orientations of the vein network are defined from mapped underground exposures (level 021 – Lynx zone) and are interpreted from measurements on oriented drill core (Fig. 2.15A to E). Three vein sets are observed, including: 1) discordant; 2) concordant; and 3) stockwork.

Discordant veins are oblique to the S<sub>2</sub> fabric and are the dominant vein set and vary in thickness from 0.1 to 1 m, are hosted in ENE- and W- trending faults, and are continuous over strike lengths of 200 m, and up to 1 km, as defined by drilling. These veins vary in orientation with respect to location in the deposit, but in general they strike E and dip 80-60° SE and locally strike W and dip 80-70° N (Fig. 2.13). Concordant veins are parallel to the S<sub>2</sub> fabric and are

splays off the discordant veins, are generally <0.5 m thick, are hosted in N-striking and moderately dipping faults (Fig. 2.13), occur over strike lengths of roughly 50 m, and locally link two larger discordant veins or can be discontinuous within several meters off the main vein. The stockwork veins are cm-wide veinlets that form conjugate sets containing concordant and discordant veinlets that generally range from 1-10 volume % of the mineralized rock.

#### *2.4.7.1.2 Replacement-type mineralization*

This mineralization type, which is dominant in the mafic and intermediate domains (i.e., Main zone; Fig. 2.2B), consists of sulfides replacing the altered host rocks (Figs. 2.8A-G, 2.14A, and 2.15F, G). At the deposit scale, it consists of a feldspar destructive alteration forming sericite-pyrite-carbonate ± silica ± tourmaline ± fuchsite assemblages cross-cut by the vein-type mineralization or occurring in high-strain zones lacking quartz veins. Economic Au mineralization is found where zones of intense replacement is associated with abundant sericite and silica with disseminated and fracture filling pyrite. This mineralization style averages 5-20 g/t Au over thicknesses of 1-10 meters. The spatial relationship of the replacement- and vein-type mineralization suggest that it partly controlled the emplacement of the latter (Fig. 2.14A, B).

#### *2.4.7.1.3 High-grade gold*

Occurrences of high-grade Au intersections with spectacular visible gold are well known at the WGD. This gold type has been observed in both drill core and underground exposures and is hosted in the vein-type mineralization or in the zones of very intense silicification. These intercepts and exposures have variable amounts of modal gold (i.e., >10s to 1000s g/t) hosted in cloudy white quartz-carbonate veins which cross-cut the earlier vein- and replacement-type

mineralization (Fig. 2.12K to N). The visible gold is commonly in discordant features cutting the vein quartz which reflects a later gold-remobilization event.

#### *2.4.7.2 Ore petrography*

Within the vein- and replacement-type mineralization, petrographic studies indicate the presence of quartz, tourmaline, sericite, carbonate and locally fuchsite (Fig. 2.16 A-B) along with various sulfide and sulfosalt phases including pyrite, arsenopyrite, sphalerite, chalcopyrite, tennantite-tetrahedrite, galena, native gold, electrum and locally minor Sb-rich and complex telluride phases (Fig. 2.16 C-N). Pyrite is the dominant sulfide phase, whereas other sulfides are accessory phases (i.e., <1 % of the sulfide content). Pyrite is zoned with an inclusion-rich and in part porous core overgrown by a homogeneous rim free of textural complexity (Fig. 2.16C-E). Accessory sulfide phases and gold occur as inclusions in pyrite cores (Fig. 2.16F, G), along rims of the pyrite, or in the host quartz and carbonate (Fig. 2.16H-N).

#### *2.4.7.3 Geochemistry of gold mineralized samples*

Multi-element analysis of Au-mineralized drill core from various rock types defines a variety of precious- and base metals associated with the high-grade mineralized zones (Fig. 2.17A). Out of 247 vein- and replacement-type samples grading >10 g/t Au throughout the deposit, the analyses define elevated concentrations of Ag, Cu, Zn, Pb, As, Sb, Se, Te, Bi, Mo and W (see summary statistics in Table 2.4). Of note when the data are compared to average crustal abundance, is the anomalous enrichment in As-Au-Ag-Sb-Se-Bi-Te, which we take to best define the chemical signature of the Au mineralization. In pyrite-rich mineralized samples, these elements and others noted, are concentrated in the crystal structure of pyrite (confirmed by

our LA-ICP-MS elemental pyrite maps; unpubl. data), as inclusions in pyrite, or as separate base- and precious-metal minerals in the host matrix.

The composition of gold grains in the WGD was characterized by EMPA analysis (Padilla, 2016) which showed the Au:Ag ratio varies from 1:1 (electrum) to 17:1 ( $\bar{x}$  = 3:1) (Fig. 2.17B). These data are consistent with the analysis of bulk-ore samples (Fig. 2.17C, Table 2.4) which also indicate a large range from 1:8 to 30:1, but with a similar average ( $\bar{x}$  = 3:1).

#### *2.4.7.4 Relative timing of gold mineralization*

The relative timing of the Au event is constrained from field observations and core logging. Development of the N-, ENE-, and W-trending faults and high-strain zones overprinting the pre-mineral QFP intrusions also contain undeformed and deformed vein- and replacement-type Au mineralization. These observations suggest that Au mineralization was broadly synchronous with D<sub>2a</sub> deformation. In addition, the presence of fragments of quartz-pyrite veins and tourmaline breccia in the early fragmental QFP intrusions (Fig. 2.4B, C and D) indicates an earlier phase of hydrothermal activity, albeit of low Au tenor, pre-dated emplacement of the WIC, whereas main phase Au mineralization, overprints the early phases of the WIC. These features are in turn all cut by the Red Dog intrusion and the fine-grained hematite-altered intrusion, thus post-dating all earlier events. These two post-mineral intrusions constrain the Au event to be broadly synchronous with the emplacement of the WIC and the early D<sub>2a</sub> deformation event. Furthermore, the presence of altered, Au-mineralized and deformed wall-rock fragments in the Red Dog intrusion also constrain the relative timing of the Au event (Fig. 2.18A-D). It is important to note that weak deformation, ankerite alteration, and a Au-barren discoloration of the red-orange color is observed to locally affect the margins of the post-mineral dikes (Fig. 2.8L,

2.18B to D. All these observations are further supported by 95,000 m of drill core that intersect thin-to-thick (i.e., 1-200 m) post-mineral dikes that are perpendicular and parallel to the ore zones throughout all areas of the deposit, and not one of these has been observed to be crosscut by Au-bearing vein- or replacement-type mineralization.

#### **2.4.8 U-Pb Geochronology**

Three samples were dated to in order to constrain the timing of important geological events in the WGD area. The oldest unit dated is from the youngest volcanic cycle, as represented by a felsic volcanic rock collected from an underground ramp exposure. It is a massive, fine-grained, light grey to beige rhyolite with weakly developed carbonate-sericite alteration. In situ LA ICP-MS analysis of prismatic-to-stubby zircon yielded a cluster of concordant data centered on  $2705 \pm 4.2$  Ma (Fig. 2.19A). This age is considered to best approximate zircon crystallization and deposition of the volcanic rock (Azevedo, 2019).

A pre-mineral small quartz eye QFP (OBM-16-579, 61.8 m), interpreted to be the oldest unit of the WIC and pre-dating the Au event was dated using CA-TIMS. The sample is a fine-grained to aphanitic, light grey, porphyritic (1-5 mm, <3%, subhedral quartz), dike rock. It provided clear and colorless, euhedral prismatic and stubby zircons (~150 to 300  $\mu\text{m}$ ). Seven single-grain fractions yielded a cluster of concordant data, but the  $^{207}\text{Pb}/^{206}\text{Pb}$  ages scatter outside of error with a range from 2698 to 2715 Ma (Table 2.5, Fig. 2.19B). The dated zircons are interpreted to represent a mixture of inherited zircons (i.e., xenocrysts), such as from the felsic volcanic unit noted above, and cognate zircons from the host QFP. Thus, the youngest dated zircon at  $2698 \pm 3$  Ma is interpreted to best approximate the crystallization age of this syn-deformation dike rock (Davis, 2017).

A post-mineral QFP (i.e., Red Dog intrusion) (EAG-15-552, 555.2 m), interpreted to be the youngest unit of the WIC based on cross-cutting relationships, cuts the main Au event and associated alteration. This sample was also dated using CA-TIMS. It is fine-grained, red- to red-grey, and porphyritic (2-5 mm, >5%, anhedral quartz), dike rock. It provided clear and colorless, euhedral prismatic and stubby fresh zircons (~150 to 300  $\mu\text{m}$ ). Seven single-grain fractions analyzed yielded a cluster of concordant data, but the  $^{207}\text{Pb}/^{206}\text{Pb}$  ages range from 2698 to 2718 Ma (Table 2.5, Fig. 2.19C), thus a similar spread as the dated QFP sample above. Thus, these data are interpreted in a similar manner as the latter with the youngest age of  $2697.6 \pm 0.4$  Ma interpreted to best approximate the time of crystallization of this post-mineral QFP dike (Davis, 2017).

## **2.5 Discussion**

### **2.5.1 Timing and nature of magmatism and Au mineralization**

The volcanic rocks and felsic intrusions of the WIC define two main stages of magmatic activity in the area: early seafloor volcanism followed by later emplacement of a swarm of felsic intrusions or dikes. The early stage includes volcanic rocks deposited on the paleo-seafloor which commenced with basic flows, locally pillowed, and followed by felsic volcanic rocks interbedded with rare and thin sedimentary horizons of black argillite; these were later cut by gabbroic and ultramafic sills. Chemically the volcanic rocks equate to tholeiitic basalts, andesite, dacites and rhyolites, based on a large lithochemical dataset (n= 9041). Outside of the deposit boundaries, about 4-5 km eastwards, occur <10 m thick horizons of black argillite, locally with pyrite framboids, that are interbedded in the volcanic sequence; these pyritiferous beds can be traced along strike for >10 km. U-Pb zircon dating of the youngest felsic volcanic unit in this

succession indicates an age of  $2705 \pm 4.2$  Ma for the volcanism. This age is inconsistent with the previous assignment of the felsic volcanic unit to the ca. 2718 Ma Macho Formation, that was dated from a felsic volcanic rock 6 km SW of the WGD that was rhyodacite in composition with a calc-alkaline affinity (Bandyayera et al. 2002). In contrast, the felsic volcanic unit dated at WGD overlaps in age with the latest volcanic cycle in the region, the Urban Formation, which is dated at 2714-2707 Ma (Bandyayera et al., 2004a), or may be a younger unit that was not previously mapped.

The felsic intrusive rocks of the WIC, which constitute a suite of several texturally distinct QFP intrusions, cut the earlier volcanic sequence and related sill-like bodies. These felsic intrusions cut at oblique angles the volcanic stratigraphy; they are interpreted as both dike and sill-like bodies. The felsic complex evolved texturally over time, from an early aphanitic matrix with small angular quartz eyes and fragments, to an aphanitic matrix with large quartz eyes, and then to a later hematite altered matrix with large quartz eyes, but their geochemical signature of calc-alkaline granodioritic composition remained similar (Fig. 2.7) and is distinct from the earlier felsic volcanic rocks (Fig 2.6C, D). The WIC was emplaced at relatively shallow crustal levels, from the average of the estimated crystallization pressure calculations (Table 2.1) the minimum average pressure equates to 138 MPa whereas the maximum average pressure equates to 297 MPa. These are equivalent to about 3.7 to 8 km depth (using average density of  $2.7 \text{ g/cm}^3$ ). It is also important to note that from the earliest to the latest phase of the WIC, the average inferred depth of crystallization increased which suggests progressive burial of the system.

The age and duration of the WIC is constrained from U-Pb zircon dating, which also brackets the timing of Au mineralization, as the earlier intrusions are cut by Au mineralization whereas the youngest intrusions post-date it. Thus, the zircon ages of  $2698 \pm 3$  Ma and  $2697.6 \pm$

0.4 Ma constrain both the time and duration of magmatism from 2701 to 2697.2 Ma and also brackets the main Au event to this interval ( $2699.1 \pm 1.9$  Ma). Importantly, this age for Au mineralization overlaps with the time for a similar Au event in the area, the Barry gold deposit of  $2697.1 \pm 0.6$  Ma (Kitney et al. 2011). At this gold deposit, located about 12 km SW of the WGD, gold mineralization occurs in albite-carbonate-quartz veins that core carbonate-quartz-pyrite  $\pm$  biotite alteration zones overprinting a sequence of folded mafic volcanic rocks of the Macho Formation that are crosscut by a series of QFP intrusions. As at the WGD, U-Pb zircon dating of pre- and post-ore calc-alkaline granodioritic intrusions constrain the age of the Au event similar to that noted above.

### **2.5.2 Structural and hydrothermal evolution of the Windfall Gold Deposit**

The geological evolution of the WGD presented in Figure 2.20 commenced with two distinct phases of seafloor volcanism which was succeeded by intrusion of gabbroic to ultramafic sills. These rocks were deformed during  $D_1$ , which produced the regional fold patterns now seen (Fig. 2.1A).

The folded volcanic rocks were then cut by early  $D_{2a}$  deformation manifested as subvertical faults. These structures overprint or are overprinted by an early, Au-poor or barren hydrothermal event recognized by the presence of quartz-pyrite fragments and tourmaline breccia fragments hosted in early QFP fragmental intrusions (Fig. 2.4B to D). The early phases of the WIC were then emplaced subparallel to the early  $D_{2a}$  structures and locally along dike-volcanic contacts. The pre-mineral dike complex is then observed to be crosscut by Au-barren sheeted blue quartz veins. Continued  $D_{2a}$ -related deformation features crosscut the volcanic and pre-mineral QFP dike complex and controlled emplacement of a second hydrothermal event

which formed the early Au-barren colloform-textured carbonate-quartz veins. This vein type occurs dominantly in mafic rock types, whereas in felsic rocks it is poorly developed and generally manifested as carbonate alteration. As noted previously, the occurrence of early colloform-crustiform veins is noted in other gold deposit settings, such as the gold-endowed Red Lake district (MacGeehan and Hodgson, 1982; Penczak and Mason, 1997; Dubé et al., 2000, 2003), the Dome mine (Holmes, 1948; Stromberg et al., 2018) and actively explored Martinière gold deposit (Létourneau et al., 2017; Castonguay et al., 2019; Létourneau, in prep.).

Continuation of the  $D_{2a}$  event overprinted the colloform-textured carbonate-quartz veins and created high-strain zones due to rheological anisotropies localized to the contacts of the subvertical, competent QFP intrusions and host volcanic rocks. These zones preferentially channeled Au mineralizing fluids which formed the shear-hosted replacement-type mineralization that is later crosscut by vein-type Au mineralization. These two types of Au mineralization account for the +6 Moz Au resource at WGD (Richard et al., 2021). Importantly, the earlier deformed rocks, QFP dike rocks, syn-Au alteration and mineralization are cut by the post-mineral hematite altered QFP dikes (i.e., Red Dog). As was noted, field relationships combined with U-Pb zircon dating of the pre- and post-mineral felsic intrusions bracket the gold event at 2701 to 2697.2 Ma. Post emplacement of the Red Dog intrusion, the entire sequence is crosscut by fault-related, barren to low-Au grade laminated quartz-tourmaline  $\pm$  pyrite veins, tourmaline  $\pm$  pyrite veinlets and tourmaline breccias. All of this is then all overprinted by continued ENE deformation associated to the  $D_{2b}$  event, as observed by deformed veins, the truncation and folding of the pre- and post-mineral phases of the WIC, and by reverse fault movement and associated drag along the post-mineral Mazères deformation zone (Fig. 2.2).

All of the above events are overprinted by several poorly constrained events: 1) a Au remobilization event that accounts for the spectacular high-grade intercepts (i.e., +1000 g/t Au) WGD is now well known for; 2) post-mineral carbonate alteration; 3) late-stage diorite dikes; 4) two hydrothermal events associated with the post-mineral quartz veins (Figs. 2.11H-J, 2.14I), 4), and 5) late brittle faulting. These rocks were then tilted 55° from an original vertical orientation to form the presently observed ENE trending 35° plunge of the ore deposit.

### **2.5.3 Early ca. 2698 Ma Au mineralization in the Abitibi greenstone belt**

In the AGB, several periods of gold mineralization are documented between 2740 and 2670 Ma (Robert, 2001; Robert et al., 2005; Dubé et al., 2017; Monecke et al., 2017; Dubé and Mercier-Langevin, 2020; Katz et al., 2021) which incorporate different styles related to both magmatic and orogenic processes. Relevant here is the ca. 2698 Ma gold event at several sites in the AGB: 1) the Barry gold deposit (Kitney et al. 2011); 2) Doyon-LaRonde-Bousquet mining camp (Mercier-Langevin, 2007b; Galley and Lafrance, 2014); and 3) the Kiena, Siscoe, and Norlartic deposits in the Val D'Or camp (Couture et al., 1994, Morasse et al., 1995; 1998).

At the Barry gold deposit in the UBGB (Fig. 2.1), vein-style Au mineralization is constrained to  $2697 \pm 1$  Ma based on U-Pb zircon ages from pre-mineral and post-mineral QFP dike rocks. In contrast to this, at LaRonde-Penna Au and base-metal mineralization is related to a sub-seafloor hydrothermal up-flow zone centered on an active ca. 2698 Ma felsic magmatic complex. Thus, although different in deposit type to the WGD, there is an overlap in regards to the timing of felsic magmatism and a potential magmatic progenitor in regards to the source of the Au and other metals (Mercier-Langevin et al., 2007b).

In the Val d'Or camp, an early >2686 Ma Au event is documented in several gold deposits and showings, including Kiena, Siscoe (Main Zone), Norlartic, and Malartic Lakeshore (Robert, 1994; Couture et al., 1994; Morasse, 1995; 1998, Guay et al., 2018; Dubé and Mercier-Langevin, 2020), where deformed Au mineralized quartz ± carbonate-albite-pyrite veins that post-date volcanism and are subsequently crosscut by post-mineral dikes (e.g., 2692 ± 2 Ma at Norlartic; 2694.3 ± 2.5 Ma at Malartic Lakeshore) that pre-date regional syn-metamorphic deformation (2669 ± 1 to 2643 ± 4 Ma; Feng and Kerrich, 1991; Powell et al., 1995; Monecke et al., 2017). This has led some researchers to suggest a potential magmatic-hydrothermal origin for the Au event (Morasse et al., 1995; Guay et al., 2018) seeing as it pre-dates regional syn-metamorphic deformation that is generally considered as a pre-requisite for the formation of orogenic gold deposits (e.g., Goldfarb et al., 2005; Gaboury, 2019).

Although not the focus of this study, we do highlight that the WIC and the Au mineralized vein system at WGD are deformed and truncated by a major regional-scale deformation zone (i.e., Mazères deformation zone) which could have implications for constraining the timing of gold to have occurred prior to regional-scale deformation. In addition to this, the timing of Au mineralization with respect to regional-scale metamorphism remains poorly documented. At WGD Au formation pre-dates regional metamorphism noted for the northern Abitibi (2677 and 2632 Ma; Dubé and Mercier-Langevin, 2020 and references therein). A similar conclusion was noted in Kitney (2009) for the Barry Au deposit which is identical in age to the WGD. Thus, while just an hypothesis, this highlights the need to unravel the timing of Au with respect to both regional-scale deformation and metamorphism at WGD and in the entire UBGB.

#### 2.5.4 Nature of mineralization and elemental signature

Further details on the characteristics of the mineralization are addressed in a companion study (see chapter 3), but we highlight here the nature of the Au and related elemental enrichment and its implications for ore-deposit formation. The element association defined for the ore zones (i.e., >10 g/t Au) of Au, Ag, As, Sb, Se, S, Bi and Te (Zn, Cu, Mo, W) is one that is generally considered more characteristic of intrusion-related gold deposits versus orogenic (Sillitoe and Thompson, 1998; Thompson et al., 1999; Goldfarb et al. 2005; Hart 2007). Relevant in regard to this assemblage is these elements are mostly hosted in pyrite via elemental substitutions or micro-inclusions. The latter is based on elemental mapping of numerous (>40) pyrite grains (see chapter 3) which revealed these metals are present in the arsenian-rich zones (Fig. 2.16), as noted in many other pyrite studies from various ore-deposit settings (e.g., Reich et al., 2005; Large et al., 2011; Deditius et al., 2008 and 2011; Romàn et al. 2019; Hastie et al., 2020). Thus, at the WGD it is suggested that Au was initially sequestered in pyrite along with associated elements and subsequently released as pyrite was zone refined (e.g., Neyedley et al., 2017; Gourcerol et al., 2018, 2020; Voisey et al., 2020a; Hastie et al., 2020). The timing of when the pyrite was texturally and chemically modified due to fluid interaction and how gold was liberated (i.e., fluid or melt mediated; see discussions in Tomkins et al., 2004; Tooth et al., 2011; Fougereuse et al., 2016; Hastie et al., 2020) is beyond the scope of the present study, but we do note two Au events are recorded (Figs. 2.12K-N, 2.16D, E). Others have reached similar conclusions in regard to multiple Au events within deposit settings, but whether the early sulfide-hosted Au is mobilized and/or further addition of Au occurs is subject to debate with different opinions. For example, at the giant Obuasi gold deposit, Ghana, it is suggested that Au was initially sequestered in early arsenopyrite (<700 ppm) and, later remobilized in response to

deformation and fluid mediated to concentrate the Au in structural traps (Fougerouse, 2017). Dubosq et al. (2018) reached similar conclusions in their study of the giant Detour Lake Au deposit, Canada, whereby early refractory Au is hosted by arsenian pyrite which was fluid mobilized as part of overprinting deformation. However, based on mass balance, they also note that there was the continued addition of Au to the system synchronous with ongoing metamorphism and fluid ingress. Lastly, for the high-grade Fosterville gold deposit, Australia, Voisey et al. (2020a, 2020b) have suggested two distinct Au events are present in this telescoped ore body: an early refractory Au hosted in arsenopyrite which is overprinted in its deeper part by ore characterized by coarse gold associated with stibnite, but which also included Au liberated from the earlier arsenopyrite. At the WGD, whether gold is zone refined from early pyrite or is continuously added to the system remains to be further evaluated, however we do note the presence of high-grade gold is not a primary feature and instead reflects a later-stage mobilization of Au.

### **2.5.5 Proposed geological classification of the Windfall gold deposit**

In order to develop a genetic model and classify the WGD, several relevant ore-deposit features must be incorporated: 1) it is proximal to and crosscut by a regional-scale (20 km-long) second-order high-angle reverse fault-shear zone; 2) the main Au event is syn-deformation and is hosted in structural and chemical traps where deformation zones are located in areas of rheological heterogeneity between competent QFP dikes and deformed host volcanic rocks; 3) it formed over a protracted time interval with early Au-poor or barren colloform-crustiform carbonate-quartz veins overprinted by the main Au event; 4) the Au ore zones with 6+ Moz Au at  $\approx 9$  g/t Au consist of an extensive network of gold mineralized quartz-carbonate-tourmaline-pyrite veins and associated sericite-pyrite  $\pm$  silica  $\pm$  tourmaline  $\pm$  fuchsite alteration zones with

Au as inclusions in dissolved or fractured pyrite, as minor Au in arsenian pyrite, but with spectacular high-grade intercepts; 5) the ore zones are semi-continuous for over 2.5 km strike length; 6) the pre-mineral granodioritic dike rocks are, along with the older volcanic rocks, altered and deformed relative to the post-mineral dike rocks; 7) the ore zones have a distinct geochemical metal signature characterized by enrichment (relative to average crust) in Au, Ag, As, Se, S, Bi and Te (Zn, Cu, Mo, W); and 8) mineralization spatially and temporally overlaps emplacement of the WIC at ca. 2698 Ma.

The question in regard to ore-deposit model is whether the noted features best conform to an orogenic versus intrusion-type, or some combination of the two. Rather than trying to account for all these highlighted features, as some are equivocal such as, the zoned alteration which is similar for orogenic (e.g., Goldfarb et al., 2005; Dubé and Gosselin, 2007), low- to intermediate-sulfidation settings (e.g., Hedenquist et al. 2000) and some intrusion-related (Hart 2007) deposit settings, we instead focus on the critical aspects of the deposit. In this regard, the relative timing of mineralization and ore-related alteration are considered paramount. As noted above, well constrained U-Pb zircon ages bracket dike rock emplacement such that they not only show a spatial relationship to ore, but also a temporal relationship. This association is supported by the fact alteration and mineralization are constrained to pre-date intrusion of the post-mineral dike rocks (e.g., Red Dog intrusion). Using this relationship as a working hypothesis, the proposed model is that the structures which controlled protracted injection of a petrogenetically related suite of felsic magmas were also exploited by the mineralizing fluids. That pre-mineral dike rocks are followed by post-mineral dike rocks, which together appear to define a fractionation pattern of increasing  $\text{Na}_2\text{O}$ , is not unlike a magmatic-hydrothermal system. Thus, we tentatively suggest the ore fluids and dike rocks share a common source analogous to magmatic-

hydrothermal deposit types (e.g., Hart 2007, Sillitoe 2010). Furthermore, we note that the early barren colloform-crustiform veins, abundance of Au-rich arsenian pyrite, and the consistent noted metal associations of the ore zones are features consistent with the proposed working model (e.g., Chouinard et al. 2005, Hedenquist et al. 2000, Robert 2001, Romàn et al. 2019). However, the presence of exceptional high-grade bonanza-type gold zones is attributed to later remobilization of Au and likely relates to an overprinting hydrothermal event synchronous with continued deformation, as has been documented in other gold settings (e.g., Tomkins and Mavrogenes, 2002; Fougereuse et al., 2017; Voisey et al., 2020b; Hastie et al., 2020). We do, however, speculate that the Au remobilization event may be associated to the overprinting hydrothermal event responsible for the formation of the laminated quartz-carbonate-tourmaline veins and tourmaline veinlets and breccias.

The association of gold mineralization with a dike swarm as characterizes the WGD is not without precedent. In the case of the giant (+50 Moz Au) Neoproterozoic Kalgoorlie deposits, western Australia, the first mineralizing stage, the Fimiston-Oroya system at ca 2.66 Ga, has been attributed to a magmatic-hydrothermal system interpreted to be related to a swarm of high-level feldspar porphyry dike rocks (Bateman and Hagemann, 2004; Mueller et al., 2020a, 2020b) whereas the later overprinting mineralization, the Mount Charlotte system, is related to an orogenic event (Bateman and Hagemann, 2004). As previously noted, another example closer to and identical in age to the WGD is the Barry gold deposit (Kitney et al., 2011), where the Au mineralization is centered on a swarm of calc-alkaline quartz-feldspar porphyry dikes. Kitney et al. (2011) compared the Barry gold deposit to other pre-2686 Ma gold deposits in the southern Abitibi (i.e., Kiena, Norlartic, and Siscoe (Main Zone)) that are coeval with felsic magmatism

and suggested these to be of magmatic-hydrothermal origin (Couture et al., 1994; Morasse et al., 1995). Thus, it is noted that WGD has analogues in regard to other intrusion-related Au systems.

Although not a focus of the present study, the structural control on emplacement of the dike complex is briefly commented on, as these over-riding structures were important for localizing both the dikes and the mineralizing fluids. The dike complex was emplaced within conjugate deformation zones consisting of N-, ENE-, and W-trending structures interpreted to be controlled by a Riedel shear-fracture system. The pre-mineralization QFP dikes were emplaced into these structures with continued deformation facilitating the channeling of Au-rich fluids into areas of high-strain. The entire deposit including the post-mineral QFP rocks, was then later deformed by the ENE deformation along the regional scale Mazères deformation zone.

In summary, based on the current understanding of the WGD setting we suggest that a magmatic-hydrothermal model best accounts for the characteristics of the Au mineralization and related alteration. Such a model is consistent with the many features highlighted above, whereas an orogenic model is inconsistent with several of these, in particular the absolute and relative timing, and associated elemental enrichments. The noted hydrothermal events which overprint the mineralized zones and the presence of local bonanza ore grades (i.e., >1000 g/t Au) are, however, attributed to a subsequent deformation event and thus this component is not to be diminished in importance.

## **2.6 Conclusions**

Based on a comprehensive and integrated study of the age and characteristics of the host rocks, relevant structure, ore-related alteration, sequence and characterization of vein types, and the geochemical and mineralogical features of Au-rich material, the relatively new, significant

(6.1 Moz Au) and previously undescribed WGD of the Urban-Barry greenstone belt, Québec (Canada) has been classified as an Archean (ca. 2698 Ma) intrusion-related Au system. The ore setting has been characterized as follows.

1. A succession of mafic- and felsic lavas ( $>2705 \pm 4.2$  Ma) and minor black argillite that are crosscut by mafic- to ultramafic sills which is crosscut at high angles by a felsic dike complex (WIC). The latter is composed of several texturally distinct calc-alkaline granodiorite quartz-feldspar porphyritic dikes that are separated in two groups: 1) pre-mineral that are overprinted by Au mineralization and the related alteration at  $2698 \pm 3$  Ma; and 2) post-mineral ( $2697.6 \pm 0.4$  Ma) that crosscut the former. These dikes therefore bracket the Au event at  $2699.1 \pm 1.9$  Ma.
2. Several distinct hydrothermal veining and alteration events are documented which span from pre to post the economic Au event. The most significant of these consist of: 1) replacement zones composed of sericite-pyrite  $\pm$  silica  $\pm$  tourmaline  $\pm$  fuchsite in intermediate- to basic host rocks of volcanic and intrusive origin; and 2) veins and stockworks composed of grey quartz-carbonate-pyrite-tourmaline dominantly in the felsic dike rocks. In addition, exceptionally high-grade visible gold commonly overprints the former types and is related to a later deformation and associated hydrothermal event.
3. The Au-mineralized veins and alteration occur in a series of conjugate- and stacked subvertical zones having lensoid geometries with true widths averaging 1 to 10 m. These zones are dominantly oriented along ENE- and W-trending structures and plunge about  $35^\circ$  and are controlled by high-strain zones often spatially associated to contacts between competent subvertical pre-mineral QFP dikes and volcanic rocks.

4. The WGD is best classified as an intrusion-related Au deposit, whereby the Au-mineralized fluid is suggested to be sourced from an inferred magmatic body at depth.

That the WGD has analogues in the Au-endowed Abitibi, both in terms of age and deposit type (i.e., magmatic-hydrothermal) and is located in an underexplored greenstone belt, is considered to be both important and relevant in the context of the future potential of this area. Furthermore, this study suggests that there is more potential elsewhere for this type of Au deposit.

## 2.7 References

- Ayer, J.A., Thurston, P.C., Bateman, R., Dubé, B., Gibson, H.L., Hamilton, M.A., Hathway, B., Hocker, S.M., Houlié, M.G., Hudak, G., Ispolatov, V.O., Lafrance, B., Leshner, C.M., MacDonald, P.J., Péloquin, A.S., Piercey, S.J., Reed, L.E., and Thompson, P.H., 2005, Overview of Greenstone Architecture Project: Discover Abitibi Initiative; Ontario Geological Survey, Open File results from the Péloquin, A.S., Piercey, S.J., Reed, L.E. and Thompson, P.H. 2005. Overview of results from the Report 6154, 146 p.
- Azevedo, C., 2019, Dating program results from the Quévillon, Windfall, and Urban-Barry projects: Internal report to Osisko Mining, p. 46.
- Bandyayera, D., Daigneault, R., and Sharma, K., 2003, Géologie de la région du lac de la Ligne (32F/01): Ministère des Ressources Naturelles, de la Faune et des Parcs, Québec, RG 2004-02, 31 p.
- Bandyayera, D., Rhéaume, P., Cadéron, S., Giguère, E., and Sharma, K., 2004b, Géologie de la région du Lac Lagacé (32B/14): Ministère des Ressources Naturelles, de la Faune et des Parcs, Québec, RG 2004-02, 32 p., 4 maps
- Bandyayera, D., Rhéaume, P., Doyon, J., and Sharma, K., 2004a, Géologie de la région du lac Hébert (32G/03): Ministère des Ressources Naturelles, de la Faune et des Parcs, Québec, RG 2003-07, 57 p., 4 maps
- Bandyayera, D., Théberge, L., and Fallara, F., 2002, Géologie de la région des lacs Piquet et Mesplet (32G/04 et 32B/13): Ministère des Ressources Naturelles, Québec, RG 2001-14, 56 p., 8 maps
- Bateman, R., Hagemann, S. 2004, Gold mineralisation throughout about 45 Ma of Archean orogenesis: protracted flux of gold in the Golden Mile, Yilgarn Craton, Western Australia: *Mineralium Deposita*, v. 39, p. 536-559.

- Card, K.D. 1990, A review of the Superior province of the Canadian Shield, a product of Archean accretion: *Precambrian Research*, v. 48, p. 99–156.
- Castonguay, S., Dubé, B., Mercier-Langevin, P., and Wodicka, N., 2019, Geological setting and mineralisation styles of the Sunday Lake and Lower Detour ‘gold trends’, northwestern Abitibi greenstone belt, Ontario and Quebec; Targeted Geoscience Initiative: 2018 report of activities, Geological Survey of Canada, Open file report 8549, p. 9–22.
- Chouinard, A., Paquette, J., and Williams-Jones, A.E., 2005, Crystallographic controls on trace-element incorporation in auriferous pyrite from the Pascua epithermal high-sulfidation deposit, Chile-Argentina. *Canadian Mineralogist*, v. 43, p. 951-963.
- Couture, J.F., Pilote, P., Machado, N., Desrochers, J.P., 1994, Timing of gold mineralization in the Val-d’Or district, Southern Abitibi Belt: Evidence for two distinct mineralizing events: *Economic Geology*, v. 89, p. 1542-1551.
- Davis, D.W., 2017, U-Pb geochronology of pre- and post-mineralization plutons from the Windfall Project, Urban-Barry greenstone belt, Québec: Report 2.: Internal report to Osisko Mining, p. 18.
- Deditius, A.P., Utsunomiya, S., Reich, M., Kesler, S.E., Ewing, R.C., Hough, R., Walshe, J., 2011, Trace metal nanoparticles in pyrite: *Ore geology reviews*, v. 42, p. 32-46.
- Deditius, A.P., Utsunomiya, S., Renock, D., Ewing, R.C., Ramana, C.V., Becker, U., Kesler, S.E., 2008, A proposed new type of arsenian pyrite: composition, nanostructure and geological significance: *Geochimica et Cosmochimica Acta*, v. 72, p. 2919-2933.
- Dubé, B., and Gosselin, P., 2007, Greenstone-hosted quartz-carbonate vein deposits, in Goodfellow, W.D., ed., *Mineral deposits of Canada: A synthesis of major deposit-types, district metallogeny, the evolution of geological provinces, and exploration methods*: Mineral Deposits Division, Geological Association of Canada, Mineral Deposits Division Special Publication no. 5, p. 49–73.
- Dubé, B., and Mercier-Langevin, P., 2020, Gold deposits of the Archean Abitibi Greenstone Belt, Canada: SEG special publications, no. 23, p. 669-708.
- Dubé, B., Balmer, W., Sanborn-Barrie, M., Skulski, T., and Parker, J., 2000, A preliminary report on amphibolite-facies, disseminated-replacement-style mineralisation at the Madsen gold mine, Red Lake, Ontario: Geological Survey of Canada Current Research 2000-C17, 12 p.
- Dubé, B., Mercier-Langevin, P., Ayer, J. Atkinson, B., Monecke, T. 2017, Orogenic Greenstone-Hosted Quartz-Carbonate Gold Deposits of the Timmins-Porcupine Camp, *Reviews in Economic Geology*, v. 19, p. 51-79.
- Dubé, B., Williamson, K., and Malo, M., 2003, Gold mineralisation within the Red Lake mine trend: Example from the Cochenour-Williams mine area, Red Lake, Ontario, with some new key information from the Red Lake mine and potential analogy with the Timmins camp: Geological Survey of Canada Current Research 2003-C21, 15 p.

- Dubosq, R., Lawley, C.J.M., Rogowitz, A., Schneider, D.A., Jackson, S., 2018, Pyrite deformation and connections to gold mobility: Insight from micro-structural analysis and trace element mapping: *Lithos*, v. 310-311, pp. 86-104.
- El-Rassi, D., Cole, G., Chartier, D., 2011, Mineral Resource Evaluation Technical report, Windfall Lake Gold Project, Québec: NI 43-101 technical report by SRK Consulting Inc. ([www.sedar.com](http://www.sedar.com)).
- Feng, R., and Kerrich, R., 1991, Single zircon age constraints on the tectonic juxtaposition of the Archean Abitibi greenstone belt and Pontiac Subprovince, Quebec, Canada: *Geochimica et Cosmochimica Acta*, v. 55, p. 3437–3441.
- Fougerouse, D., Micklethwaite, S., Tomkins, A.G., Mei, Y., Kilburn, M., Guagliardo, P., Fisher, L.A., Halfpenny, A., Gee, M., and Paterson, D., 2016, Gold remobilisation and formation of high grade ore shoots driven by dissolution-reprecipitation replacement and Ni substitution into auriferous arsenopyrite: *Geochimica et Cosmochimica Acta*, v. 178, p. 143–159.
- Fougerouse, D., Micklethwaite, S., Ulrich, S., Miller, J., Godel, B., Adams, McCuaig T.C., 2017, Evidence for Two Stages of Mineralization in West Africa's Largest Gold Deposit: Obuasi, Ghana: *Economic Geology*, v. 112, p. 3-22.
- Gaboury, D., 2019, Parameters for the formation of orogenic gold deposits: *Applied Earth Science*, v. 128, p. 124-133.
- Galley, A.G., Lafrance, B. 2014, Setting and Evolution of the Archean Synvolcanic Mooshla Intrusive Complex, Doyon-Bousquet-LaRonde Mining Camp, Abitibi Greenstone Belt: Emplacement History, Petrogenesis, and Implications for Au Metallogenesis: *Economic Geology*, v. 109, p. 205-229
- Goldfarb, R.J., and Groves, D.I., 2015, Orogenic gold: Common or evolving fluid and metal sources through time: *Lithos*, v. 233, p. 2-26.
- Goldfarb, R.J., Baker, T., Dubé, B., Groves, D.I., Hart, C.J., and Gosselin, P. 2005, Distribution, character, and genesis of Gold deposits in metamorphic terranes: *Economic Geology 100th Anniversary Volume*, p. 407-450
- Gourcerol, B., Kontak, D.J., Petrus, J.A., Thurston, P.C. 2020, Application of LA ICP-MS analysis of arsenopyrite to gold metallogeny of the Meguma Terrane, Nova Scotia, Canada: *Gondwana Research*, v. 81, p. 265-290.
- Gourcerol, B., Kontak, D.J., Thurston, P.C., Petrus, J.A. 2018, Application of LA-ICP-MS sulfide analysis and methodology for deciphering elemental paragenesis and associations in addition to multi-stage processes in metamorphic gold settings: *The Canadian Mineralogist*, v. 56, p. 36-64.
- Grant, J., 1986, The Isocon Diagram - A simple solution to Gresens' equation for metasomatic alteration: *Economic Geology*, v. 81, p. 1976-982.
- Guay, F., Pilote, P., Daigneault, R., McNicoll, V., 2018, Early gold-bearing quartz veins within the Rivière-Héva fault zone, Abitibi Subprovince, Québec, Canada: *Canadian Journal of Earth Sciences*, v. 55, p. 1139-1157.

- Hart, C.J.R., 2007, Reduce intrusion-related, in Goodfellow, W.D., ed., Mineral deposits of Canada: A Synthesis of Major Deposit Types, District Metallogeny, the Evolution of Geological Provinces, and Exploration Methods: Geological Association of Canada, Mineral Deposits Division, Special Publication No. 5, p. 95-112.
- Hastie, E.C.G., Kontak, D.J., Lafrance, B. 2020, Gold remobilization: Insights from gold deposits in the Archean Swayze greenstone belt, Abitibi Subprovince, Canada: *Economic Geology*, v. 115, p. 241-277.
- Hedenquist, J.W., Arribas, A., and Gonzalez-Urien, E., 2000, Exploration for epithermal gold deposits: *Reviews in Economic Geology*, v. 13, p. 245–277.
- Holmes, T.C., 1948, Dome mine: Structural Geology of Canadian Ore Deposits, A Symposium Arranged by a Committee of the Geology Division: Canadian Institute of Mining and Metallurgy, p. 539–547.
- Ishikawa, Y., Sawaguchi, T., Iwaya, S., and Horiuchi, M., 1976, Delineation of prospecting targets for Kuroko deposits based on modes of volcanism of underlying dacite and alteration halos: *Mining Geology*, v. 26, p. 105–117
- Jensen, L.S., 1976, A New Cation Plot for Classifying Subalkalic Volcanic Rocks, Ontario Div. Mines, MP 66, 22 p.
- Joly, M., 1990, Géologie de la région du lac aux Loutres et du lac Lacroix: Ministère de l'Énergie et des Ressources, Gouvernement du Québec, MB 90-42, 55 p.
- Katz, L.R., Kontak, D.J., Dubé, B., and McNicoll, V. 2017, The geology, petrology, and geochronology of the Archean Côté Gold large-tonnage, low-grade intrusion-related Au(-Cu) deposit, Swayze greenstone belt, Ontario, Canada: *Canadian Journal of Earth Sciences*, v. 54, p. 273-302.
- Katz, L.R., Kontak, D.J., Dubé, B., McNicoll, V., Creaser, R., Petrus, J.A., 2021, An Archean Porphyry-Type Gold Deposit: The Côté Gold Au(-Cu) Deposit, Swayze Greenstone Belt, Superior Province, Ontario, Canada: *Economic Geology*, v. 116, p. 47-89.
- Kelsey, C.H. 1965. Calculation of the CIPW Norm: *Mineralogical Magazine*, Vol. 34, p. 276-282.
- Kitney, K., 2009, Structural, mineralogical, geochemical and geochronological investigation of the Barry gold deposit, Abitibi Subprovince, Canada: Unpublished M.Sc. thesis, Kingston, Ontario, Queen's University, 436 p.
- Kitney, K.E., Olivo, G.R., Davis, D.W., Desrochers, J-P., Tessier, A., 2011, The Barry Gold Deposit, Abitibi Subprovince, Canada: A greenstone Belt-Hosted gold Deposit Coeval with Late Archean Deformation and Magmatism: *Economic Geology*, v. 106, p. 1129-1154
- Krogh, T.E. 1973, A low contamination method for hydrothermal decomposition of zircon and extraction of U and Pb for isotopic age determinations: *Geochimica et Cosmochimica Acta*, v. 37: p. 485-494.

- Large, R., Gemmell J.B., and Paulick, H. 2001, The alteration box plot: a simple approach to understanding the relationship between alteration mineralogy and lithogeochemistry associated with volcanic-hosted massive sulfide deposits: *Economic Geology*, v. 96, p. 957-971.
- Large, R., Thomas, H., Craw, D., Henne, A., Henderson, S., 2012, Diagenetic pyrite as a source for metals in orogenic gold deposits, Otago Schist, New Zealand: *New Zealand Journal of Geology and Geophysics*, v. 55, p. 137-149.
- Le Maitre, R.W., Bateman, P., Dudek, A., Keller, J. et al. 1989, A classification of igneous rocks and glossary of terms: Blackwell Scientific Publications, Oxford. 193 p.
- Letourneau, M., in prep., Characterization of the West Zone Gabbro: Auriferous foot wall rock of the Archean Bug North gold deposit – Martinière gold system, Quebec. Unpubl. M.Sc. Thesis, Laurentian University, Sudbury, ON.
- Létourneau, M., Kontak, D.J., and Leybourne, M., 2017, Alteration zonation associated with Au mineralization along the northern Bug Lake Gold Trend of the Archean La Martinière Gold system, west-central Quebec: Geological Association of Canada, Mineralogical Association of Canada, Kingston, Ontario, Canada, Program with Abstracts, vol. 40.
- Ludwig, K.R. 2012, Isoplot 3.75: A geochronological toolkit for Microsoft Excel, Special Publication, no. 5, Berkeley Geochronology Center, Berkeley, California, 75 p.
- MacGeehan, P.J., and Hodgson, C.J., 1982, Environments of gold mineralisation in the Campbell Red Lake and Dickenson mines, Red Lake district, deposits: Canadian Institute of Mining and Metallurgy Special Volume 24, Ontario, in Hodder, R.W., and Petruk, W., eds., *Geology of Canadian gold*, p. 184–207.
- MacLean, W.H., Barrett, T.J., 1993, Lithogeochemical techniques using immobile elements: *Journal of Geochemical Exploration*, v. 48, p. 109-133
- Mattinson, J. 2005, Zircon U-Pb chemical abrasion (CA-TIMS) method: Combined annealing and multi-step partial dissolution analysis for improved precision and accuracy of zircon ages: *Chemical Geology*, v. 220, p. 47-66.
- Mercier-Langevin, P., Dubé, B., Hannington, M.D., Davis, D.W., Lafrance, B., Gosselin, G. 2007, The LaRonde Penna Au-Rich Volcanogenic Massive Sulfide Deposit, Abitibi Greenstone Belt, Québec: Part 1. *Geology and Geochronology: Economic Geology*, v. 102, p. 585-609
- Mercier-Langevin, P., Dubé, B., Lafrance, B., Hannington, M., Galley, A., Moorhead, J., and Gosselin, P., 2007b, Metallogeny of the Doyon-Bousquet-LaRonde mining camp, Abitibi greenstone belt, Quebec, in Goodfellow, W.D., ed., *Mineral Deposits of Canada: A Synthesis of Major Deposit-Types, District Metallogeny, the Evolution of Geological Provinces, and Exploration Methods: Geological Association of Canada, Mineral Deposits Division, Special Publication No. 5*, p. 673-701.
- Middlemost, E. 1994, Naming materials in the magma/igneous rock system: *Earth-Science Reviews*, v. 37, p. 215-224

- Milner, R.L., 1939. Barry Lake Area, Abitibi County and Abitibi Territory, Department of Mines, Québec, RP 143, 9 p.
- Monecke, T., Mercier-Langevin, P., Dubé, B., and Frieman, B.M. 2017, Geology of the Abitibi Greenstone Belt. *Reviews in Economic Geology*, v. 19, p. 7-49.
- Morassee, S., 1998, Geology, structure and timing of gold mineralization at the Kiena deposit, Val d'Or, Quebec. Ph.D. Thesis, Queen's University, Kingston, ON, p. 628.
- Morassee, S., Wasteneys, H.A., Cormier, M., Helmstaedt, H., Mason, R., 1995, A pre-2686 Ma intrusion-related gold deposit at the Kiena mine, Val d'Or, Quebec, Southern Abitibi Subprovince: *Economic Geology*, v. 90, p. 1310-1321.
- Mueller, A.G., Hagemann, S.G., Brugger, J., Xing, Y., Roberts, M.P. 2020a, Early Fimiston and late Oroya Au-Te ore, Paringa South mine, Golden Mile, Kalgoorlie: 4. Mineralogical and thermodynamic constraints on gold deposition by magmatic fluids at 420-300 °C and 300 MPa: *Mineralium Deposita*, v. 55, p. 767-796.
- Mueller, A.G., Hagemann, S.G., McNaughton, N.J., 2020b, Neoproterozoic orogenic, magmatic, and hydrothermal events in the Kalgoorlie-Kambalda area, Western Australia: constraints on gold mineralization in the Boulder Lefroy-Golden Mile fault system: *Mineralium Deposita*, v. 55, p. 633-663.
- Neyedley, K., Hanley, J.J., Fayek, M., Kontak, D.J. 2017, Textural, fluid inclusion, and stable oxygen isotope constraints on vein formation and gold precipitation at the 007 deposit, Rice Lake greenstone belt, Bissett, Manitoba, Canada: *Economic Geology*, v. 112, p. 629-660.
- Padilla, R., and Savard, M. 2018, Geology of the Windfall Lake Gold Project: Society of Economic Geologists Meeting, September 22–25, 2018, Keystone, Colorado, Proceedings.
- Padilla, R. 2016. Characterization of mineralisation zones at the Windfall Gold Deposit, Quebec. Internal report for Osisko Mining Inc. p. 27
- Paton, C., Hellstrom, J., Paul, B., Woodhead, J., Hergt, J. 2011. Iolite: Freeware for the visualisation and processing of mass spectrometric data: *Journal of Analytical Atomic Spectrometry*, v. 26, p. 2508-2518
- Pearce, J.A., 1996, A user's guide to basalt discrimination diagrams, in Wyman, D.A., ed., *Trace Element Geochemistry of Volcanic Rocks: Applications for Massive Sulphide Exploration: Geological Association of Canada, Short Course Notes*, v. 12, p. 79-113
- Pearce, J.A., and Norry, M.J., 1979, Petrogenetic implications of Ti, Zr, Y and Nb variations in volcanic rocks: *Contributions to Mineralogy and Petrology*, v. 69, p. 33-47.
- Penczak, R.S., and Mason, R., 1997, Metamorphosed Archean epithermal Au-As-Sb-Zn-(Hg) vein mineralisation at the Campbell mine, northwestern Ontario: *Economic Geology*, v. 92, p. 696–719.
- Poulsen, K.H., Robert, F. and Dubé, B. 2000, Geological Classification of Canadian Gold Deposits: Geological Survey of Canada, Bulletin 540, 1-113

- Reich, M., Kesler, S.E., Utsunomiya S., Palenik, C.S., Chryssoulis, S. and Ewing R.C., 2005, Solubility of gold in arsenian pyrite: *Geochimica & Cosmochimica Acta*, v. 69, p. 2781-2796.
- Rhéaume, P., and Bandyayera, D., 2006, Révision stratigraphique de la Ceinture d'Urban-Barry: Ministère des Ressources naturelles et de la Faune, Québec, RP 2006-08, 11 p.
- Rhéaume, P., Bandyayera, D., Fallara, F., Boudrias, G., and Cheng, L.Z., 2004, Géologie et métallogénie du secteur du lac aux Loutres, synthèse métallogénique d'Urban-Barry (phase 1 de 2): Ministère de Ressources naturelles et de la Faune et des Parcs, Québec, RP 2004-05, 10 p.
- Richard, P.L., Athurion, C., Houde, M., 2021, Mineral resource estimate update for the Windfall project, NI 43-101 technical report by BBA Inc. ([www.sedar.com](http://www.sedar.com)).
- Riedel, W., 1929. Zur mechanic geologischer brucherscheinungen. *Centralblatt für Mineralogie, Geologie, und Paleontologie* 1929B, 354
- Robert, F., 1994, Vein fields in gold districts: the example of Val d'Or, southeastern Abitibi Subprovince, Quebec: Geological Survey of Canada Paper 94-1C, p. 295-302.
- Robert, F., 2001, Syenite-associated disseminated gold deposits in the Abitibi greenstone belt, Canada: *Mineralium Deposita*, v. 36, p. 503-516.
- Robert, F., Brommecker, R., Bourne, B.T., Dobak, P.J., McEwan, C.J., Rowe, R.R., Zhou, X. 2007, Model and Exploration Methods for Major Gold Deposit Types: *Proceedings of Exploration 07*, p. 691-711
- Robert, F., Poulsen, K.H., Cassidy, K.F., Hodgson, C.J. 2005, Gold Metallogeny of the Superior and Yilgarn Cratons: *Economic Geology 100th Anniversary Volume*, p. 1001-1033.
- Romàn, N., Reich, M., Leisen, M., Morata, D., Barra, F., Deditius, A.P., 2019, Geochemical and micro-textural fingerprints of boiling in pyrite: *Geochimica et Cosmochimica Acta*, v. 246, p. 60–85.
- Seedorf, E., Dilles, J.H., Proffett, J.M., Jr., Einaudi, M.T., Zurcher, L., Stavast, W.J.A., Johnson, D.A., Barton, M.D. 2005, Porphyry deposits: Characteristics and origin of hypogene features, *Economic Geology*, v. 100, p. 251-298.
- Sillitoe, R., 2010, Porphyry copper systems: *Economic Geology*, v. 105, p. 3–41.
- Sillitoe, R., Thompson, J.F.H., 1998, Intrusion-related vein gold deposits: types, tectono-magmatic settings and difficulties of distinction from orogenic gold deposits: *Resource Geology*, v. 48, p. 237-250.
- Stanley, C.R. and Madeisky, H.E., 1996, Lithochemical exploration for metasomatic zones associated with hydrothermal mineral deposits using molar element ratio analysis: Introduction: Lithochemical Exploration Research Project, Mineral Deposit Research Unit, University of British Columbia, Short Course Notes, 200 p.

- Stanley, C.R. and Russell, J.K., 1989, Petrologic hypothesis testing with Pearce element ratio diagrams: derivation of diagram axes: *Contributions to Mineralogy and Petrology*, v. 103, p. 78-89.
- Stromberg, J.M, Barr, E., Banerjee, N.R., 2018, Early carbonate veining and gold mineralisation in the Timmins camp: Depositional context of the Dome mine ankerite veins: *Ore Geology Reviews*, v. 97, p. 55-73.
- Sun, S., McDonough, W.F. 1989, Chemical and isotopic systematics of oceanic basalts: implications for mantle composition and processes: *Geological Society of London, special publications*, v. 42, p. 313-345
- Thompson, J.F.H., Sillitoe, R.H., Baker, T., Lang, J.R., and Mortensen, J.K., 1999, Intrusion-related gold deposits associated with tungsten-tin provinces: *Mineralium Deposita*, v. 34, p. 323-334.
- Thurston, P., Ayer, J.A., Goutier, J., Hamilton, M.A. 2008, Depositional Gaps in Abitibi Greenstone Belt Stratigraphy: A Key to Exploration for Syngenetic Mineralisation: *Economic Geology*, v. 103, p. 1097–1134.
- Tompkins A.G., Pattinson, D.R., and Zaleski, E. 2004, The Hemlo gold deposit, Ontario: an example of melting and mobilization of a precious metal-sulfosalt assemblage during amphibolite facies metamorphism and deformation: *Economic Geology*, v. 99, p. 1063-1084.
- Tompkins, A.G., and Mavrogenes, J.A., 2002, Mobilization of gold as a polymetallic melt during pelite anataxis at the Challenger deposit, South Australia: A metamorphosed Archean gold deposit: *Economic Geology*, v. 97, p. 1249–1271.
- Tooth, B., Ciobanu, C.L., Green, L., O'Neill, B., and Brugger, J. 2011, Bi-melt formation and gold scavenging from hydrothermal fluids: and experimental study: *Geochimica and Cosmochimica Acta*, v. 75, p. 5423-5443.
- Vielreicher, N.M., Groves, D.I., McNaughton, N.J. 2016, The giant Kalgoorlie Gold Field revisited: *Geoscience Frontiers* 7, p. 359-374.
- Voisey, C.R., Tomkins, A.G., Xing, Y., 2020b, Analysis of a Telescoped Orogenic Gold System: Insights from the Fosterville Deposit: *Economic Geology*, v. 115, p. 1645–1664.
- Voisey, C.R., Willis, D., Tomkins, A.G., Wilson, C.J.L., Micklethwaite, S., Salvemini, F., Bougoure, J., and Rickard, W.D.A., 2020a, Aseismic refinement of orogenic gold systems: *Economic Geology*, v. 115, p. 33-50.
- Yang, X-M., 2017, Estimation of crystallization pressure of granite intrusions: *Lithos*, v. 286-287, p. 324-329
- Yang, X-M., Lentz, D.R., Chi, G., 2017, Ferric-ferrous iron oxide ratios: Effect on crystallization pressure of granites estimated by Qtz-geobarometry: *Lithos*, v. 380-381, 105920.

## 2.8 Figures

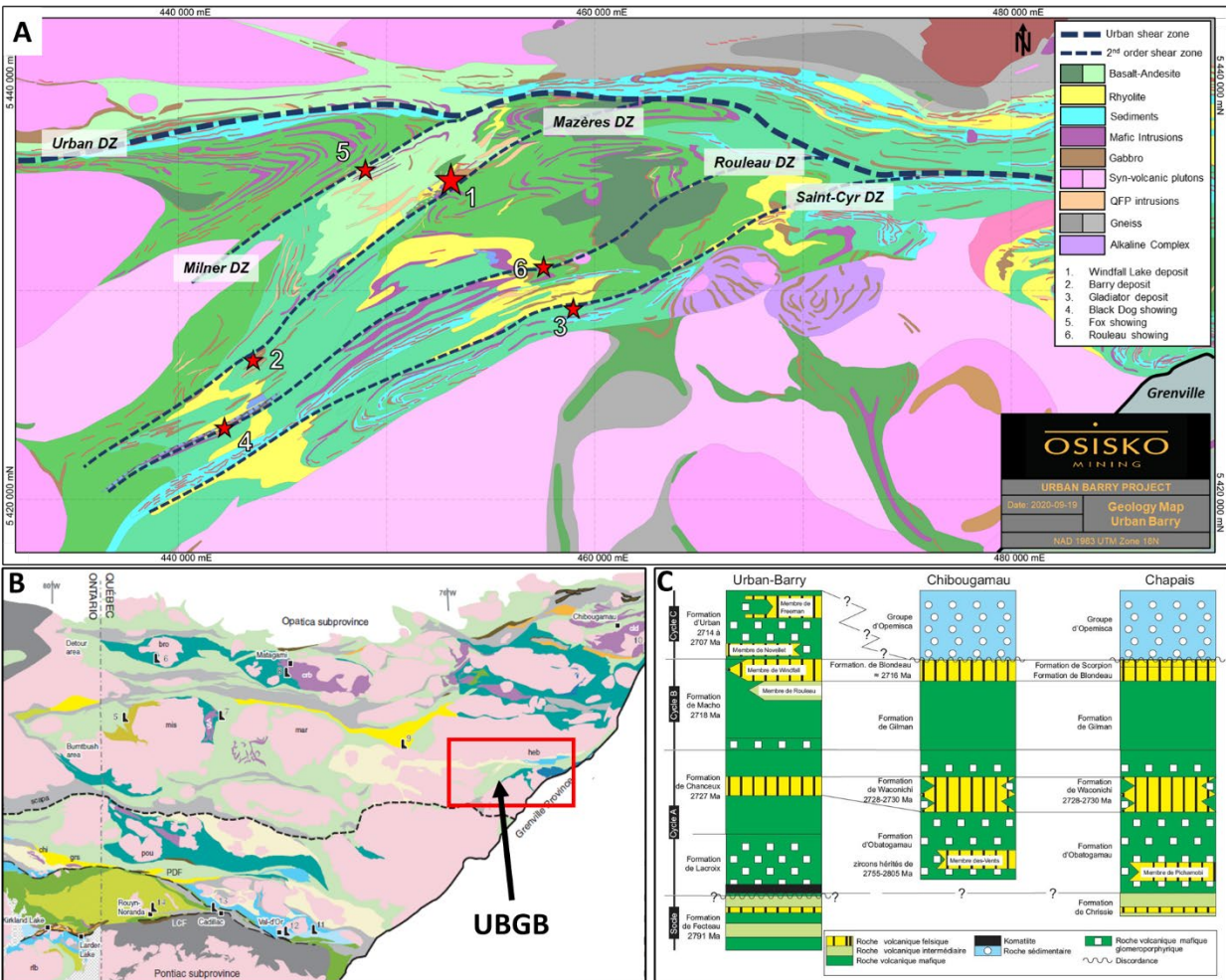


Figure 2.1. A) Geological map of the Urban-Barry greenstone belt showing the location of the significant mineral occurrences and the traces of the major regional-scale deformation zones (DZ): Urban-Barry DZ, Mazères DZ, the Rouleau DZ, and the Saint-Cyr DZ. Map provided courtesy of Osisko Mining. B) Regional geological setting of the Superior Province, Canada (modified from Thurston et al., 2008). C) Stratigraphic column and stratigraphic correlations of the Urban-Barry, Chibougamau and Chapais regions (from Rhéaume and Bandyayera, 2006).

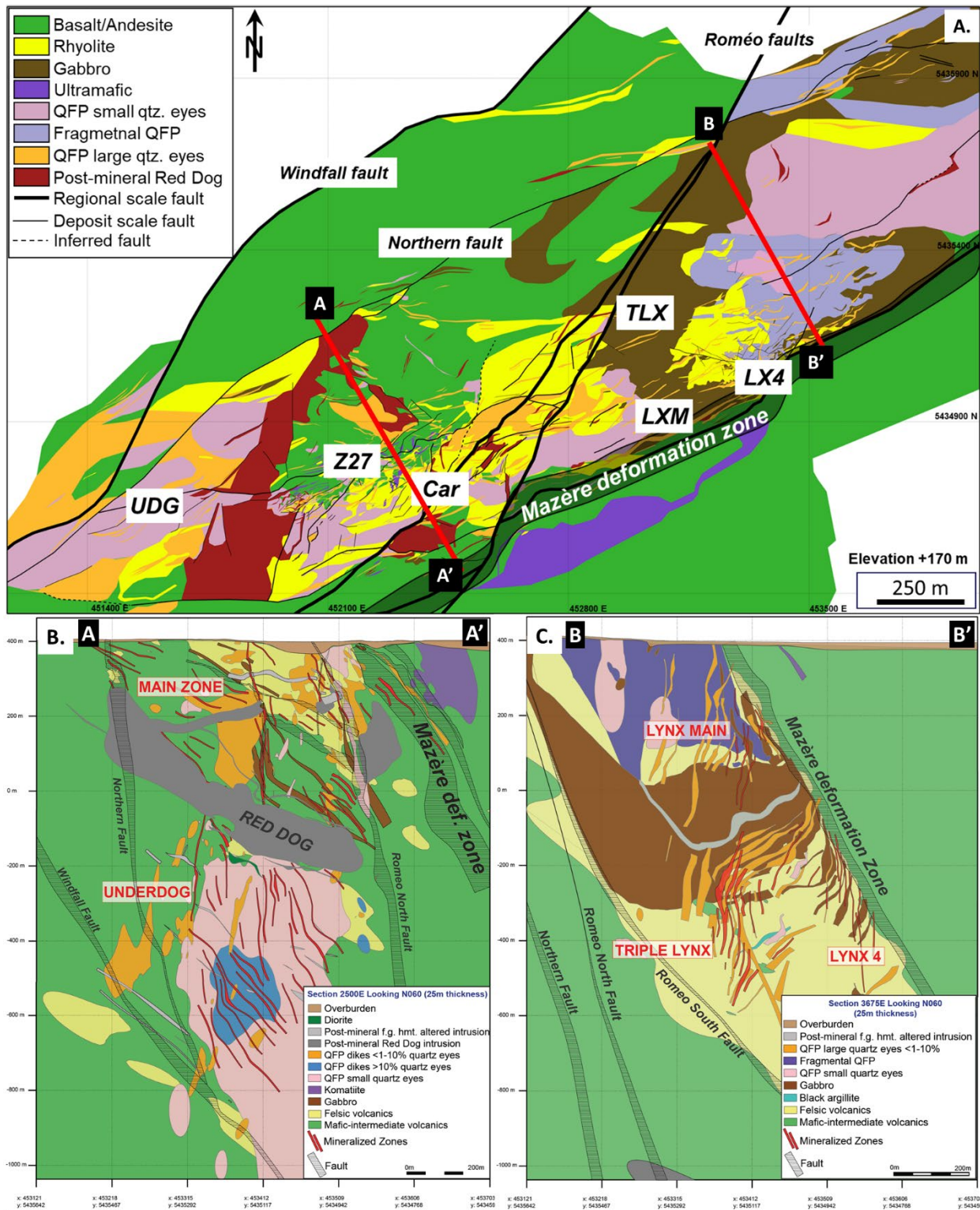


Figure 2.2: Interpreted plan map (+170 m elevation (i.e., 230 m below surface)) (A) and cross-sectional (B, C) geology maps (facing northeast) of the WGD created using diamond drill-hole

pierce points. Cross-section locations are indicated on the plan map along section lines A and B. Maps used are courtesy of Osisko Mining.

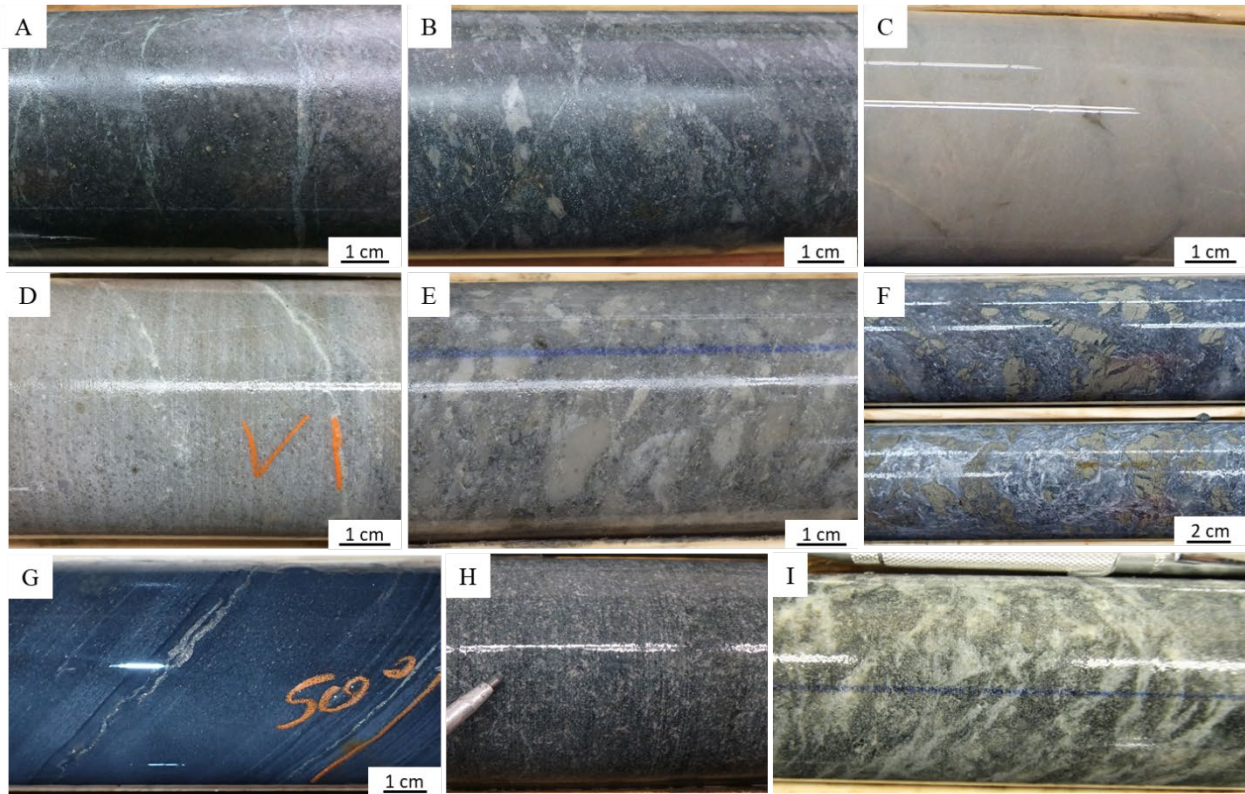


Figure 2.3: Representative images of volcanic and synvolcanic rocks in the Windfall deposit area. A) Massive fine-grained green andesite. B) Fragmental andesite with a fine-grained green groundmass containing angular fragments of mafic and felsic rocks. C) Massive beige aphanitic rhyolite. D) Porphyritic rhyolite with a light-grey aphanitic groundmass containing 20% anhedral quartz. E) Fragmental rhyolite with a fine-grained light grey groundmass containing angular fragments of felsic volcanic rocks. F) Altered rhyolite containing pyrite fragments suggesting pyrite event prior to formation of rhyolite. G) dark grey-green bedded argillite with pyrite-pyrrhotite laminations. H) Massive gabbro with a fine-grained medium green groundmass and a spotty chlorite alteration. I) Altered ultramafic intrusion with a fine-grained dark green groundmass crosscut and overprinted by carbonate veining and alteration.

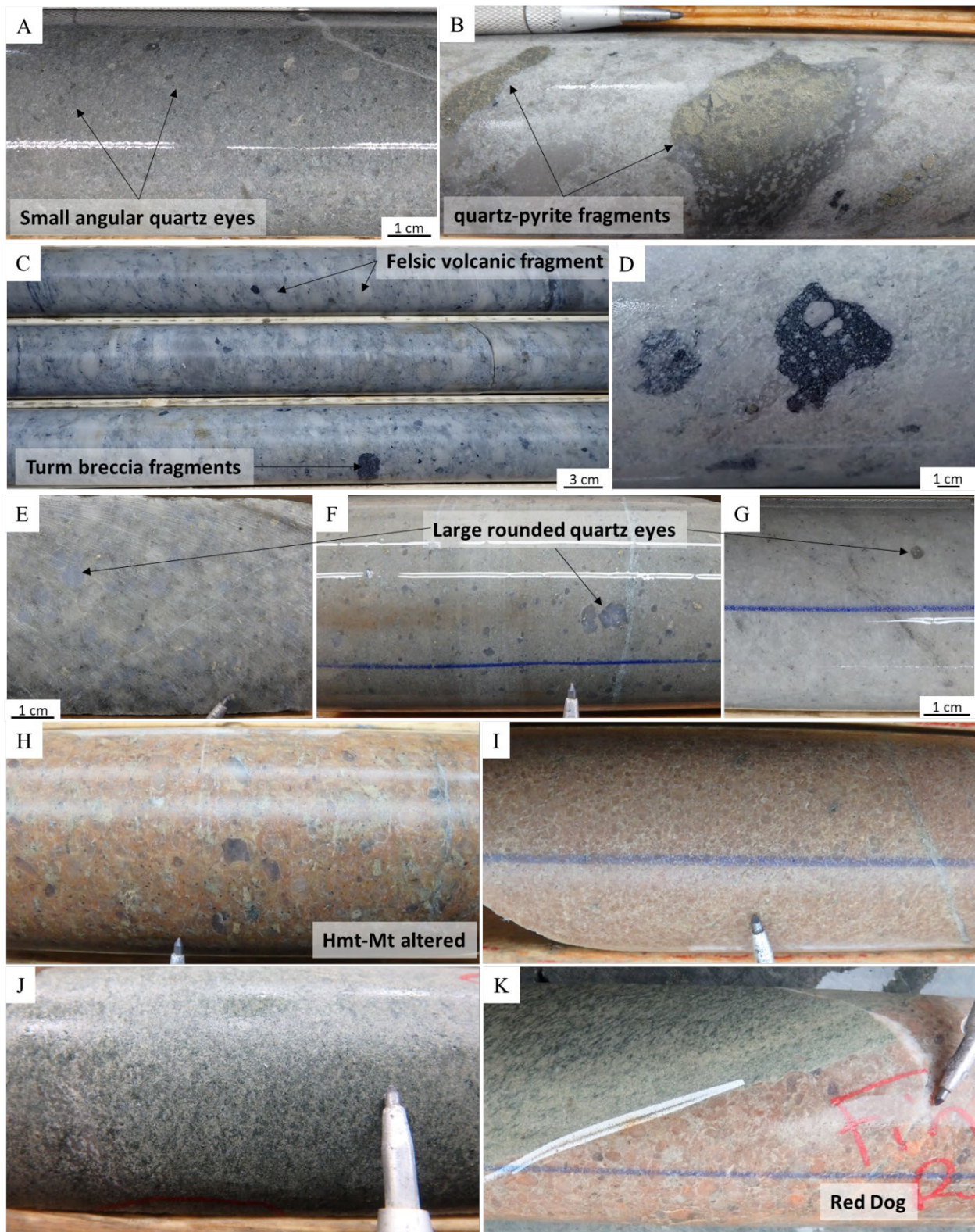


Figure 2.4: Representative images of core samples for each rock type of the Windfall intrusive complex (WIC) and of late diorite. A) Pre-mineral porphyritic and fragmental QFP with small

anhedral quartz eyes and volcanic fragments. B-D) Pre-mineral fragmental QFP with an aphanitic light-grey groundmass containing sub-rounded fragments of felsic volcanic, QFP intrusive, tourmaline breccia and pyritized material. E-G) Pre-mineral QFP with a light-grey to beige aphanitic groundmass and 1-15% large quartz eye phenocrysts. H) Post-mineral QFP with a fine-grained red-orange hematite magnetite altered groundmass containing large quartz eye phenocrysts (i.e., the Red Dog unit). I) Post-mineral dike with a fine-grained red-orange hematite altered groundmass. J) Post-mineral diorite intrusion with a fine-grained medium green chlorite-carbonate altered groundmass. K) Post-mineral diorite intrusion cross-cutting the post-mineral Red Dog intrusion, not part of the WIC.

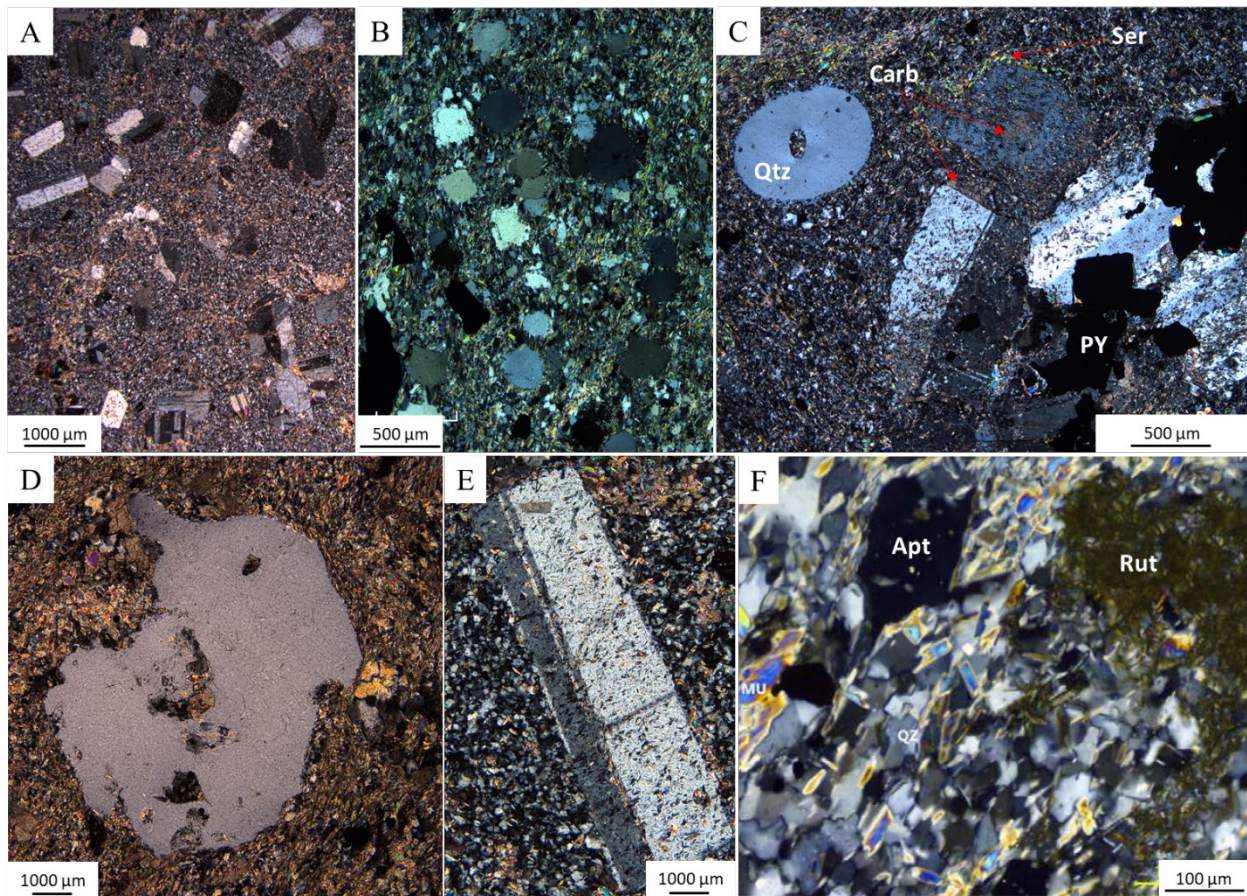


Figure 2.5: Thin section pictures of felsic intrusions of the Windfall intrusive complex (WIC). A, B) Felsic intrusions with small quartz eyes and plagioclase phenocrysts in an aphanitic quartz-plagioclase matrix that is altered to carbonate and sericite. C) Felsic intrusion with rounded quartz (Qtz) eyes and altered plagioclase phenocrysts in a quartz-plagioclase matrix altered to sericite (Ser) and carbonate (Carb). D) Felsic intrusion with large resorbed quartz eye in a sericite-carbonate altered felsic matrix. E) Plagioclase with polysynthetic twinning in a felsic intrusion with a sericite-carbonate altered matrix. F) Fine-grained quartz-plagioclase matrix altered to sericite-carbonate with accessory apatite (Apt) and rutile (Rut).

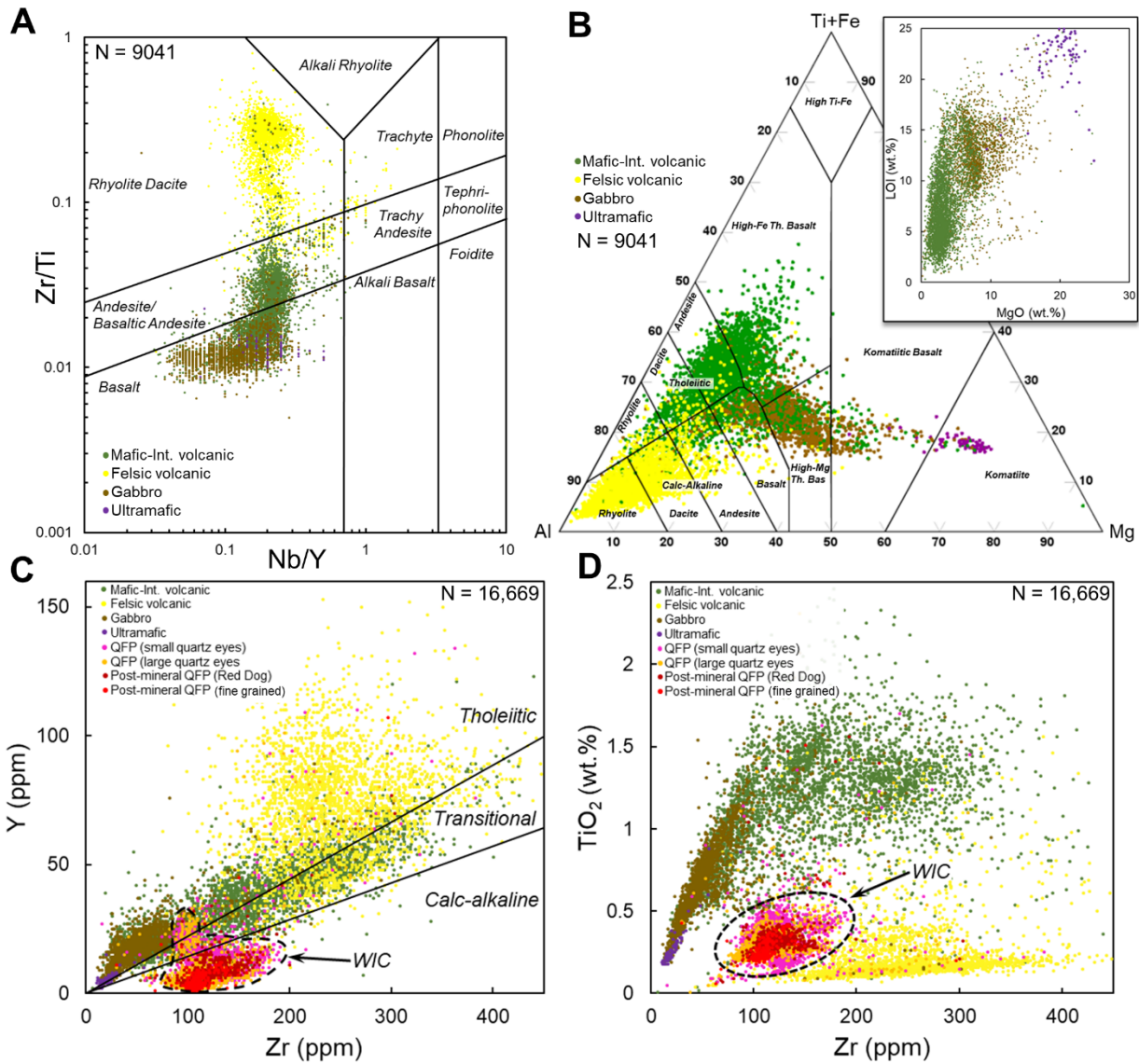


Figure 2.6: A) Geochemical data for mafic- and felsic volcanic rock types plotted on a Pearce (1996) discriminant diagram. Note that lithologies logged as mafic- and ultramafic volcanic and intrusive units fall into the basalt to basaltic-andesite to andesite field, whereas the felsic volcanic rocks fall into the rhyolite-dacite field. B) Geochemical data for volcanic rock types plotted in a Jensen Cation Plot (Jensen, 1976). Note that lithologies logged as mafic- to felsic volcanic define a trend from High-Mg and High-Fe tholeiitic basalts to rhyolite, whereas the mafic to ultramafic intrusions fall into the fields of High-Mg tholeiitic basalt to komatiite. Important to note is the most mafic rocks (i.e., ultramafic, gabbro) are significantly altered by carbonate as observed in the inset plot of MgO versus LOI. C-D) Geochemical data for volcanic and intrusive rock types (mafic and felsic) plotted in Zr versus Y and Zr versus TiO<sub>2</sub> binary diagrams. Note that the volcanic- and mafic intrusive rocks have a transitional- to tholeiitic signature whereas the Windfall intrusive rocks (WIC) have a calc-alkaline signature. Fields

shown are from Maclean and Barrett (1993). Plot D shows that the volcanic rocks of mafic and felsic affinity are easily distinguished by their TiO<sub>2</sub> contents and that intrusive rocks fall into a narrow range of 75-175 ppm Zr and 0.2-0.6 wt. % TiO<sub>2</sub>.

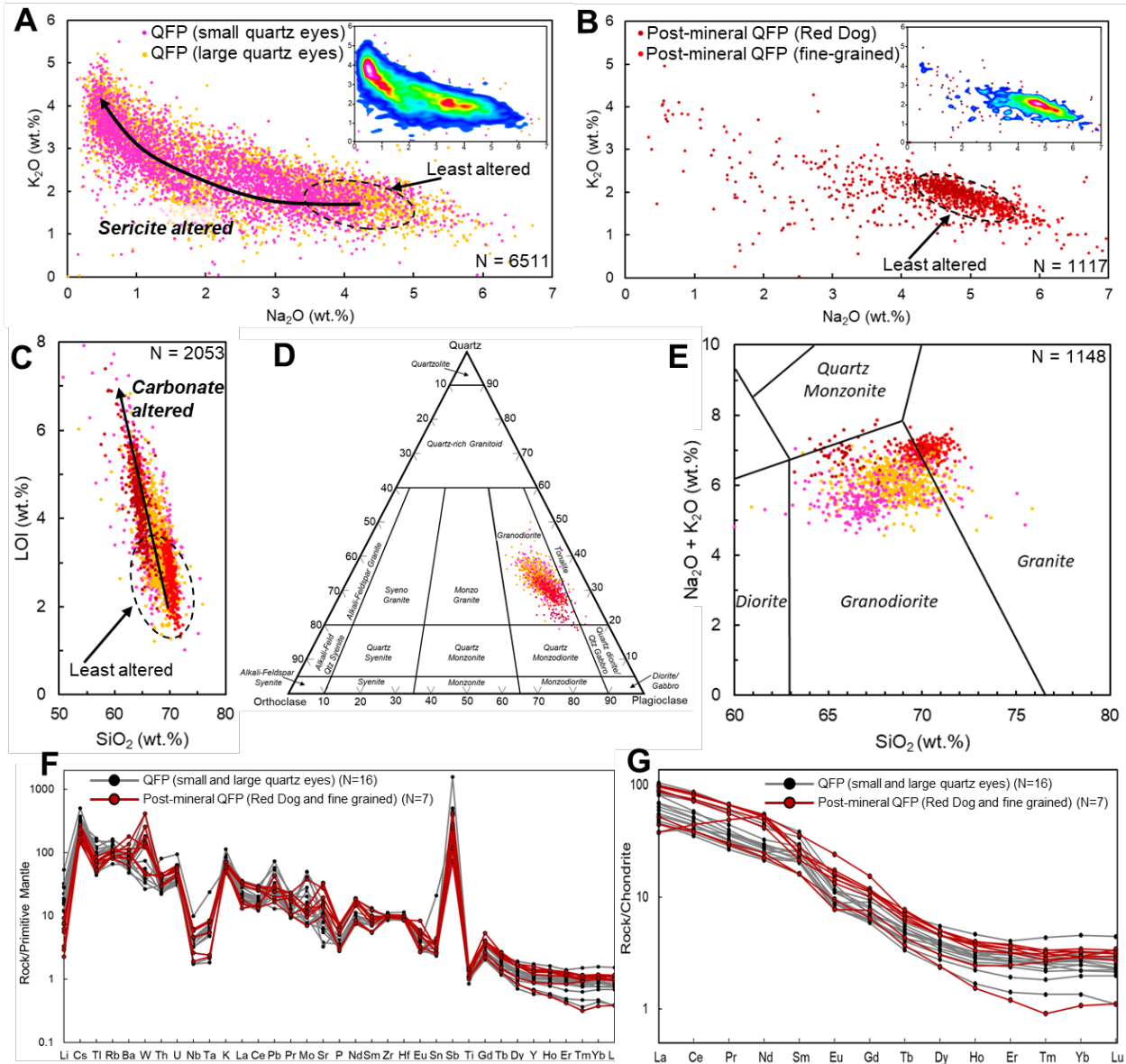


Figure 2.7: Major- and trace element geochemistry for Windfall intrusive complex (WIC) rock types. A, B) Plots of Na<sub>2</sub>O versus K<sub>2</sub>O for pre-mineral (A) and post-mineral (B) QFP dikes with an inset point density plot. Note the least sericite altered field for these rock types. C) Plot of SiO<sub>2</sub> versus LOI for least sericite altered WIC rocks, note that all rock types are affected by a carbonate alteration and the least affected fall in the least carbonate altered field. D) QAP ternary diagram with least altered WIC rocks showing that data plot dominantly in the granodiorite field. E) Total alkali silica (TAS) diagram (modified after Middlemost, 1994) showing least-altered WIC rocks; note that data plot dominantly in the granodiorite field. F) Primitive-mantle normalized multi-element plot (values of Sun and McDonough, 1989) for the WIC, including

pre- and post-mineral QFPs, least altered equivalents. G) Chondrite-normalized rare-earth element plot (values from Sun and McDonough, 1989) for the WIC, including pre- and post-mineral QFPs, least-altered equivalents.

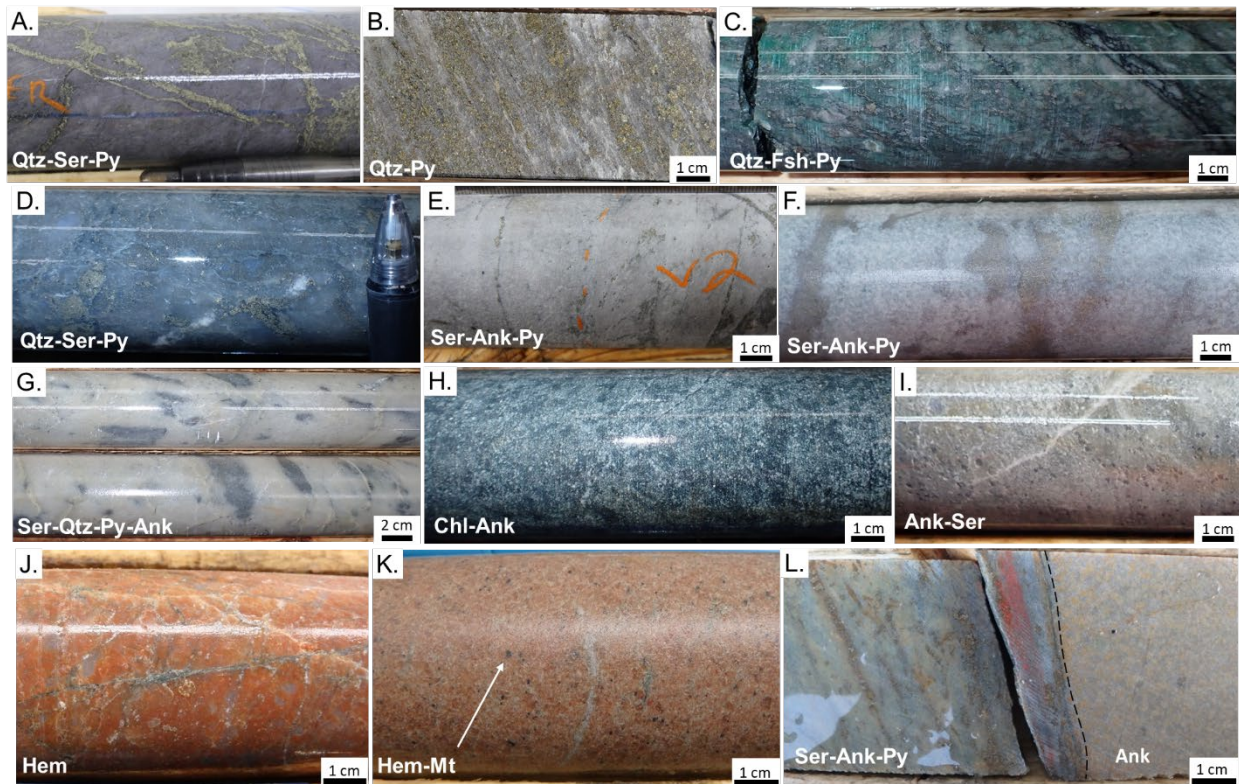


Figure 2.8: Representative images of alteration types observed at the WGD. A, B) Proximal pervasive quartz-sericite-pyrite alteration of an andesite. C) Proximal pervasive quartz-fuchsite-pyrite alteration of a mafic intrusion. D) Proximal pervasive quartz-pyrite alteration of a rhyolite. E, F) Distal pervasive sericite-ankerite-pyrite alteration of an andesite and a mafic intrusion. G) Distal patchy quartz-sericite-pyrite alteration of a rhyolite. H) Distal chlorite-ankerite alteration of a mafic intrusion. I) Distal pervasive ankerite-sericite alteration of a rhyolite. J) Pervasive hematite alteration of the post-mineral Red Dog QFP intrusion, K) Pervasive hematite alteration with disseminated magnetite alteration of a post-mineral fine-grained intrusion. L) Post-mineral intrusion with spotted ankerite alteration cross-cutting syn-mineral sericite-ankerite-pyrite alteration of a bleached andesite. Mineral abbreviations: Ank = ankerite, Chl = chlorite, Hem = hematite, Fsh = fuchsite, Mt = magnetite, Py = pyrite, Qtz = quartz, Ser = sericite.

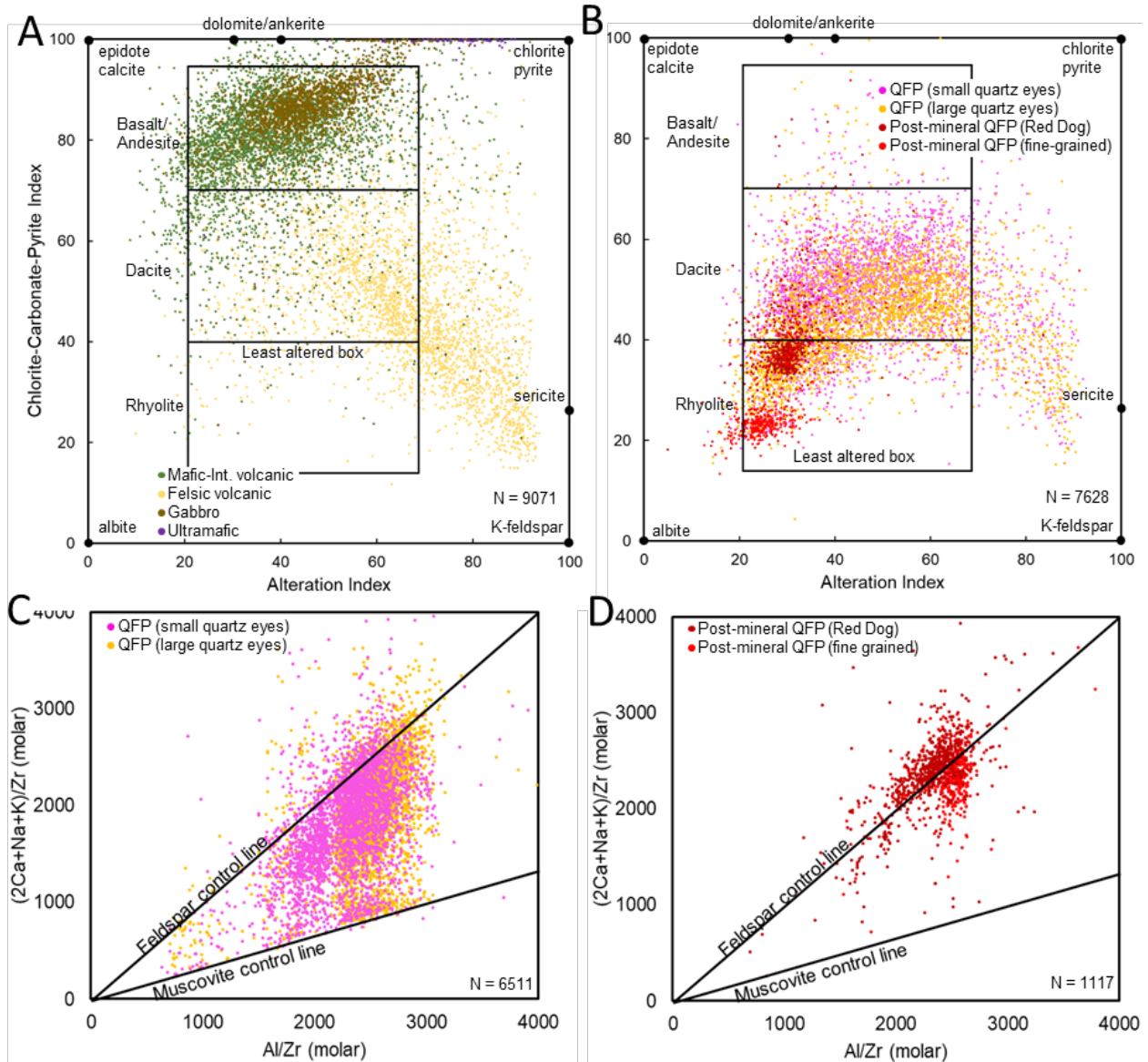


Figure 2.9: A, B) Geochemical data for major rock types plotted in alteration diagrams with the CCP index on the y axis and alteration index on the x axis; see text for explanation: A) synvolcanic lithologies; B) pre- and post-mineral QFP intrusions. C, D) Pearce-element ratio (PER) diagrams for pre- and post-mineral QFP intrusions using molar  $2Ca+Na+K/Zr$  versus molar  $Al/Zr$  where  $Zr$  is the conserved element. Data that is on the feldspar control line defines the least altered samples, whereas data that trends downwards towards the muscovite control line defines sericite altered samples.

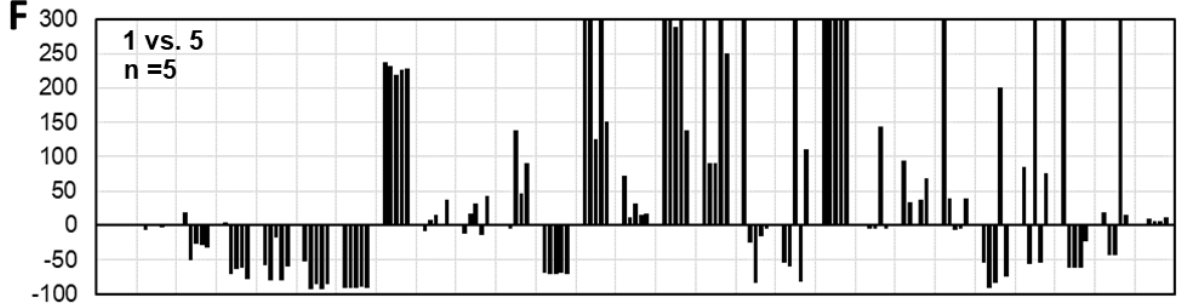
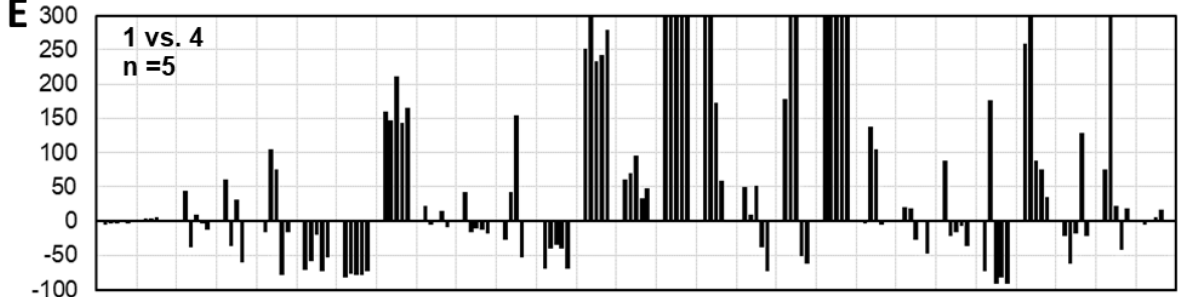
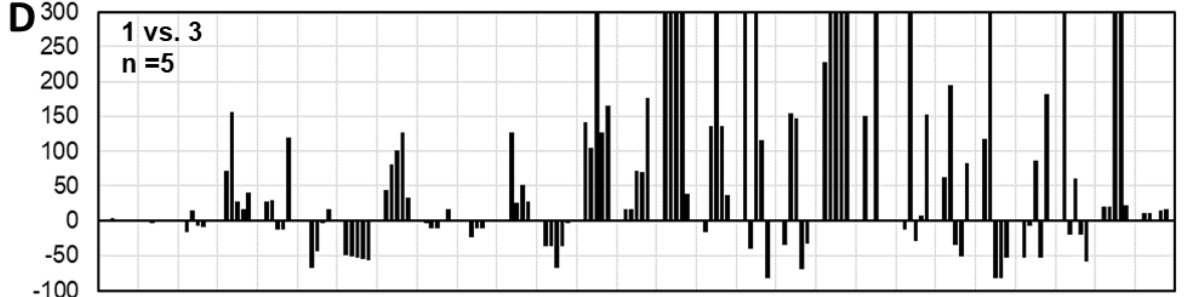
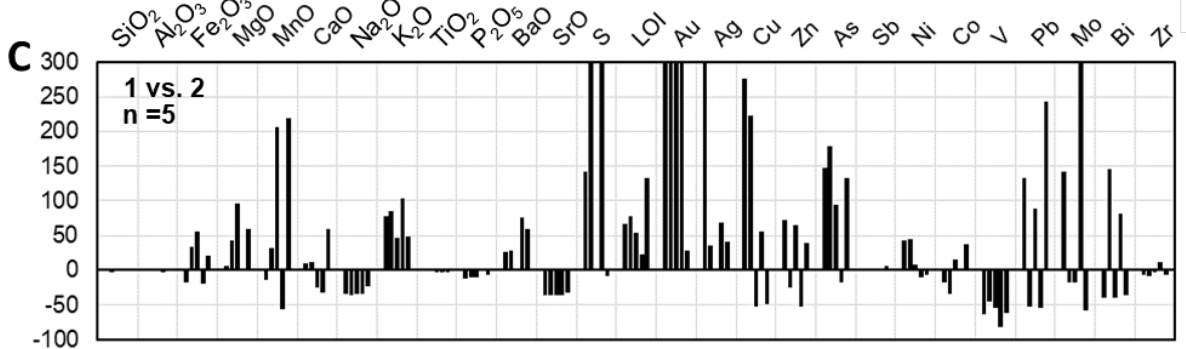
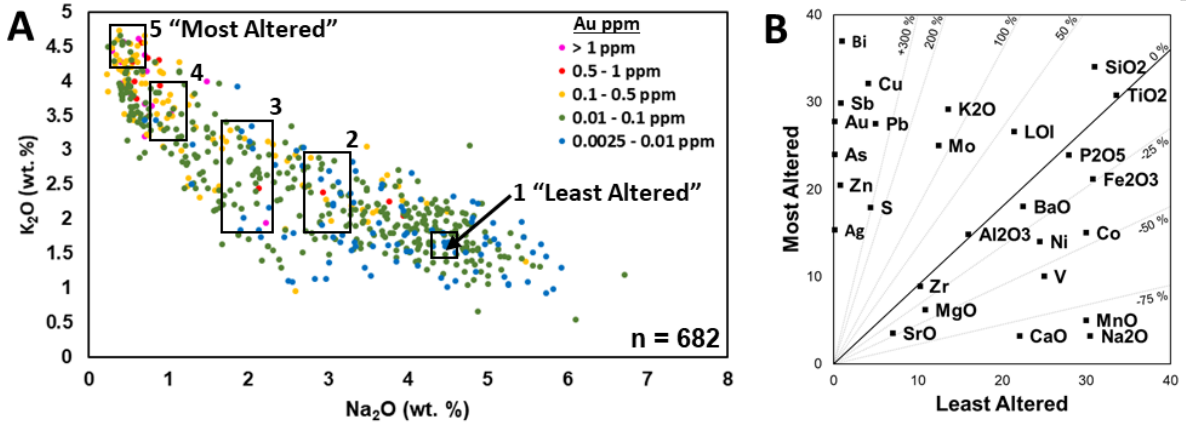


Figure 2.10: Mass balance for samples of progressively altered pre-mineral QFPs with large quartz eyes. A)  $\text{Na}_2\text{O}$  versus  $\text{K}_2\text{O}$  binary diagram colored for Au grades, note that Au grades generally increase with the depletion of  $\text{Na}_2\text{O}$  related to formation of sericite. Plot also shows least altered to most altered sample groups that are selected to represent the change of geochemistry during progressive alteration and mineralization of the rock. B) Mass balance plot for an average of least altered rocks (1) versus a most altered (5) sample. C-F) Histograms showing the gains and losses of major- and trace elements of 4 groups progressively altered and mineralized rocks versus one least altered rock using the Grant-type isocon method.

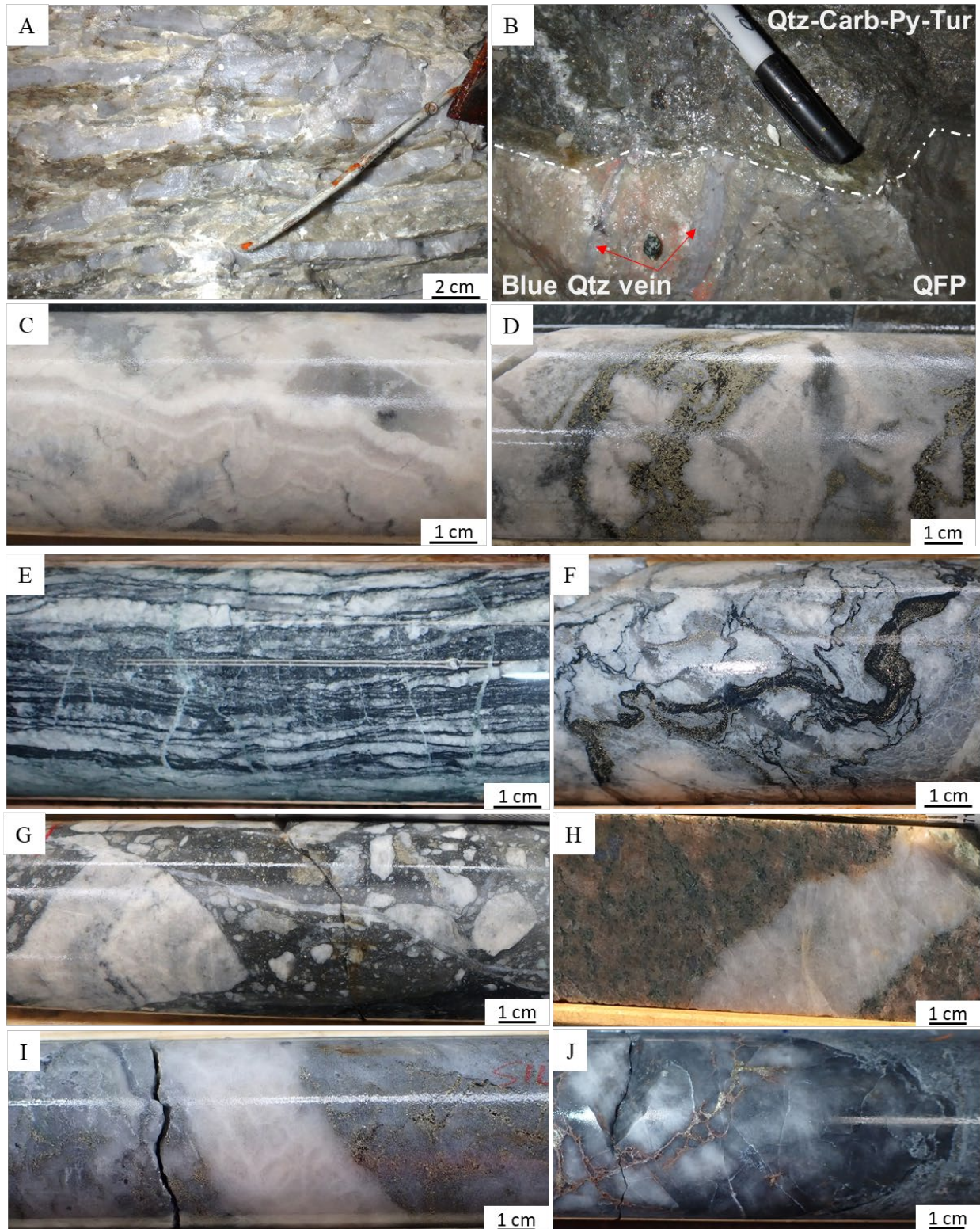


Figure 2.11: Representative images of the pre- (A-D) and post-mineral (E-J) vein types. A) Blue quartz veins forming a sheeted vein array, as seen in underground exposure. B) Equivalent to

previous image, but truncated by quartz-carbonate-pyrite vein. The wall rock is a QFP intrusion. C) Colloform-crustiform carbonate-quartz vein in drill core. D) Equivalent vein as in A, but it is overprinted by syn-mineral quartz-carbonate-pyrite-tourmaline-gold. E) Drill core image of post-mineral laminated quartz-carbonate-tourmaline vein. F) Drill core image of post-mineral ptymatic tourmaline veinlets with pyrite. G) Drill core sample of post-mineral breccia-type vein containing pyrite altered and colloform-textures carbonate-quartz vein clasts cemented in fine-grained tourmaline matrix containing disseminated pyrite. H) Post-mineral white quartz vein that cuts a post-mineral hematite altered QFP. I) Post-mineral white quartz veins that cuts a silica-pyrite-tourmaline alteration of a felsic host rock. J) Post-mineral dark grey quartz vein with late fracture filling sphalerite and pyrite.

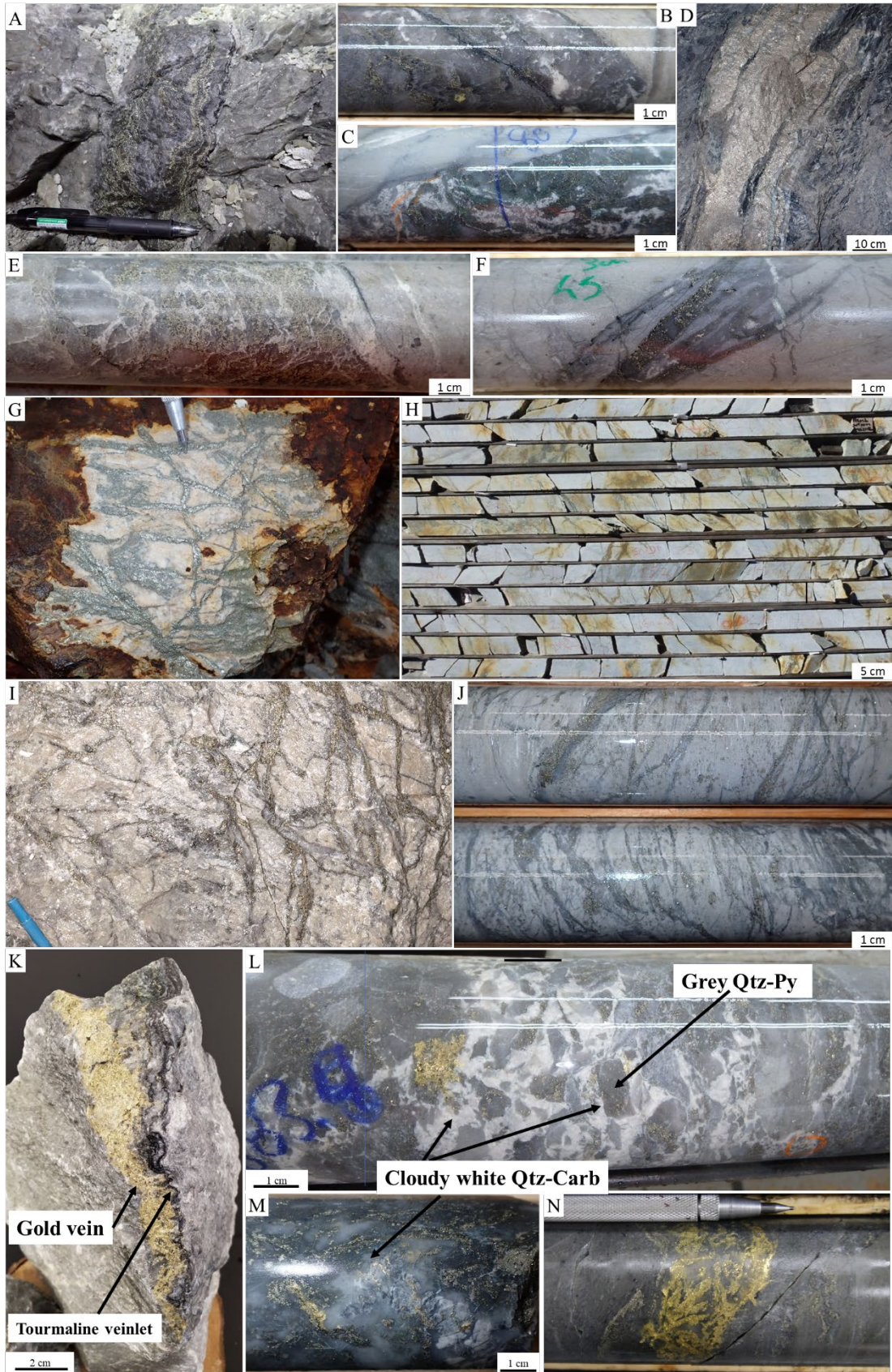


Figure 2.12: Representative images of syn-mineral veins and gold-rich veins in the WGD. A) Underground image of massive grey quartz vein with subordinate carbonate, pyrite, and tourmaline. B, C) Drill core sample of massive grey quartz veins with subordinate carbonate, pyrite, tourmaline, fuchsite and visible Au. D) Underground image of pyrite-rich quartz vein. E-F) Drill core sample of massive grey quartz veins with subordinate carbonate, pyrite, tourmaline, and beige colored sphalerite. G, H) Outcrop, core box, and underground images of pyrite and quartz-pyrite stockworks. K) A boulder from the Lynx zone bulk sample on level 021 cut by veins of quartz-carbonate-pyrite-tourmaline and massive gold. L, M) Brecciated grey quartz-pyrite vein cemented by cloudy white quartz-carbonate with remobilized gold. N) Image of high-grade Au grey quartz vein with spectacular visible gold. Abbreviations: Qtz = quartz, Py = pyrite, Carb = carbonate.

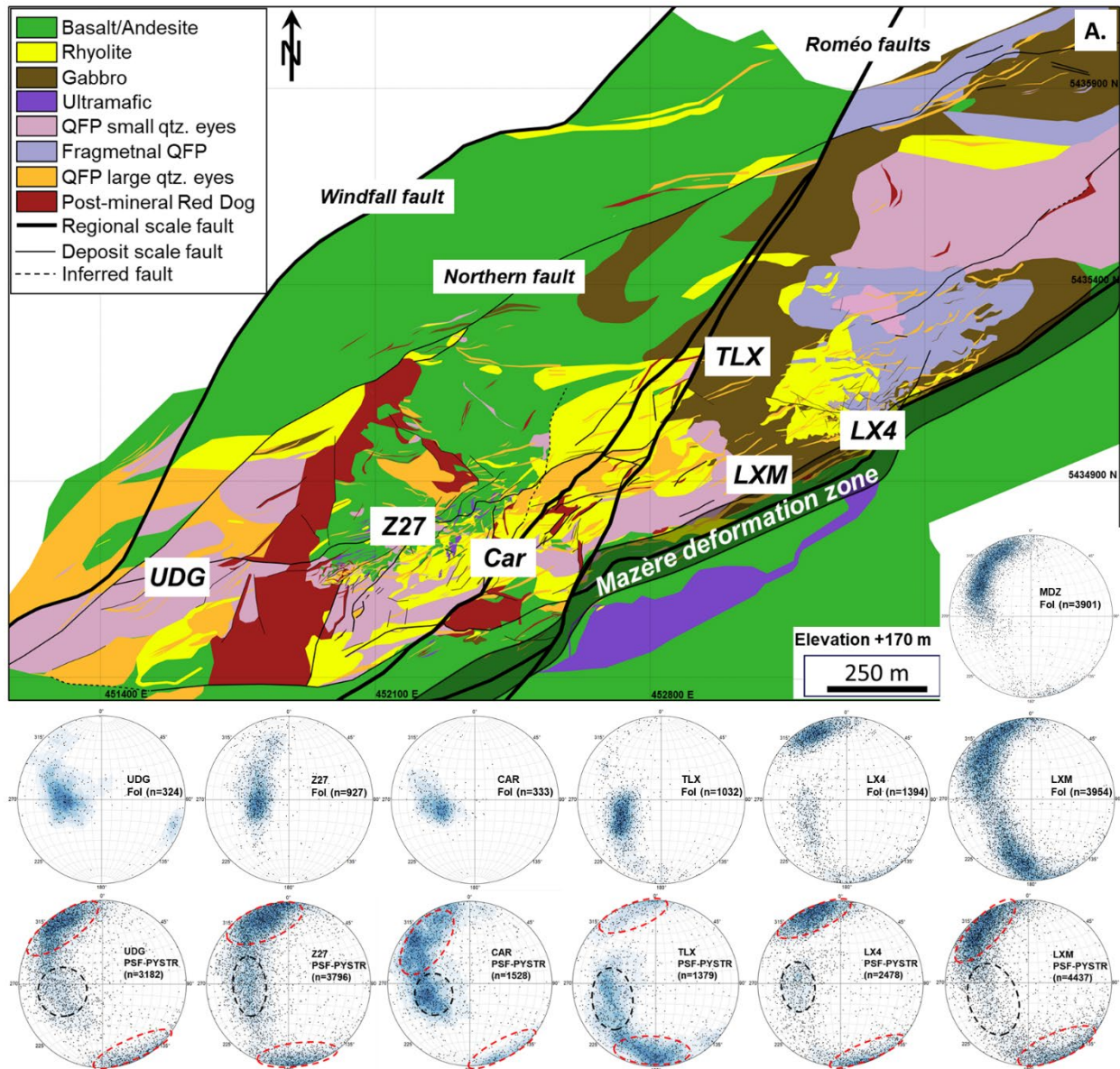


Figure 2.13: A) Geological map of the Windfall deposit at elevation +170 m (i.e., 230 m below surface) showing the locations of the structural data from oriented core used in the stereoplots. The red-dashed ellipses are the main vein orientations hosted in ENE- and W-trending faults, whereas the black-dashed ellipses are the secondary vein splays hosted in the N-trending shear zones. From west to east the data for foliation (FOL) and for syn-mineral quartz-pyrite-carbonate-tourmaline veins (PSF) and for pyrite veinlets (PYSTR) are filtered with respect to specific mineral zones in the deposit (Underdog (UDG), Zone 27 (Z27), Caribou (CAR), Triple Lynx (TLX), Lynx Main (LXM), Lynx 4 (LX4), and one plot for foliation in the hanging of the Mazères deformation zone (MDZ).

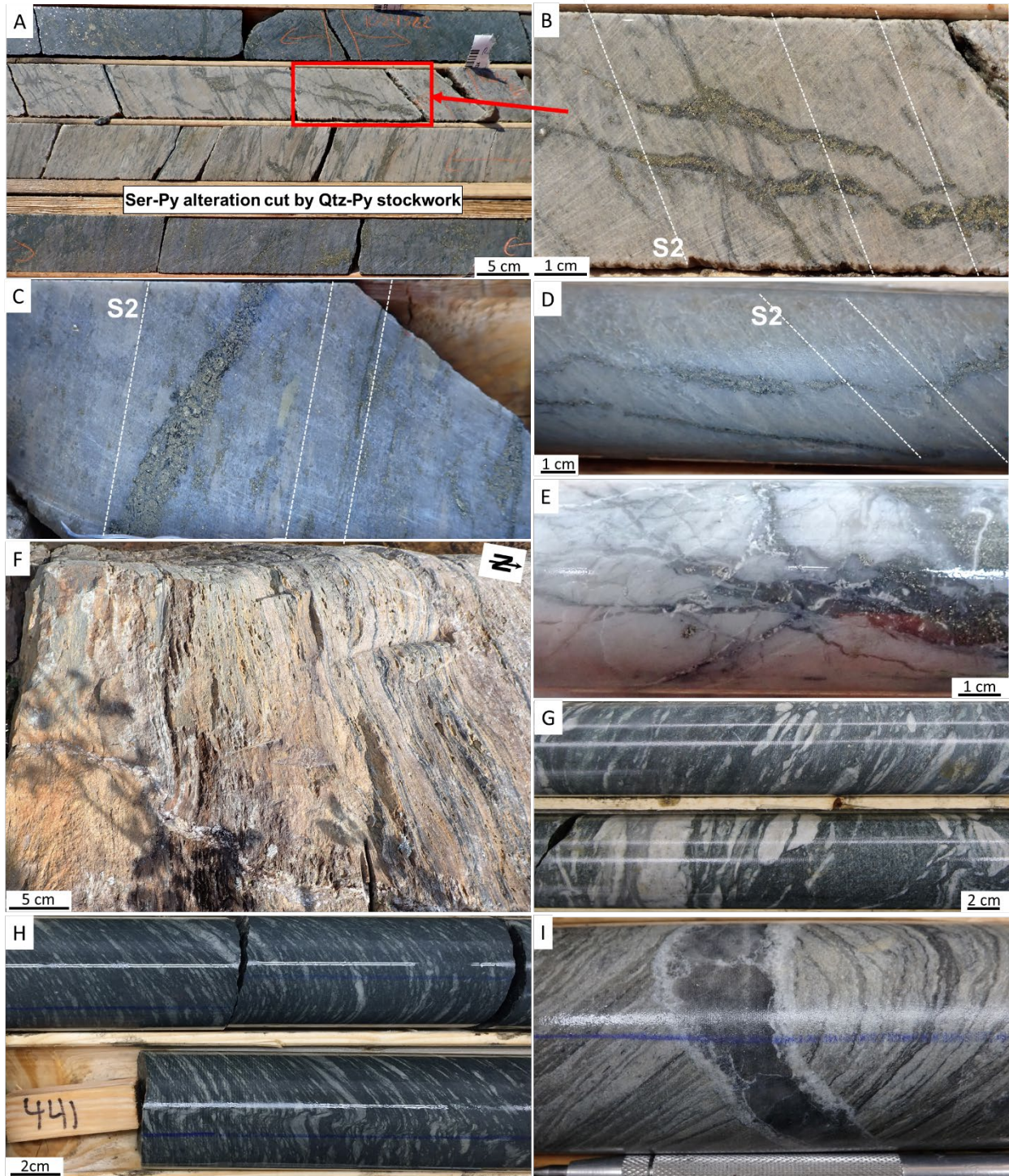


Figure 2.14: Representative images of pre-syn, and post-mineral  $D_2$  deformation. A, B) Andesite altered to sericite-pyrite and later crosscut by syn-mineral quartz-pyrite stockwork. Dashed white line shows the  $S_2$  fabric. C, D) Syn-mineral pyrite veinlet cutting stretched volcanic fragments and well-developed foliation. E) Example of brittle deformation features that control vein emplacement in felsic domains. F) Highly-strained felsic intrusion within 20 m of the Mazères fault showing the ductile overprint. G-I) Representative images of Au barren rocks in the

hanging wall of the Mazères fault: G - boudinaged quartz-carbonate veins, H - highly deformed boudinaged and folded quartz-carbonate veins, I - highly-deformed andesite cut by smoky quartz vein.

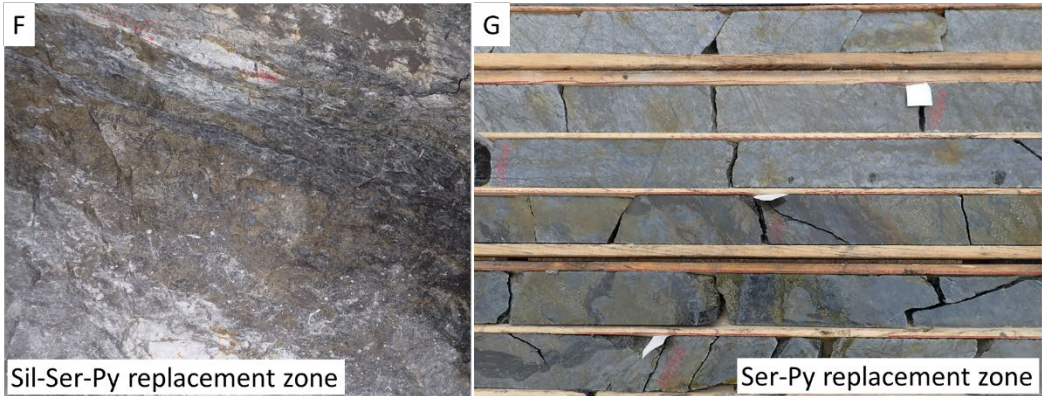
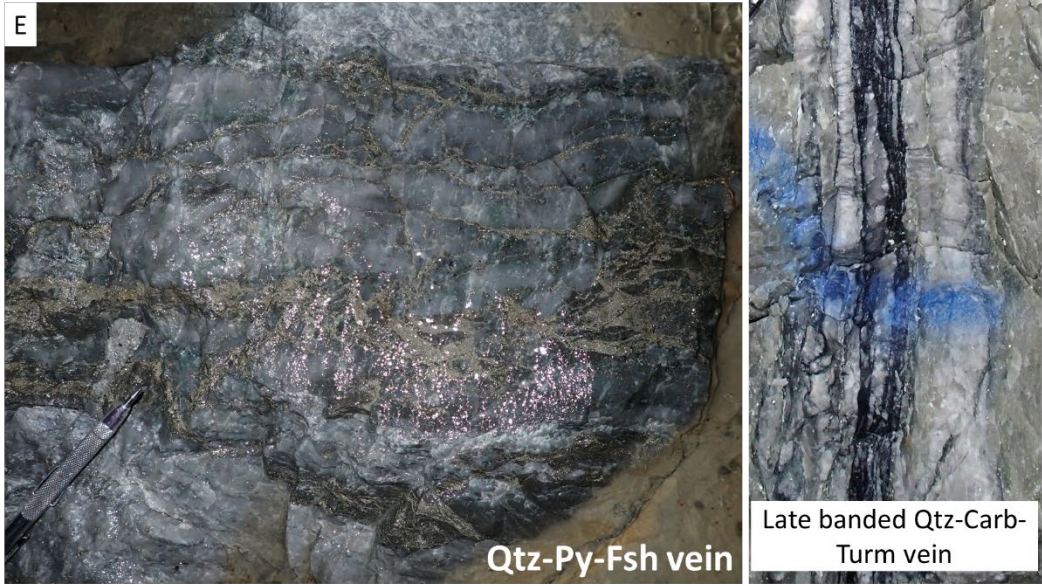
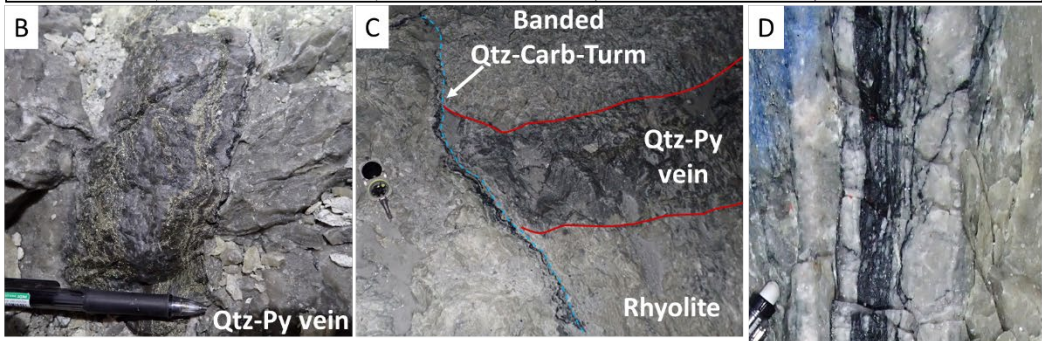
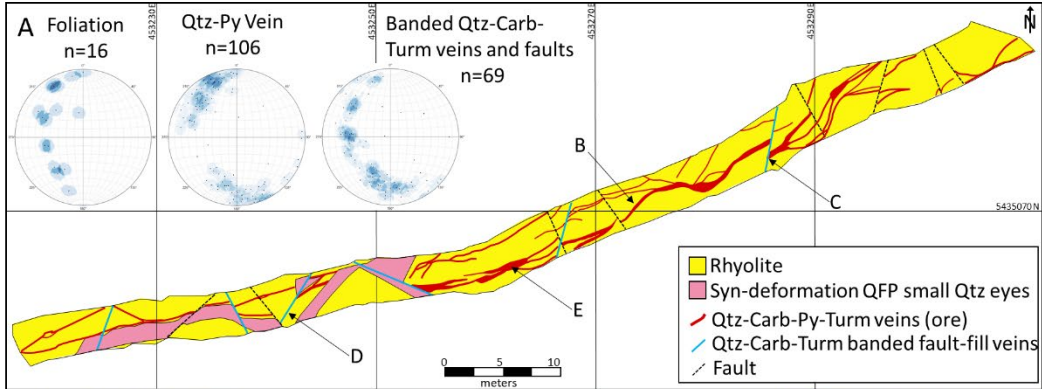


Figure 2.15: Examples of vein- (B-D) and replacement- (F) style mineralization. A) Underground geology map of the Lynx Au zone that was bulk sampled along with stereo plots for foliation, quartz-carbonate-pyrite-tourmaline-Au veins (see images B, C, E), and for late banded quartz-carbonate-tourmaline veins (see photo D). F) Photo taken of underground exposure of silica-sericite-pyrite alteration of an andesite. G) Core boxes showing a sericite-pyrite alteration zone cut by later tourmaline veinlets. Map in A courtesy of Osisko Mining. Abbreviations: Qtz = quartz, Carb = carbonate, Turm = tourmaline, Py = pyrite, Fsh = fuchsite, Sil = silica, and Ser = sericite.

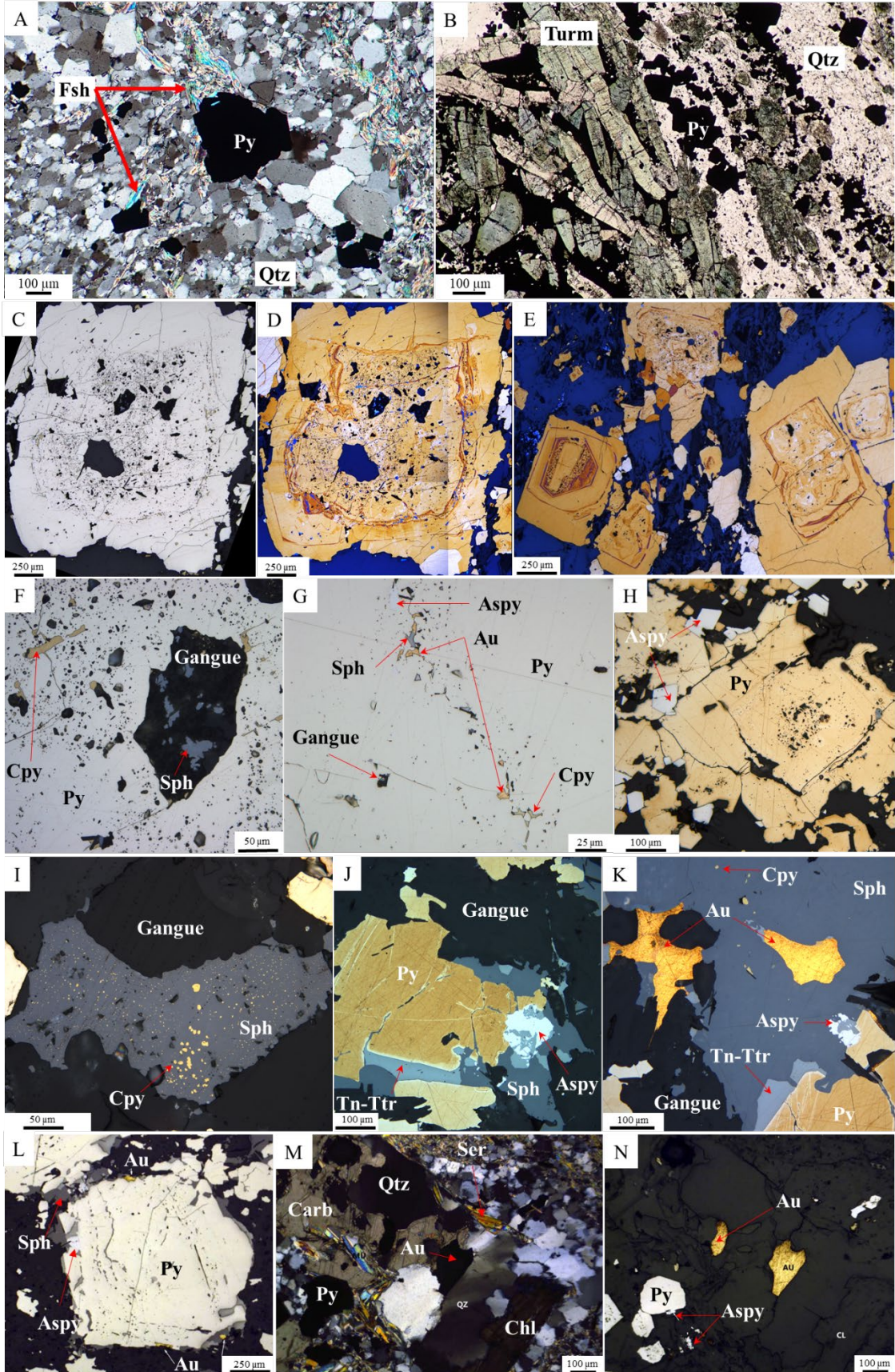


Figure 2.16: Representative transmitted (A, B, and M) and reflected light photomicrographs of polished thin sections showing gangue and sulfide mineralogy in syn-mineral veins. Note that in some cases samples are etched with bleach (NaClO). A) Image showing the fine-grained texture of the vein quartz which has a granoblastic polygonal texture and the associated  $120^\circ$  triple junctions, also observed are small grains of pyrite and fuchsite, as determined from hand sample observations. B) Image of quartz-tourmaline-pyrite vein showing the euhedral shape of tourmaline crystals that vary in color from light blue-green in the core to light green in the rim. C-D) Original pyrite and etched equivalent showing inclusion-rich core overgrown by a darker band which is in turn overgrown by an inclusion-poor pyrite. E) Etched syn-mineral vein (quartz, carbonate, pyrite, tourmaline and gold) which reveals abundant zoned pyrite grains. F, G) Inclusion-rich pyrite (Py) cores containing chalcopyrite (Cpy), sphalerite (Sph), arsenopyrite (Aspy), gold (Au) and unknown gangue minerals. H) Euhedral- to subhedral arsenopyrite grains post-dating pyrite. I) Sphalerite with chalcopyrite disease. J, K, L) Veins containing pyrite overgrown by later sphalerite, chalcopyrite, arsenopyrite, tennantite-tetrahedrite (Tn-Ttr) and late-stage gold. M, N) Sericite-chlorite altered rhyolite cut by a quartz-carbonate-pyrite-arsenopyrite-gold vein in transmitted (M) and reflected light (N). Photos A, B, and M, N are taken from internal petrographic reports by É.C. Lavoie and L. Tremblay.

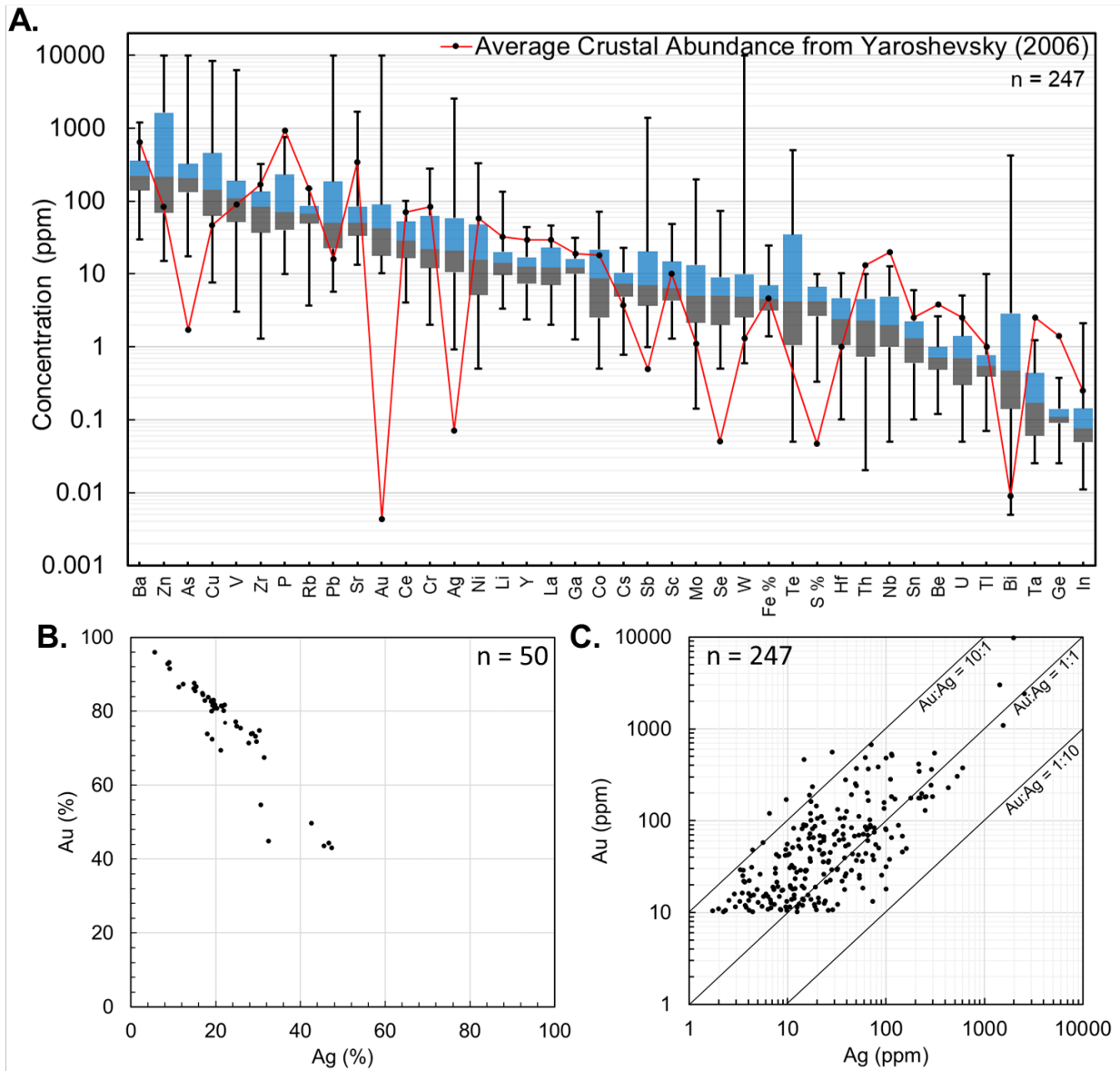


Figure 2.17: A) Multi-element assays (MEA) for Au-mineralized vein samples having >10 g/t Au. Trace elements are given in ppm, whereas the major elements (Fe and S) are in wt. %. Plot illustrates the various anomalous metals that are enriched relative to the average crustal abundance in the high-grade Au samples. B) Binary plot of Ag versus Au for EMPA analysis of gold grains in syn-mineral quartz-carbonate-tourmaline-pyrite-Au veins, note the trend from low to high Au:Ag. C) Plot of Ag versus Au for MEA bulk analyses of the Au-mineralized samples having >10 g/t Au.

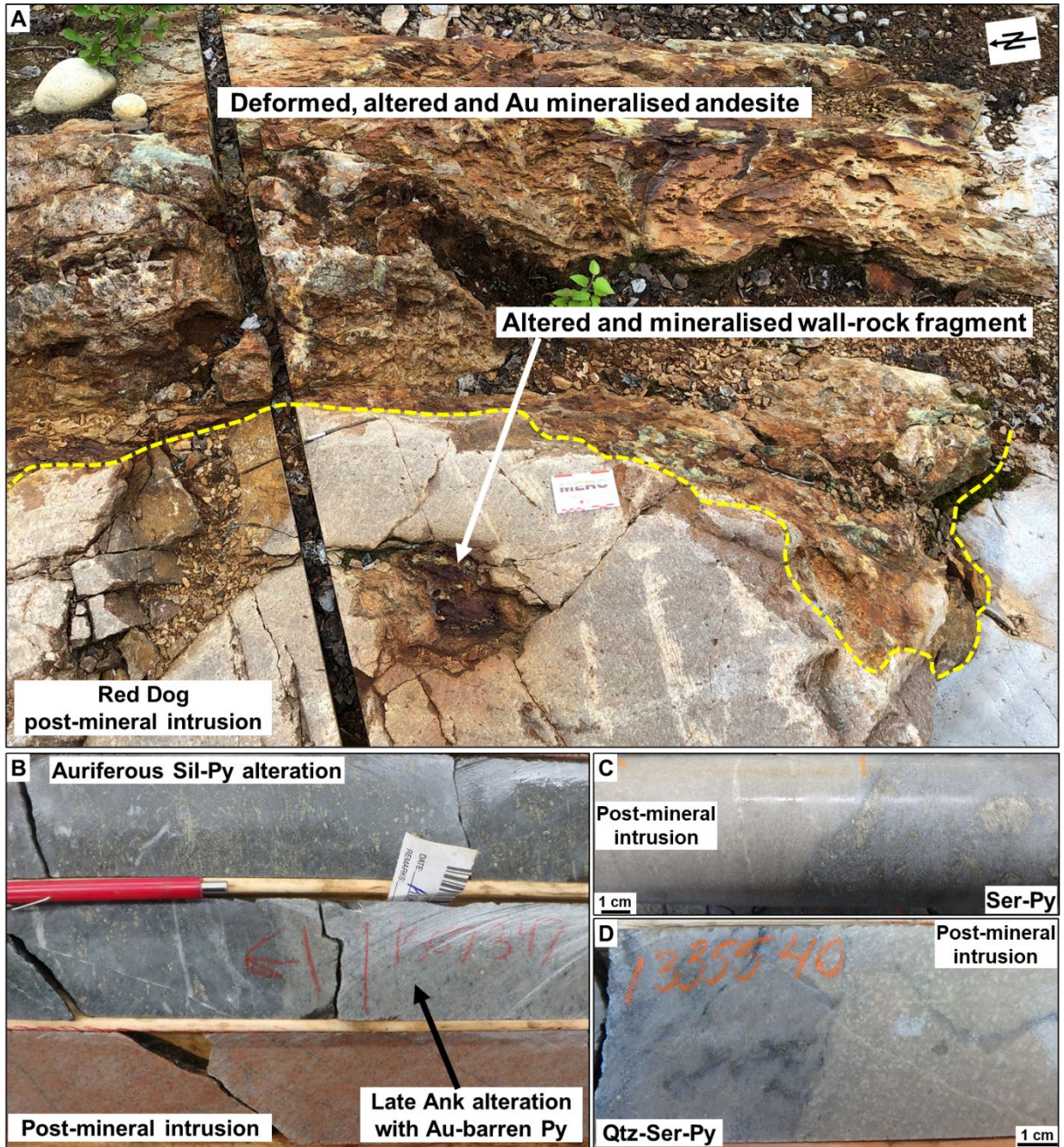


Figure 2.18: A) Outcrop photograph taken proximal the Main Zone in the WGD showing strongly-deformed sericite-carbonate-pyrite altered andesite (top) crosscut by the post-mineral Red Dog intrusion (bottom). Note that the intrusion has an irregular contact that is not affected by the intense deformation seen in the enclosed altered fragment. B-D) Drill core photos showing auriferous silica-pyrite (B) and sericite-pyrite (C-D) assemblages hosted in felsic rocks that are in turn crosscut by post-mineral fine-grained hematite-altered felsic intrusions. The margins of the post-mineral dikes are altered by Au-barren post-mineral ankerite alteration attributed to a later event.

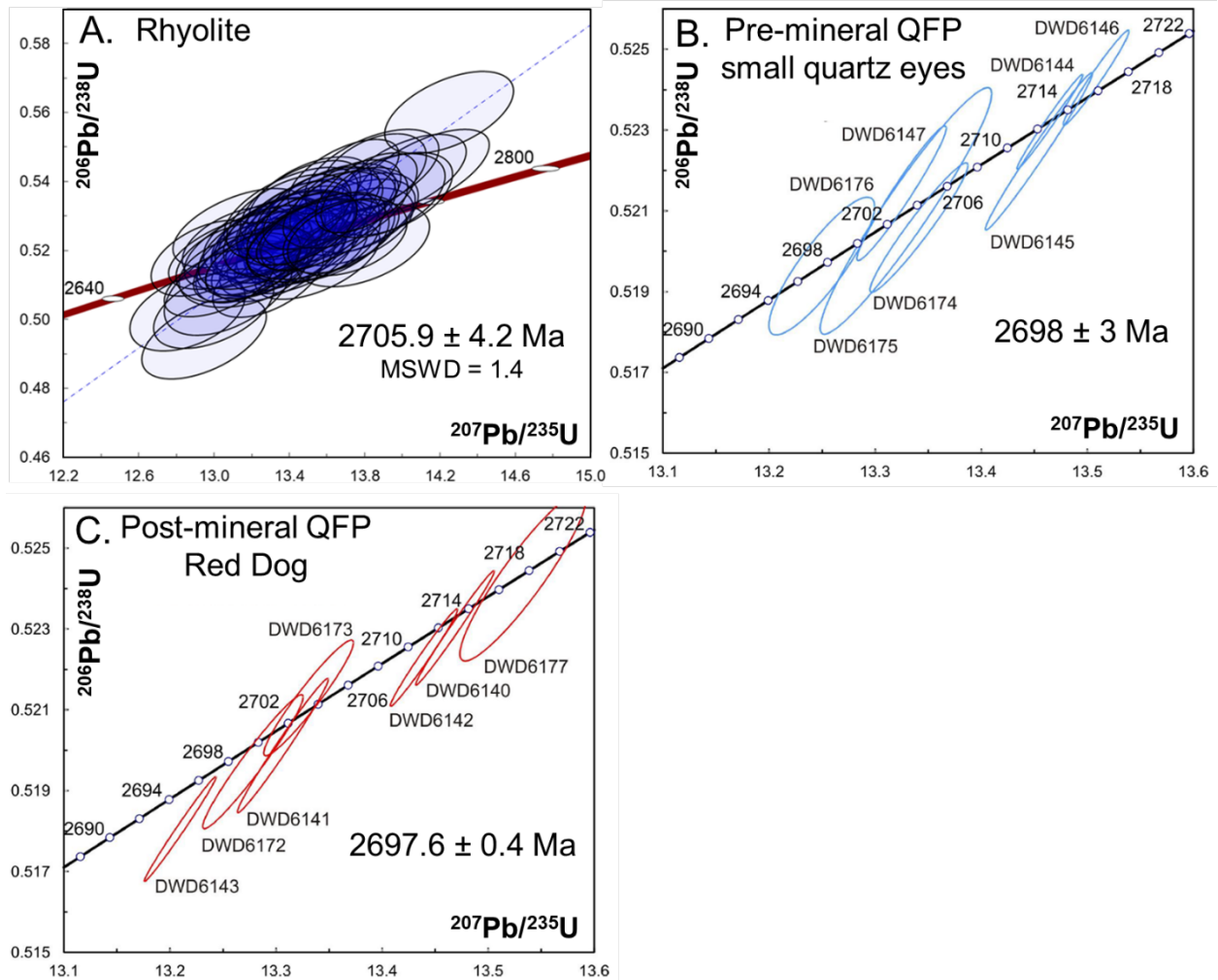


Figure 2.19: Concordia plots for U-Pb zircon analyses of samples from Windfall deposit area. A) LA ICP-MS data for felsic volcanic rock sample collected from an underground exposure (Azevedo, 2019). B, C) CA-TIMS data for pre- and post-mineral felsic dike rocks collected from drillholes OBM-16-579 and EAG-15-552 (Davis, 2017).

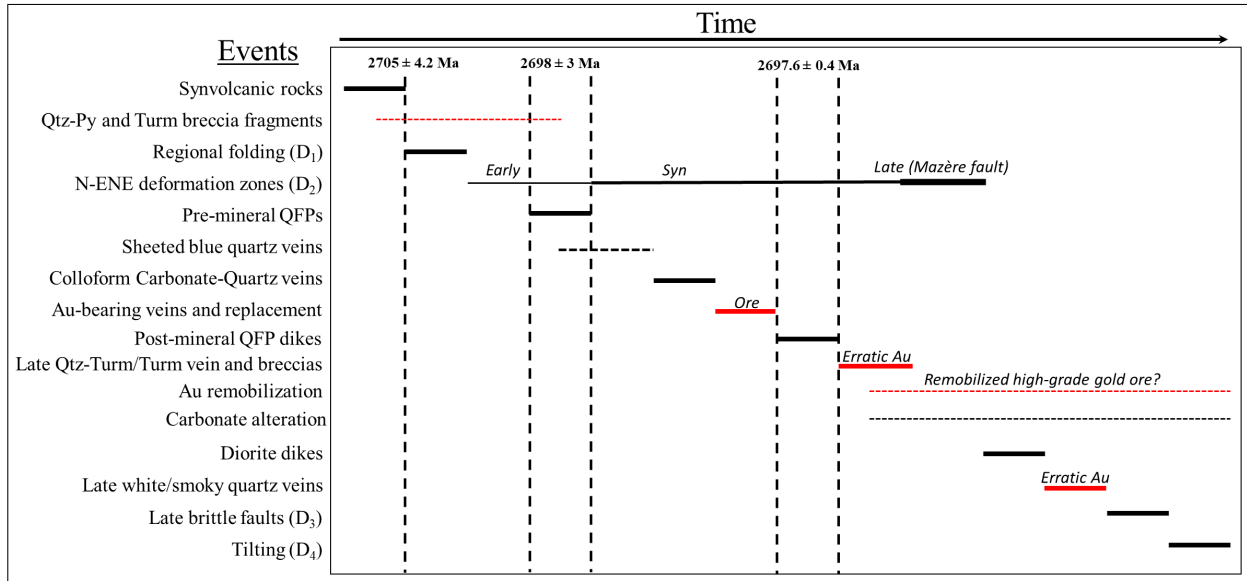


Figure 2.20: A simplified paragenesis for WGD that summarizes the sequence of events. Note that Au events are shown by red lines.

## 2.9 Tables

**Table 2.1 - Average compositions of least altered phases of the WIC used for calculations of crystallisation pressure**

	<u>QFP Sm. Qtz. Eye</u>	<u>QFP Lg. Qtz. Eye</u>	<u>Post-mineral Red Dog</u>	<u>Post-mineral f.g. hmt. dike</u>
SiO <sub>2</sub>	66.94	68.45	68.26	69.67
Al <sub>2</sub> O <sub>3</sub>	14.87	14.95	15.20	15.08
Fe <sub>2</sub> O <sub>3</sub>	3.56	2.37	2.50	1.79
FeO*	3.20	2.14	2.25	1.61
MgO	1.30	1.05	1.05	0.65
MnO	0.04	0.03	0.03	0.03
CaO	3.40	2.94	2.86	2.37
Na <sub>2</sub> O	4.27	4.85	4.97	5.54
K <sub>2</sub> O	1.52	1.53	1.67	1.50
TiO <sub>2</sub>	0.36	0.26	0.27	0.24
P <sub>2</sub> O <sub>5</sub>	0.10	0.08	0.10	0.07
Cr <sub>2</sub> O <sub>3</sub>	0.01	0.01	0.01	0.01
BaO	0.05	0.05	0.06	0.06
SrO	0.03	0.02	0.03	0.02
LOI	2.64	2.61	2.58	2.40
Total	99.05	99.21	99.57	99.39
Zr	110	102	111	108
# analyses averaged	24	37	9	24
P (Qtz)	142.57	202.84	266.1	301.44
P (Ab+Or)	134.13	193.91	256.69	291.8
P (Mpa) (average)	138.35	198.38	261.39	296.62
Emplacement depth (km)	3.74	5.36	7.06	8.01

Note: Major elements and LOI are in weight percent, Zr is in ppm. Pressure calculations were done using the excel spreadsheet and following the guidelines presented in Yang et al., 2021.

**Table 2.2 - Average composition of progressively altered rocks from the WLGD**

	<u>Least-altered</u>			<u>Altered 2</u>			<u>Altered 3</u>			<u>Altered 4</u>			<u>Altered 5</u>		
	Average	STD	n	Average	STD	n	Average	STD	n	Average	STD	n	Average	STD	n
SiO <sub>2</sub>	69.38	0.72	5	67.25	1.63	5	69.30	1.33	5	68.94	2.03	5	71.92	0.96	5
Al <sub>2</sub> O <sub>3</sub>	15.36	0.21	5	14.92	0.18	5	15.03	0.21	5	16.30	0.35	5	15.74	0.73	5
Fe <sub>2</sub> O <sub>3</sub>	2.67	0.25	5	2.99	0.86	5	2.54	0.27	5	2.72	0.72	5	2.11	0.59	5
MgO	1.29	0.27	5	1.78	0.46	5	2.07	0.64	5	1.30	0.57	5	0.61	0.38	5
MnO	0.02	0.01	5	0.04	0.02	5	0.03	0.01	5	0.03	0.02	5	0.01	0.01	5
CaO	2.75	0.56	5	2.82	0.55	5	2.19	0.86	5	1.25	0.51	5	0.51	0.40	5
Na <sub>2</sub> O	4.45	0.10	5	2.95	0.07	5	2.07	0.12	5	1.00	0.15	5	0.44	0.05	5
K <sub>2</sub> O	1.36	0.23	5	2.29	0.28	5	2.38	0.47	5	3.68	0.24	5	4.61	0.08	5
TiO <sub>2</sub>	0.27	0.03	5	0.26	0.01	5	0.26	0.03	5	0.29	0.04	5	0.31	0.05	5
P <sub>2</sub> O <sub>5</sub>	0.08	0.01	5	0.07	0.00	5	0.07	0.01	5	0.08	0.02	5	0.09	0.02	5
BaO	0.04	0.01	5	0.05	0.01	5	0.06	0.02	5	0.05	0.03	5	0.06	0.02	5
SrO	0.03	0.01	5	0.02	0.00	5	0.02	0.01	5	0.02	0.00	5	0.01	0.00	5
S	0.36	0.07	5	1.00	0.63	5	1.02	0.37	5	1.81	1.03	5	1.54	0.61	5
LOI	2.11	0.45	5	3.51	0.42	5	3.55	1.19	5	3.49	0.39	5	2.82	0.43	5
Au	0.01	0.01	5	0.30	0.35	5	0.47	0.56	5	1.45	1.52	5	0.35	0.36	5
Ag	0.30	0.15	5	0.66	0.57	5	1.25	1.49	5	1.64	1.40	5	0.96	0.30	5
Cu	58.00	30.51	5	108.80	74.85	5	126.80	94.71	5	59.00	28.17	5	203.60	325.62	5
Zn	25.83	3.80	5	30.20	13.99	5	34.00	24.72	5	370.80	418.05	5	39.00	40.08	5
As	3.67	2.49	5	7.40	2.68	5	35.20	18.73	5	47.00	38.07	5	38.20	14.92	5
Sb	1.00	0.00	5	1.00	0.00	5	8.50	14.26	5	1.50	0.63	5	1.30	0.60	5
Ni	5.67	1.25	5	6.40	1.30	5	13.60	13.18	5	5.40	1.62	5	8.60	1.74	5
Co	6.17	2.48	5	6.00	1.12	5	9.20	5.42	5	6.40	2.87	5	11.20	7.52	5
V	11.00	7.26	5	4.20	1.48	5	17.00	19.33	5	7.80	12.12	5	9.00	12.57	5
Pb	2.17	1.34	5	3.60	1.79	5	2.80	1.94	5	11.20	13.01	5	4.20	3.66	5
Mo	1.25	1.68	5	2.70	2.86	5	3.50	4.77	5	1.30	0.87	5	8.90	16.55	5
Bi	1.67	0.75	5	2.00	1.30	5	8.80	9.43	5	3.20	2.48	5	7.00	11.01	5
Zr	106.17	6.04	5	101.60	8.56	5	116.00	6.32	5	113.00	8.44	5	118.00	5.02	5

Note: Major elements, S and LOI are in weight percent, trace elements are in ppm

**Table 2.3 - Calculated gains and losses in percent for progressively altered rocks compared to an average least altered rock from the WLGD**

	2a	2b	2c	2d	2e	3a	3b	3c	3c	3d	3e	4a	4b	4c	4d	4e	5a	5b	5c	5d	5e
SiO <sub>2</sub>	-1.2	-3.5	-1.8	2.0	1.1	0.6	4.0	0.7	-0.1	-0.8	-5.0	-3.9	-3.0	-1.2	-2.7	1.3	0.0	0.0	-1.4	2.2	-0.3
Al <sub>2</sub> O <sub>3</sub>	1.1	-0.5	-0.2	-2.1	-0.7	-0.6	-3.7	-0.7	-1.1	0.3	4.6	4.5	6.2	6.2	1.5	-6.0	1.1	1.1	1.8	-2.0	0.9
Fe <sub>2</sub> O <sub>3</sub>	-18.3	34.1	56.7	-19.4	20.7	-15.7	15.0	-8.1	-8.4	-2.5	43.6	-38.3	8.9	-4.0	-12.6	19.9	-50.1	-50.1	-26.5	-27.7	-31.5
MgO	7.3	42.4	96.2	3.4	60.0	71.3	155.3	26.8	17.5	40.8	60.3	-37.2	31.3	-60.1	-0.4	3.9	-70.5	-70.5	-63.7	-61.4	-78.5
MnO	-13.4	31.2	206.1	-56.7	219.1	28.6	29.9	-13.4	-13.4	118.7	-16.8	104.1	74.9	-79.6	-16.0	-57.1	-79.6	-79.6	-18.0	-79.1	-59.0
CaO	10.9	12.4	-24.0	-32.5	60.1	0.7	-68.4	-44.2	-3.1	16.4	-71.8	-57.8	-19.9	-74.0	-53.0	-53.1	-92.7	-92.7	-85.4	-92.6	-86.1
Na <sub>2</sub> O	-33.3	-36.7	-33.5	-34.0	-22.8	-50.1	-51.4	-52.4	-54.6	-56.9	-82.6	-77.8	-79.1	-78.8	-72.5	-90.1	-91.7	-91.7	-90.8	-88.6	-91.4
K <sub>2</sub> O	77.2	85.8	47.4	103.3	49.0	43.7	81.7	101.0	127.1	32.4	160.5	147.1	210.6	142.9	164.5	236.9	232.7	232.7	219.5	226.5	228.7
TiO <sub>2</sub>	0.4	1.4	-2.3	-3.3	-2.1	-4.3	-10.8	-10.8	0.4	16.4	21.5	-5.3	-2.3	15.7	-9.8	-8.0	8.7	8.7	16.2	0.6	37.4
P <sub>2</sub> O <sub>5</sub>	-11.4	-10.5	-10.5	1.2	-6.7	0.2	-24.1	-11.4	-11.4	2.3	42.3	-16.5	-10.5	-12.9	-18.9	-12.3	16.9	16.9	31.9	-14.5	43.8
BaO	26.3	27.6	2.0	76.8	59.6	0.0	127.3	26.3	51.5	27.6	-27.2	42.9	155.1	-52.4	-2.0	0.0	-4.8	-4.8	139.2	46.3	91.4
SiO	-36.2	-35.6	-35.6	-36.2	-32.8	-36.8	-36.2	-68.1	-36.2	-3.3	-69.3	-39.8	-35.6	-39.8	-69.0	-68.4	-69.9	-69.9	-69.8	-69.2	-69.8
S	143.0	309.1	-1.3	464.2	-8.8	140.6	103.9	386.0	126.2	165.2	251.7	919.1	232.9	242.3	279.5	591.2	305.5	305.5	124.9	396.3	151.4
LOI	66.6	78.0	53.3	23.5	132.9	17.1	15.9	71.4	70.4	175.7	61.5	70.2	95.9	33.2	47.8	71.6	11.5	11.5	32.9	15.1	16.6
Au	6638.8	2545.8	585.1	477.2	29.2	10114.3	5599.9	347.3	318.5	38.5	26182.9	18539.5	811.1	3246.9	782.4	7185.7	2199.3	2199.3	289.6	1920.9	139.2
Ag	472.4	36.1	2.0	68.4	41.8	-16.7	135.7	1314.1	135.7	36.1	806.1	1106.3	172.1	58.7	-2.0	300.0	90.5	90.5	91.4	322.8	250.9
Cu	276.2	222.0	-52.5	56.7	-48.6	308.6	-40.8	298.8	116.0	-82.4	49.0	8.4	51.3	-37.6	-73.0	1372.4	-24.5	-24.5	-83.5	-15.9	-4.3
Zn	72.0	-25.0	65.9	-53.1	40.0	-34.2	154.2	146.3	-68.7	-32.9	178.1	3424.4	3063.9	-52.1	-62.0	-53.5	-59.4	-59.4	307.5	-81.1	111.1
As	147.9	178.3	94.8	-17.4	132.1	227.3	1277.4	1580.4	368.3	901.9	641.4	3068.8	595.7	939.0	434.8	390.9	1510.4	1510.4	917.8	645.0	1048.3
Sb	1.0	2.0	2.0	1.0	6.4	150.0	1.0	3637.4	1.0	2.0	-2.9	138.1	104.1	-4.8	-2.0	0.0	-4.8	-4.8	-4.3	143.9	-4.3
Ni	42.6	44.1	8.0	-10.9	-6.1	-11.8	595.2	-28.7	7.0	152.1	19.9	17.6	-28.0	0.8	-48.1	94.1	34.5	34.5	1.3	37.7	68.9
Co	-18.1	-33.8	15.8	-1.7	38.0	62.2	194.8	-34.5	-50.9	82.0	88.9	-22.8	-17.3	-7.3	-36.4	321.6	39.0	39.0	-6.9	-5.1	39.7
V	-63.3	-44.3	-53.6	-81.6	-61.3	118.2	377.5	-81.6	-81.6	-53.6	-73.5	177.1	-90.7	-82.7	-91.1	-54.5	-91.3	-91.3	-82.6	201.6	-73.9
Pb	133.1	-52.9	88.4	-53.4	243.7	-53.8	-6.8	86.5	-53.4	182.6	258.5	1526.4	88.4	75.8	35.7	84.6	-56.0	-56.0	385.8	-55.0	76.7
Mo	142.4	-18.4	-18.4	546.5	-57.4	940.0	-19.2	61.6	-19.2	-59.2	-22.3	-61.9	-18.4	-21.6	-21.6	3260.0	-61.9	-61.9	-61.7	-61.0	-23.4
Bi	-39.4	144.9	-38.8	81.8	-36.2	20.0	21.2	1475.8	627.3	22.4	74.8	357.1	22.4	42.9	17.6	20.0	42.9	42.9	-42.6	1597.6	14.8
Zr	-5.8	-7.7	-2.9	12.3	-5.8	11.1	10.4	-1.1	14.2	17.3	-4.9	0.5	5.7	15.7	1.6	3.6	9.4	9.4	7.3	5.7	11.8

Note: Major elements, S and LOI are in weight percent, trace elements are in ppm

**Table 2.4 - Ore geochemistry for samples >10 g/t Au**

Element	Min	Q1	Median	Q3	Max
Au	10.15	17.825	42.5	88.8	9830
Ag	0.93	10.45	21	58.5	2550
As	17.2	131.5	207	321.5	>10000
Ba	30	140	220	355	1190
Be	0.12	0.485	0.72	0.99	2.6
Bi	0.005	0.14	0.47	2.85	418
Ce	4	16.5	28.3	52.45	99
Co	0.5	2.5	8.6	21.65	71.7
Cr	2	12	22	62.5	279
Cs	0.78	4.845	7.41	10.4	22.5
Cu	7.6	62.35	142.5	454.5	8320
Fe	1.4	3.15	4.55	6.94	24.7
Ga	1.26	10	12.25	16.15	31.2
Ge	0.025	0.09	0.11	0.14	0.37
Hf	0.1	1.05	2.4	4.65	10.3
In	0.011	0.049	0.076	0.143	2.12
La	2	7	12.3	22.9	46.1
Li	3.3	9.7	14.1	20.1	133
Mo	0.14	2.135	5	13.225	195.5
Nb	0.05	1	2	4.9	12.8
Ni	0.5	5.15	15.5	47.7	329
P	10	40	70	230	750
Pb	5.7	22.4	50.4	184.75	>10000
Rb	3.7	49	67	85.9	149
S	0.33	2.645	4.22	6.595	10
Sb	1	3.64	7	20.35	1370
Sc	1.3	4.3	6.3	14.8	48.5
Se	0.5	2	5	9	73
Sn	0.1	0.6	1.3	2.25	5.9
Sr	13.3	33.2	49.7	84.15	1680
Ta	0.025	0.06	0.17	0.435	1.22
Te	0.05	1.04	4.23	34.45	>500
Th	0.02	0.725	2.28	4.545	10
Tl	0.07	0.39	0.55	0.77	10
U	0.05	0.3	0.7	1.4	5
V	3	51.5	110	189.5	6260
W	0.6	2.55	4.9	9.9	>10000
Y	2.4	7.3	12.6	16.9	43.9
Zn	15	68	216	1630	>10000
Zr	1.3	36.6	83.2	134.5	318

Note: major elements Fe and S are given in %, trace elements are in ppm, greater than > is above detection limit.

**Table 2.5 - Summary of U-Pb zircon geochronology**

Grain	No.	Analysis Description	Weight (mg)	U (ppm)	Th/U	PbT (pg)	PbC (pg)	$\frac{^{207}\text{Pb}}{^{204}\text{Pb}}$	Meas.	$\frac{^{207}\text{Pb}}{^{234}\text{U}}$	$2\sigma$	$\frac{^{206}\text{Pb}}{^{238}\text{U}}$	$2\sigma$	Error	Correl.	$\frac{^{206}\text{Pb}}{^{238}\text{U}}$	$2\sigma$	$\frac{^{207}\text{Pb}}{^{235}\text{U}}$	$2\sigma$	$\frac{^{207}\text{Pb}}{^{206}\text{Pb}}$	$2\sigma$	Disc.
<b>Sample EAG-15-552</b>																						
dwd6143	4	pr, ck	0.0033	788	0.46	1519	0.3	46097		13.21	0.03	0.518	0.001	0.9916	0.9916	2691	4.5	2695	2	2698	0.4	0.3
dwd6172	5	pl, ck	0.004	283	0.19	625	0.5	15021		13.28	0.04	0.52	0.001	0.966	0.966	2698	5.7	2700	2.8	2701	1.3	0.1
dwd6173	6	pl, ck	0.0011	563	0.36	356	0.8	4864		13.33	0.04	0.521	0.001	0.9536	0.9536	2705	5	2703	2.5	2702	1.3	-0.1
dwd6141	2	eq	0.0046	97	0.22	249	0.4	6728		13.31	0.04	0.52	0.001	0.9872	0.9872	2700	5.8	2702	2.5	2703	0.7	0.2
dwd6142	3	eq	0.0027	116	0.43	184	0.3	7498		13.44	0.03	0.522	0.001	0.9859	0.9859	2709	4.2	2711	1.8	2713	0.5	0.2
dwd6140	1	tip	0.0041	122	0.64	307	0.2	13158		13.47	0.03	0.523	0.001	0.9906	0.9906	2712	4.9	2713	2.1	2714	0.5	0.1
dwd6177	7	tip	0.0011	729	0.23	452	8.7	599		13.53	0.05	0.524	0.002	0.9166	0.9166	2717	7.3	2718	3.4	2718	2.4	0
<b>Sample OBM-16-579</b>																						
dwd6176	14	pl, ck	0.0005	329	0.56	99	1.9	547		13.25	0.04	0.52	0.001	0.8628	0.8628	2698	5.9	2698	2.9	2698	2.6	0
dwd6147	11	tab	0.0015	197	0.47	175	0.4	4204		13.33	0.03	0.521	0.001	0.9685	0.9685	2705	5.8	2703	2.4	2701	1.1	-0.2
dwd6175	13	pl, ck	0.0011	264	0.59	175	2.8	666		13.33	0.07	0.521	0.003	0.9515	0.9515	2703	11	2703	4.7	2703	2.5	0
dwd6174	12	pl, ck	0.0058	133	0.37	444	0.4	10927		13.34	0.04	0.521	0.001	0.962	0.962	2702	5.5	2704	2.7	2706	1.3	0.2
dwd6145	9	pr, ck	0.0026	213	0.37	321	0.3	11522		13.47	0.03	0.523	0.001	0.9885	0.9885	2713	4.1	2713	1.8	2713	0.5	0
dwd6144	8	eq	0.0037	108	0.48	238	1	2618		13.45	0.04	0.523	0.002	0.9874	0.9874	2710	6.7	2712	2.9	2714	0.8	0.2
dwd6146	10	eq	0.0016	397	0.56	384	0.3	12588		13.51	0.03	0.524	0.001	0.9787	0.9787	2717	4.1	2716	1.8	2715	0.6	-0.1

**Footnotes**

analyses are ordered from oldest to youngest  $^{207}\text{Pb}/^{206}\text{Pb}$  age  
tip - tip of grain, eq - equant, pr - prismatic, tab - tabular, ck - cracked, pl - polished  
PbC - Common Pb from measured  $^{204}\text{Pb}$  assuming the isotopic composition of blank: 206/204 - 18.221; 207/204 - 15.612; 208/204 - 39.36  
Error Correl - Correlation between errors in measured concordia coordinates  
Disc - Percent discordance relative to  $^{207}\text{Pb}/^{206}\text{Pb}$  age  
U decay constants:  $^{238}\text{U}$  - 1.55125 X 10<sup>-4</sup>/Ma;  $^{235}\text{U}$  - 9.8485 X 10<sup>-4</sup>/Ma (Jaffey et al., 1972)

**Chapter 3: A fluid chemical study of the Archean Windfall gold deposit, Quebec, Canada:  
Evidence for fluid mixing in an intrusion-related gold system.**

Brandon Choquette<sup>1</sup>, Daniel J. Kontak<sup>1</sup>, Édouard Côté-Lavoie<sup>2</sup>, Mostafa Fayek<sup>3</sup>, Ryan Sharpe<sup>3</sup>

<sup>1</sup>*Harquail School of Earth Sciences, Laurentian University, Sudbury, Ontario*

<sup>2</sup>*Osisko Mining Inc., Chicoutimi, Québec*

<sup>3</sup>*Department of Geological Sciences, University of Manitoba, Winnipeg, Manitoba*

## Abstract

The Archean intrusion-associated 6+ Moz Windfall Au deposit (WGD) in the Urban-Barry greenstone belt (Québec, Canada) is a recently explored but at present an enigmatic deposit type. The Au resource, related to vein and replacement zones of quartz-carbonate-pyrite-tourmaline veins and stockworks that cut sericite-pyrite  $\pm$  silica  $\pm$  tourmaline  $\pm$  fuchsite replacement zones, overprints a swarm of quartz-feldspar porphyry dikes ( $2698 \pm 3$  Ma) that intrude a sequence of  $2705.9 \pm 4.2$  Ma mafic-felsic volcanic rocks; all of this is crosscut by post-mineral dikes ( $2697.6 \pm 0.4$  Ma) which thus constrain the time of the main Au event. To address the deposit genesis, ore petrology and SEM-EDS imaging and analysis, LA-ICP-MS elemental mapping of pyrite, cathodoluminescence of magmatic hydrothermal quartz, fluid inclusion (FI), and in situ SIMS isotopic studies (O, S) were completed. The ore-related sulfides and sulfosalts are dominated by pyrite with lesser arsenopyrite, sphalerite, chalcopyrite, tennantite-tetrahedrite, galena, gold, electrum, and minor Sb-rich and telluride alloys. Four pyrite generations are noted (Py1-Py4) with primary Au related to arsenic-rich Py2 that is accompanied enrichment in Ag-Sb-Hg-Cu-Zn-Pb-Bi-Te. Dissolution of Py2 synchronous with Py3 formation released Au and metals now seen as micro-inclusions and also mobilized to form the high-grade Au zones. SIMS  $\delta^{34}\text{S}_{\text{pyrite}}$  data is similar for Py1 to Py3 and center on 5‰, which is consistent with a magmatic reservoir taking into account isotopic fractionation of sulfur between fluid and melt (i.e.,  $\Delta\text{fluid-melt} = 4\text{‰}$ ). In contrast, SIMS  $\delta^{18}\text{O}_{\text{quartz}}$  data for both igneous (5.4-12.2‰) and vein (5.7-14.6‰) quartz suggest an initial magmatic fluid that was diluted due to mixing with an  $^{18}\text{O}$ -depleted reservoir such as meteoric water. FI studies of vein quartz from pre- to post-ore veins indicate the dominance of a carbonic ( $\pm\text{CH}_4$ ) fluid, which is rarely reported in other Au deposits; rare aqueous-carbonic ( $\text{CO}_2 = 4.6\text{-}97.9$  mol %) and variably saline aqueous types are also present.

The origin of this carbonic fluid and its role in the genesis of the WGD remains unresolved.

Overall, the data are considered to favor an intrusion-related deposit model versus orogenic, but we note that some data are equivocal and further studies are needed to resolve these aspects.

### 3.1 Introduction

World-class gold deposits are the products of protracted hydrothermal systems that incorporate high-fluid flux and overprinting hydrothermal events that are focused into areas of active brittle and/or ductile deformation (e.g., Goldfarb et al., 2005; Dubé and Gosselin, 2007; Wyman et al., 2016; Gaboury, 2019). The unravelling of such complex systems requires detailed studies of the structural environment, characteristics of the hydrothermal veins and their infill, detailed paragenesis of the associated sulfide mineralization and accompanying fluid-chemical studies (e.g., Kontak et al., 1996; Mueller et al., 2015, Kerr et al. 2018; Zohier et al., 2019). The advent in recent years of advanced analytical methods, such as in situ measurement of stable isotopes using secondary ion mass spectrometry (SIMS), laser ablation inductively coupled mass spectrometry (LA ICP-MS) to generate elemental maps of sulfide phases and also to quantify the chemistry of mineralizing fluids preserved in fluid inclusions, 3D tomographic maps of gold distribution and transmission electron microscopy (e.g., Large et al., 2009, 2011; Neyedley et al., 2017; Gourcerol et al., 2018; Kerr et al., 2018; Voisey et al., 2020; Hastie et al., 2020; Petrella et al., 2020; McDivitt et al., 2021) has provided the means to further quantify processes related to primary gold mineralization and its later remobilization and upgrading of these ore systems. All of the aforementioned aspects contribute to a much improved understanding of the ore forming processes and in doing so help to improve ore-deposit models which benefit and enhance exploration for, in this particular case, gold deposits (e.g., Robert et al., 2007; Groves et al., 2020).

This paper applies some of the aforementioned protocol to further the understanding of the genesis of the high-grade (measured and indicated resource of 6.023 Mt at 9.6 g/t Au and an inferred resource of 16.401 Mt at 8.0 g/t Au (Richard et al, 2021)) Archean Windfall gold

deposit (WGD) located in the eastern and lesser explored part of the gold-endowed Abitibi Subprovince of contiguous Ontario and Québec, Canada. This contribution follows on a complementary study of the age and petrology of the host rocks, vein and alteration types and structural evolution of the several ore zones that collectively define the deposit (see chapter 2). The deposit is of particular interest for several reasons. Firstly, it represents a significant gold discovery in a previously unrecognized greenstone belt setting, the Urban-Barry greenstone belt (UBGB), and therefore a better understanding the deposit genesis is paramount for directing further exploration at both the deposit- and regional scales. Secondly, the WGD is well known for the presence of exceptional high-grade Au intercepts (i.e., >1000s g/t) but, as with other gold deposits (e.g., Fosterville, Australia; Voisey et al., 2020), the origin of such bonanza zones remains unresolved as recently discussed by Hastie et al. (2020; and references therein) and references therein. And lastly, as demonstrated already (see chapter 2), the spatial and temporal overlap of the ore zones with a swarm of felsic intrusive dike rocks strongly suggests an intrusion-related origin. The latter is of particular significance given the growing appreciation of such deposits in the Archean Superior Province of Canada (e.g., Mercier-Langevin et al., 2007; Kontak et al., 2013; Yergeau et al., 2015; Katz et al., 2017, 2021; McDivitt et al., 2017; 2021).

To further develop the genesis of the WGD, we herein assess its fluid-chemical evolution following on our earlier study by using carefully selected samples based on exhaustive logging of drill core (i.e., 35,000 m) and detailed mapping of recently accessed underground exposures. Samples studied were collected from three vein generations that span a period from pre-, syn-, to post the main auriferous event. Vein types examined are: 1) pre-mineral colloform-textured carbonate-quartz veins; 2) syn-mineral quartz-carbonate-pyrite-tourmaline-gold veins; and 3) post-mineral quartz veins. The timing of these vein generations is constrained in the field by

cross-cutting relationships and their timing is defined by U-Pb dating of pre- and post-mineral QFP intrusions. This foundation provides the basis for constraining the fluid-chemical evolution of the deposit by integrating the following: ore petrography and SEM-EDS analysis of barren and mineralized samples, cathodoluminescence (CL) of magmatic quartz in dike rocks and vein quartz, fluid inclusion (FI) petrography and microthermometry of all vein types, LA-ICP-MS mapping of syn-mineral pyrite, and in situ secondary ion mass spectrometry (SIMS) measurement of  $\delta^{18}\text{O}_{\text{Quartz}}$  for dike rocks and, the three vein types, and in situ SIMS of  $\delta^{34}\text{S}$  for syn-mineral pyrite. These data combined with our previous work are used to provide the first attempt to understand the PTX conditions and the complex hydrothermal history recorded in the WGD.

### **3.2 Geology of the Windfall gold deposit**

The WGD is located in the UBGB, part of the Abitibi Subprovince of Canada (Fig. 1). A more detailed account of the geological setting, age and petrology of the host rocks is given in Chapter 2. A summary of this work is provided below.

The UBGB is an east-west trending, 6.5 to 20 km wide belt dominated by mixed mafic to felsic volcanic rocks with lesser fine-grained clastic sedimentary sequences (Milner, 1939; Joly, 1990; Bandyayera et al., 2003, 2004a, 2004b; Rhéaume et al., 2004; Rhéaume and Bandyayera, 2006). This sequence of dominantly volcanic rocks was deformed during the 2.71 to 2.66 Ga Kenoran orogeny (Card, 1990) and generally records greenschist-grade metamorphism (i.e., albite-chlorite-carbonate assemblage), but locally can reach amphibolite facies within corridors of intense deformation and proximal to contacts with large felsic plutonic bodies (Joly, 1990). The deposit is located along a regional-scale, second-order deformation zone known as the

Mazères deformation zone which is interpreted to be a splay off the larger first-order Urban deformation zone (Fig. 1).

The WGD is a structurally controlled deposit type with gold-bearing quartz and sulfide veins and replacement zones. As of February 2021, the deposit has a measured and indicated resource of 1.86 Moz Au (6.023 Mt at 9.6 g/t Au) and an inferred resource of 4.24 Moz Au (16.401 Mt at 8.0 g/t Au) (Richard et al, 2021). The gold event overprints a sequence of volcanic rocks intruded by a pre-mineralization swarm of felsic dike rocks (Fig. 2A-C). In turn, this mineralized package is crosscut by later post-mineralization felsic- and mafic dikes. The gold mineralization is contained within auriferous alteration zones and veins contained within a series of conjugate brittle-ductile deformation zones that are locally concentrated along subvertical, pre-mineralization intrusive contacts.

### **3.2.1 Rock types and timing constraints**

In the WGD, tholeiitic volcanic rocks mapped as part of the Macho Formation (Bandyayera et al., 2002) are crosscut at high angles by calc-alkaline felsic dike rocks referred to as the Windfall intrusive complex (WIC). The volcanic succession is composed of texturally variable basalt, andesite, and rhyolite with minor black, Fe-sulfide-bearing graphitic argillite horizons (Fig. 3 A-F). This sequence is in turn crosscut by synvolcanic gabbro and ultramafic sills (Fig. 3 G-H). The aforementioned rhyolite is the youngest volcanic unit observed and thus its U-Pb zircon age of  $2705 \pm 4.2$  Ma from a sample collected within the deposit (see Chapter 2) provides an upper age limit for the volcanic sequence.

The WIC is composed of seven distinct phases of calc-alkaline granodiorite quartz-feldspar porphyritic (QFP) intrusions that form dikes and stocks that crosscut the volcanic

succession at high-angles. The dikes are divided into three groups based on textural criteria, color, and timing with respect to gold mineralization. The first group, which pre-dates gold mineralization, and consists of: 1) fine-grained small quartz eye phyric porphyry with 2-10 % angular quartz eyes (1-2 mm) and locally volcanic fragments (Fig. 3I); and 2) magmatic breccia with sub-rounded fragments of rhyolite, gabbro, QFP intrusive, tourmaline breccia, and pyritized material cemented in a fine-grained to aphanitic, small quartz eye phyric (1-2 mm) to aphanitic matrix (Fig. 3 J-L). The latter unit occurs along the margins of a singular intrusive body of the first intrusive phase where it has sharp- to gradational contacts. The second group of intrusions also pre-date gold mineralization and include in order of appearance: 1) a large quartz eye phyric porphyry with 10-20% sub-rounded blue quartz eyes (0.2-2 cm) (Fig. 3M); 2) a large quartz eye phyric porphyry with 1-10% sub-rounded grey quartz eyes (0.2-2 cm) (Fig. 3N); and 3) a large quartz eye phyric porphyry with <1% sub-rounded grey quartz eyes (0.2-2 cm) (Fig. 3O). Where least altered, these large quartz eye porphyry intrusions contain plagioclase phenocrysts. The third group of intrusions post-date gold mineralization based on cross-cutting relationships seen in drill core, surface, and underground exposures. The late dikes consist of: 1) a hematite-altered large quartz eye phyric porphyry with 1-10% sub-rounded grey quartz eyes (0.2-2 cm), plagioclase phenocrysts (i.e., Red Dog intrusion) (Fig. 3P); and 2) a fine-grained hematite-altered dike with no quartz eyes (Fig. 3Q). Locally these late intrusives locally contain disseminated magnetite.

The age and duration of the WIC is constrained by U-Pb zircon dating, which also brackets the timing of gold mineralization since the oldest intrusive bodies are cut by mineralization whereas the youngest bodies crosscut it (see chapter 2 for details). The earliest magmatic phase of the small quartz eye porphyry was dated at  $2698 \pm 3$  Ma whereas the last

magmatic phase, the hematite altered large quartz eye porphyry (i.e., Red Dog intrusion), was dated at  $2697.6 \pm 0.4$  Ma. Thus, these ages constrain both the time and duration of magmatism between 2701 to 2697.2 Ma and also brackets the gold mineralization to this interval.

Importantly, this age for gold mineralization overlaps with the time for a similar Au event in the UBGB, the Barry gold deposit of  $2697.1 \pm 0.6$  Ma (Kitney et al. 2011).

### **3.2.2 Alteration Types**

Within the WGD four alteration assemblages are observed in drill core. Whereas some are developed over a regional scale of kilometers along major structures (e.g., chlorite-ankerite), others developed locally at a meter scale (e.g., silicification). These alteration assemblages are sub-divided based on distribution and timing with respect to mineralization: 1) background; 2) proximal; 3) distal; and 4) post-mineralization.

The background mineral assemblage is one typical of greenschist facies metamorphism. It consists of a weak-to-moderate, pervasive-to-spotty chlorite, sericite and carbonate with local biotite, amphibole and epidote seen at depth in the deposit. This observation is consistent with the regional scale mineralogy noted by Bandyayera et al. (2001).

Proximal and distal alteration assemblages are associated with the main auriferous event and form a zoned alteration pattern. The distal zone consists of a patchy-to-pervasive sericite-chlorite-ankerite assemblage with minor disseminated pyrite-tourmaline. The core of the alteration zone defines the proximal alteration assemblage consisting of an intense and pervasive sericite-pyrite  $\pm$  silica  $\pm$  tourmaline  $\pm$  fuchsite. Where the proximal alteration assemblage is most prevalent and intense, there is a strong correlation with high-Au grades. These auriferous alteration zones are referred to as replacement-type mineralization (discussed below). In drill

core, they vary from a few cm to several meters width and are heavily influenced by host-rock lithology (i.e., composition) and intensity of deformation.

The post-mineral alteration occurs as: 1) a hematite  $\pm$  magnetite alteration that affects the post-mineral QFP intrusions and is not associated with gold mineralization, and 2) a late ankerite alteration that is poorly constrained and is observed to overprint the deposit. The latter is commonly observed overprinting post-mineral intrusions not previously altered by the alteration related to the gold event.

### **3.2.3 Vein types and mineralization styles**

Seven distinct hydrothermal veining events have been documented and are constrained by cross-cutting relationships, as observed in drill core and underground exposures. The events, in order of appearance, include: 1) pre-mineral sheeted blue quartz veins (Fig. 3.4A, B); 2) pre-mineral, colloform-textured, carbonate-quartz veins (Fig. 3.4C, D); 3) syn-mineral sericite-pyrite  $\pm$  silica  $\pm$  tourmaline  $\pm$  fuchsite alteration zones (i.e., replacement-type ore) (Fig. 3.5); 4) syn-mineral grey quartz-carbonate-pyrite-tourmaline veins and stockworks (i.e., vein-type ore) (Fig. 3.6A-E); 5) post-mineral laminated quartz-carbonate-tourmaline  $\pm$  pyrite veins, tourmaline  $\pm$  pyrite veinlets, and tourmaline-pyrite breccias (Fig. 3.5 E-H); 6) remobilized gold that overprints earlier vein types (Fig. 3.6F-H); and 7) post-mineral white- and grey colored quartz veins (Fig. 3.4I-L). A summary of these hydrothermal events in relation to their timing with respect to rock types and deformation is presented in the paragenetic diagrams shown in Figure 3.7.

The earliest pre-mineral and gold-barren veins consist of the sheeted blue quartz veins and the colloform-textured carbonate-quartz veins. These veins are crosscut by the syn-mineralization Au event which occurs in two stages. The first stage consists of gold-rich

deformation zones hosting an alteration assemblage of sericite-ankerite  $\pm$  silica  $\pm$  tourmaline  $\pm$  fuchsite with 1-10% disseminated pyrite and tourmaline. The latter zones are then crosscut by the second stage which consists of gold-rich, grey-colored quartz veins and stockworks with minor carbonate and 1-10 % disseminated pyrite and tourmaline. These are all then overprinted by post-mineral gold-poor laminated quartz-carbonate-tourmaline veins, tourmaline-pyrite veinlets, and tourmaline-pyrite breccias. The aforementioned sequence is all overprinted by a gold remobilization event that is associated with carbonate  $\pm$  quartz veins that crosscuts the earlier auriferous veins and remobilizes and/or adds gold along these structures. These stages are all crosscut by white and grey colored quartz veins that locally contain coarse pyrite, sphalerite, and locally erratic nuggety gold.

### **3.2.4 Deformation history**

The rocks of the WGD area are weakly to locally strongly deformed. At least four recognizable deformation events are recorded at the deposit scale that are simply denoted as D<sub>1</sub>-D<sub>4</sub>: 1) early folding; 2) N, ENE and W-trending faults, shear zones, and related tectonic fabric; 3) late brittle faulting and shear zones; and 4) late tilting.

Within the deposit, the volcanic sequence is folded into open-to-tight structures with fold axes trending N60°E and plunging roughly 35° ENE (D<sub>1</sub>). The second deformation event is represented by N, ENE and W-trending deformation zones (D<sub>2</sub>) that crosscut the earlier folds and are defined by a series of conjugate steep-to-moderately dipping faults, fractures, and shear zones with the local development of a weak to strong penetrative fabric. These deformation zones appear to have controlled the emplacement of the pre-mineral QFP intrusions. Continued D<sub>2</sub> deformation is localized in areas of rheological contrast, which occur at contacts between the

competent, subvertical QFP dikes and the deformed host volcanic rocks. Economic gold mineralization is concentrated within these deformation zones and are often spatially associated to the contacts of some, but not all of the large quartz eye porphyry dikes. The mineralized veins and pyrite-rich alteration zones are emplaced within and overprint these deformation zones and form an extensive anastomosed conjugate vein and alteration network that plunges roughly 35° towards the ENE. Post emplacement of the mineralized system, continued ENE deformation along the Mazères deformation zone crosscuts and deforms the deposit (Fig. 3.2).

The third deformation (D<sub>3</sub>) event is associated with late brittle-ductile deformation that is represented by intervals of broken core and fault gouge, and locally thin shear zones. These late structures locally displace and deform the mineralized system and crosscut the late post-mineral QFP intrusions, indicating its late timing with respect to the formation of the deposit and emplacement of the WIC. The fourth deformation (D<sub>4</sub>) event is a tilting event that rotates all rock types, deformation zones and gold mineralized vein system 55° from an inferred original vertical orientation to its present-day inclined orientation at 35° towards the ENE.

### **3.2.5 Ore zones geometries**

Gold mineralization occurs in series of stacked subvertical to moderately dipping zones having lensoid geometries with true widths averaging 1 to 10 m and generally oriented ENE with plunges about 35° ENE. These lenses are controlled by high-strain zones often spatially associated to contacts between competent subvertical pre-mineral QFP dikes and volcanic rocks. In addition, gold zones are also controlled locally by strong chemical contrasts along the contacts between Fe-Mg rich gabbro sills and enveloping felsic volcanic and QFP rocks. The deformation

zones hosting gold are characterized by a planar fabric defined by a weak- to locally strong foliation or by a series of parallel fractures and faults.

Two dominant styles of mineralization occur, replacement- and vein-type (Fig. 3.5 and 3.6A-E). In addition, there are numerous exceptionally high-grade gold veins associated to late-stage remobilization of gold (Fig. 3.6F-H). The occurrence of replacement- and vein-type mineralization is dependent on host rock composition. In the mafic- to intermediate rocks, a replacement style of mineralization is dominant and consists of networks of auriferous altered deformation zones that are associated with a pervasive to patchy sericite-pyrite with local silica, tourmaline and fuchsite. In the felsic rocks, a vein style of mineralization is dominant and consist of arrays of grey colored quartz veins with disseminated pyrite-tourmaline that are hosted in sericite-pyrite altered deformation zones. The deformation zones that control the emplacement of the ore form a series of conjugate sets, one that is parallel to the orientation of the dominant tectonic fabric, and a second that is oblique to that. These structures are interpreted to reflect Riedel shear-fracture patterns (Riedel, 1929).

Occurrences of high-grade Au intersections with spectacular visible gold are well known in the WGD. This gold type has been observed in both drill core and underground exposures and is hosted in the vein-type mineralization or in the replacement zones with very intense silicification (Fig. 3.6F-H). These intercepts and exposures have variable amounts of modal gold (i.e., >10s to 1000s g/t) hosted in a cloudy white quartz-carbonate which crosscut the earlier vein- and replacement-type mineralization. The visible gold is commonly associated to late carbonate occurring in discordant features cutting the quartz vein which it reflects a later gold-remobilization event.

### **3.3 Methods**

#### **3.3.1 Previous geological studies and research**

The current study benefited from previous workers and their data is incorporated into the present synthesis of the geology of the WGD. This work included: 1) 13 internal petrographic reports by L. Tremblay (2014-2019; IOS Services Géoscientifiques). These reports documented the styles of alteration and mineralization; 2) an internal gold department study by R. Padilla (2016; Talisker Exploration Services) that characterized the ore-related minerals by using reflected light microscopy and microprobe analyses; and 3) an internal LA-ICP-MS study by É.C. Lavoie (2016; Osisko Mining Inc.) that documented the pyrite types and their chemistry.

#### **3.3.2 Petrography, mineral identification and mineral chemistry**

Several petrographic studies of mineral identification for gangue and ore-related minerals have been complete from 2014 to 2020. The relevant studies are from several internal reports by L. Tremblay of IOS Services Géoscientifiques, one by R. Padilla of Talisker Exploration Services, and two by É.C. Lavoie of Osisko Mining Inc.

The studies by L. Tremblay primarily focused on mineral identification of gangue and ore-related minerals in mineralized and unmineralized rocks. The studies used a Leica Wild MC3 polarizing stereo-microscope and a Zeiss Axio Imager M2m petrographic microscope attached to a Caniplex PixelLink camera. The petrographic reports are used as a reference for common ore-mineral assemblages.

The aforementioned study by R. Padilla primarily focused on sulfide minerals and their chemistry in addition to the characteristics of gold. The petrographic work and mineral

chemistry, done at the Lunar and Planetary Science Department of the University of Arizona, USA, used polished thin sections studied in reflected and transmitted light with select samples analyzed using a CAMECA SX-100 microprobe. A total of 358 points were analyzed for 11 elements (S, Fe, Cu, Zn, Ag, Au, Te, Pb, Bi, As, Sb) in pyrite, chalcopyrite, sphalerite, galena, tennantite, arsenopyrite, Bi-Te mineral grains, Ag-Sb-S mineral grains, and native Au/electrum grains. This work was supplemented using additional samples as part of the current study that were analyzed at Laurentian University.

The aforementioned study by É.C. Lavoie primarily focused on mineral identification of gangue and ore-related minerals in mineralized rocks from the Lynx zone of the deposit. The study used an Olympus BX-51 petrographic microscope. The petrographic report was used as a reference for common ore mineral assemblages.

### **3.3.3 LA-ICP-MS pyrite mapping and binary plots**

The LA-ICP-MS analysis of pyrite done by É.C. Lavoie was integrated into this study to assist in unravelling the complex evolution of the hydrothermal system following on the protocol of Gourcerol et al. (2018, 2020). Select grains of pyrite (n=42) from Au-bearing samples (n=22) collected from the Main and Underdog zones were analyzed at the Earth's Material Laboratory (LabMaTer), University of Chicoutimi, Québec. Measurements were made by ablating sulfides with a RESolution M-50 Excimer (193 nm) ArF laser ablation microprobe coupled to an Argilent 7900X qICP-MS. The data were collected during several sessions spanning a period of three days. The analyses were done using a frequency of 15 Hz, a laser fluence of  $3\text{J}/\text{cm}^3$ , and at a traverse speed of  $10\ \mu\text{m}/\text{sec}$  with a beam diameter of  $33\ \mu\text{m}$ . Quantification of the data was done with the trace element reduction scheme in Iolite 3 (Paton et al., 2011), using Fe as an

internal standard with calibration done using the standards: MASS-1C, LAFLAM\_C, and GSE-1g\_A. The data generated from the aforementioned pyrite elemental maps was used to construct binary plots presented below. The traverse data was converted to singular point analysis, or time slice domain (TSD) data, by reducing the analysis to increments of 0.32 seconds, which is the time for a complete elemental analysis. Further details of the data treatment are found in Gourcerol et al. (2018).

### **3.3.4 Cathodoluminescence**

Cathodoluminescence (CL) was integrated into the present study to assist with the classification of FIs, identify different generations of quartz, growth zoning, and fractures in quartz from both veins and the quartz phenocrysts from QFP units. In addition, CL was used to track the possible modification of the  $\delta^{18}\text{O}$  signature of quartz by fluids. This work follows on the results of others who have shown the usefulness of it in hydrothermal ore deposit studies, in particular in the context to interpret fluid inclusions, isotopes, trace element chemistry, vein generations, ore minerals and alteration (e.g., Götze et al., 2001; Rusk and Reed, 2002; Allan and Yardley, 2007). The CL images of quartz presented were collected using a JEOL JSM-6400 scanning electron microscope coupled to a GatanChromaCL mirror-type CL detector and the supporting ChromaCL software housed in the Central Analytical Facilities (CAF) at Laurentian University. The images shown are stitches of several smaller images needed to create the final collages presented, thus there are unavoidable artefacts present; however, this does not compromise the conclusions drawn from the images.

### 3.3.5 Fluid inclusions petrography and microthermometry

Twenty vein samples from the WGD were collected for fluid inclusion (FI) analysis and for each of these a doubly-polished thick section (100  $\mu\text{m}$ ) prepared for FI analysis of vein quartz and carbonate. All samples were examined in detail using the 2x to 100x lenses mounted on an Olympus BX-51 petrographic microscope equipped with a Q-imaging digital capture system. Classification and interpretation of FI and fluid inclusion assemblages (FIAs), such as the timing of inclusions and notation as primary, secondary and pseudosecondary, were made following the methods outlined in Goldstein & Reynolds (1994) which incorporate a specific set of rules known as “Roedder’s Rules” (Bodnar 2003a).

The FI microthermometry was performed on 13 vein samples at the Fluid Inclusion Laboratory at Laurentian University, Sudbury, Ontario. Measurements were made using a Linkham THMSG 600 heating and freezing stage attached to an Olympus BX-51 petrographic microscope; the stage was operated with a computer controller unit which regulated the heating and cooling rate. The stage is calibrated with synthetic fluid inclusions: triple point of  $\text{CO}_2$  (-56.6°C), the triple point of  $\text{H}_2\text{O}$  (0°C) and the critical point of  $\text{H}_2\text{O}$  (374°C). In this study samples were first cooled to -125°C and then incrementally heated while observing phase changes as reported below. Salinities of inclusions are reported as wt. % equiv. NaCl and were calculated in two ways: 1) for aqueous inclusions the melting temperature of ice ( $T_{\text{m ice}}$ ) or hydrohalite ( $T_{\text{m HH}}$ ); and 2) for halite bearing inclusions the dissolution temperature of halite ( $T_{\text{m H}}$ ). The small size of aqueous-carbonic FIs precluded seeing phase changes needed for salinity determination. The presence of dissolved gases in  $\text{CO}_2$ -bearing inclusions are estimated from the melting of the carbonic phase ( $T_{\text{m CO}_2}$ ), whereas their mole %  $\text{CO}_2$  was calculated based on; 1) estimated volume fraction of the carbonic phase; and 2) the density of the carbonic

phase determined from its homogenization to liquid or vapor ( $T_{h\ CO_2}$ ). The minimum temperature of entrapment is based on the observation of total homogenization of all the phases in a fluid inclusion ( $T_{h\ Total}$ ).

Calculation for compositions, densities and isochores were done using numerical models specific to each FI type. For carbonic inclusions, the mole fractions of gases were approximated using diagrams from Van den Kerkhof and Thiery (2001), whereas densities and isochores were calculated using the equation of state of Span and Wagner (1996). For aqueous-carbonic inclusions, composition, density, and isochores were calculated using the numerical model of Steele-MacInnis (2018). For saline aqueous inclusions, calculations were done using HOKIEFLINCS\_H<sub>2</sub>O-NACL program (Steele-MacInnis et al. 2012) except for inclusions containing hydrohalite in which case salinities were calculated using the H<sub>2</sub>O-NaCl-CaCl<sub>2</sub> model of Steele-MacInnis et al. (2011).

### **3.3.6 Carbon isotopes of FI extracts**

Samples of quartz vein material was crushed and mm-size fragments of pure quartz handpicked using tweezers and a high-magnification binocular microscope to ensure purity of separates. From these concentrates, 10-20 mg of quartz hosting FI was loaded into tin capsules and heated to release the carbonic phase of the FI. The C isotopic composition was measured using a Costech ECS 4010 Elemental Analyzer coupled to a Thermo-Finnigan DeltaPlus XP Continuous-Flow Isotope Ratio Mass Spectrometer (CF-IRMS) following the methods of Vennemann & O'Neil (1993) and Köhler et al. (2008). The  $\delta^{13}C$  values are reported using the delta ( $\delta$ ) notation in units of permil (‰) relative to Vienna Pee Dee Belemnite (VPDB)

international standard. A precision of 0.2‰ is estimated based on replicate analysis of standard material.

### **3.3.7 SIMS in situ oxygen isotopes**

Quartz from vein and phenocrysts in QFP dikes were crushed into mm-sized fragments and hand sorted using tweezers and a high-magnification binocular microscope to avoid impurities (e.g., carbonate, sulfide, feldspar). The grains were mounted in epoxy pucks, ground, and polished with 1 µm grit polishing powder. The quartz grains were then imaged in reflected light, transmitted light, and CL. The areas for spot analysis were selected based on these images and in particular to compare results in CL-light and dark areas.

Twenty-two quartz chips of vein quartz (n = 13) and phenocryst quartz (n = 9) were selected for in situ  $\delta^{18}\text{O}$  analysis using the SIMS at the Department of Geological Sciences, University of Manitoba, Canada. The samples were cleaned with ethanol, polished with a 1 µm diamond cleaning compound, and immersed in an ultrasonic cleaner. The cleaned samples were sputter-coated with a thin layer of gold to produce a conductive surface. The data were collected with a CAMECA 7f SIMS attached with an ETP 133H electron multiplier detector. A cesium ( $\text{Cs}^+$ ) primary ion beam with a current of ~4nA was accelerated at 10 kV onto the sample surface with 1 second of detection for  $^{16}\text{O}$  and 5 seconds on  $^{18}\text{O}$  per cycle for 70 cycles. The beam size used was of 15 µm. The  $\delta^{18}\text{O}$  values collected are referenced to Vienna Standard Mean Ocean Water (VSMOW) and reported in standard delta ( $\delta$ ) notation in units permil (‰). Measurements on standards indicate the spot-to-spot reproducibility ranges from 0.6 to 0.9 ‰ for the different sessions.

### 3.3.8 SIMS in situ sulfur isotopes of pyrite

Two representative pyrite grains were selected for in situ  $\delta^{34}\text{S}$  analysis with areas selected based on petrography in order to compare areas of porous versus non-porous pyrite. The data were collected with the same SIMS instrument as described above and similar operating conditions, except that the cesium ( $\text{Cs}^+$ ) primary ion beam had a current of  $\sim 2$  nA with counting of 1 second of detection for  $^{32}\text{S}$  and 5 secs on  $^{34}\text{S}$  per cycle for 50 cycles. The spot size was  $\sim 15$   $\mu\text{m}$ . The  $\delta^{34}\text{S}$  values collected were standardized to Vienna Cañon Diablo Troilite (VCDT) and reported in standard delta ( $\delta$ ) notation in units of permil (‰). Measurements on a standard indicate the spot-to-spot reproducibility is 0.3‰.

## 3.4 Results

### 3.4.1 Ore petrography and mineral identification

Within the vein- and replacement-type mineralization (Figs. 3.5, 3.6A-E), petrographic studies indicate the mineralization assemblage consists of quartz, carbonate, tourmaline, sericite, fuchsite, pyrite, arsenopyrite, sphalerite, chalcopyrite, tennantite-tetrahedrite, galena, gold, electrum, and minor Sb-rich and telluride alloys, as summarized Figure 3.8. In all cases, pyrite is the dominant sulfide phase with others as accessories and generally  $<1\%$ .

The quartz in the vein- and replacement-type mineralization is fine-grained commonly occurs as small crystals ( $<30$   $\mu\text{m}$ ) that exhibit granoblastic polygonal textures and the associated  $120^\circ$  triple junctions (Fig. 3.9A, B). These textures are evidence of recrystallization and this is further discussed below.

The pyrite records a complex growth history, as seen by the abundance and characteristics of zones revealed after etching in bleach (NaOCl; Fig. 3.9). Based on examining several hundred etched pyrite grains, four phases of distinct pyrite (Py) growth are identified. The first pyrite (Py1) is a cubic pyrite whose texture records a partial dissolution event and in addition it is locally porous with non-metallic inclusions. Py1 is overgrown by Py2 which is arsenian (1-5 wt.% As); this pyrite can either overgrow Py1 or occur by itself. Py2 has a euhedral pentagon shape and records variable dissolution features. The pore features are lined by gangue (i.e., quartz, carbonate, other non-metallic phases), various sulfides and sulfosalts (i.e., chalcopyrite, sphalerite, arsenopyrite galena, tennantite, tetrahedrite, electrum, tellurides) and gold (Figs. 3.8 and 3.9). This is followed by Py3, a non-porous overgrowth of Py2, which also has a euhedral pentagon shape and locally a complex colloform texture. This pyrite stage is overgrown by euhedral arsenopyrite. Last is Py4 which is a late euhedral non-porous cubic pyrite.

Gold mineralization at the micro-scale is observed to occur as inclusions (Fig. 3.8E, F, G, H) or along fractures (Fig. 3.8D) in pyrite, in matrix quartz (Fig. 3.8L, K, J), or as invisible gold within pyrite, as identified by LA-ICP-MS mapping discussed below.

### **3.4.2 Cathodoluminescence of quartz**

CL imaging was done on quartz from: 1) quartz-eye phenocrysts from the large quartz eye porphyry QFP dike rocks; 2) syn-mineral grey quartz-carbonate-pyrite-tourmaline veins; and 3) post-mineral Au-barren white quartz veins (Fig. 3.10).

All of the quartz examined exhibited a CL response, varying in color from light- to dark blue and showing homogenous or mottled textures with no observed evidence of primary zoning,

as is commonly reported in quartz that is from metamorphic terranes (Rusk et al., 2012). The large (>1 cm) quartz-eye phenocrysts exhibit a bright blue homogeneous CL that is overprinted by fracture-controlled a dark blue homogenous CL (Fig. 3.10A, B). For the syn-gold mineralization quartz-carbonate-pyrite-tourmaline veins, quartz exhibit a homogeneous or mottled CL which defines sub-domains based on intensity of CL of about 30  $\mu\text{m}$  size (Fig. 3.10C-E). For the post-mineral gold-barren quartz veins, quartz grains are large (>500  $\mu\text{m}$ ) and exhibit a homogeneous bright blue CL that is overprinted by a later, fracture controlled, dark blue homogenous CL (Fig. 3.10F, G).

### **3.4.3 Fluid inclusions petrography and inclusion types**

Three FI types occur along healed fracture planes and as three-dimensional arrays in quartz and carbonate. All FIs are considered to be of secondary or indeterminate origin (Bodnar, 2003a) based on the lack of primary zoning in the host quartz and carbonate and CL imaging that shows FIs are aligned on zones crosscutting the host. The FIs range from <1 to 30  $\mu\text{m}$  size and vary from equant- to negative and highly irregular shapes, which we note is not uncommon and relates to post-entrapment modification (Bodnar, 2003b).

Type 1a FIs are  $L_{\text{CO}_2} \pm V_{\text{CO}_2}$  and are the most dominant type in all samples. They are monophasic or bi-phasic at room temperature depending on their densities (Fig. 3.11A, B). They are equant to irregular in shape, <1 to 30  $\mu\text{m}$  size, and occur as both three-dimensional arrays or along healed fracture planes. The inclusions are hosted within the early colloform-textured carbonate veins, syn-mineral quartz-carbonate-pyrite-tourmaline veins and also within the late gold-barren quartz veins. Within the early colloform-textured veins, these FIs are small (<5  $\mu\text{m}$ ) and occur as three-dimensional arrays that inundate the core of carbonate crystals. Within syn-

mineral veins, they are small ( $<1 \mu\text{m}$ ), scarce and dominantly occur along small fractures in vein quartz or in quartz pressure shadows of sulfide minerals (Fig. 3.11B). In the post-mineral quartz veins, they are abundant and occur along healed fractures and as three-dimensional arrays (Fig. 3.11A). It is noted that, although no aqueous component is observed, it is possible that small amounts ( $<10 \text{ vol}\%$  of the FI) of an aqueous liquid may have gone unnoticed on the walls of the inclusions (Roedder, 1984; Bakker and Diamond, 2006).

Type 1b FIs are  $\text{L}_{\text{H}_2\text{O}}\text{-L}_{\text{CO}_2}\text{-V}_{\text{CO}_2}$ , are rare ( $<0.1 \%$ ) and only seen in early colloform-textured veins and post-mineral quartz veins. The volume fraction of  $\text{CO}_2$  ranges from 0.20 to 0.80 and the carbonic phase is monophasic or bi-phasic at room temperature. They are sub-rounded,  $<1\text{-}5 \mu\text{m}$  in size, occur along secondary healed fracture planes (Fig. 3.11C) and do not show any spatial relationships with other FI types.

Type 2 FIs are of  $\text{L}_{\text{H}_2\text{O}}\text{-V}_{\text{H}_2\text{O}} \pm \text{Halite}$  type, are rare ( $<0.1 \%$ ) and are hosted in syn-mineral and post-mineral quartz veins. In these inclusions,  $\text{V}_{\text{H}_2\text{O}}$  ranged from 5-80 vol. %, they are equant- to irregular in shape, are  $<1$  to  $5 \mu\text{m}$  size and occur along healed fracture planes (Fig. 3.11D). Locally the presence of a cubic-shaped solid phase (i.e., halite) indicates salinity is  $>26 \text{ wt.}\%$  equiv. NaCl for some of these inclusions (Fig. 3.11E).

All these FI types reflect variable degrees of re-equilibration, as indicated by textures that reflect processes such as necking, stretching and/or decrepitation with the later producing haloes of neonate inclusions (Pêcher, 1981; Pêcher and Bouillier, 1984; Bodnar, 2003b; Tarantola et al., 2010). Decrepitate textures are the most common and are generally associated with type 1a inclusions (Fig. 3.11F, G), whereas stretching and necking of FIs is less well developed.

#### 3.4.4 Microthermometric measurements and PTX calculations

Microthermometry is discussed below in the context of analyzing FIAs from several samples for each of three vein groups. The data for type 1 and 2 inclusions is presented in Tables 3.1, 3.2, and 3.3.

For type 1a inclusions, data for 562 FIs from 106 FIAs were measured. Results indicate  $T_{m\ CO_2}$  ranges from  $-63.0^\circ$  to  $-56.9^\circ\text{C}$  with the data centred on  $-58^\circ\text{C}$  (Fig. 3.12A). The depression of the triple point of  $\text{CO}_2$  indicates the presence of low abundances of dissolved gases ( $X_{\text{CH}_4} = 0.01\text{-}0.25$  mol % according to diagrams in Thiéry et al. (1994) and Van den Kherkof and Thiéry (2001)). The results for  $T_{h\ CO_2}$ , which occurred along the bubble point curve, spanned a range between  $-37^\circ$  and  $31^\circ\text{C}$  with a clear bimodal distribution (Fig. 3.12B). Notably, the higher  $T_{h\ CO_2}$  values are mostly for the early colloform-textured carbonate vein samples (i.e., pre-mineral).

For type 1b inclusions, data was only acquired for 19 FIs from 7 FIAs. The  $T_{m\ CO_2}$  ranges from  $-58.8^\circ$  to  $-57^\circ\text{C}$  (Fig. 3.12A) and indicates low amounts of dissolved gases (i.e.,  $X_{\text{CH}_4} < 0.08$  mol%). For  $T_{h\ CO_2}$  homogenization was on the bubble point curve and, as in type 1a inclusions, spanned a large range between  $-40.8^\circ$  and  $31^\circ\text{C}$  (Fig. 3.12B). Calculation of  $\text{CO}_2$  content in these inclusions indicates a range from 4.6 to 97.9 mol %  $\text{CO}_2$ . Salinity for these inclusions was not determined, their small size precluded measuring  $T_{m\ \text{Clath}}$  even when applying the cycling technique (Goldstein and Reynolds, 1994). Final homogenization or  $T_{h\ \text{Total}}$  was to the liquid phase between  $265^\circ$  to  $350^\circ\text{C}$ , but in one case to vapor at  $320^\circ\text{C}$ . For this inclusion type, decrepitation was frequent prior to total homogenization, as is commonly reported for  $\text{H}_2\text{O}-\text{CO}_2$  type inclusions (Roedder, 1984).

For type 2 aqueous inclusions, data for 90 FIs from 21 FIAs was acquired. The microthermometric data combined with petrographic observations indicated the presence of two distinct types in syn- and post-mineral vein types which further divided into three groups based on their  $T_{\text{Total}}$  and salinity data.

Type 2a and 2b  $L_{\text{H}_2\text{O}}\text{-}V_{\text{H}_2\text{O}}$  inclusions have a large range in  $V_{\text{H}_2\text{O}}$  from 5 to 80% with type 2b being more V-rich. For these inclusions,  $T_{\text{m HH}}$  varied from  $-31^\circ$  to  $-23^\circ\text{C}$  and  $T_{\text{m Ice}}$  from  $-26^\circ$  to  $-0.2^\circ\text{C}$ . The presence of hydrohalite combined with the low first melting or eutectic temperatures (i.e., ca.  $-50^\circ\text{C}$ ) indicates the presence of dissolved divalent cations (i.e., Steele-MacInnis et al., 2016). Based on the melting behavior of these inclusions, their calculated salinities range from 0.04 to 26.2 wt. % equiv. NaCl. The  $T_{\text{Total}}$  ranged from  $129^\circ$  to  $447^\circ\text{C}$  and was on the bubble point curve, but for a few inclusions it was along the dew point curve from  $430^\circ$  to  $475^\circ\text{C}$ . As seen in Figure 3.12C, types 2a and 2b are easily separated based on their  $T_{\text{Total}}$  and salinity.

Type 2c  $L_{\text{H}_2\text{O}}\text{-}V_{\text{H}_2\text{O}}\text{-}Halite$  inclusions have  $V_{\text{H}_2\text{O}}$  from 5-20 %. In these inclusions,  $T_{\text{m HH}}$  ranged from  $-36^\circ$  to  $-28^\circ\text{C}$ ,  $T_{\text{m Ice}}$  from  $-21.7^\circ$  to  $-11.7^\circ\text{C}$ , and  $T_{\text{m H}}$  from  $124^\circ$  to  $250^\circ\text{C}$ . Calculated salinities range from 15.5 to 34.3 wt. % equiv. NaCl. The  $T_{\text{Total}}$  occurred along the liquid curve and ranged from  $69^\circ$  to  $250^\circ\text{C}$ .

Isochores for type 1 inclusions are separated into three groups simply based on vein types and their time of formation with respect to gold mineralization, thus allowing assessment of the PT evolution of the hydrothermal system with time, which is colour coded in Figure 3.12. For the first vein group, the pre-mineral colloform-textured carbonate veins, the estimated temperature based on type 1b  $\text{H}_2\text{O}\text{-CO}_2$  FIs suggest a minimum temperature of  $\sim 265^\circ$  to  $350^\circ\text{C}$  and pressure of entrapment from 500 to 2464 bars (avg. = 1495 bars) (Fig. 3.12D). For the

second vein group, the syn-mineral quartz-carbonate-pyrite-tourmaline veins, no appropriate  $T_{\text{Total}}$  data are available for these  $\text{CO}_2$ -type given they homogenize at low temperatures (i.e.,  $<31^\circ\text{C}$ ). The isochores for these FIs are instead extrapolated to  $350^\circ\text{C}$  based on the surrounding sericite-carbonate-pyrite alteration which is considered a reasonable assumption for this vein style and related alteration (e.g., Goldfarb et al., 2005; Baker, 2002; Sillitoe, 2010). The projected isochores for  $350^\circ\text{C}$  equate to pressures of 1541 to 4338 bars (avg. = 3094 bars) (Fig. 3.12E). For the third vein group, the post-mineral quartz veins, the minimum  $T_{\text{Total}}$  from type 1b inclusions suggest minimum formation of  $364^\circ\text{C}$  based on one FIA. For consistency a trapping of  $350^\circ\text{C}$  was used for pressure estimation which equates to 815 to 4259 bars (avg. = 3027 bars) (Fig. 3.12F).

Isochores for type 2 aqueous FIs equate to two groups, one high temperature (type 2a), and the other low temperature (types 2b, c). The high temperature FIs have isochores that overlap at high temperature with type 1a carbonic FIs from the colloform-textured carbonate veins (Fig. 3.12D, G). However, it is noted that no type 2a FIs were observed in these earlier carbonate veins, thus precluding any relationship between the two vein types and use of intersection isochore to infer PT conditions of entrapment.

Isochores for type 2b and 2c FIs are steeper than for type 2a FIs and notably have lower  $T_{\text{Total}}$  values. These isochores, overlap with some isochores for types 1a and 1b inclusions (Fig. 3.12E, F, G). The lack of co-existing L- and V-rich FIs for type 2b and 2c in any FIA precludes an independent pressure estimate for these inclusion types. It is apparent based on the isochores for type 2 inclusions however that type 2a must have been trapped at low pressures (i.e.,  $<1000$  bars) than types 2b and 2c which, for vein formation of  $<250^\circ\text{C}$ , are about 1000 to 2500 bars.

### 3.4.5 Stable isotopes

#### 3.4.5.1 $\delta^{18}\text{O}$ values for magmatic and hydrothermal quartz

The results for 81 in situ  $\delta^{18}\text{O}$  quartz analysis for 28 quartz grains from quartz phenocrysts in QFP dike rocks, 10 quartz grains from pre-mineral colloform-textured carbonate veins, 35 quartz grains from syn-mineral quartz-carbonate-pyrite-tourmaline veins, and 8 quartz grains from post-mineral white quartz veins are summarized in Figure 3.10 and Table 3.4.

The  $\delta^{18}\text{O}$  values for the magmatic quartz phenocrysts range from 5.4 to 12.2‰, which is much greater than that attributed to analytical uncertainty of 0.6 to 0.9‰. In addition, when the data are examined in relation to CL intensity, no correlation is noted (Fig. 3.10B). For the various quartz veins, the  $\delta^{18}\text{O}$  values follow: 1) for early colloform-textured carbonate-quartz veins, they range from 7.9 to 12.7‰; 2) for syn-mineral quartz-carbonate-pyrite-tourmaline veins they range from 5.8 to 14.6‰; and 3) for post-mineral quartz veins, they range from 5.7 to 9.9‰. Again, the range in  $\delta^{18}\text{O}$  values is much greater than that attributed to analytical uncertainty of 0.6 to 0.9‰. Furthermore, as with the magmatic quartz, there is no correlation of the  $\delta^{18}\text{O}$  values with variable CL brightness of the vein quartz (Fig. 3.10 E, G).

#### 3.4.5.2 $\delta^{13}\text{C}$ of fluid inclusion extracts

The results for seven  $\delta^{13}\text{C}$  analyses of fluid inclusion extracts from pre-, syn- and post-mineral veins are summarized in Table 3.5. The results are as follows: 1) two samples from pre-mineral colloform-textured carbonate veins gave are -0.2 and -0.6‰; 2) three samples from syn-mineral quartz-carbonate-pyrite-tourmaline veins gave -2.0, -5.6 and -10.1‰; and 3) two

samples from post-mineral quartz veins gave -2.0 and -3.8‰. Thus overall, the data fall in the narrow range of -0.2 to -5.6‰ except for one outlier at -10.1‰.

#### 3.4.5.3 $\delta^{34}\text{S}$ of pyrite

The results for 26 in situ  $\delta^{34}\text{S}$  analyses from two grains of pyrite from one syn-mineral quartz-carbonate-pyrite-tourmaline vein are summarized in reflected-light and bleach-stained images that reveal the various pyrite types and zones in Figure 3.13 whereas data are presented in Table 3.6. The values of eight analyses for early porous-free core of Py1 range from 0.6 to 1.6 ‰. The values of five analyses for the later, As- and inclusion-rich Py2 range from 0.8 to 1.6 ‰. The values of 13 analyses for the later non-porous overgrowth Py3 range from 0.8 to 2.9 ‰. The aforementioned values summarized per pyrite type in Figure 3.13E highlight the difference among the different pyrite types and provide the means to evaluate possible isotopic shifts during the pyrite growth. We note therefore that the average  $\delta^{34}\text{S}$  values through the paragenesis are: Py1 = 0.9‰  $\pm$  0.3‰, Py2 = 1.1‰  $\pm$  0.3‰, and Py3 = 1.6‰  $\pm$  0.3‰. Thus, Py1 and Py2 have similar signatures, although the overall range is outside of the analytical error of  $\pm$  0.3‰, whereas Py3 has a slightly higher average with the overall range of 2.1 ‰ falling outside analytical error.

#### 3.4.6 LA-ICP-MS mapping and $\delta^{34}\text{S}$ of pyrite

Three representative LA-ICP-MS generated elemental maps and corresponding binary plots of the data selected from the 42 pyrite grains mapped are shown in Figures 3.14-3.16. These samples are in each case from syn-mineral quartz-carbonate-pyrite-tourmaline veins and in each case the chemistry of Py1, Py2 and Py3 are well defined by the elemental maps, whereas that for the late Py4 remains to be documented. As discussed above, the pyrite within

mineralized samples records complex growth histories that involved multiple stages involving dissolution and reprecipitation (CDP) (Putnis, 2009).

Pyrite 1 is seen in Figure 3.14 where it has an annulus of inclusion-rich Py2 and in Figure 3.15 where it was corroded (see left side of image) and overgrown by Py2 which has a euhedral outline zone. The elemental maps show Py1 has a relatively simple chemistry with weak to strong enrichments in Ni, Se, and possibly some Co. Local spikes for Ag, Bi and Te are noted and likely reflect inclusions.

Pyrite 2 occurs in all 3 images, but is variable in its geometry, dimensions and the abundance of inclusions; in all cases it is overgrown by Py 3. Thus, Py2 forms an annulus about Py1 in Figure 3.14, but as an inclusion-rich domain overgrown by later-stage clear Py3 in Figures 3.15 and 3.16. The corresponding elemental maps reveal a complex chemistry for Py2 and reflects two ways in which chemical enrichment occurs: 1) as a uniform distribution, variably seen for As, Se, Te, Cu, Au, Ag and Pb; and 2) as elemental spikes irregularly distributed and as best seen for Co, Sb, Cu, Bi, Te, Au, Ag, Zn and Pb. We note in particular that these spikes characterize Py2 in Figure 3.14, but are variably distributed in Figure 3.15 such that some elements are enriched at the interfaces of Py2 with both and Py2 and Py3, best seen for Co, Pb, Bi, Sb, Au, Ag, and Cu. In the inclusion-rich Py2 in Figure 3.16, it seen that different elements are enriched in various parts of this domain, such that there is both coupling (e.g., Ag-Te) and decoupling (Co and Sb) of elements.

Pyrite 3 is observed to overgrow Py2 in all the maps, but best seen in Figures 3.14 and 3.16. Similar to Py1, Py3 has a simple chemistry and shows strong enrichments in Se and Ni and lesser Co with variable concentrations of As. Although this pyrite does not show any lattice-

bound or inclusions of precious-metal mineralization, we do note that the metals appear to preferentially crystallize in the host matrix rather in the pyrite during this growth stage.

Binary plots were constructed for each of the pyrites mapped in order to evaluate elemental enrichment in relation to Au and Ag. These plots show: 1) the Au:Ag ratio is highly variable from 0.001 to 100 and shows that as Au content increases the Au:Ag ratio does also; 2) Au correlates with increasing As with the majority of data falling below the Au solubility line of Reich et al. (2005). Thus, some of the Au occurs as  $Au^{1+}$ , or invisible gold within pyrite, whereas most occurs as  $Au^0$  that is as particulate gold along fractures in the pyrites and within the quartz matrix (Fig. 3.8A-J). These plots correlate well with the elemental maps for Au discussed above (e.g., Fig. 3.15); 3) in Figures 3.14 and 3.15 there is a good correlation of increasing Au with elevated values of the low-melting-point chalcophile elements (LMCE), in particular Sb, Hg, Pb, Te and Bi, in addition to As and Zn. The strong correlations of Au with Ag, Te, Bi, and Ag reflects the presence of complex alloy phases and tellurides, in addition to Au in sulfides and sulfosalts based on correlations with As, Cu and Sb.

## **3.5 Discussion**

### **3.5.1 Cathodoluminescence observations**

The CL imaging of quartz from a variety of vein types and QFP dike rocks was primarily done to locate unmodified spots in quartz for in situ  $\delta^{18}O$  spot analysis, but it also provides insight into the conditions of formation of these samples. We address the latter issue below.

Quartz from syn-mineral quartz-carbonate-pyrite-tourmaline veins is characterized by a variably dark- to light bluish CL that is homogenous or mottled. In addition, it is particularly

characterized by development of small equant quartz grains of 30  $\mu\text{m}$  size which commonly exhibit granoblastic polygonal textures with corresponding  $120^\circ$  triple junctions (Fig. 3.8A, B; 3.10C-E). According to Rusk (2012) and Seyedolali (1997), among others, such homogenous and mottled textures are not uncommon in quartz from metamorphic terranes. However, whereas this homogenous- to mottled texture may be primary, other suggest it can also result from annealing of quartz during prograde metamorphism or deformation (Sprunt et al., 1978; Boggs and Krinsley, 2006; Spear and Wark, 2009), that is dynamic recrystallization due to dislocation creep (De Bresser et al., 1998), and related to this the redistribution of intrinsic- and extrinsic lattice defects, which thus give rise to different CL intensities. Relevant in regard is the presence of granoblastic polygonal textures and the corresponding  $120^\circ$  triple junctions, as is expected if the quartz has been recrystallized. Also absent is any obvious fracture pattern that may have facilitated ingress of fluids and accompanying CDP processes. The latter feature has been observed and interpreted by several authors (e.g., Rusk and Reed, 2002; Betsi and Lentz, 2010; Freilinger et al., 2015; Zohier et al., 2019) to reflect originally CL-bright quartz domains being fractured with and these permeably areas then flushed with hydrothermal fluids that dissolve the quartz, in some cases due to retrograde quartz solubility (Zohier et al. 2019), with complementary precipitation of CL-dark quartz in the newly formed space. In regards to syn-mineral vein quartz (Fig. 3.10C-E), we note that neither these nor other samples of this generation examined showed any zoning, which contrasts with its presence in some (e.g., Rezeau et al., 2017; McDivitt et al., 2021; Taylor et al., 2021) studies of orogenic vein quartz, and contrasts markedly with that seen for quartz from porphyry-epithermal settings where zoning is very common (e.g., Rusk and Reed 2002; Landtwing et al., 2005; Mao et al., 2017; Rottier et al., 2018).

We also note the pervasive development of fractures in the post-mineral vein quartz (Fig. 10F, G) with differential development of the dull-CL quartz zones relates to incipient versus protracted CDP processes. It is also noted that the dull-CL zones observed coincide with planes of secondary carbonic FIs. These aforementioned features are all consistent with formation of the quartz veins in a protracted fluid regime of moderate but uniform temperature, thus the lack of CL zoning that waned with time and thus a late CL-dark quartz (e.g., Rusk et al., 2006).

The CL features of the magmatic quartz are notable for two reasons. First is the lack of CL zoning, which is a common feature in magmatic quartz (e.g., Wiebe et al., 2007; Betsi and Lentz, 2010; Vasyukova et al., 2013; Breiter et al., 2013, 2017; Wehlre and McDonald, 2019), and secondly the overprint of dull-CL quartz. The lack of the former in the QFP rocks raises the issue of the possible effects of later metamorphic overprinting. The dark CL zones observed in samples from the WGD are most likely due, however, to the ingress of later fluids along brittle channel ways accompanied by CDP processes (Betsi and Lentz, 2010; Vasyukova et al., 2013; Breiter et al., 2017). Thus, in regards to samples in this study, the lack of CL zoning in the quartz phenocryst likely reflect a simple versus complex crystallization history (e.g., Wiebe et al., 2007; Breiter et al., 2013), whereas the dark CL records the overprinting effects of a later, low-temperature fluid.

In terms of CL colour, studies show that the luminescence emission bands of quartz have been observed to range significantly from blue, red, yellow, and green CL colours, which is attributed to various defects due to vacancies of oxygen, silicon, oxygen excess, or the incorporation of several trace elements (Marshall, 1988; Stevens Kalceff et al., 2000; Götze, 2001). Of particular relevance here is the dominance of various hues of blue, which are commonly reported for quartz of various origins (Götze et al., 2001; Boggs et al., 2002). For the

magmatic quartz in the QFP dikes (Fig. 3.10A, B), the bright blue luminescence is consistent with quartz of plutonic settings, whereas the fracture-controlled dark blue luminescence is attributed to an ingress of later fluids. For the syn-mineral vein quartz (Fig. 3.10C-E), the quartz exhibits a dull luminescence; similar observations have been noted elsewhere and interpreted to be caused by the near complete removal of CL-activating defects and trace elements from the crystal structure during metamorphism or deformation (Matter and Ramseyer, 1985; Bennett and Bassett, 2005; Boggs et al., 2007). This interpretation is consistent with the recrystallization features observed and the mottled CL-texture of the quartz. And for the post-mineral vein quartz (Fig. 3.10F-G), the bright CL luminescence is consistent with the colors noted for some hydrothermal vein quartz (Götze, 2001).

### **3.5.2 Implications of O and S isotope data for fluid reservoirs**

#### *3.5.2.1 Oxygen isotopic data*

The  $\delta^{18}\text{O}_{\text{quartz}}$  data show an overall range for all vein types from 5.6 to 14.8‰ and for phenocrysts from QFP dike rocks of 5.4 to 12.2‰, which in both cases is well outside the range of analytical reproducibility (i.e., 0.6 to 0.9‰). Furthermore, in both cases there is no correlation of the data with CL intensity, as noted previously. As the phenocryst data provide the means to assess the source of the magma for the WIC and also a potential reservoir for the mineralizing fluids, these are first discussed followed by the quartz vein data.

The range of  $\delta^{18}\text{O}$  values for the quartz phenocrysts of 5.4 to 12.2 ‰ does not correlate with variable CL intensity (Fig. 3.10) and thus cannot simply be attributed to post-crystallization CDP processes, as reported in some studies (e.g., Zhang et al., 2020; McDivitt et al., 2021). Furthermore, the range is also too large to relate to primary variation in magmas in general (e.g.,

Taylor, 1979; Sheppard, 1986). Also relevant is that the range for  $\delta^{18}\text{O}_{\text{quartz}}$  in Archean felsic magmas of the Superior Province is calculated to be 7 to 10‰ based on robust  $\delta^{18}\text{O}_{\text{zircon}}$  data of 4.5 to 7.5‰ (King et al., 1998; Peck et al., 2000; Valley et al., 2005) and using the Trail et al. (2009) quartz-zircon fractionation equation (i.e.,  $\Delta_{\text{quartz-zircon}} = 2.5\text{‰}$  at 700°C). Based on these datasets, we consider the  $\delta^{18}\text{O}_{\text{quartz}}$  values <10‰ to be best estimate the primary  $\delta^{18}\text{O}_{\text{quartz}}$  signature for samples from the WIC given the lack of evidence for  $^{18}\text{O}$ -enriched magmas at this time in Earth history (King et al., 1998; Peck et al., 2000; Valley et al., 2005). Furthermore, using these results and noting the data are equally distributed about the median of 6 to 10‰, we consider 8‰ to be most reasonable estimate for  $\delta^{18}\text{O}_{\text{quartz}}$  of the WIC and is used to model the evolution of  $\delta^{18}\text{O}_{\text{H}_2\text{O}}$ . We further note that if the maximum analytical error of 0.9‰ for the analysis is applied, then most of the data in the 7 to 9‰ range is accommodated. In regards to the remaining  $\delta^{18}\text{O}_{\text{quartz}}$  values, they are uniformly distributed from 9 to 12‰ which suggests some of the felsic magma was selectively enriched in  $^{18}\text{O}$  via contamination due to assimilation of appropriate wall rocks, which King et al. (1998) also noted for some Archean granites studied.

In regards to the veins, the ranges for  $\delta^{18}\text{O}_{\text{quartz}}$  are 7.9 to 12.7‰ for the early colloform-textured carbonate-quartz veins, 5.8 to 14.6‰ for syn-ore quartz-carbonate-pyrite-tourmaline veins, and 5.7 to 9.9‰ for the post-ore quartz veins and, as we noted before, there is no correlation of the data with CL intensity. The  $\delta^{18}\text{O}_{\text{H}_2\text{O}}$  values that equate to the  $\delta^{18}\text{O}_{\text{quartz}}$  are calculated for 350°C, a reasonable assumption for the vein style and related alteration (e.g., Goldfarb et al., 2005; Baker, 2002; Sillitoe, 2010) and the data calculated at this temperature are summarized in Figure 3.17. The large range inferred for  $\delta^{18}\text{O}_{\text{H}_2\text{O}}$  from about 0 to 9‰ strongly suggests fluid mixing given that a single fluid model is not plausible. Firstly, considering the highest  $\delta^{18}\text{O}_{\text{H}_2\text{O}}$  value of 9 ‰, this can only account for quartz having  $^{18}\text{O}$  values  $\geq 14$  ‰ and thus

excludes most of the data. As for a fluid with  $\delta^{18}\text{O}_{\text{H}_2\text{O}}$  value of 0 ‰, it is not plausible for two reasons: 1) such an initially  $^{18}\text{O}$ -depleted fluid equates to meteoric water (Fig. 3.17), which is not generally considered as a metalliferous reservoir; and 2) such a fluid would have to cool over a range of 150-200°C from 350°C to accommodate the range in  $\delta^{18}\text{O}_{\text{quartz}}$  (Fig. 3.17). Thus, given that a mixing model is more likely, two fluid types are explored below – magmatic versus metamorphic, for which the same general model can be used (Fig. 3.17).

For the magmatic model, the average  $\delta^{18}\text{O}_{\text{quartz}}$  value of 8‰ discussed above equates to an initial fluid with  $\delta^{18}\text{O}_{\text{H}_2\text{O}}$  of about 7‰ based on  $\Delta_{\text{quartz-H}_2\text{O}}$  fractionation values of 1.5 and 1.0 at 600° and 700°C, respectively (Matsuhisa et al., 1979). Cooling of such a fluid can account for much of the  $^{18}\text{O}$ -enriched vein quartz data, as denoted by the mauve-coloured polygon in Figure 3.17 that incorporates the maximum error of 0.9‰ for the measured  $\delta^{18}\text{O}_{\text{quartz}}$ . For the remaining data, the following processes are suggested: 1) for data >8‰, either cooling or mixing with a fluid that is relatively enriched in  $^{18}\text{O}$  is permissible; and 2) for data <6‰, mixing with an  $^{18}\text{O}$ -depleted fluid reservoir is needed, such as meteoric water with a  $\delta^{18}\text{O}$  value of <0‰; Fig. 3.17). Based simply on mass balance, this implies >50% mixing of the magmatic fluid with the latter fluid to accommodate the most  $^{18}\text{O}$ -depleted quartz data. In the metamorphic fluid model, the initial fluid has a minimum initial  $\delta^{18}\text{O}$  value of 8‰ which we note may already have mixed with another fluid to an unknown extent given that this falls at the low end of the field for metamorphic fluids (Sheppard, 1986) and Archean lode-Au fluids in particular (e.g., McCuaig and Kerrich, 1998; Hageman and Cassidy, 2000). As in the previous model, mixing with an  $^{18}\text{O}$ -depleted fluid reservoir is required to accommodate all the data. We also note that the effect of fluid cooling, which increases the  $\delta^{18}\text{O}_{\text{quartz}}$  values, means that higher amount of mixing with the

<sup>18</sup>O-depleted fluid is needed. The preferred origin of the mineralizing fluid, that is metamorphic or magmatic, is later addressed below.

### 3.5.2.2 Sulfur isotopic data

The sulfur isotopic signatures for Py1, Py2 and Py3 were obtained for a single auriferous sample and collectively indicate a range from 0.5 to 2.8‰. Whereas there is partial overlap of all the data, there appears to be a systematic enrichment of <sup>34</sup>S through the pyrite paragenesis with Py3 having the highest  $\delta^{34}\text{S}$  values. Important to note is that both the range for individual pyrite types and the data overall fall well outside the analytical error of 0.3‰. Relevant here are the implications of the  $\delta^{34}\text{S}_{\text{pyrite}}$  signatures for source reservoirs and the implications of the shift in the <sup>34</sup>S values.

In order to interpret the actual  $\delta^{34}\text{S}$  signature of sulfides in the context of reservoirs, that is  $\delta^{34}\text{S}_{\text{pyrite}} \approx \delta^{34}\text{S}_{\text{fluid}}$ , it is first necessary to account for the variable effects of isotopic fractionation due to mineral precipitation, temperature and fluid chemistry (pH,  $f\text{O}_2$ ) during pyrite formation (Ohmoto and Rye, 1979; Seal, 2006). That the veins are estimated to be formed at 300° to 350°C, which is not unreasonable for the vein style and related alteration (e.g., Goldfarb et al., 2005; Baker, 2002; Sillitoe, 2010), means that mineral-fluid fractionation was minimal (i.e., the  $\Delta_{\text{pyrite-H}_2\text{S}} < 1-1.2\%$ ; Ohmoto and Rye, 1979). As for possible fluid-mediated fractionation due to variable  $\text{SO}_4:\text{H}_2\text{S}$  of the fluid, the dominance of sericite fixes pH to being slightly acidic, however that pyrite is the dominant sulfide without pyrrhotite means that  $f\text{O}_2$  is not well constrained and thus also the  $\text{SO}_4:\text{H}_2\text{S}$  ratio of the mineralizing fluid. At 300° to 350°C the  $\Delta$  value or amount of fraction of <sup>34</sup>S:<sup>32</sup>S between sulfur species in the fluid (i.e.,  $\Delta = \delta^{34}\text{S}_{\text{H}_2\text{S}} - \delta^{34}\text{S}_{\text{fluid}}$ ) can vary from -5 to -15‰ near the pyrite-magnetite buffer (Ohmoto and Rye, 1979).

Using the measured  $\delta^{34}\text{S}_{\text{pyrite}}$  values of 0.5 to 2.8‰ and aforementioned range of fluid-related fraction due to variable  $\text{SO}_4:\text{H}_2\text{S}$ , this indicates the  $\delta^{34}\text{S}_{\text{fluid}}$  could have ranged from 5.5 to 7.8‰ or 15.5 to 17.8‰, respectively. The slight overall range in the  $\delta^{34}\text{S}_{\text{pyrite}}$  values of about 2.3‰ is consistent with a slight increase in  $\text{SO}_4:\text{H}_2\text{S}$  during vein formation, which may relate to progressive fluid oxidation accompanying alteration. A similar, but more extreme case of this was documented by Evans et al. (2006) in their study of the variation of  $\delta^{34}\text{S}_{\text{pyrite}}$ , from -10 to -2‰, in the Archean Kalgoorlie gold deposit, Australia. They showed the latter values could be generated from a fluid with an initial  $\delta^{34}\text{S}_{\Sigma\text{S}}$  value of 0‰ as a result of fluid oxidation accompanying the observed wall-rock alteration from a distal pyrrhotite-stable assemblage to pyrite-magnetite-hematite assemblage marginal to the mineralized lodes.

The above discussion indicates that the  $\delta^{34}\text{S}_{\text{H}_2\text{S}}$  value for the mineralizing fluid may have ranged between about 5 to 18‰, which has important implications for the sulfur reservoir. In this regard, we note that compilation and discussion of  $\delta^{34}\text{S}$  values for Fe-As sulfides in Archean gold deposits centre on 0 to 10‰ with most data between 0 to 5‰. (e.g., Kerrich, 1987; McCuaig and Kerrich, 1998; Hagemann and Cassidy, 2000). This suggests, therefore, that it is unlikely for there to be a reservoir characterize by isotopically heavy sulfur such as sulfate. Instead, the rare examples of excursions to such values are most likely due to fluid oxidation, as noted here. For this reason, we interpret the original  $\delta^{34}\text{S}_{\Sigma\text{S}}$  value for the mineralizing fluid in the WGD as being close to the low end of the range noted, that is 5.5 to 7.8‰ with the noted enrichment in  $^{34}\text{S}$  values from Py1 to Py3 due to variation in the fluid  $\text{SO}_4:\text{H}_2\text{S}$ .

Based on the above, two models are considered for the origin of the sulfur, metamorphic (i.e., orogenic) versus magmatic. In the former, sulfur would be sourced from desulfidation of various sulfide phases hosted in crustal rocks, likely the equivalent buried metavolcanic rocks

and also the volumetric lesser metasedimentary rocks seen in the local stratigraphy, as is conventional for this model (McCuaig and Kerrich, 1998; Groves et al, 1998; Hageman and Cassidy, 2000; Goldfarb et al., 2005; Dubé and Gosselin, 2007; Goldfarb and Groves, 2015). In this case, the  $\delta^{34}\text{S}_{\text{fluid}}$  signature would be similar to that of the sulfides (Ohmoto and Rye, 1979). In contrast, for the magmatic model one must consider fractionation between the fluid and melt (i.e.,  $\Delta = \delta^{34}\text{S}_{\text{fluid}} - \delta^{34}\text{S}_{\text{melt}}$ ) which is for felsic rocks, as for the WGD, estimate to be 3 to 4‰ (Ohmoto and Rye, 1979). Thus, in this model the original  $\delta^{34}\text{S}_{\Sigma\text{S}}$  value would be close to 0‰ and consistent with a magmatic sulfur reservoir. We further discuss which of these two models is most appropriate for the WGD below.

### **3.5.3 Implications of fluid inclusions**

#### *3.5.3.1 Fluid inclusion types, timing of entrapment and post-entrapment changes*

The three types of FIs noted at the WGD are not unusual in terms of their chemistries, that is types 1a CO<sub>2</sub>-rich and 1b H<sub>2</sub>O-CO<sub>2</sub> plus type 2 H<sub>2</sub>O with variable salinity, but their absolute and relative abundances and proportions are not typical for either orogenic (e.g., Ridley and Diamond, 2000; Hagemann and Cassidy, 2000; Bodnar et al., 2014) or for intrusion-related (e.g., Lang and Baker, 2001; Baker, 2002) gold deposits where a H<sub>2</sub>O-CO<sub>2</sub> fluid of low- to moderate salinity is common. That a CO<sub>2</sub>-rich ( $\pm$  CH<sub>4</sub>) fluid dominates at the WGD, is rare, but it has been noted by others (see discussion below). Important in this regard are: 1) what is the time of entrapment of the different FIs (i.e., primary versus secondary) since this is relevant in the context of the overall evolution of the ore system; and 2) whether some aspects of the FI populations are primary features or the product of post-entrapment modification.

In regards to timing and origin of the different FI types, the following is noted: 1) type 1a occur in all vein types along healed fracture planes, but it is only in the early colloform-textured carbonate-quartz veins and post-ore quartz veins where it is abundant as three-dimensional arrays in the cores of carbonate crystals. Importantly, these FIs are rare in the syn-mineral veins; 2) type 1b are overall very rare (<0.1 %) and present as secondary FIs in early colloform-textured veins and post-mineral quartz veins; and 3) type 2 are also rarely observed (<0.1 %) and occur on healed fractures in quartz of syn-mineral and post-mineral quartz veins. The aforementioned indicates that the only likely candidates for primary inclusions are type 1a in the earliest and latest veins, whereas in other FI types are secondary. Of particular note is that the syn-mineral vein quartz only rarely has FIs and when present are of secondary origin. The aforementioned is also supported by CL studies which show that some quartz types are cut by planes of dull CL, likely healed fracture planes decorated by FIs, which cut areas of bright CL quartz barren of FIs.

That the dominant FI type is CO<sub>2</sub>-rich, the origin of which is usually related to fluid unmixing (e.g., Ridley and Diamond, 2000; Hagemann and Cassidy, 2000), implies the coexistence of other appropriate FI types, these being the original unmixed H<sub>2</sub>O-CO<sub>2</sub> fluid and the unmixed complementary H<sub>2</sub>O (±CO<sub>2</sub>) fluid (e.g., Roedder, 1984). Whereas the former may be poorly represented due to PT conditions which control the degree of unmixing, the latter should in fact be abundant based on mass balance and appropriate phase diagrams and the observation that the most common H<sub>2</sub>O-CO<sub>2</sub> fluid in both orogenic and intrusion-related ore systems has X(CO<sub>2</sub>) ≈ 0.1-0.3 (see references above). That CO<sub>2</sub>-rich fluids dominate the FI assemblage through the entire paragenesis raises issues about the origin of this fluid – is it primary, an artefact of a process, or does it represent some unusual process? The relevance of this FI type is discussed later in this context.

Also relevant in regards to the above is the variable chemistry and density for type 2 aqueous FIs (Fig. 3.12C), of which three subtypes are noted - types 2a, 2b and 2c. In the possible unmixing model alluded to above, only one of these fluids would be generated, the other two having a different origin. Type 2a inclusions have the likely  $Th_{Total}$  and salinity values, hence isochores (Fig. 3.12G), to be this fluid, although trapped during periods of pressure cycling (i.e.,  $P_{lithostatic}$  to  $P_{hydrostatic}$ ) since they fall at the low end of the field for type 1a FI (Fig. 3.12D). Although a reasonable supposition, we note the lack of petrographic evidence for the coexistence of FI types 1a and 2a. Also important is that type 2a FIs are only observed as secondary types in quartz of syn- and post-ore veins, thus not even present in the early veins where type 1a FIs are abundant.

Of further relevance is the variable degrees of re-equilibration for the FIs. Whereas the uniform density recorded for most FIAs combined with their large overall range in densities and generally equant shapes for smaller inclusions attests to the robustness of the FI data, the presence of decrepitate textures commonly associated with large ( $>30 \mu m$ ) type 1a inclusions (Fig. 3.10 F, G) suggests some post-entrapment modification of FIs. The texture commonly seen is stellate with a radiating planar cluster of inclusions (i.e., neonates) about a central V-rich core. Such textures have long been observed as part of FI studies based on both natural examples (e.g., Pêcher and Boullier, 1984; Vityk et al., 1995; Boullier, 1999; Kontak, 2002; Diamond and Tarantola, 2015) and reproduced under controlled experimental conditions (e.g., Pêcher, 1981; Sterner and Bodnar, 1989; Tarantola et al., 2010). Their origin is attributed to those cases where an inclusion's internal pressure ( $P_i$ ) exceeds the confining pressure ( $P_c$ ), such as during pressure cycling in orogenic (e.g., Sibson et al., 1988; Kontak and Tuba, 2017) or porphyry (Redmond et al., 2004; Monecke et al., 2018) settings (i.e., from  $P_{lithostatic}$  to  $P_{hydrostatic}$ ). Relevant also is that

experimental studies reveal, as expected, a size dependence such that larger inclusions (i.e., generally >10 µm) are more prone to decrepitate than smaller ones where quartz is the host (Bodnar et al., 1989). For the WGD setting it is the largest FIs that display the most pronounced evidence of decrepitate textures.

### 3.5.3.2 PTX conditions for vein fluids

The PTX for the ore fluid is constrained in part by the microthermometric properties of the FIs. Two aspects are critical for using the FI to infer PT conditions. First is the timing of entrapment which we noted are rarely primary except for type 1a. Regardless of this, the presence of secondary FIs may still record the continued flux of syn-mineralizing fluids (Roedder, 1984; Goldstein and Reynolds, 1994; Bodnar 2003a). Second is that most FIs are type 1a CO<sub>2</sub>-rich and although their origin is controversial (discussed below), this does not mean they cannot be used to infer entrapment conditions as others have done (e.g., Schmidt-Mumm et al., 1997; Klein and Fuzikawa, 2010; Cheng et al., 2016; Kontak et al., 2016; Kontak and Tuba, 2017; Sahoo et al., 2018) With these limitations, the FI data are interpreted below.

Given that type 1a FIs are the only type present through the paragenesis, we note the apparent progressive increase in pressure retained in these FIs from pre-, syn- and post-mineral veins. That the FIs in the pre-mineral veins retain a different density compared to later veins (e.g., higher Th<sub>CO2</sub> values; Fig. 3.12B), provides confirmation that post-entrapment modification is not the reason for their different isochores (Fig. 3.12D-G). Furthermore, that the Th<sub>CO2</sub> values for these FIs equate to a range of densities but that the average variation of density for any FIA is small (i.e., <0.045 g/cm<sup>3</sup> (Table 3.1, 3.2) is further support that these FIs have remained isochoric (i.e., Roedder's 2<sup>nd</sup> rule; Roedder, 1984) and thus retained meaningful information and

not affected by post-entrapment processes. Noteworthy therefore is that in the other studies where CO<sub>2</sub>-rich FIs have been noted (see above), consistent densities for FIAs have also been recorded and used to argue against post-entrapment modification. The density changes within each of the vein stages at the WGD suggest cycling of P<sub>fluid</sub> (e.g., Sibson et al., 1988), as also noted by other studies cited above, and is further supported by the presence of decrepitate textures in all vein stages. Thus these features, combined with the observations that the syn-mineral veins cut the earlier colloform-textured carbonate veins, indicate over pressuring or deepening of the ore system with time. As noted before, if vein formation temperature of 350°C is assumed, then the average pressures for the vein stages derived from the isochores (see above) are 1495 bars, 3094 bars, and 3027 bars, which equate to paleodepths of 4.0, 8.4, and 8.2 km for lithostatic conditions. This change in pressure commensurate with vein formation is supported by other independent evidence, which is now discussed below.

First are the colloform textures in the early carbonate veins that dominantly occur in the gabbro sills and basaltic flows and which are attributed to open-space infilling typically found in high-level crustal environments (e.g., Dowling and Morrison, 1989; Moncada et al., 2012; but see Chi et al. (2009) for discussion). Similar textures are noted in the early part of vein paragenesis at other Archean gold settings in Canada, such as Red Lake (e.g., Campbell mine; Penczak and Mason, 1997), Timmins (e.g., Dome mine; Stromberg et al., 2018), Martinière East (Castonguay et al., 2019). Second is that use of the quartz geobarometer of Yang et al. (2017, 2021) for the felsic dike rocks the WIC, based on the normative mineralogy of these rocks, suggest increasing pressures of magma crystallization for pre-, and post-ore samples ca. 1380 to 2960 bars or 3.7 to 8.0 km (see chapter 2). Third is that fine-grained to aphanitic texture of the QFP intrusions and presence of magmatic breccias are both features typical of magmatic-

hydrothermal ore systems in upper crustal settings (e.g., Sillitoe, 2010). In contrast, evidence for a later deep crustal setting is evidenced by brittle-ductile faults and shear zones that overprint the gold mineralization and crosscut the deposit (see chapter 2). The most notable of the ductile structures is the Mazères deformation zone, which truncates and partially transposes the deposit and mineralized vein systems.

The aforementioned suggest the hydrothermal system initiated at high-crustal levels, as presented by early colloform-textured carbonate veins, which was subsequently buried and overprinted by later auriferous fluid event, now seen as syn-mineral quartz-carbonate-tourmaline-pyrite-gold veins, and lastly formation of gold-poor to barren later post-mineral quartz-tourmaline laminated veins, breccias and quartz veins. That the early colloform-textured carbonate veins are commonly overprinted by the later auriferous fluid suggests the presence of long-lived structures that were conduits for multiple fluid events. Such examples where multiple stages of fluid-flux occur in ore systems are not uncommon and are well documented (e.g., Mériaud and Jébrak, 2017; Voisey et al., 2020b; Taylor et al., 2021; Mueller et al., 2020a-d)

### *3.5.3.3 Origin and implications of the aqueous and carbonic fluids*

The dominant FI type in the WGD is type 1a CO<sub>2</sub>-rich with lesser (<0.1%) H<sub>2</sub>O-CO<sub>2</sub> (type 1b) and variably saline H<sub>2</sub>O (type 2). The origin of the latter is first addresses followed by the dominant CO<sub>2</sub> fluids.

The lesser, variably saline H<sub>2</sub>O fluids are seen in syn- and post-mineral veins and in all cases are secondary. That they have different salinities and isochores, indicates a variety of origins. For type 2a, two possible origins are discussed. Unmixing from a H<sub>2</sub>O-CO<sub>2</sub> fluid (type 1b) as noted before, but the large range in salinity requires mixing with another more saline fluid

given the generally low salinities of such fluids (e.g., Baker, 2002; Bodnar et al., 2014). In this model, this fluid would be considered to be part of the ore event. Alternatively, this fluid may relate to a later post-mineral hydrothermal event whose timing is unconstrained. We do note however that the isochores suggest it would relate to a mid- to upper crustal process (i.e., <300 MPa) and with high geothermal gradient. For type 2b and c fluids, they share similar densities and  $Th_{Total}$ , but vary greatly in salinity (Fig. 3.12C). Again, different models are considered. The simplest is mixing of two fluids, one saline and the other possibly meteoric water given the low salinities. In this model, the former is related to crustal fluids termed “shield brines” (Fritz and Frapé, 1982) which are often reported in Archean gold settings and interpreted to post-date the mineralized systems (McCuaig and Kerrich, 1998; Boullier et al., 1998; Garofalo, 2000; Rezeau et al., 2017, Tuba et al., under review). Alternatively, these fluids may not be related and would therefore reflect different hydrothermal events with origins as noted already.

Although the type 1a CO<sub>2</sub>-rich FIs are uncommon in gold settings, others have also reported their occurrence, generally in orogenic type deposits, where CO<sub>2</sub>-rich ( $\pm N_2$ , CH<sub>4</sub>) FIs dominate to the exclusion of any H<sub>2</sub>O (e.g., Garba and Akande, 1992; Schmidt Mumm et al., 1997; Chi et al., 2006, 2009; Klein and Fuzikawa, 2010; Cheng et al. 2016; Sahoo et al., 2018), including several sites in Abitibi greenstone belt (Neumayr and Hagemann, 2002; Kontak and Tuba, 2017; Tuba et al., under review). The favored models for generating such CO<sub>2</sub>-rich FIs generally fall into three models: 1) post-entrapment leakage of H<sub>2</sub>O; 2) preferential trapping of a carbonic fluid due to wetting properties; or 3) trapping of a single CO<sub>2</sub>-type fluid. At present there is no generally favored model to account for such a fluid type and most agree that at present there is no supporting data based on natural samples or experiments that such a fluid is capable of transporting the large amounts of Si, As, Au and other solutes (e.g., see discussions in

Ridley and Diamond, 2000; Lowenstern, 2001; Chi et al., 2006, 2009; Klein and Fuzikawa, 2010). In regards to the occurrence of these CO<sub>2</sub> FIs at WGD and the aforementioned models, the following aspects are noted: 1) the H<sub>2</sub>O-leakage model is precluded based on the fact these FIs occur in both undeformed or highly-strained quartz (cf., Hollister, 1990), they lack haloes of H<sub>2</sub>O-type FIs (Hollister, 1990; Bakker and Jansen 1994), leakage would decrease their densities but yet they range from low- to high-density in all vein types with small variations for FIAs (Crawford and Hollister, 1986; Hollister, 1990), and we, as do others, consider it unlikely that all FIs would lose their H<sub>2</sub>O component; 2) the generation of a fluid dominated by CO<sub>2</sub> due to unmixing with subsequent preferential trapping (e.g., Watson and Brennan, 1987) demands an appropriate primary fluid which has been modeled as H<sub>2</sub>O- CO<sub>2</sub> with XCO<sub>2</sub> = 0.8 (Chi et al., 2006, 2009). However, at the WGD the H<sub>2</sub>O-CO<sub>2</sub> present, type 1b, does not have this composition. Thus, the needed fluid is lacking at WGD and in gold-deposit settings in general. Furthermore is the lack of petrographic evidence supporting fluid unmixing for the syn-mineral veins where type 1a, 1b and 2a inclusions occur, whereas for the early veins type 2a FIs are altogether absent; and 3) the generation of a special CO<sub>2</sub>-type fluid (i.e., the single-fluid model) related to metamorphism or magma degassing has issues. Whereas the former is inconsistent with the timing of mineralization (i.e., post D<sub>1</sub> and pre-major D<sub>2</sub> deformation), the latter, which is founded on preferential loss of CO<sub>2</sub> in degassing and depressurizing felsic magmas (e.g., Lowenstern, 2001), is limited for a variety of reasons: 1) as noted previously, such a fluid lacks the solvent capacity to transport solutes and metals; 2) if degassing was relevant, then there should be a change in the CO<sub>2</sub>:H<sub>2</sub>O of the FIs through the paragenesis; and 3) we find it suspicious that such a fluid is not common in intrusion-related gold systems given their association with felsic magmas (Lang and Baker, 2001). Furthermore, with respect to the

whether such a fluid was even present at the WGD setting is that both replacement and vein-type mineralization are strongly associated with an extensive and pervasive sericite alteration on a cm to multi-metre scale for >2 km. This alteration, at the expense of feldspar, requires hydrolysis and thus ingress of an acidic aqueous fluid.

Although the origin of the CO<sub>2</sub>-rich fluid is not to be resolved here, we do offer an alternative model for consideration given that large and continuous graphitic sedimentary horizons occur throughout the UBGB, and thin horizons are identified at depth in the deposit. Thus, fluid-rock interactions between the ore fluid and such C-rich horizons may have periodically generated a CO<sub>2</sub>-rich fluid via oxidation of graphite (e.g., Ohmoto and Rye, 1979). The subsequent unmixing of such a fluid with XCO<sub>2</sub>>0.8 (Chi et al. 2006, 2009) could produce the observed type 1a FIs at WGD and also other noted settings referred to. A similar process has been noted in the AGB where mineralized quartz veins cutting graphitic sedimentary rock horizons are characterized by CO<sub>2</sub>-rich FIs (e.g., Bell Creek deposit, Timmins, Ontario; Tuba et al., under review). Also relevant is that the latter fluids have  $\delta^{13}\text{C}$  signature between -25 and -30‰ (Kontak and Tuba, 2017), as do many other settings in the AGB (Kontak unpub. data), thus supporting a local source for the C. Relevant also is that Klein et al. (2006) report  $\delta^{13}\text{C}$  values of -17.6‰ for FI extracts for auriferous quartz veins in the Paleoproterozoic metavolcanic- and metasedimentary-hosted Serrinha gold deposit, Brazil, versus -23.6‰ for graphite in the host sedimentary rocks. Although such depleted values are not recorded for WGD, that values fall to -10.1‰ and thus well below the expected  $\delta^{13}\text{C}_{\Sigma\text{C}}$  value for vein fluid in AGB deposits of -4‰ (Kerrick, 1990) implicates a <sup>13</sup>C-depleted C reservoir such as graphitic sedimentary rocks. Based on this, we suggest therefore that the presence of CO<sub>2</sub>-rich FIs at the WGD may relate to pulses of such fluids invading the mineralized system during its evolution.

### 3.5.4 Implications of pyrite mapping for primary and secondary gold enrichment

In the WGD, four types of pyrite are noted in the syn-mineral vein- and replacement-type mineralization. The pyrites record complex textural growth with porous and non-porous zones with the former containing abundant mineral inclusions. Such mineral textures are considered to reflect CDP (Putnis, 2002, 2009) and are now widely reported in the literature for Fe-As sulfide phases in various gold deposit settings (e.g., Neyedley et al., 2017; Kerr et al., 2018; Gourcerol et al., 2018, 2020; Dubosq et al., 2018; Hastie et al., 2020; Daver et al., 2020). This process involves the replacement of initial pyrite by another which may be caused by: 1) an evolving hydrothermal fluid; or 2) introduction of a new externally derived fluid that came in contact with a pre-existing pyrite whereby the new fluid was undersaturated with respect to the earlier sulfide phase. Both processes could lead to the subsequent dissolution and reprecipitation of multiple pyrite generations (Py1-Py4) as seen in the gold mineralized samples from the WGD. Here we discuss how the integration of petrography, etching, and LA-ICP-MS elemental mapping and derived plots provides the means to unravel the complex evolution of the fluid chemistry at the WGD as retained in different pyrite generations.

The elemental maps reveal initial pyrite (Py1) was relatively enriched in Ni (<1400 ppm, Co (<300 ppm) and Se (>30 ppm) and depleted in most other elements. This pyrite underwent variable degrees of dissolution (i.e., from none to pervasive) and was overgrown by Py2. The chemical changes recorded from Py1 to Py2 include addition of As-Au-Ag-Sb-Hg-Cu-Zn-Pb-Bi-Te. Thus, early Py1 was overprinted and dissolved by an As-bearing fluid carrying precious- and base-metal mineralization. This auriferous event was then overprinted by Py3 and, as with Py-Py2 transition, first involved variable degrees of CDP of Py2. The latter is attributed to generating the abundant mineral inclusions and pits which characterize Py2, which is commonly

observed in other gold settings (see references above). The overgrowth Py3 was again enriched relative to other elements in Ni-Co-Se in proportions similar as in Py1, but also does show weak enrichment of As. Although there is little metal enrichment in Py3, we do note that euhedral arsenopyrite crystals overprint Py3 and that base- and precious metal phases are observed crystalizing around Py3 in the matrix (Figs. 3.8, 3.9). The presence of a clear euhedral pyrite (Py4) overgrowing Py3 (Fig. 9B, C) completes the pyrite paragenesis.

The binary element plots provide the means to track both metal enrichment in Py2 and related development of micro-inclusions, as the other studies cited have shown. Discussing first the Au versus Ag and As plots, we note each of these have consistent patterns which show: 1) low initial Au-Ag enrichment that increases with As content and with this the Au:Ag ratio changes from  $<0.1$  to  $>10$ ; 2) a maximum amount of refractory Au ( $\text{Au}^{1+}$ ) achieved (see red dashed lines) at about 1 wt.% As and past this, at Au values  $>100$  ppm, there is no further increase in As; and 3) for Au values  $>100$  ppm, which reflect micro-inclusions, the Au:Ag ratio is uniform at 10. These latter points have all been discussed in detail elsewhere using similar binary plots (Neyedley et al., 2017; Gourcerol et al., 2018, 2020; Hastie et al. 2020; McDivitt et al., 2021) and argued to favor the mobilization of refractory Au via zone refining of pyrite to from new particulate Au as  $\text{Au}^0$ . Important in regards to these observations is that the presence of As in pyrite has been shown to facilitate incorporation of Au as  $\text{Au}^{1+}$  (e.g., Reich et al., 2005; Kusebach et al., 2018, 2019). Furthermore, using the As values for Py2, limiting values of As in the fluid responsible for As enrichment in Py2 are calculated at  $<2$  ppm for 1000 ppm As to 6-20 ppm for 10,000 ppm based on partition coefficients in Kusebach et al. (2018).

As with Au, enrichment of other elements also correlates with As content and this can be subdivided into enrichment coincident with the two types of Au, that is  $\text{Au}^{1+}$  and  $\text{Au}^0$ . Thus,

whereas the former represents primary enrichment in pyrite the latter reflects formation of micro-inclusions related to CDP processes. Interestingly, both the metals and level of elemental enrichment are similar (general values in ppm): Hg (100s to 100,000), Te (10s to 2500), Cu (100s to 1000s), Sb (10s to 1000s), Bi (100s to >10,000), Pb (100s to 5000), and Zn (10s to >10,000). These elemental enrichments reflect the presence of varied mineral inclusions in Py2 such as chalcopyrite, sphalerite, tennantite-tetrahedrite, galena, various tellurides, mixed Hg-Sb-Au-Ag-Te phases, electrum and gold. Thus the formation of secondary minerals encapsulated in Py2 can be accommodated by the primary chemistry of this stage of pyrite. It is worth noting in this regard that Hastie et al. (2020) made similar conclusions and, based on mass balance, concluded that all observed secondary minerals in similar pyrite could be accommodated via CDP processes.

An obvious extrapolation of the above observations is whether the spectacular, high-grade gold observed at the WGD (e.g., Fig. 3.6F, G) is related to the features observed in Py2. Although beyond the scope of this study, it is relevant to note however that many of the elements in Py2 are part of the LMCE suite (Frost et al., 2002) which have been attributed to mobilized sulfides melts and also suggested as a way to also cause Au migration from refractory Fe-As sulfides either as melts and/or fluids (see Tomkins et al., 2004, 2007; Tooth et al., 2011). The Au-LMCE association in Py2 ties this to part of the CPD processes which produced the pitted or sieved textures in this pyrite which is now commonly reported in a variety of gold deposit settings (Lawley et al., 2017; Roman et al., 2019; Hastie et al., 2020; Daver et al., 2020; Feng et al., 2020). We suggest therefore that there is a likely causative association between the zone refining of pyrite and formation of coarse gold but further work is needed to better constrain the process.

### 3.5.5 A working model for Windfall gold deposit

In the previous chapter, it was proposed that the WGD is best classified as an intrusion-related Au deposit, as supported by the absolute and relative timing of the main Au mineralizing event that is spatially and temporally constrained by a suite of petrogenetically related pre- and post-mineral calc-alkaline granodiorite QFP dikes dated at ca. 2698 Ma. This age of Au mineralization in the AGB is not unique, and where present is commonly attributed to magmatic-hydrothermal systems that form prior to regional-scale deformation and metamorphism. Deposits occurring at this period in the AGB include: 1) the Au-rich VMS deposits of the LaRonde-Bousquet and Rouyn Noranda mining camps (e.g., LaRonde-Penna, Bousquet, Horne, Quémont) (Mercier-Langevin, 2007; Gibson and Galley, 2007); and 2) a group of pre-Timiskaming intrusion-associated gold deposits (Doyon, Kiena, Norlartic, Barry) (Dubé and Mercier-Langevin, 2020; and references therein). Thus, although unique in character, the WGD shares a similar timing with respect to other Au deposits interpreted by some to be magmatic-hydrothermal systems which formed at this time during the evolution of the AGB. In order to further test the deposit classification, the various microanalytical techniques used in this study aimed to define the PTX conditions of the hydrothermal system and to provide supporting evidence for the proposed intrusion-related deposit model. The interpretation provided below addresses how these data are accommodated in a magmatic-hydrothermal model.

As described in chapter 2, the ore-related mineralization consists of vein- and replacement-type characterized, respectively, by arrays of high-grade Au quartz-carbonate-pyrite  $\pm$  tourmaline veins hosted in auriferous phyllic-altered wall rocks (i.e., sericite-pyrite  $\pm$  silica  $\pm$  tourmaline  $\pm$  fuchsite). The sulfide and sulfosalt-ore assemblage is dominated by pyrite with lesser, arsenopyrite, sphalerite, chalcopyrite, tennantite-tetrahedrite, galena, gold, electrum, and

minor Sb-rich and telluride alloys. This mineral assemblage reflects the geochemical signature of whole-rock multi-element assays data that defines an enrichment (relative to average crust) in Au, Ag, As, Sb, Se, S, Bi and Te (Zn, Cu, Pb, Mo, W) (see chapter 2). Important in regard to this is that petrography, SEM-EDS imaging, chemical staining and elemental mapping of pyrite highlight multiple growth stages (Py1-Py4) whereby precious- and associated base-metals were sequestered into different pyrite generations. The most significant of these was Py2 when As in the fluid catalysed substitution of Au and metals into arsenian pyrite (e.g., Kusebach et al. 2018, 2019). The textures of Py2 reflect CDP processes whereby this pyrite generation underwent zone refining that released its entrained Au ( $\text{Au}^{1+}$ ) to form micro-inclusions of gold ( $\text{Au}^0$ ), but also likely contributed to the many high-grade gold zones the WGD is known for. However, whether this was due to continued fluid flux during the main mineralizing event or later overprinting events remains to be resolved.

To accommodate the mineralogical and geochemical features noted for the WGD ore zones, the ore fluid responsible for the main Au event must have been a reduced and acidic and periodically enriched in As along with the precious- and base metals noted. Fluids of this character characterize a variety of ore-deposit settings (e.g., orogenic: McCuaig and Kerrich, 1998; Goldfarb and Groves, 2015; porphyry: Sillitoe, 2010; reduced intrusion-related: Hart, 2007), which is why sericite-pyrite  $\pm$  carbonate is such a common alteration type and not diagnostic for discriminating ore-deposit types. Of particular note is the lack of a suitable FI-type that represents the ore fluid at the WGD. The predominance of a carbonic-only fluid (type 1a FI), which is of highly controversial origin in Au deposit genesis, cannot account for the origin of the ore-related alteration and transport of the associated metals.

Although the FI evidence for the fluid responsible for the formation of the WGD has not been resolved in this study, type 1a carbonic FIs are observed as a pre-, syn- and post-mineral fluids based on cross-cutting relationships. This FI type define internally robust FIAs with uniform microthermometric data (i.e., densities) that indicate pressures (lithostatic) of entrapment of about 4 km for pre-mineral colloform-textured veins, but about 8 km for syn- to post-mineral quartz veins. Thus, this unusual FI is used to bracket the Au event to between 4 and 8 km depth and is consistent with the depth emplacement noted for the dike rocks of the WIC (i.e., 4 to 8 km, see chapter 2).

The  $\delta^{18}\text{O}$  isotope data for syn-mineral vein quartz calculated for 350°C equates to  $\delta^{18}\text{O}_{\text{H}_2\text{O}}$  of 0-9‰. The high values are consistent with the range noted for primary magmatic fluids (i.e., 5.5-10‰; Taylor, 1974; Sheppard 1986), for Precambrian Au fluids (i.e., 6-11‰; McCuaig and Kerrich, 1998), and for orogenic gold deposits in general (i.e., 4-15‰; Ridley and Diamond, 2000). In contrast, the lower values demand mixing with a  $^{18}\text{O}$ -depleted reservoir, such as meteoric waters, which is generally not considered as part of the orogenic gold model (Goldfarb and Groves, 2015), but is commonly reported in various types of magmatic-hydrothermal systems, such as porphyry deposits (e.g., Allan and Yardley, 2007; Shanks, 2014; Fekete et al., 2016). Thus, a logical interpretation for the WGD is that the  $\delta^{18}\text{O}$  signature of the syn-mineral quartz reflects a magmatic fluid that has variably mixed with meteoric fluids during vein formation. This is consistent with the emplacement level of the dike complex (4-8 km) and related main Au-event.

The S isotopic signature of various growth phases of pyrite (i.e., Py1-Py3) indicate maximum calculated  $\delta^{34}\text{S}_{\text{fluid}}$  values of 5.5 to 7.8‰ taking into account potential fluid-related oxidation (i.e.,  $\Delta = \delta^{34}\text{S}_{\text{H}_2\text{S}} - \delta^{34}\text{S}_{\text{fluid}}$ ). However, as previously noted the lower value of 5‰

applies to the main Au event represented by Py2. This S isotopic signature does not discriminate any specific S reservoir, as it overlaps with multiple fields (Ohmoto, 1986; Seal, 2006).

However, if a magmatic reservoir is considered, as is here argued, and one corrects for  $\Delta_{\text{fluid-melt}}$  fractionation (Ohmoto and Rye, 1979), then the  $\delta^{34}\text{S}_{\Sigma\text{S}}$  is 0‰ for a magmatic reservoir and consistent with this model.

The C isotopic signature for FIs extracts indicates a range from -0.2 to -10.1‰ across all vein types. These data can simply be broken into two FI groups related to the vein paragenesis as noted before: 1) low pressure (i.e., pre-mineral colloform-textured carbonate veins); and 2) high-pressure (syn- and post-mineral quartz veins). The earliest veins record  $\delta^{13}\text{C}$  values that are -0.2 and -0.6‰ that are not diagnostic of any one carbon source and is consistent with C originating from both igneous reservoirs and also oxidized C in carbonate-altered metavolcanic rocks (Ohmoto and Rye, 1979; Kerrich, 1990; McCuaig and Kerrich, 1998). The later higher pressure veins record  $\delta^{13}\text{C}$  values between -2 to -10.1‰, which again do not discriminate one specific reservoir and overlap with the  $^{13}\text{C}$  values for most Archean lode-gold deposits (-6 to 0‰; McCuaig and Kerrich, 1998; Ridley and Diamond, 2000). However, the more negative values suggest input of oxidized graphite originating from sedimentary rocks, as noted before for gold deposits dominantly hosted in metasedimentary sequences (e.g., Kerrich, 1990; Kontak and Kerrich, 1997). Thus, the  $\delta^{13}\text{C}$  data are not inconsistent with a magmatic fluid reservoir but require input of other C from other sources, both oxidized and reduced as can be sourced from carbonatized metavolcanic rocks and graphitic metasedimentary rocks, both of which are in the local stratigraphy to the WGD.

Based on the arguments noted above and geological aspects presented in chapter 2, the WGD is classified as an intrusion-related gold system. The data noted above, such as ore-related

alteration, chemical signature of the Au ore, O and S isotopic signatures of syn-mineral quartz and pyrite, and the depth constraints for the ore-forming event can all be accommodated by a magmatic-hydrothermal model.

### 3.6 Conclusions

The identification and significance of intrusion-related Au deposits in Archean greenstone belts remains underappreciated. The 6+ Moz gold resource defined at the WGD of the underexplored UBGB, where Au is centered on and constrained genetically to a swarm of ca. 2698 Ma felsic dike rocks, therefore represents a significant discovery in this context. In this paper we integrated the results of earlier geological studies with detailed mineralogical and fluid-chemical data based on various micro-analytical methods to further evaluate the genesis of this world-class Au deposit. The data presented, that includes in situ isotopes (O, S), fluid inclusion microthermometry, and pyrite characterization and elemental mapping, strongly supports the previously suggested magmatic-hydrothermal model for this setting. Several aspects of the study are noted: 1) documentation of fluid mixing between a dominantly magmatic-sourced fluid and meteoric water based on in situ SIMS  $\delta^{18}\text{O}_{\text{quartz}}$  measurements; 2) recognition of multiple generations of pyrite (i.e., Py1-Py4) and the role of As in catalyzing the uptake of Au and associated elements (Ag-Sb-Hg-Cu-Zn-Pb-Bi-Te) in the main ore-stage pyrite (Py2); and 3) the role of zone refining to account for the current department of Au which includes widespread mobilization and upgrading of it in the deposit. Importantly, the characteristics of the veins (quartz-carbonate-pyrite  $\pm$  tourmaline) and alteration (sericite-pyrite  $\pm$  silica  $\pm$  tourmaline  $\pm$  fuchsite) which host the Au mineralization are similar to that found in orogenic-type Au deposit settings. Thus, this study has shown that the type of veins and alteration are not deposit specific

and, instead, deposit classification should be made based on integrated field studies and advanced analytical protocol.

### 3.7 References

- Allan, M. M., and Yardley, B. W. D., 2007, Tracking meteoric infiltration into a magmatic-hydrothermal system: A cathodoluminescence, oxygen isotope and trace element study of quartz from Mt. Leyshon, Australia: *Chemical Geology*, v. 240, p. 343–360.
- Baker, T., 2002, Emplacement depth and carbon dioxide-rich fluid inclusions in intrusion-related gold deposits: *Economic Geology*, v. 97, p. 1111-1117.
- Bakker, R.J., Diamond, L.W., 2006, Estimation of volume fractions of liquid and vapor phases in fluid inclusions, and definition of inclusion shapes: *American Mineralogist*, v. 91, p. 635-657.
- Bakker, R.J., Jansen, J.B.H., 1994, A mechanism for preferential H<sub>2</sub>O leakage from fluid inclusions in quartz, based on TEM observations: *Contributions to Mineralogy and Petrology*, v. 116, p. 7-20.
- Bandyayera, D., Daigneault, R., and Sharma, K., 2003, Géologie de la région du lac de la Ligne (32F/01): Ministère des Ressources Naturelles, de la Faune et des Parcs, Québec, RG 2004-02, 31 p.
- Bandyayera, D., Rhéaume, P., Cadéron, S., Giguère, E., and Sharma, K., 2004b, Géologie de la région du Lac Lagacé (32B/14): Ministère des Ressources Naturelles, de la Faune et des Parcs, Québec, RG 2004-02, 32 p., 4 maps.
- Bandyayera, D., Rhéaume, P., Doyon, J., and Sharma, K., 2004a, Géologie de la région du lac Hébert (32G/03): Ministère des Ressources Naturelles, de la Faune et des Parcs, Québec, RG 2003-07, 57 p., 4 maps.
- Bandyayera, D., Théberge, L., and Fallara, F., 2002, Géologie de la région des lacs Piquet et Mesplet (32G/04 et 32B/13). Ministère des Ressources Naturelles, Québec, RG 2001-14, 56 p., 8 maps.
- Bernet, M., Basset, K., 2005, Provenance analysis by single-quartz-grain SEM-CL/optical microscopy: *Journal of Sedimentary Research*, v. 75, p. 496-504.
- Betsi, T.B., Lentz, D.R., 2010, The nature of “quartz eyes” hosted by dikes associated with Au-Bi-As-Cu, Mo-Cu, and base-metal-Au-Ag mineral occurrences in the Mountain Freegold region, (Dawson Range), Yukon, Canada: *Journal of Geosciences*, v. 55, p. 347-368.
- Bodnar, R. J., 2003a, Introduction to fluid inclusions: Fluid inclusions: analysis and interpretation, p. 1–8.

- Bodnar, R. J., 2003b, Reequilibration of fluid inclusions: Fluid inclusions: Analysis and Interpretation, v. 32, p. 213–230.
- Bodnar, R.J., Binns, P.R., Hall, D.L., 1989, Synthetic fluid inclusions – VI. Quantitative evaluation of the decrepitation behavior of fluid inclusions in quartz at one atmosphere confining pressure: *Journal of Metamorphic Geology*, v. 7, p. 229-242.
- Bodnar, R.J., Lecumberri-Sanchez, P., Moncada, D., and Steele-MacInnis, M., 2014, Fluid inclusions in hydrothermal ore deposits: In Holand, H.D. and Turelian, K.K. eds., *Treatise on geochemistry* 2nd ed. Oxford/San Diego, Elsevier, p. 119-142.
- Bodnar, R.J., Reynolds, T.J., Kuehn, C.A., 1985, Fluid-inclusion systematics in epithermal systems: *Reviews in Economic Geology*, v. 2, p. 73-97.
- Boggs, S.J. and Krinsley, D., 2006, *Application of cathodoluminescence imaging to the study of sedimentary rocks*: Cambridge University Press, Cambridge, p. 165.
- Boggs, S.J., Kagami, H., Taniguchi, H., 2007, Cathodoluminescence Study of Quartz Recrystallization in Contact-Metamorphosed Rocks of the Shimanto Supergroup, Kanto Mountains, Japan: *Josai University Bulletin of Liberal Arts*, v. 30, pp. 15-32.
- Boggs, S.J., Kwon, Y., Gordon, G.G., Rusk, B.G., Krinsley, D., Seyedolali, A., 2002, Is quartz cathodoluminescence color a reliable provenance tool? A quantitative examination: *Journal of Sedimentary Research*, v. 72, p. 408-415.
- Boullier, A.M., Firdaus, K., and Robert, F., 1998, On the significance of aqueous fluid inclusions in gold-bearing quartz vein deposits from the southeastern Abitibi Subprovince, Quebec, Canada: *Economic Geology*, v. 93, p. 216-223.
- Boullier, A-M., 1999, Fluid inclusions: tectonic indicators: *Journal of Structural Geology*, v. 21, p. 1229-1235.
- Breiter, K., Ackerman, L., Svojtka, M., Müller, A., 2013, Behavior of trace elements in quartz from plutons of different geochemical signature: A case study from the Bohemian Massif, Czech Republic: *Lithos*, v. 175-176, p. 54-67.
- Breiter, K., Ďurišová, J., Dosbaba, M., 2017, Quartz chemistry – A step to understanding magmatic-hydrothermal processes in ore-bearing granites: Cínovec/Zinnwald Sn-W-Li deposit, Central Europe: *Ore Geology Reviews*, v. 90, p. 25-35.
- Card, K.D. 1990, A review of the Superior province of the Canadian Shield, a product of Archean accretion: *Precambrian Research*, v. 48, p. 99–156.
- Castonguay, S., Dubé, B., Mercier-Langevin, P., and Wodicka, N., 2019, Geological setting and mineralisation styles of the Sunday Lake and Lower Detour ‘gold trends’, northwestern Abitibi greenstone belt, Ontario and Quebec; Targeted Geoscience Initiative: 2018 report of activities, Geological Survey of Canada, Open file report 8549, p. 9–22.
- Cheng, X., Xu, J., Wang, J., Xue, Q, Zhang, H., 2016, Carbonic fluids in the Hamadi gold deposit, Sudan: origin and contribution to gold mineralization: *Canadian Journal of Earth Sciences*, v. 54, p. 494-511.

- Chi, G., Dubé, B., Williamson, K., Williams-Jones, A.E., 2006, Formation of the Campbell-Red Lake gold deposit by H<sub>2</sub>O-poor, CO<sub>2</sub>-dominated fluids: *Mineralium Deposita*, v. 40, p. 726-741.
- Chi, G., Yongxing, L., Dubé, B., 2009, Relationship between CO<sub>2</sub>-dominated fluids, hydrothermal alterations and gold mineralisation in the Red Lake greenstone belt, Canada. *Applied Geochemistry*, v. 24, p. 504-516.
- Choquette, B., 2017, A comprehensive study of fluid inclusions, cathodoluminescence, evaporate mound and SIMS oxygen isotopes of vein quartz from the Caribou gold deposit, Nova Scotia: One sample provides insight into vein forming processes. Unpublished undergraduate thesis, Laurentian University, p. 80.
- Crawford, M.L., and Hollister, L.S., 1986, Metamorphic fluids: The evidence from fluid inclusions, in Walther, J.V. and Woods, B.J. eds., *Fluid-rock interactions during metamorphism*: New York, Springer, p. 1-35.
- Daver, L., Jébrak, M., Beaudoin, G., Trumbull, R.B., 2020, Three-stage formation of greenstone-hosted orogenic gold deposits in the Val d'Or mining district, Abitibi, Canada: Evidence from pyrite and tourmaline: *Ore Geology Reviews*, v. 120, p. 34-49.
- De Bresser, J.H.P., Peach, C.J., Reus, J.P.J., and Spiers, C.J., 1998, On dynamic recrystallization during solid state flow: Effects of stress and temperature: *Geophysical Research Letter*, v. 25, p. 3457-3460.
- Diamond, L.W., and Tarantola, A., 2015, Interpretation of fluid inclusions in quartz deformed by weak ductile shearing: Reconstruction of differential stress magnitudes and pre-deformation fluid properties: *Earth and Planetary Science Letters*, v. 417, p. 107–119.
- Dowling, K., Morrison, G., 1989, Application of quartz textures to the classification of gold deposits using North Queensland examples: *Economic Geology*, v. 6, p. 342-355.
- Dubé, B., and Gosselin, P., 2007, Greenstone-hosted quartz-carbonate vein deposits, in Goodfellow, W.D., ed., *Mineral deposits of Canada: A synthesis of major deposit-types, district metallogeny, the evolution of geological provinces, and exploration methods*: Mineral Deposits Division, Geological Association of Canada, Mineral Deposits Division Special Publication no. 5, p. 49–73.
- Dubosq, R., Lawley, C.J.M., Rogowitz, A., Schneider, D.A., Jackson, S., 2018, Pyrite deformation and connections to gold mobility: Insight from micro-structural analysis and trace element mapping: *Lithos*, v. 310-311, pp. 86-104
- Evans, K., Phillips, G., Powell, R., 2006, Rock-buffering of auriferous fluids in altered rocks associated with the Golden Mile-style mineralization, Kalgoorlie Gold Field, Western Australia: *Economic Geology*, v. 101, pp. 805-817.
- Fekete, S., Weis, P., Driesner, T., Bouvier, A.S., Baumgartner, L., Heinrich, C.A., 2016, Contrasting hydrological processes of meteoric water incursion during magmatic-hydrothermal ore deposition: An oxygen isotope study by ion microprobe: *Earth and Planetary Science Letters*, v. 451, p. 263-271.

- Feng, Y., Zhanga, Y., Xie, Y., Shaoa, Y., Laie, C., 2020, Pyrite geochemistry and metallogenic implications of Gutaishan Au deposit in Jiangnan Orogen, South China: *Ore Geology Reviews*, v. 117.
- Frelinger, S.N., Ledvina, M.D., Kyle, J.R., Zhao, D., 2015, Scanning electron microscopy cathodoluminescence of quartz: Principle, technique and applications in ore geology, *Ore Geology Reviews*, v. 65, p. 840-852.
- Fritz, P., Frape, S.K., 1982, Saline groundwaters in the Canadian Shield – A first overview: *Chemical Geology*, v. 36, p. 179-190.
- Frost, B.R., Mavrogenes, J.A., and Tomkins, A.G., 2002, Partial melting of sulphide ore deposits during medium- and high-grade metamorphism: *The Canadian Mineralogist*, v. 40, p. 1–18.
- Gaboury, D., 2019, Parameters for the formation of orogenic gold deposits: *Applied Earth Science*, v. 128, p. 124-133.
- Garba, I., Akande, S.O., 1992, The origin and significance of non-aqueous CO<sub>2</sub> fluid inclusions in the auriferous veins of Bin Yauri, northwestern Nigeria: *Mineralium Deposita*, v. 27, p. 249-255.
- Garofalo, P.S., 2000, Gold precipitation and hydrothermal alteration during fluid flow through the vein network of the mesothermal gold deposit of Sigma, Abitibi belt, Canada: Unpublished PhD Thesis, Zurich, Swiss Federal Institute of Technology, 252 p.
- Gibson, H.L. and Galley, A.G., 2007, Volcanogenic massive sulphide deposits of the Archean Noranda District, Québec: in Goodfellow, W.D., ed., *Mineral deposits of Canada: a synthesis of major deposit types, district metallogeny, the evolution of geological provinces, and exploration methods*: Geological Association of Canada, Mineral Deposits Division, Special Publication 5, p. 533-552.
- Goldfarb, R.J., Baker, T., Dubé, B., Groves, D.I., Hart, C.J.R., Gosselin, P., 2005, Distribution character, and genesis of gold deposits in metamorphic terranes: *Economic Geology 100th Anniversary*, p. 407-450.
- Goldfarb, R.J., Groves, D.I., 2015, Orogenic gold: Common or evolving fluid and metal sources through time: *Lithos*, v. 233, p. 2-26.
- Goldstein, R. H., and Reynolds, J. T., 1994, *Systematics of Fluid Inclusions in Diagenetic Minerals*: SEPM Short Course, no. 31, p. 9-53.
- Götze, J., Plötze, M., and Habermann, D., 2001, Origin, spectral characteristics, and practical applications of the cathodoluminescence of quartz - A review: *Mineralogy and Petrology*, v. 71, p. 225–250.
- Gourcerol, B., Kontak, D.J., Petrus, J.A., Thurston, P.C., 2020, Application of LA ICP-MS analysis of arsenopyrite to gold metallogeny of the Meguma Terrane, Nova Scotia, Canada: *Gondwana Research*, v. 81, p. 265-290.
- Gourcerol, B., Kontak, D.J., Thruston, P.C., Petrus, J.A., 2018, Application of LA-ICP-MS sulfide analysis and methodology for deciphering elemental paragenesis and associations

- in addition to multi-stage processes in metamorphic gold settings: *The Canadian Mineralogist*, v. 56, p. 39-64.
- Groves, D.I., Santosh, M., Zhang, L., 2020, A scale-integrated exploration model for orogenic gold deposits based on a mineral system approach: *Geoscience Frontiers*, v. 11, p. 719-738.
- Groves, D.I., Goldfarb, R.J., Gebre-Mariam, M., Hagemann, S.G., Robert, F. 1998, Orogenic gold deposits: A proposed classification in the context of their crustal distribution and relationship to other gold deposit types: *Ore Geology Reviews*, v. 13, p. 7-27.
- Hagemann, S., and Cassidy, K., 2000, Archean orogenic lode gold deposits: *Reviews in Economic Geology*, v. 13, p. 9-68.
- Hastie, E.C.G., Kontak, D.J., Lafrance, B. 2020, Gold remobilization: Insights from gold deposits in the Archean Swayze greenstone belt, Abitibi Subprovince, Canada: *Economic Geology*, v. 115, p. 241-277.
- Hollister, L.S., 1990, Enrichment of CO<sub>2</sub> in fluid inclusions in quartz by removal of H<sub>2</sub>O during crystal-plastic deformation: *Journal of Structural Geology*, v. 12, p. 895-901.
- Joly, M., 1990, *Géologie de la région du lac aux Loutres et du lac Lacroix*: Ministère de l'Énergie et des Ressources, Gouvernement du Québec, MB 90-42, 55 p.
- Katz, L.R., Kontak, D.J., Dubé, B., and McNicoll, V. 2017, The geology, petrology, and geochronology of the Archean Côté Gold large-tonnage, low-grade intrusion-related Au(-Cu) deposit, Swayze greenstone belt, Ontario, Canada: *Canadian Journal of Earth Sciences*, v. 54, p. 273-302.
- Katz, L.R., Kontak, D.J., Dubé, B., McNicoll, V., Creaser, R., Petrus, J.A., 2021, An Archean Porphyry-Type Gold Deposit: The Côté Gold Au(-Cu) Deposit, Swayze Greenstone Belt, Superior Province, Ontario, Canada: *Economic Geology*, v. 116, p. 47-89.
- Kerr, M., Hanley, J.J., Kontak, D.J., Morrison, G.G., Petrus, J., Fayek, M., Zajacz, Z., 2018, Evidence of upgrading of gold tenor in an orogenic quartz-carbonate vein system by late magmatic-hydrothermal fluids at the Madrid Deposit, Hope Bay Greenstone Belt, Nunavut, Canada: *Geochimica et Cosmochimica Acta*, v. 241, p. 180-218.
- Kerrick, R., 1987, The stable isotope geochemistry of Au-Ag vein deposits in metamorphic rocks: In *Stable isotope geochemistry of low temperature fluids*. Edited by J.K. Kyser. Mineral Association of Canada, Short Course Handbook, v. 13, p. 287-326.
- Kerrick, R., 1990, Carbon-isotope systematics of Archean Au-Ag vein deposits in the Superior Province: *Canadian Journal of Earth Sciences*, v. 27, p. 40-56.
- King, E.M., Valley, J.W., Davis, D.W., Edwards, G.R., 1998, Oxygen isotope ratios of Archean plutonic zircons from granite-greenstone belts of the Superior Province: indicator for magmatic source: *Precambrian Research*, v. 92, p. 365-387.
- Kitney, K.E., Olivo, G.R., Davis, D.W., Desrochers, J-P., Tessier, A., 2011, The Barry Gold Deposit, Abitibi Subprovince, Canada: A greenstone Belt-Hosted gold Deposit Coeval

- with Late Archean Deformation and Magmatism: *Economic Geology*, v. 106, p. 1129-1154.
- Klein, E.L., Fuzikawa, K., 2010, Origin of the CO<sub>2</sub>-only fluid inclusions in the Palaeoproterozoic Carará vein-quartz gold deposit, Ipitinga auriferous district, SE-Guiana Shield, Brazil: Implications for orogenic gold mineralisation: *Ore geology reviews*, v. 37, p. 31-40.
- Klein, E.L., Harris, C., Renac, C., Giret, A., Moura, C.A.V., Fuzikawa, K., 2006, Fluid inclusion and stable isotope (O, H, C, and S) constraints on the genesis of the Serrinha gold deposit, Gurupi Belt, northern Brazil: *Mineralium Deposita*, v. 41, p. 160-178.
- Köhler, J., Konnerup-Madsen, J., Markl, G., 2008, Fluid geochemistry in the Ivigtut cryolite deposit, South Greenland: *Lithos*, v. 103, p. 369-392.
- Kontak, D.J., (2002): Fluid inclusion decrepitate textures in metamorphic vein-gold deposits and granitic pegmatites of the Meguma Terrane, Nova Scotia, Canada: Overlooked phenomenon or local anomaly. PACROFI VIII Meeting, Halifax, Nova Scotia, July 21-25, Program with Abstracts, p. 43-45.
- Kontak, D.J., Behuniak, L., Jibb, A., Tinkham, D., 2016, Evidence for pressure cycling and fluid unmixing as relevant processes in gold deposits from fluid inclusion studies of Archean and Phanerozoic orogenic and intrusion-related settings in Canada: Abstract in Pan-American Current Research on Fluid Inclusions (PACROFI-XIII), p. 65-66.
- Kontak, D.J., Horne, R.J., and Smith, P.K., 1996, Hydrothermal characterization of the West Gore Au-Sb deposit, Meguma Terrane, Nova Scotia: *Economic Geology*, v. 91, p. 1239-1262.
- Kontak, D.J., Katz, L., Creaser, R.A., and Hamilton, M., 2013, The Archean Côté Gold Au(-Cu) deposit, northern Ontario, Canada: A large tonnage, low-grade Au deposit centred on a 2740 Ma magmatic-hydrothermal diorite complex [abs.]: Geological Association of Canada-Mineralogical Association of Canada, Annual Meeting, Winnipeg, Manitoba, 2013, Abstracts.
- Kontak, D.J., Kerrich, R., 1997, An isotopic (C, O, Sr) study of vein gold deposits in the Meguma Terrane, Nova Scotia; implications for source reservoirs: *Economic Geology*, v. 92, p. 161-180.
- Kontak, D.J., Tuba, G., 2017, How can fluid inclusion studies better constrain orogenic gold deposit models: case studies from the superior Province and Meguma Terrane, Canada: In Volume Proceedings of Extended Abstracts, Quebec, Canada, p.55.
- Kusebach, C., Gleeson, S.A., Oelze, M., 2019, Coupled partitioning of Au and As into pyrite controls formation of giant Au deposits: *Science Advances*, v. 5.
- Kusebach, C., Oelze, M., Gleeson, S.A., 2018, Partitioning of arsenic between hydrothermal fluid and pyrite during experimental siderite replacement: *Chemical Geology*, v. 500, p. 136-147.
- Landtwing, M.R., Pettke, T., Halter, W.E., Heinrich, C.A., Redmond, P.B., Einaudi, M.T., Kunze, K., 2005, Copper deposition during quartz dissolution by cooling magmatic-

- hydrothermal fluids: the Bingham porphyry: *Earth and Planetary Science Letters*, v. 235, p. 229-243.
- Lang, J.R., Baker, T., 2001, Intrusion-related gold systems: the present level of understanding: *Mineralium Deposita*, v. 36, p. 477-489.
- Large, R., Thomas, H., Craw, D., Henne, A., Henderson, S., 2012, Diagenetic pyrite as a source for metals in orogenic gold deposits, Otago Schist, New Zealand: *New Zealand Journal of Geology and Geophysics*, v. 55, p. 137-149.
- Large, R.R., Danyushevsky, L., Hollit, C., Maslennikov, V., Meffre, S., Gilbert, S., Bull, S., Scott, R., Emsbo, P., Thomas, H., Singh, B., Foster, J., 2009, Gold and trace element zonation in pyrite using a laser imaging technique: Implications for the timing of gold in orogenic and carlin-style sediment-hosted deposits: *Economic Geology*, v. 104, p. 635-668.
- Lawley, C.J.M., Jackson, S., Yang, Z., Davis, W., and Eglinton, B., 2017, Tracing the transition of gold from source to sponge to sink: *Economic Geology*, v. 112, p. 169–183.
- Lowenstern, J.B., 2001, Carbon dioxide in magmas and implications for hydrothermal systems: *Mineralium Deposita*, v. 36, p. 490-502.
- Mao, W., Rusk, B., Yang, F., and Zhang, M., 2017, Physical and chemical evolution of the Dabaoshan porphyry deposit, South China: Insights from fluid inclusions, cathodoluminescence, and trace elements in quartz: *Economic Geology*, v. 112, p. 889-918.
- Marshall, D.J., 1988, *Cathodoluminescence of Geological Materials*: Boston, Massachusetts, Unwin Hyman, 146 p.
- Matsuhisa, Y., Goldsmith, J.R., Clayton, R.N., 1979, Oxygen isotopic fractionation in the system quartz-albite-anorthite-water: *Geochimica et Cosmochimica Acta*, v. 43, p. 1131-1140.
- Matter, A. and Ramseyer, K., 1985, Cathodoluminescence microscopy as a tool for provenance analysis: in Zuffa, G.G., ed., *Provenance of Arenites*: D. Reidel Publishing Co., Boston, p. 191-211.
- McCuaig, T.C., Kerrich, R., 1998, P-T-t-deformation-fluid characteristics of lode gold deposits: evidence from alteration systematics: *Ore Geology Reviews*, v. 12, p. 381-453.
- McDivitt, J.A., Kontak, D.J., Lafrance, B., Petrus, J.A., Fayek, M., 2021, A trace metal, stable isotope (H, O, S), and geochronological (U-Pb titanite) characterization of hybridized gold orebodies in the Missanabie-Renabie district, Wawa Subprovince (Canada): *Mineralium Deposita*, v. 56, p. 561-582.
- McDivitt, J.A., Lafrance, B., Kontak, D.J., Robichaud, L., 2017, The structural evolution of the Missanabie-Renabie gold district: Pre-orogenic veins in an orogenic gold setting and their influence on the formation of hybrid deposits, *Economic Geology*, v. 112, p. 1959-1975.
- Mercier-Langevin, P., Dubé, B., Lafrance, B., Hannington, M., Galley, A., Moorhead, J., and Gosselin, P., 2007, Metallogeny of the Doyon-Bousquet-LaRonde mining camp, Abitibi

- greenstone belt, Québec: in Goodfellow, W.D., ed. Mineral Deposits of Canada: A synthesis of Major Deposits Division, Special Publication No. 5, p. 673-701.
- Mériaud, N., Jébrak, M., 2017, From intrusion-related to orogenic mineralization: The Wasamac deposit, Abitibi Greenstone Belt, Canada: *Ore Geology Reviews*, v. 84, p. 289-308.
- Milner, R.L., 1939, Barry Lake Area, Abitibi County and Abitibi Territory, Department of Mines, Québec, RP 143, 9 p.
- Moncada, D., Mutchler, S., Nieto, A., Reynolds, T.J., Rimstidt, J.D., Bodnar, R.J., 2012, Mineral textures and fluid inclusion petrography of the epithermal Ag-Au deposits at Guanajuato, Mexico: Application to exploration: *Journal of Geochemical Exploration*, v. 114, p. 20-35.
- Monecke, T., Monecke, J., Reynolds, T.J., Tsuruoka, S., Bennett, M.M., Skewes, W.B., Palin, R.M., 2018, Quartz solubility in the H<sub>2</sub>O-NaCl system: A framework for understanding vein formation in porphyry copper deposits: *Economic Geology*, v. 113, p. 1007-1046.
- Mueller, A., 2015, Structure, alteration, and geochemistry of the Charlotte quartz vein stockwork, Mt Charlotte gold mine, Kalgoorlie, Australia: time constraints, down-plunge zonation, and fluid source: *Mineralium Deposita*, v. 50, p. 221-244.
- Mueller, A.G., 2020a, Paragonite-chloritoid alteration in the Trafalgar Fault and Fimiston- and Oroya-style gold lodes in the Paringa South mine, Golden Mile, Kalgoorlie: 2. Muscovite-pyrite and silica-chlorite-telluride ore deposited by two superimposed hydrothermal systems: *Mineralium Deposita*, v. 55, p. 697-730.
- Mueller, A.G., 2020b, Structural setting of Fimiston- and Oroya-style pyrite-telluride-gold lodes, Paringa South mine, Golden Mile, Kalgoorlie: 1. Shear zone systems, porphyry dikes and deposit-scale alteration zones: *Mineralium Deposita*, v. 55, p. 665-695.
- Mueller, A.G., Hagemann, S.G., Brugger, J., Xing, Y., Roberts, M.P. 2020c, Early Fimiston and late Oroya Au-Te ore, Paringa South mine, Golden Mile, Kalgoorlie: 4. Mineralogical and thermodynamic constraints on gold deposition by magmatic fluids at 420-300 °C and 300 MPa: *Mineralium Deposita*, v. 55, p. 767-796.
- Mueller, A.G., Muhling, J.R., 2020d, Early pyrite and late telluride mineralization in vanadium-rich gold ore from the Oroya Shoot, Paringa South mine, Golden Mile, Kalgoorlie: 3. Ore mineralogy, Pb-Te (Au-Ag) melt inclusions, and stable isotope constraints on fluid sources: *Mineralium Deposita*, v. 55, p. 733-766.
- Nassif, M.T., 2019, Structural-metallogenic evolution of the Garrison gold camp of the Archean southern Abitibi greenstone belt, Ontario, Canada: Unpublished thesis, Colorado School of mines, p. 160.
- Neumayr, P., Hagemann, S.G., 2002, Hydrothermal fluid evolution within the Cadillac Tectonic Zone, Abitibi Greenstone Belt, Canada: relationship to auriferous fluids in adjacent second- and third-order shear zones: *Economic Geology*, v. 97, p. 1203-1225.
- Neyedley, K., Hanley, J.J., Fayek, M., Kontak, D.J. 2017, Textural, fluid inclusion, and stable oxygen isotope constraints on vein formation and gold precipitation at the 007 deposit,

- Rice Lake greenstone belt, Bissett, Manitoba, Canada: *Economic Geology*, v. 112, p. 629-660.
- Ohmoto, H., 1986, Stable isotope geochemistry of ore deposits: *Reviews in Mineralogy and Geochemistry*, v. 16, p. 491-559.
- Ohmoto, H. and Rye, R.O., 1979, Isotope of sulfur and carbon, in Barnes, H.L.Ed., *Geochemistry of Hydrothermal deposits*, John Wiley & Sons, p. 509-567.
- Paton, C., Hellstrom, J., Paul, B., Woodhead, J., Hergt, J., 2011, Iolite: freeware for the visualization and processing of mass spectrometric data: *Journal of Analytical Atomic Spectrometry*, v. 26, p. 2508-2518.
- Pêcher, A., 1981. Experimental decrepitation and reequilibration of fluid inclusions in synthetic quartz. *Tectonophysics* 78, 567-584.
- Pêcher, A., Boullier, A-M., 1984, Évolution à pression et température élevées d'inclusions fluides dans un quartz synthétique : *Bull. Minéral.*, v. 107, p. 139-153.
- Peck, W.H., King, E.M., Valley, J.W., 2000, Oxygen isotope perspective on Precambrian crustal growth and maturation, *Geology*, v. 28, p. 363-366.
- Penczak, R., Mason, R., 1997, Metamorphosed Archean epithermal Au-As-Sb-Zn-(Hg) vein mineralization at the Campbell Mine, northeastern Ontario: *Economic Geology*, v. 92, p. 696-719.
- Petrella, L., Thébaud, N., Laflamme, C., Martin, L., Occhipinti, S., Bigelow, J., 2020, In-situ sulfur isotopes analysis as an exploration tool for orogenic gold mineralization in the Granites-Tanami Gold Province, Australia: Learnings from the Callie deposit: *Journal of Geochemical Exploration*, v. 214,
- Putnis, A., 2002, Mineral replacement reactions: from macroscopic observations to microscopic mechanisms: *Mineralogical Magazine*, v. 66, p. 689-708
- Putnis, A., 2009, Mineral Replacement Reactions: *Reviews in Mineralogy and Geochemistry*, v. 70, p. 87-124.
- Redmond, P.B., Einaudi, M.T., Inan, E.E., Landtwing, M.R., and Heinrich, 2018, Copper deposition by fluid cooling in intrusion-centered systems: New insights from the Bingham porphyry ore deposit, Utah: *Geology*, v. 32, p. 217–220.
- Reich, M., Kesler, S.E., Utsunomiya, S., Palenik, C.S., Chryssoulis, S.L. Ewing, R.C., 2005, Solubility of gold in arsenian pyrite: *Geochimica and Cosmochimica Acta*, v. 69, p. 2781-2796.
- Rezeau, H. Moritz, R., and Beaudoin, G., 2017, Formation of Archean batholith-hosted gold veins at the Lac Herbin deposit, Val D'Or district, Canada: *Mineralogical and fluid inclusion constraints: Mineralium Deposita*, v. 52, p. 421-442.
- Rhéaume, P., and Bandyayera, D., 2006, Révision stratigraphique de la Ceinture d'Urban-Barry: Ministère des Ressources naturelles et de la Faune, Québec, RP 2006-08, 11 p.

- Rhéaume, P., Bandyayera, D., Fallara, F., Boudrias, G., and Cheng, L.Z., 2004, Géologie et métallogénie du secteur du lac aux Loutres, synthèse métallogénique d'Urban-Barry (phase 1 de 2): Ministère de Ressources naturelles et de la Faune et des Parcs, Québec, RP 2004-05, 10 p.
- Richard, P.L., Athurion, C., Houde, M., 2021, Mineral resource estimate update for the Windfall project, NI 43-101 technical report by BBA Inc. ([www.sedar.com](http://www.sedar.com)).
- Ridley J.R. and Diamond L.W., 2000, Fluid chemistry of lode-gold deposits and implications for genetic models. In: Hagemann S.G., Brown P. (Eds.), *Gold in 2000: Reviews in Economic Geology*, v. 13, p. 141-162.
- Riedel, W., 1929. Zur mechanic geologischer brucherscheinungen. *Centralblatt für Mineralogie, Geologie, und Paleontologie* 1929B, 354
- Robert, F., Brommecker, R., Bourne, B.T., Dobak, P.J., McEwan, C.J., Rowe, R.R., Zhou, X., 2007, Models and Exploration Methods for Major Gold Deposit Types: In "Proceedings of Exploration 07: Fifth Decennial International Conference on Mineral Exploration" edited by B. Milkereit, 2007, p. 691-711.
- Roedder, E., 1984, Fluid inclusions: Reviews in Mineralogy: Mineralogical Society of America.
- Romàn, N., Reich, M., Leisen, M., Morata, D., Barra, F., Deditius, A.P., 2019, Geochemical and micro-textural fingerprints of boiling in pyrite: *Geochimica et Cosmochimica Acta*, v. 246, p. 60–85.
- Rottier, B., Kouzmanov, K., Casanova, V., Wälle, M., Fontboté, L., 2018, Cyclic dilution of magmatic metal-rich hypersaline fluids by magmatic low-salinity fluid: A major process generating the giant epithermal polymetallic deposit of Cerro de Pasco, Peru: *Economic Geology*, v. 113, p. 825-856.
- Rusk, B., 2012, Cathodoluminescent Textures and Trace Elements in Hydrothermal Quartz: In: Götze, Jens, and Möckel, Robert, (eds.) *Quartz: deposits, mineralogy and analytics*. Springer Geology. Springer, Berlin, Germany, p. 307-329.
- Rusk, B., and Reed, M., 2002, Scanning electron microscope-cathodoluminescence analysis of quartz reveals complex growth histories in veins from the Butte porphyry copper deposit, Montana: *Geology*, v. 30, p. 727–730.
- Rusk, B., Reed, M.H., Dilles, J.H., Kent, A.J.R., 2006, Intensity of quartz cathodoluminescence and trace-element content in quartz from the porphyry copper deposit at Butte, Montana: *American Mineralogist*, v. 91, p. 1300-1312.
- Sahoo, A.K., Krishnamurthi, R., Sangurmth, P., 2018, Nature of ore forming fluids, wallrock alteration and P-T conditions of gold mineralization at Hira-Buddini, Hutti-Maski Greenstone Belt, Dharwar Craton, India: *Ore Geology Reviews*, v. 99, p. 195-216.
- Schmidt Mumm, A., Oberthür, T., Vetter, U. and Blenkinsop, T.G., 1997, High CO<sub>2</sub> content of fluid inclusions in gold mineralisations in the Ashanti belt, Ghana: a new category of ore forming fluids: *Mineralium Deposita*, v. 32, p. 107-118.

- Seal, R.R., 2006, Sulfur isotope geochemistry of sulfide minerals: *Reviews in Mineralogy and Geochemistry*, v. 61, p. 663-677.
- Seyedolali, A., Krinsley, D. H., Boggs, S., Hara, P. F. O., Dypvik, H., Gordon, G., Krinsley, D. H., Boggs, S., Exploration, K., and Drive, R., 1997, Provenance interpretation of quartz by scanning electron microscope – cathodoluminescence fabric analysis: *Geology*, v. 25, p. 787–790.
- Shanks, W.C.P., 2014, Stable Isotope Geochemistry of Mineral Deposits: in *Treatise on Geochemistry* 2<sup>nd</sup> edition, v. 13, p. 59-85.
- Sheppard, S.M.F., 1986, Characterization and isotopic variations in natural waters. In *Stable Isotopes in High Temperature Geological Processes*, J.W. Valley, H.P. Taylor Jr., and J.R. O’Neil (eds): *Reviews in Mineralogy*, v. 16, p. 165-184.
- Sibson, R.H., Robert, F., Poulsen, K.H., 1988, High-angle reverse faults, fluid pressure cycling, and mesothermal gold-quartz deposits: *Geology*, v. 16, p. 551-555.
- Sillitoe, R., 2010, Porphyry copper systems: *Economic Geology*, v. 105, p. 3–41.
- Span, R., and Wagner, W., 1996, A new equation of state for Carbon Dioxide covering the fluid region from the triple-point temperature to 1100 K at pressures up to 800 MPa: *Journal of Physical and Chemical Reference Data*, v. 25, p. 1509-1596.
- Spear, F. S., and Wark, D. A., 2009, Cathodoluminescence imaging and titanium thermometry in metamorphic quartz: *Journal of Metamorphic Geology*, v. 27, p. 187–205.
- Sprunt, E., Dengler, L., and Sloan, D., 1978, Effects of metamorphism on quartz cathodoluminescence: *Geology*, v. 6, p. 305-308.
- Steele-MacInnis, M., 2018. Fluid inclusions in the system H<sub>2</sub>O-NaCl-CO<sub>2</sub>: An algorithm to determine composition, density and isochore. *Chemical Geology*, v. 498, p. 31-44.
- Steele-MacInnis, M., Bodnar, R. J. & Naden, J., 2011, Numerical model to determine the composition of H<sub>2</sub>O-NaCl-CaCl<sub>2</sub> fluid inclusions based on microthermometric and microanalytical data: *Geochimica et Cosmochimica Acta*, v. 75, p. 21-41.
- Steele-MacInnis, M., Lecumberri-Sanchez, P., Bodnar, R.J., 2012, HOKIEFLINCS\_H<sub>2</sub>O-NaCl: A Microsoft Excel spreadsheet for interpreting microthermometric data from fluid inclusions based on the PVTX properties of H<sub>2</sub>O-NaCl: *Computers & Geosciences*, v. 49, p. 334-337.
- Sterner, S.M., Bodnar, R.J., 1989. Synthetic fluid inclusions. VII. Re-equilibration of fluid inclusions in quartz during laboratory simulated metamorphic burial and uplift. *Journal of Metamorphic Geology* 7, 243-360.
- Steven Kalceff, M.A., Phillips, M.R., Moon, A.R., Kalceff, W., 2000, Cathodoluminescence microcharacterisation of silicon dioxide polymorphs: In M. Pagel, V. Barbin, P. Blanc, and D. Ohnenstetter (Eds.), *Cathodoluminescence in Geosciences*, Springer-Verlag Berlin Heidelberg New York, p. 193-224.

- Stromberg, J.M., Barr, E., Banerjee, N.R., 2018, Early carbonate veining and gold mineralisation in the Timmins camp: Depositional context of the Dome mine ankerite veins: *Ore Geology Reviews*, v. 97, p. 55-73.
- Tarantola, A., Diamond, L.W., and Stünitz, H., 2010, Modification of fluid inclusions in quartz by deviatoric stress I: Experimentally induced changes in inclusion shapes and microstructures: *Contributions to Mineralogy and Petrology*, v. 160, p. 825–843.
- Taylor, H.P., 1974, The application of oxygen and hydrogen isotope studies to problems of hydrothermal alteration and ore deposition: *Economic Geology*, v. 69, p. 843-883.
- Taylor, H.P., 1979, Oxygen and hydrogen isotope relationships in hydrothermal mineral deposits. In: Barnes HL (ed) *Geochemistry of Hydrothermal Ore Deposits*, 2nd edition, p. 236-277.
- Taylor, R.D., Monecke, T., Reynolds, T.J., Monecke, J., 2021, Paragenesis of an Orogenic Gold Deposit: new insights on mineralizing processes at the Grass Valley District, California: *Economic Geology*, v., 116, p. 323-356.
- Thiéry R., Vidal, J., Dubessy, J., 1994, Phase equilibria modelling applied to fluid inclusions: liquid-vapor equilibria calculation of the molar volume in the CO<sub>2</sub>-CH<sub>4</sub>-N<sub>2</sub> system: *Geochimica et Cosmochimica Acta*, v. 58, p. 1073-1082.
- Tomkins, A.G., Pattison, D.R.M., and Frost, B.R., 2007, On the initiation of metamorphic sulfide anatexis: *Journal of Petrology*, v. 48, p. 511–535.
- Tomkins, A.G., Pattison, D.R.M., and Zaleski, E., 2004, The Hemlo gold deposit, Ontario: An example of melting and mobilization of a precious metal-sulfosalt assemblage during amphibolite facies metamorphism and deformation: *Economic Geology*, v. 99, p. 1063–1084.
- Tooth, B., Ciobanu, C.L., Green, L., O'Neill, B., and Brugger, J., 2011, Bi-melt formation and gold scavenging from hydrothermal fluids: An experimental study: *Geochimica et Cosmochimica Acta*, v. 75, p. 5423–5443.
- Trail, D., Bindeman, I.N., Watson, E.B., Schmitt, A.K., 2009, Experimental calibration of oxygen isotope fractionation between quartz and zircon: *Geochimica et Cosmochimica Acta*, v. 73, p. 7110-7126.
- Tuba, G., Kontak, D.J., Choquette, B.G., Pfister, J., Hastie, E., van Hees, E., under review, Fluid diversity in the gold-endowed Archean orogenic systems of the Abitibi greenstone belt (Canada) I: Constraining the PTX of prolonged hydrothermal systems.
- Valley, J.W., Lackey, J.S., Cavosie, A.J., Clechenko, C.C., Spicuzza, M.J., Basei, M.A.S., Bindeman, I.N., Ferreira, V.P., Sial, A.N., King, E.M., Peck, W.H., Sinha, A.K., Wei, C.S., 2005, 4.4 billion years of crustal maturation: oxygen isotope ratios of magmatic zircon: *Contributions to Mineralogy and Petrology*, v. 150, p. 561-580.
- Van den Kerkhof, A. and Thiéry, R., 2001, Carbonic inclusions, *Lithos*, v. 55, p. 49-68.

- Vasyukova, O.V., Kamenetsky, V.S., Goemann, K., Davidson, P., 2013, Diversity of primary CL textures in quartz from porphyry environments: implications for origin of quartz eyes: *Contributions to Mineralogy and Petrology*, v. 166, p. 1353-1268.
- Vennemann, T.W., and O'Neill, J.R., 1993, A simple and inexpensive method of hydrogen isotope and water analyses of minerals and rocks based on zinc reagent, *Chemical Geology*, v. 103, p. 227-234.
- Vityk, M.O., Bodnar, R.J., Dudok, I.V., 1995, Natural and synthetic re-equilibration textures of fluid inclusions in quartz (Marmarosh Diamonds): Evidence for refilling under conditions of compressive loading: *European Journal of Mineralogy*, v. 7, p. 1071-1087.
- Voisey, C.R., Tomkins, A.G., Xing, Y., 2020b, Analysis of a Telescoped Orogenic Gold System: Insights from the Fosterville Deposit: *Economic Geology*, v. 115, p. 1645–1664.
- Voisey, C.V., Willis, D., Tomkins, A.G., Wilson, C.J.L., Micklethwaite, S., Salvemini, F., Bougoure, J., and Rickard, W.D.A., 2020, Aseismic refinement of orogenic gold systems: *Economic Geology*, v. 115, p. 33-50. Williams-Jones, A.E., Bowell, R.J., Migdisov, A.A., 2009, *Gold in solution: Elements*, v. 5, p. 281-287.
- Watson, E.B., Brenan, J.M., 1987, Fluids in the lithosphere, 1. Experimentally-determined wetting characteristics of CO<sub>2</sub>-H<sub>2</sub>O fluids and their implications for fluid transport, host-rock physical properties, and fluid inclusion formation: *Earth Planetary Science Letter*, v. 85, p. 497–515.
- Weidenbeck, M., Allé, P., Corfu, F., Griffin, W.L., Meier, M., Oberli, F., Von Quadt, A., Roddick, J.C., and Spiegel, W., 1995, Three natural zircon standards for U-Th-Pb, Lu-Hf, trace element and REE analyses: *Geostandards Newsletter*, v. 19, p. 1-23.
- Wehrle, E.A., McDonald, A.M., 2019, Cathodoluminescence and trace-element chemistry of quartz from the Sudbury offset dikes: Observations, interpretations, and genetic implications: *The Canadian Mineralogist*, v. 57, p. 947-963.
- Wiebe, R.A., Wark, D.A., Hawkins, D.P., 2007, Insights from quartz cathodoluminescence zoning into crystallization of the Vinalhaven granite, coastal Maine: *Contributions to Mineralogy and Petrology*, v. 154, p. 439-453.
- Wyman, D.A., Cassidy, K.F., and Hollings, P., 2016, Orogenic gold and the mineral system approach: resolving fact, fiction and fantasy: *Ore Geology Reviews*, v. 78, p. 322-335.
- Yang, X-M., 2017, Estimation of crystallization pressure of granite intrusions: *Lithos*, v. 286-287, p. 324-329.
- Yergeau, D., Mercier-Langevin, P., Dubé, B., Malo, M., McNicoll, V.J., Jackson, S.E., Savoie, A., and La Rochelle, F., 2015, The Archean Westwood Au deposit, southern Abitibi: Telescoped Au-rich VMS and intrusion-related Au systems: *Geological Survey of Canada Open File 7852*, p. 177-191.
- Zhang, W., Lentz, D.R., Thorne, K.G., 2020, Petrogenesis of the Nashwaak Granite, West-Central New Brunswick, Canada: Evidence from Trace Elements, O and Hf Isotopes of Zircon, and O Isotopes of Quartz: *Minerals*, v. 10, 614.

Zohier, B., Johnson, P.R., Goldfarb, R.J., Klemm, D.D., 2019, Orogenic gold in Egyptian Eastern Desert: Widespread gold mineralization in the late stages of Neoproterozoic orogeny: Gondwana Research, v. 75, p. 184-217.

### 3.8 Figures

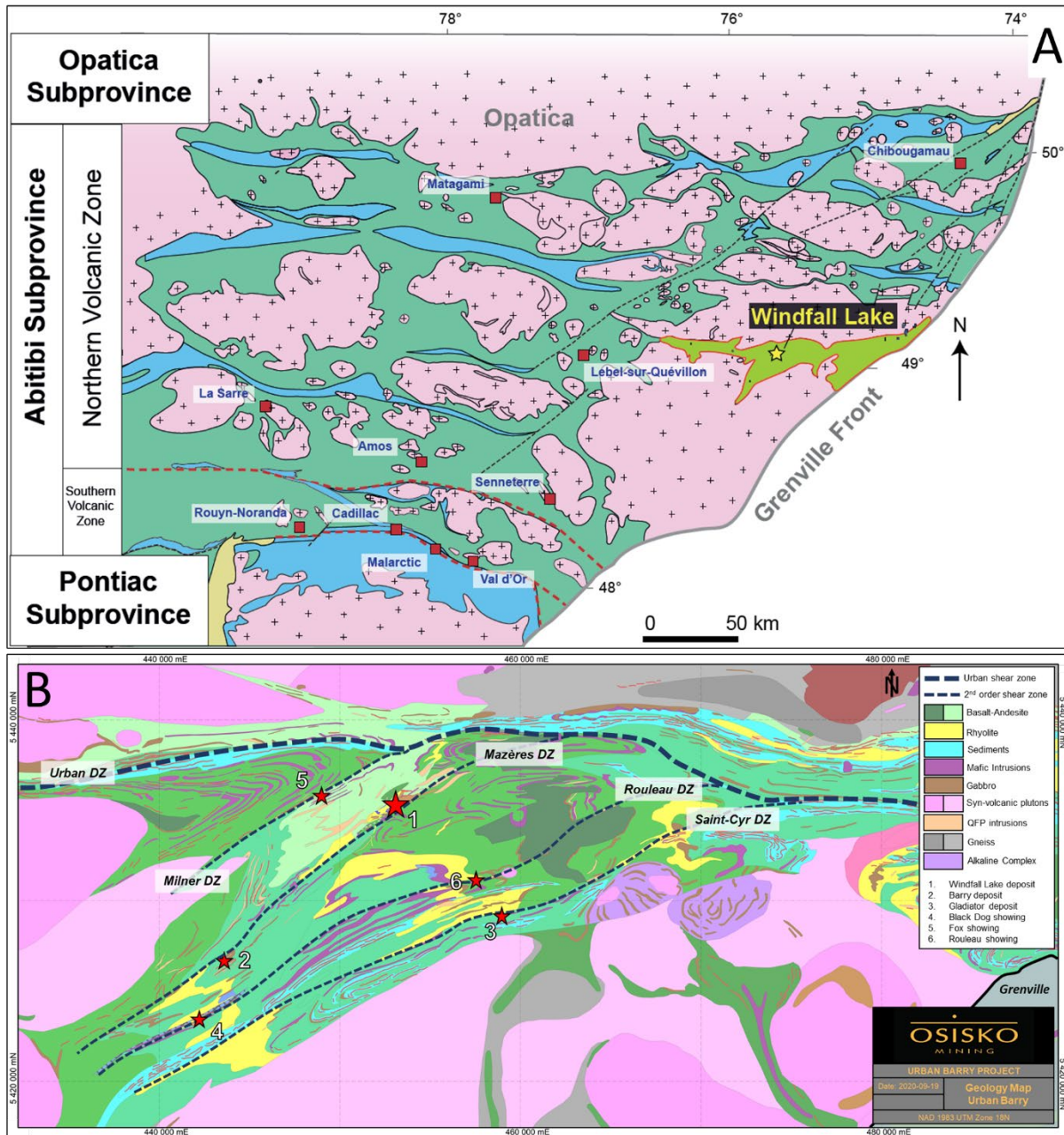


Figure 3.1: A) Map of the Abitibi Subprovince of the Canadian Shield showing the location of the Urban-Barry greenstone belt (UBGB). B) Geological map, courtesy of Osisko Mining, of the UBGB showing the location of the Windfall gold deposit (WGD), other significant mineral

occurrence (red stars) and the traces of the major regional scale deformation zones (DZ), as discussed in the text.

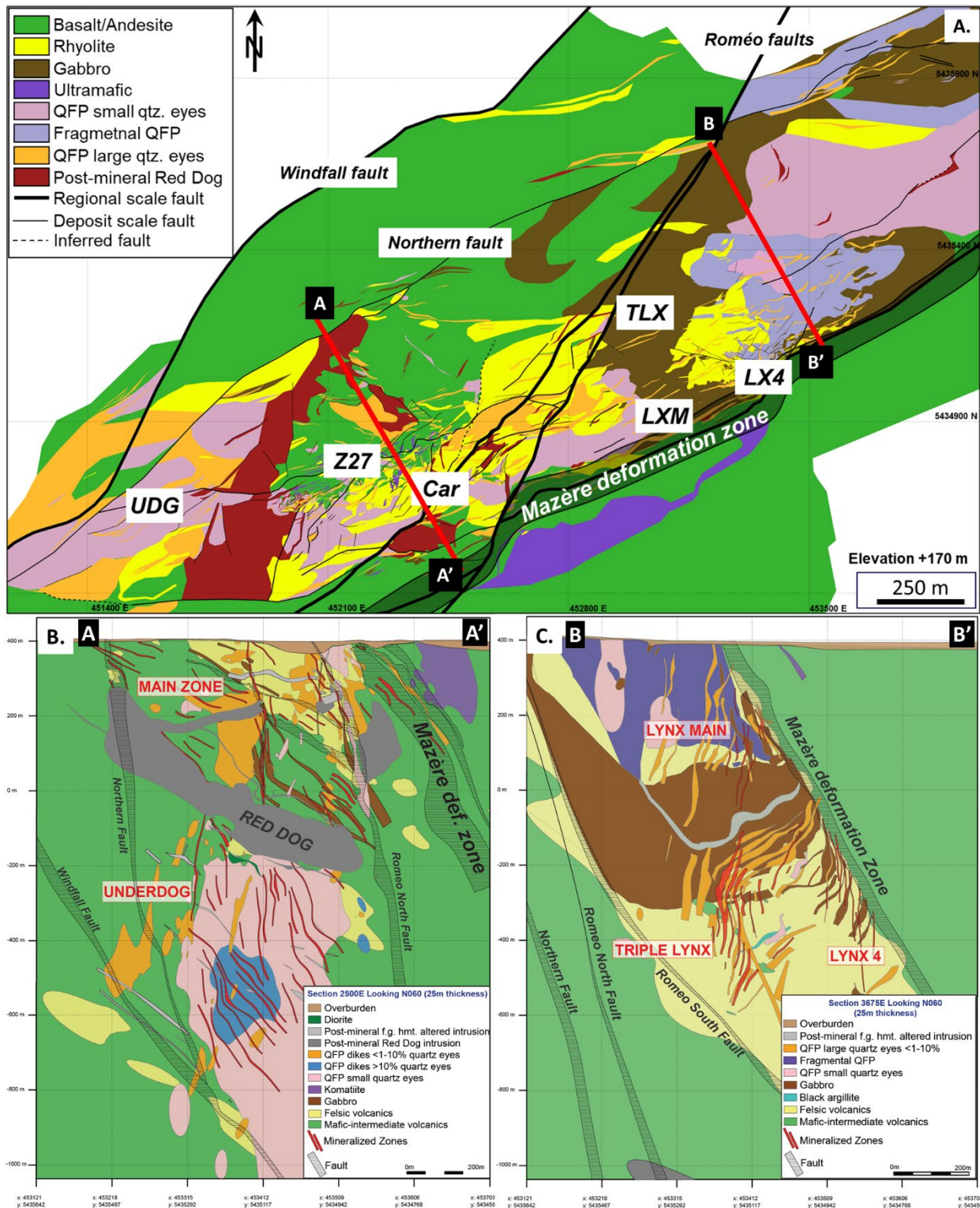


Figure 3.2: Interpreted surface (A) and cross-sectional (B, C) geology maps (facing northeast) of the WGD created using diamond drill-hole pierce points. The plan map is at +170 m elevation

(i.e., -230 m below surface). Cross-section locations shown are indicated on the plan map along section lines A-A' and B-B'. Maps used are courtesy of Osisko Mining.

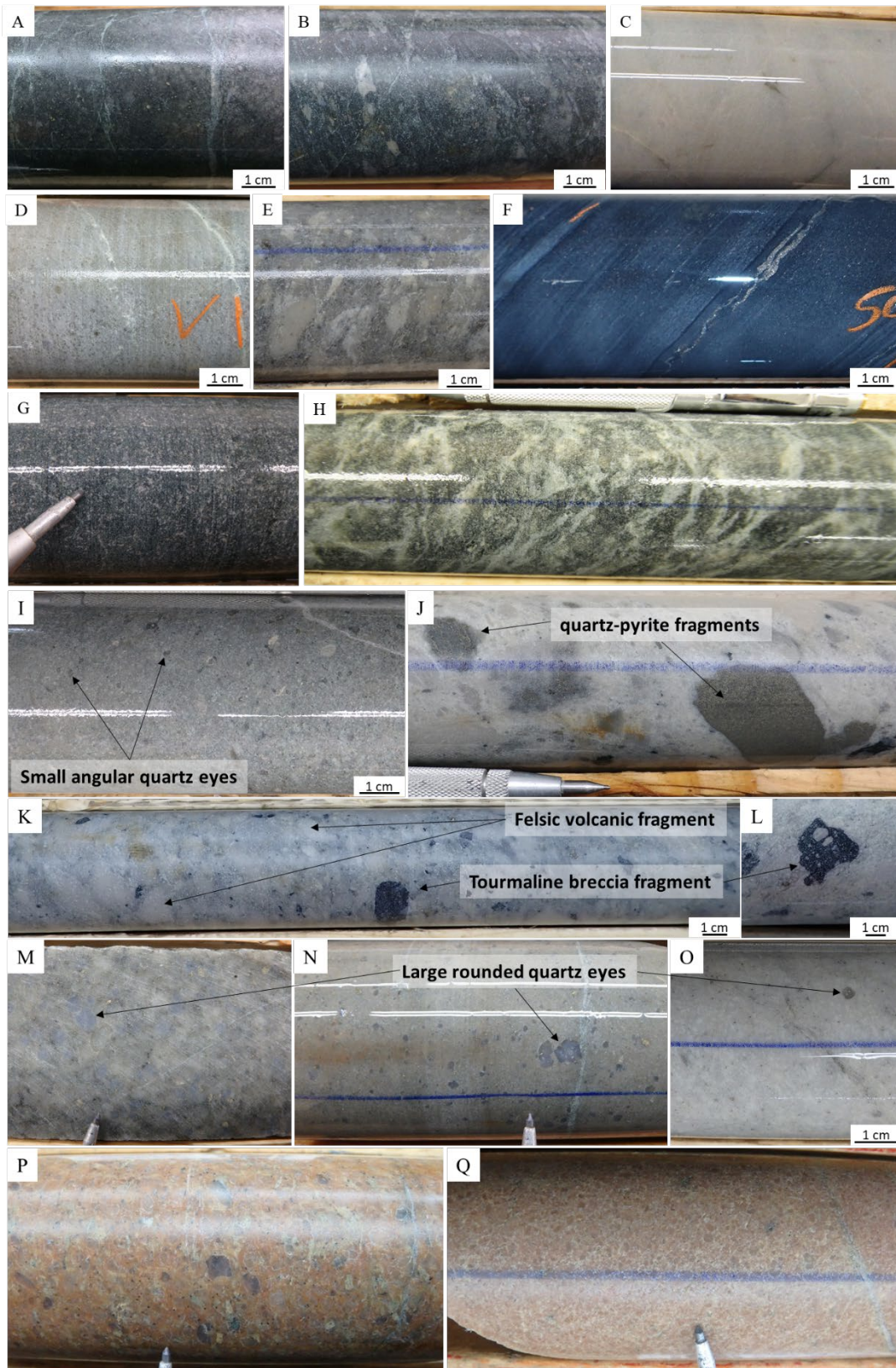


Figure 3.3: Representative images of rock types in the WGD seen in drill core. Volcanic rocks are shown in images A-H whereas intrusive rocks from the Windfall Intrusive Complex are

shown in images I-Q. A, B) Mafic- to intermediate volcanic rocks. Image A is a massive fine-grained green andesite whereas B a fragmental andesite with angular fragments of mafic and felsic rocks in a fine-grained green groundmass. C) Massive beige aphanitic rhyolite. D) Porphyritic rhyolite with a light grey aphanitic groundmass containing 20% anhedral quartz. E) Fragmental rhyolite with a fine-grained light grey groundmass containing angular fragments of felsic volcanic rocks. F) dark grey-green bedded argillite with pyrite-pyrrhotite laminations. G) Massive gabbro with a fine-grained medium green groundmass and a spotty chlorite alteration. H) Altered ultramafic with a fine-grained dark green groundmass crosscut and overprinted by carbonate veining and alteration. I) Pre-mineral porphyritic and fragmental QFP with small anhedral quartz eyes and volcanic fragments. J-L) Pre-mineral fragmental QFP with an aphanitic light-grey groundmass containing sub-rounded fragments of felsic volcanic, QFP intrusive, tourmaline breccia and pyritized material. M-O) Pre-mineral QFP with a light grey to beige aphanitic groundmass and 1-15% large (<1 cm) quartz phenocrysts. P) Post-mineral QFP with a fine-grained red-orange hematite-magnetite (Hmt-Mt) altered groundmass containing large (<1 cm) anhedral quartz phenocrysts (i.e., the Red Dog unit). Q) Post-mineral fine-grained felsic intrusion with red-orange hematite altered groundmass.



Figure 3.4: Representative images of the of pre- and of post-mineral vein types at WGD seen in drill core and underground workings. A, B) Blue quartz veins that define a sheeted-vein array, as seen in underground exposure and drill core. C) Colloform-textured carbonate-quartz veins in drill core. D) Equivalent vein as in C, but it is overprinted by quartz-carbonate-pyrite-tourmaline-gold. E, F) Drill core and underground images of post-mineral banded quartz-carbonate-tourmaline  $\pm$  pyrite vein. G) Ptygmatic folding of post-mineral tourmaline-pyrite veinlet. H) Post-mineral breccia vein containing clasts of fuchsite altered rock and colloform-textures carbonate-quartz vein material cemented in fine-grained pyrite tourmaline matrix. I) Post-mineral white quartz veins cutting a silica-pyrite-tourmaline (Sil-Py-Turm) alteration in felsic rock. J) Post-mineral quartz vein with late remobilized gold. K) Post-mineral dark grey quartz vein. L) Equivalent vein as in K, but here it is cut by late-fracture filling red sphalerite (Sph) and pyrite (Py).

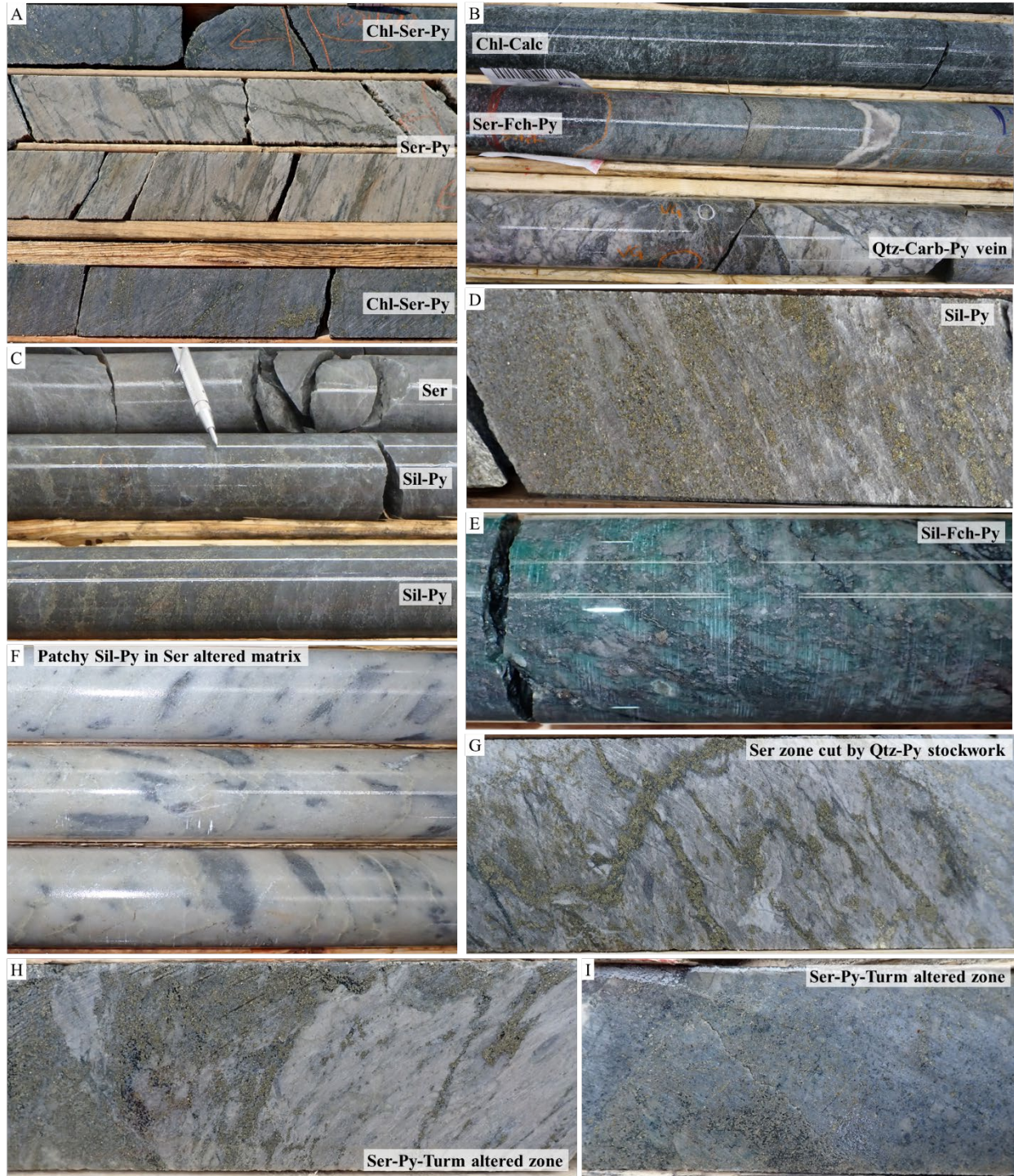


Figure 3.5: Representative images of replacement-type mineralization at WGD seen in drill core. A) Andesite with a zoned alteration from a distal chlorite (Chl)-sericite (Ser)-pyrite (Py) towards a core of intense sericite-pyrite crosscut by a quartz (Qtz)-pyrite stockwork (dark veins). B) Gabbro (Chl-Calc altered unit) crosscut by a grey quartz-pyrite-carbonate (Carb) vein with a selvage that is altered to sericite-pyrite-fuchsite (Fch). C, D) Strongly silicified rhyolite with disseminated pyrite. E) Pervasive silica-fuchsite-pyrite alteration developed in a gabbro. F)

Patchy silica-pyrite alteration cutting intense sericite altered rhyolite. G) Strong sericite alteration crosscut by quartz-pyrite stockwork. H-I) Pervasive sericite alteration with disseminated pyrite-tourmaline (Turm) overprinting felsic rocks.

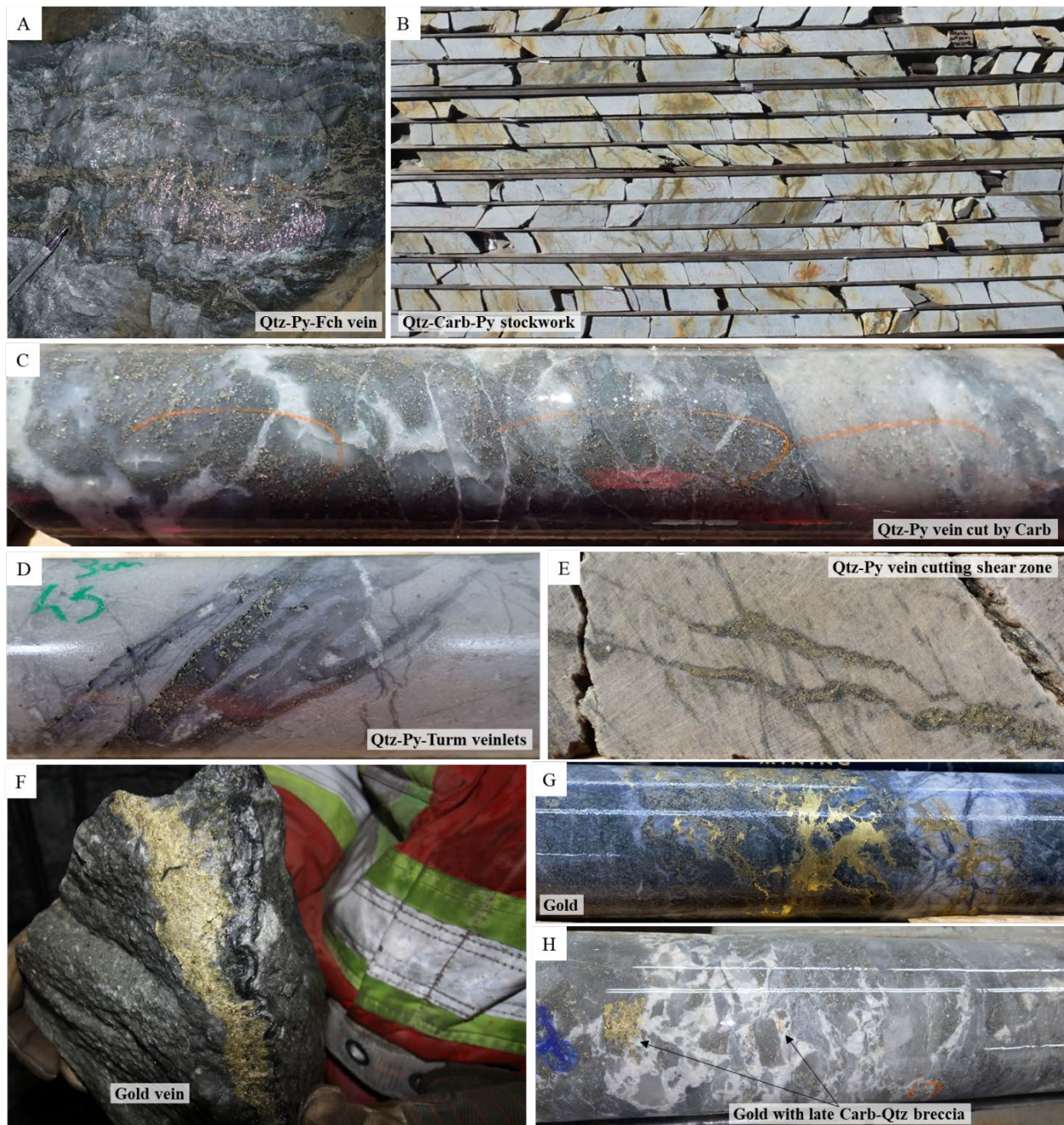


Figure 3.6: Representative images of syn-mineral veins at WGD seen in drill core and underground workings. A) Quartz (Qtz)-fuchsite (Fch)-pyrite (Py) vein in the area of the Lynx Main bulk sample. B) Quartz-carbonate (Carb)-pyrite stockwork cutting felsic volcanic rock. C) Quartz-pyrite vein crosscut by later carbonate. D) Fracture-filling quartz-pyrite-tourmaline veinlets cutting weakly deformed felsic volcanic. E) Quartz-pyrite veinlets cutting strongly-

deformed and sericite altered felsic volcanic. F) Boulder from the Lynx zone bulk sample (level 021) showing a quartz-carbonate-pyrite-tourmaline vein with massive gold. G) High-grade gold crosscutting grey quartz-pyrite-tourmaline veinlets and a colloform textured carbonate vein. H) Brecciated grey quartz-pyrite vein cemented by late cloudy white quartz-carbonate containing high-grade gold.

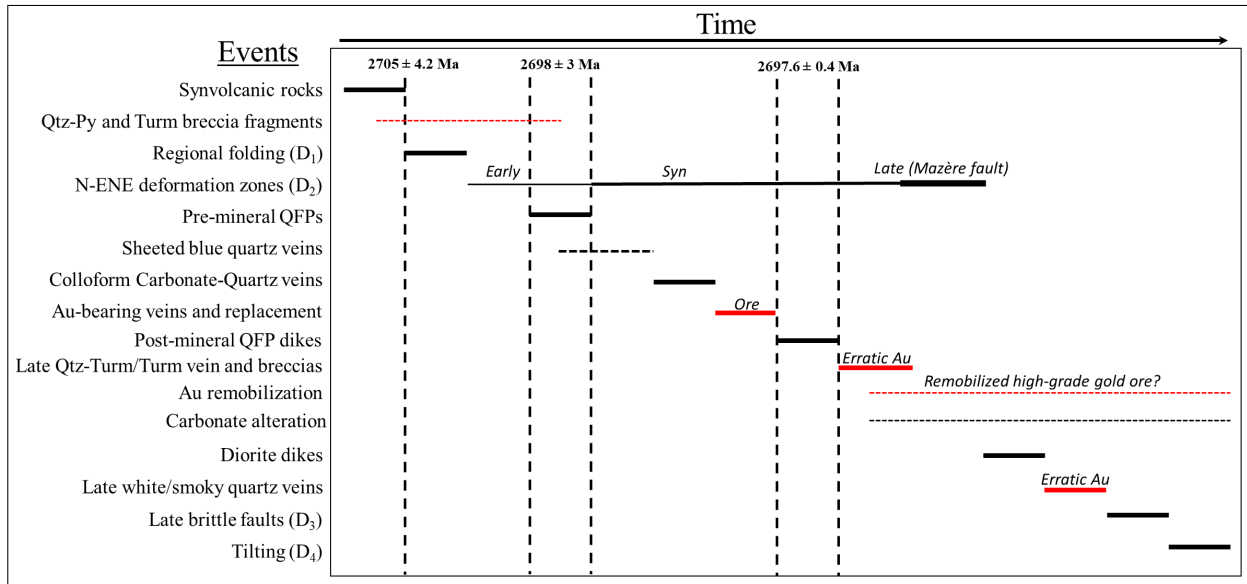


Figure 3.7: A simplified paragenesis summarising the sequence of events for the WGD.

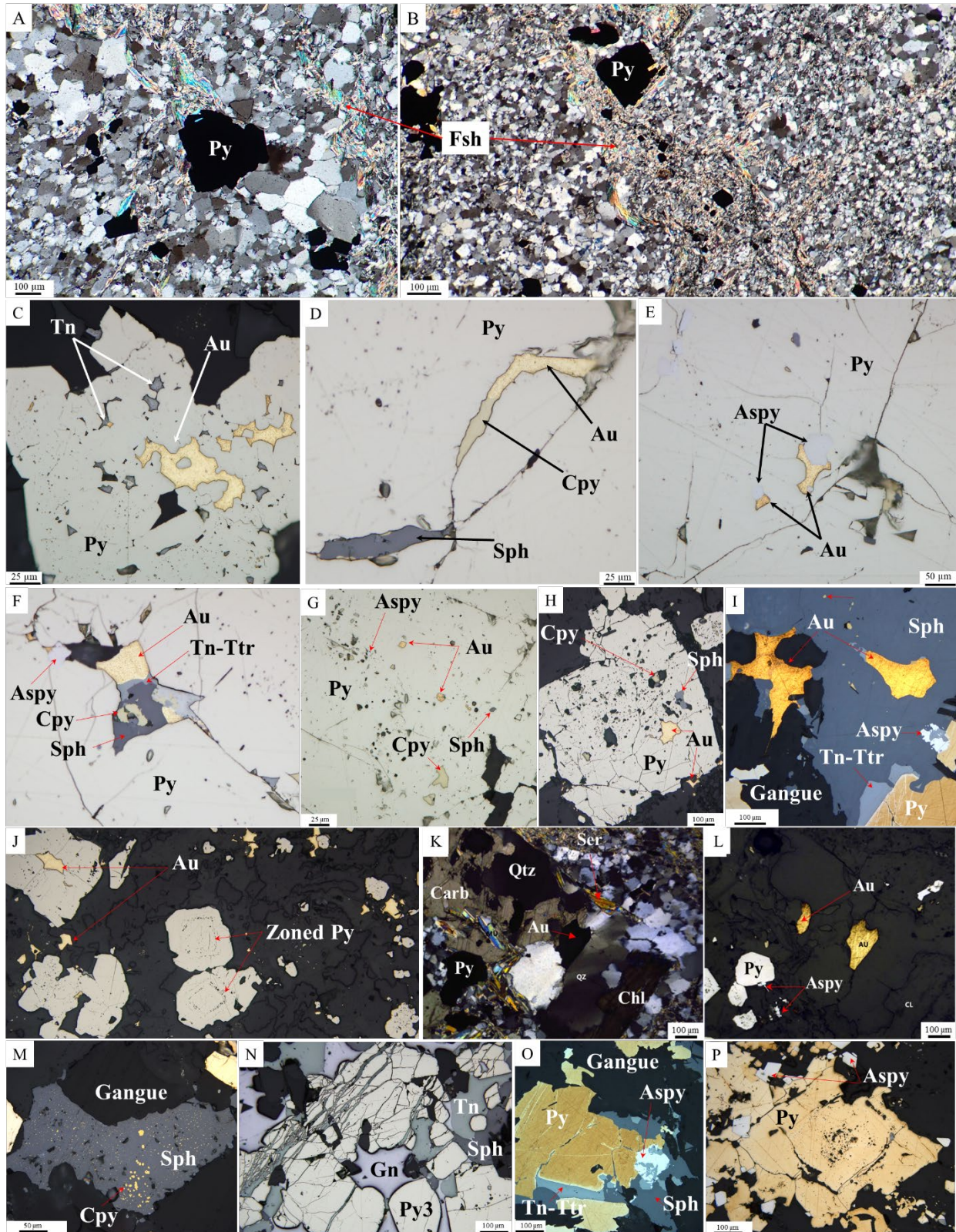


Figure 3.8: Representative transmitted (TL)- and reflected (RL)-light images, showing the ore mineralogy from syn-mineral veins in the WGD. A, B) Transmitted-light images showing the fine-grained texture of the quartz which has a granoblastic polygonal texture with 120° triple

junctions; also seen are small grains of pyrite and fuchsite. C-H) Variably pitted and fractured pyrite (Py) grains containing abundant inclusions of gangue, chalcopyrite (Cpy), sphalerite (Sph), tennantite (Tn), tetrahedrite (Ttr), arsenopyrite (Aspy), and gold (Au). I) Quartz vein with pyrite and later sphalerite, chalcopyrite, arsenopyrite, tennantite-tetrahedrite and gold. J) Zoned pyrites in a quartz-carbonate vein later cut by gold. K, L) Sericite-chlorite altered rhyolite cut by a quartz-carbonate-pyrite-arsenopyrite-gold vein in TL (K) and RL (L). M) Sphalerite with chalcopyrite disease in a vein of quartz-carbonate-pyrite-tourmaline-gold vein. N) Pyrite grains cut by fractures lined with sphalerite, tennantite, and galena (Gn). O) Quartz vein with pyrites and later sphalerite, chalcopyrite, arsenopyrite, tennantite-tetrahedrite and gold. P) Pyrite grains overgrown by euhedral arsenopyrite crystals. Note that photos A-H, J, N are taken from an internal petrographic report by É.C. Lavoie, and photos K and L are taken from internal petrographic report by L. Tremblay, both for Osisko Mining.

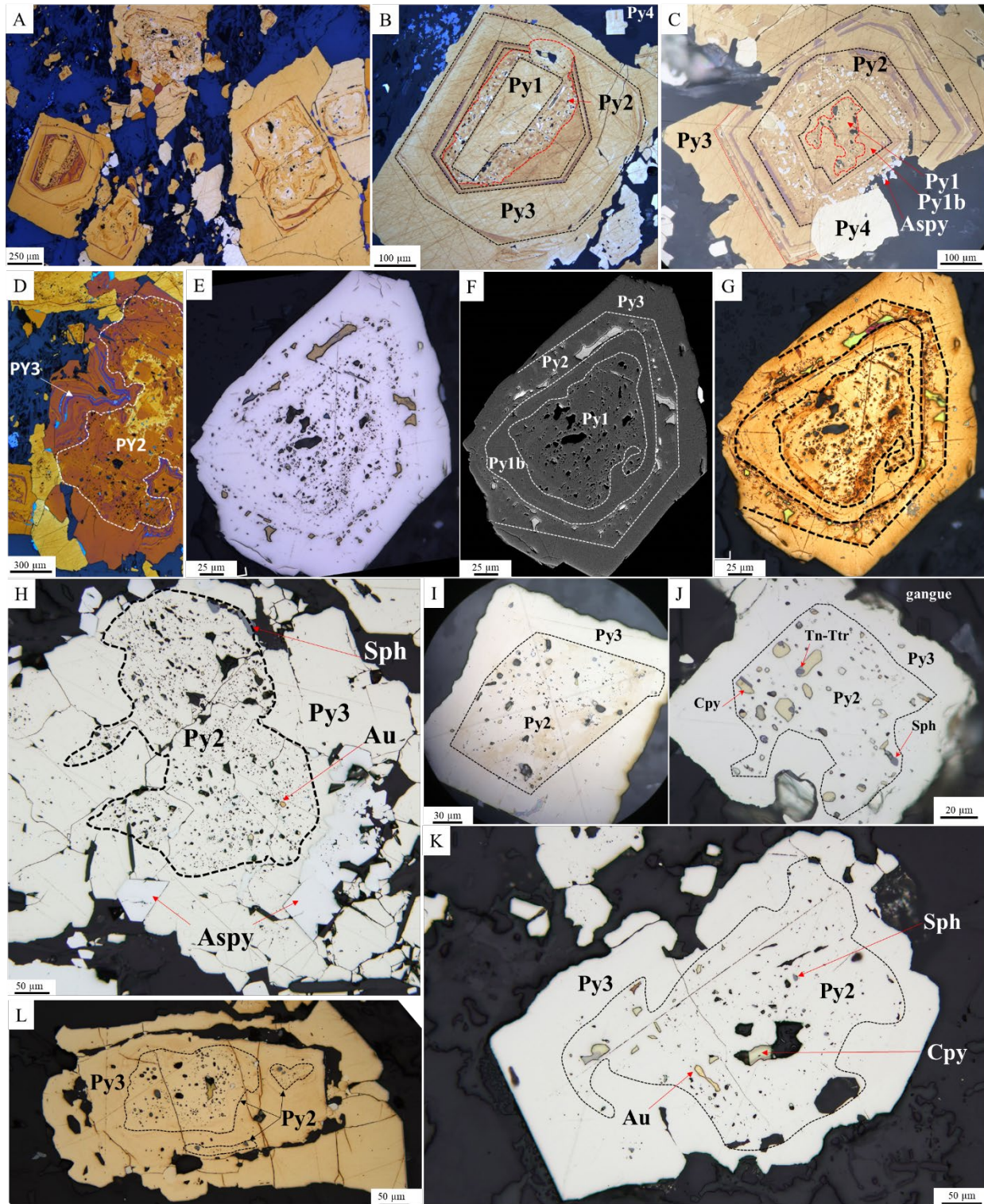


Figure 3.9: Representative reflected-light (RL) and back-scattered electron (BSE) images of different pyrite types at the WGD. Note that images with enhanced zoning (A, B, C, D, G, I) have been etched with NaOCl. A-D) RL images of zoned, pitted- and inclusion-rich pyrites (Py). Different generations of pyrite (Py1, Py2, Py3, Py4) are noted, as discussed in the text. E-G) A zoned pyrite as seen in RL (E), BSE image (F) and RL after etching with NaOCl (G). H-K) RL

images of zoned, pitted- and inclusion-rich Py2 and Py3. Mineral abbreviations: arsenopyrite (Aspy), gold (Au), sphalerite (Sph), chalcopyrite (Cpy), tennantite (Tn), tetrahedrite (Ttr). Note that photos H, J, and K are taken from internal petrographic report by E.C. Lavoie for Osisko Mining.

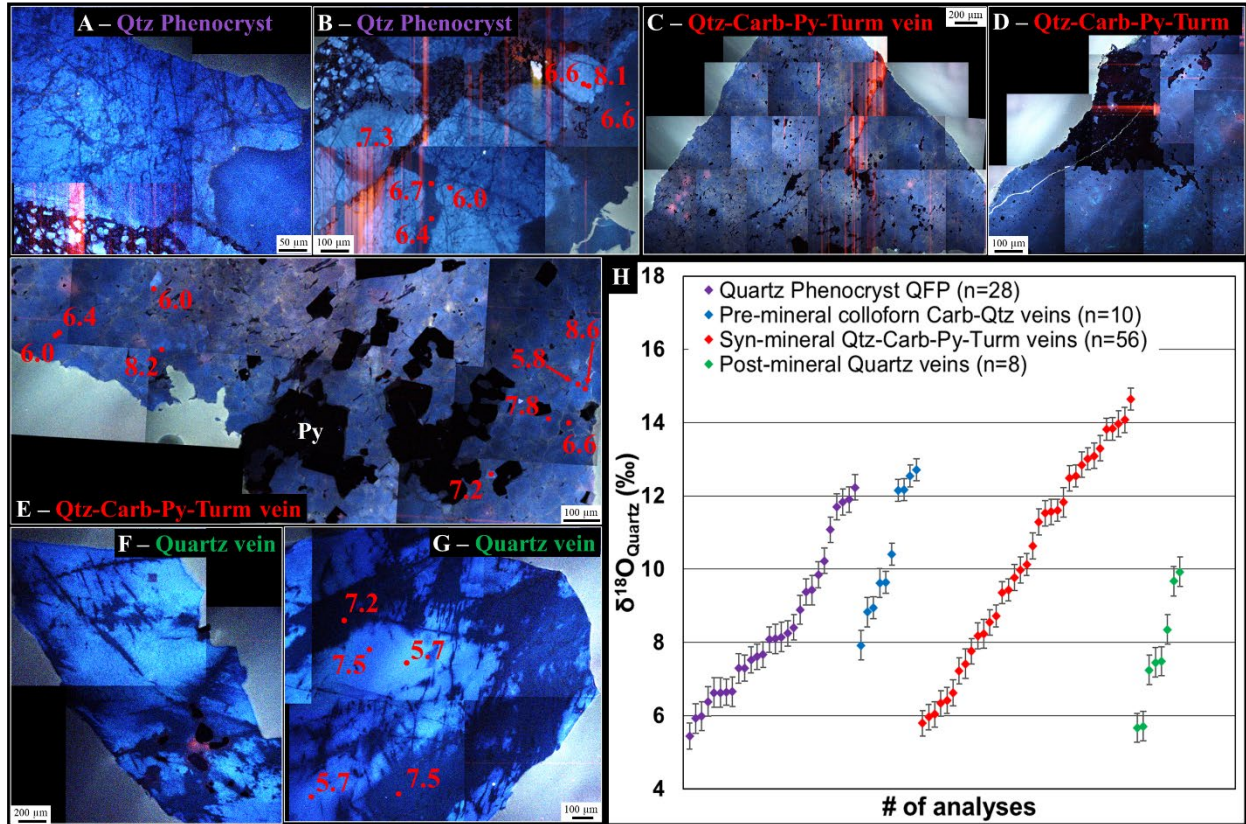


Figure 3.10: Stitched cathodoluminescence (CL) images of vein quartz with locations and values of in situ SIMS  $\delta^{18}\text{O}$ . A, B) Quartz phenocrysts from QFP intrusive rocks showing a primary bright CL signature that is overprinted by a fracture controlled dull CL signature. C-E) CL images of syn-mineral quartz-carbonate-pyrite-tourmaline veins. F, G) CL image of post-mineral quartz vein showing bright-CL areas that are overprinted by dull-CL areas. H) Histogram summarizing results from lowest to highest values for in situ SIMS  $\delta^{18}\text{O}$  quartz for different vein types.

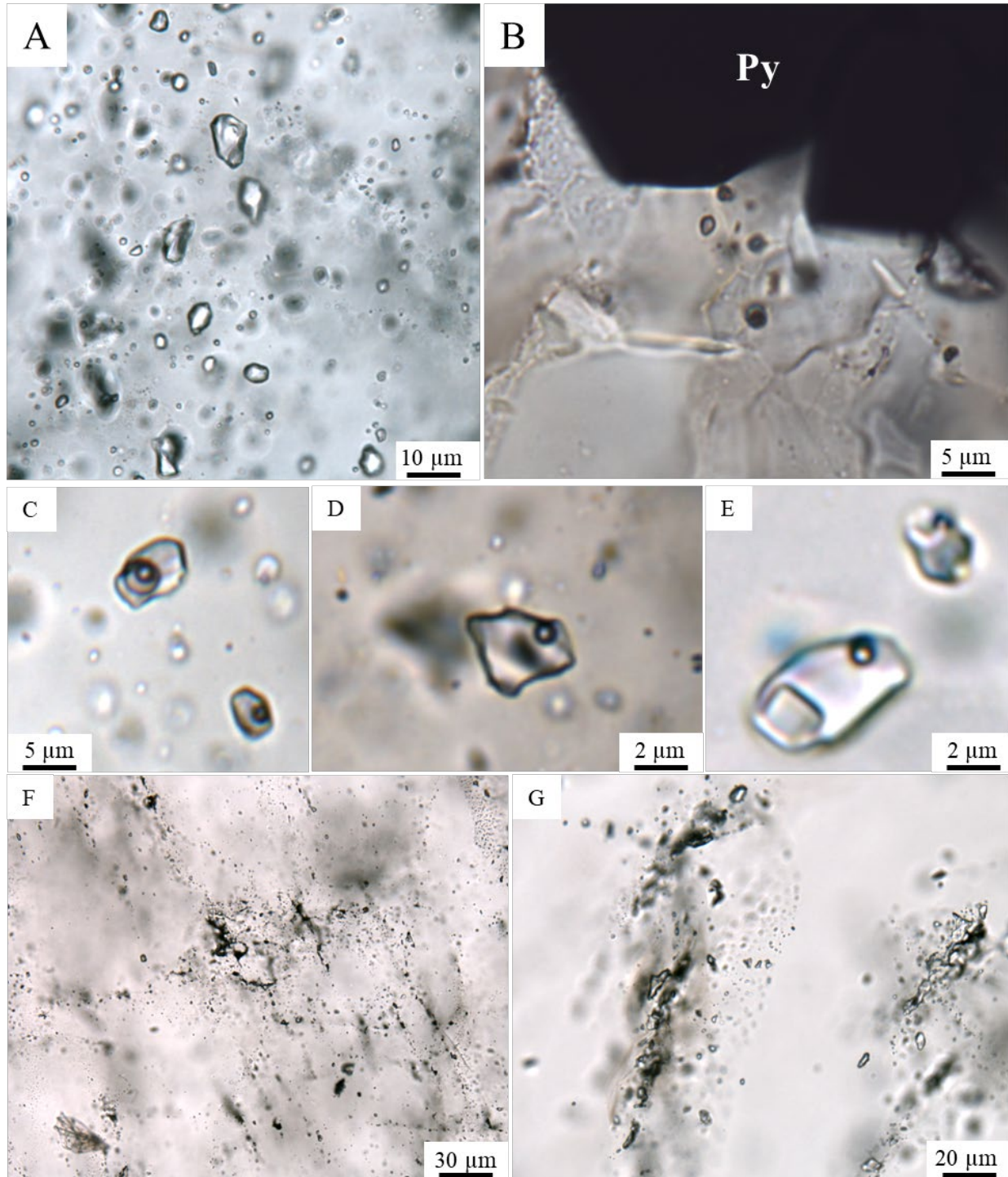


Figure 3.11: Representative images of fluid inclusion (FI) types and textures observed in quartz vein samples from the WGD. A) Type 1a monophasic  $\text{CO}_2$  (L) FIs hosted in post-mineral quartz vein. B) Type 1a monophasic  $\text{CO}_2$  (L) FIs hosted in quartz from syn-mineral quartz-carbonate-pyrite-tourmaline vein. Note the FIs are hosted in the pressure shadow of pyrite which is common for this FI-poor vein-type. C) Rare type 1b three-phase  $\text{H}_2\text{O}-\text{CO}_2$  (L)- $\text{CO}_2$  (V) FI hosted in a post-mineral quartz vein. D, E) Rare type 2 aqueous  $\text{H}_2\text{O}$  (L) –  $\text{H}_2\text{O}$  (V)  $\pm$  Halite FIs hosted

in quartz. Note the similar L:V ratios for the two FIs, thus similar densities. F) A FIA of type 1a FIs hosted in post-mineral quartz vein which show the commonly observed decrepitate textures indicative of post-entrapment modification. G) Close-up of a decrepitated type 1a FIs. Note the halo of around the irregular-shaped remnant of the original FIs.

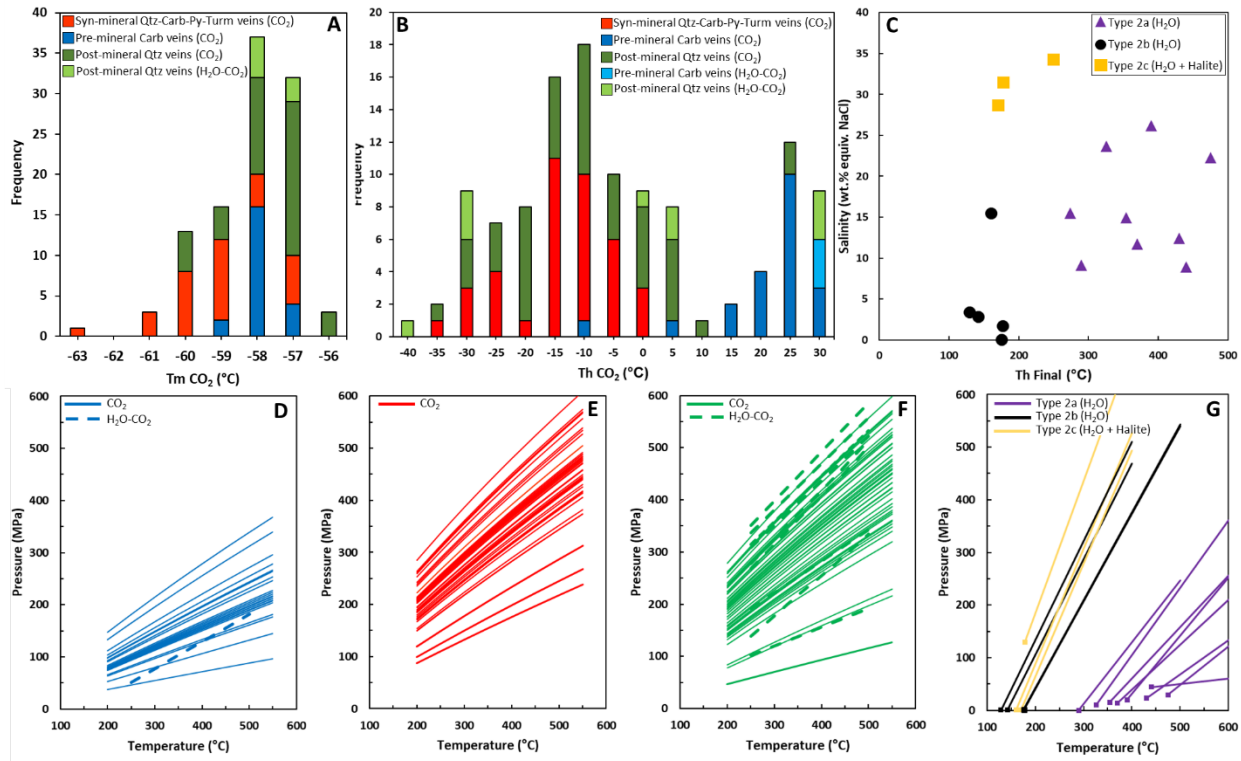


Figure 3.12: Summary of thermometric data (A-C) and corresponding isochore plots (D-F) for fluid inclusions from pre-, syn-, and post-mineral vein types – colloform-textured carbonate, quartz-carbonate-pyrite-tourmaline, and quartz. A) Histogram for  $T_m(\text{CO}_2)$ . B) Histogram for  $T_h(\text{CO}_2)$ . Note that in all cases the carbonic phase homogenized to the liquid phase. C) Plot of homogenization ( $T_h$ ) versus salinity for aqueous-type FIs in FIAs of three distinct populations: 1) low salinity and low  $T_h$ ; 2) high salinity and low  $T_h$ ; and 3) high salinity and high  $T_h$ . D) Isochores for Type 1a and 1b FIs hosted in early colloform-textured carbonate veins. E) Isochores for Type 1a  $\text{CO}_2$  FIs hosted in syn-mineral quartz-carbonate-pyrite-tourmaline veins. F) Isochores for Type 1a  $\text{CO}_2$  and 1b  $\text{CO}_2-\text{H}_2\text{O}$  FIs hosted in post-mineral quartz veins. G) Isochores for type 2 aqueous FIs hosted in various vein types.

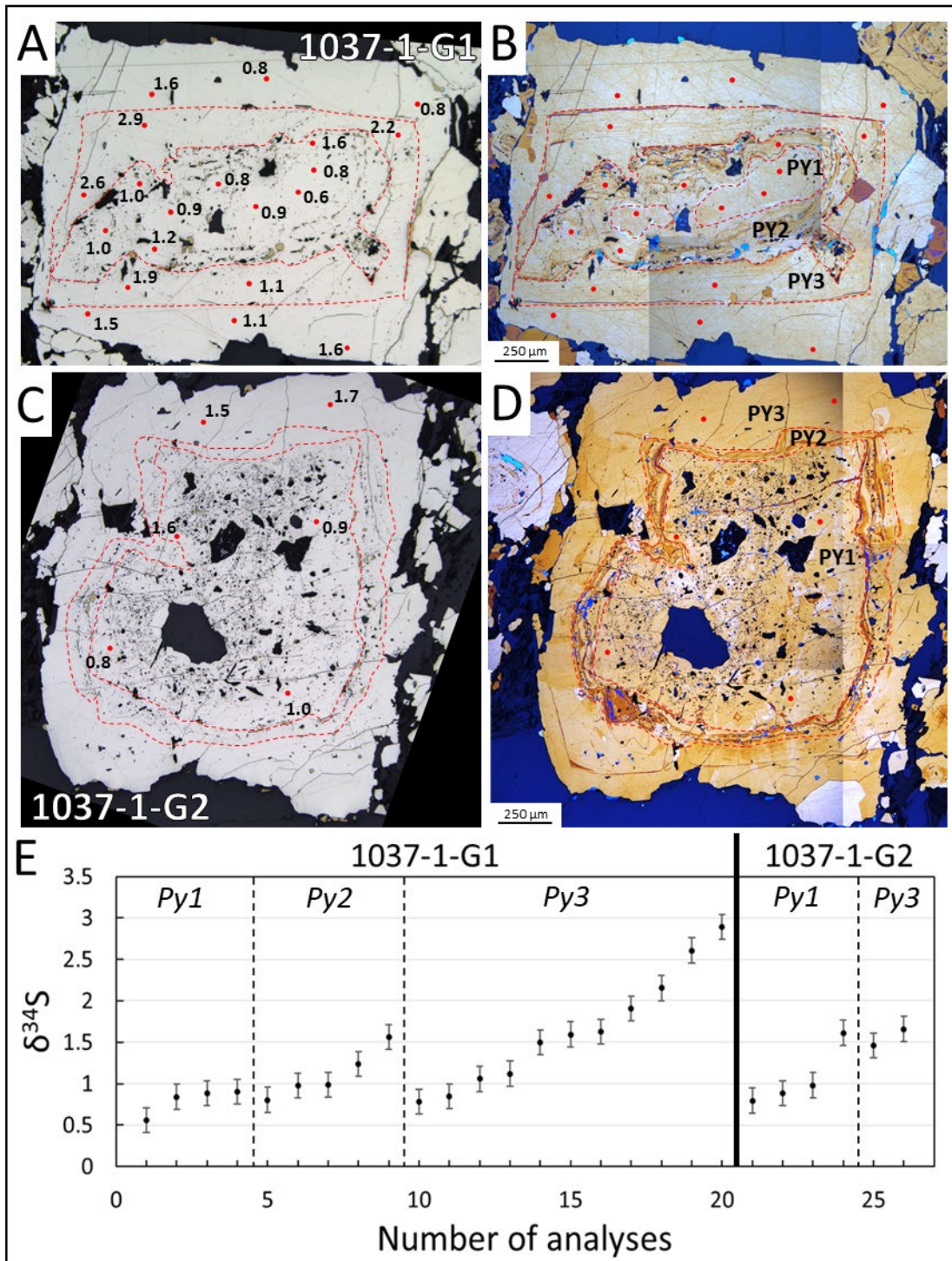


Figure 3.13: Reflected light images of etched (NaOCl) pyrite in polished thin sections from a syn-mineral quartz-carbonate-tourmaline-pyrite vein with the location of in situ SIMS  $\delta^{34}\text{S}$  analyses. Note locations of analyzed spots was done to test the signature of the inner porous core versus the outer non-porous rim. A, B) Images of polished (left) and etched (right) sample 1037-1-G1, C, D) Equivalent images for sample 1037-1-G2. E) Summary plot for the in situ SIMS  $\delta^{34}\text{S}$  analyses for each pyrite. The error bar on the graph is 0.3‰.

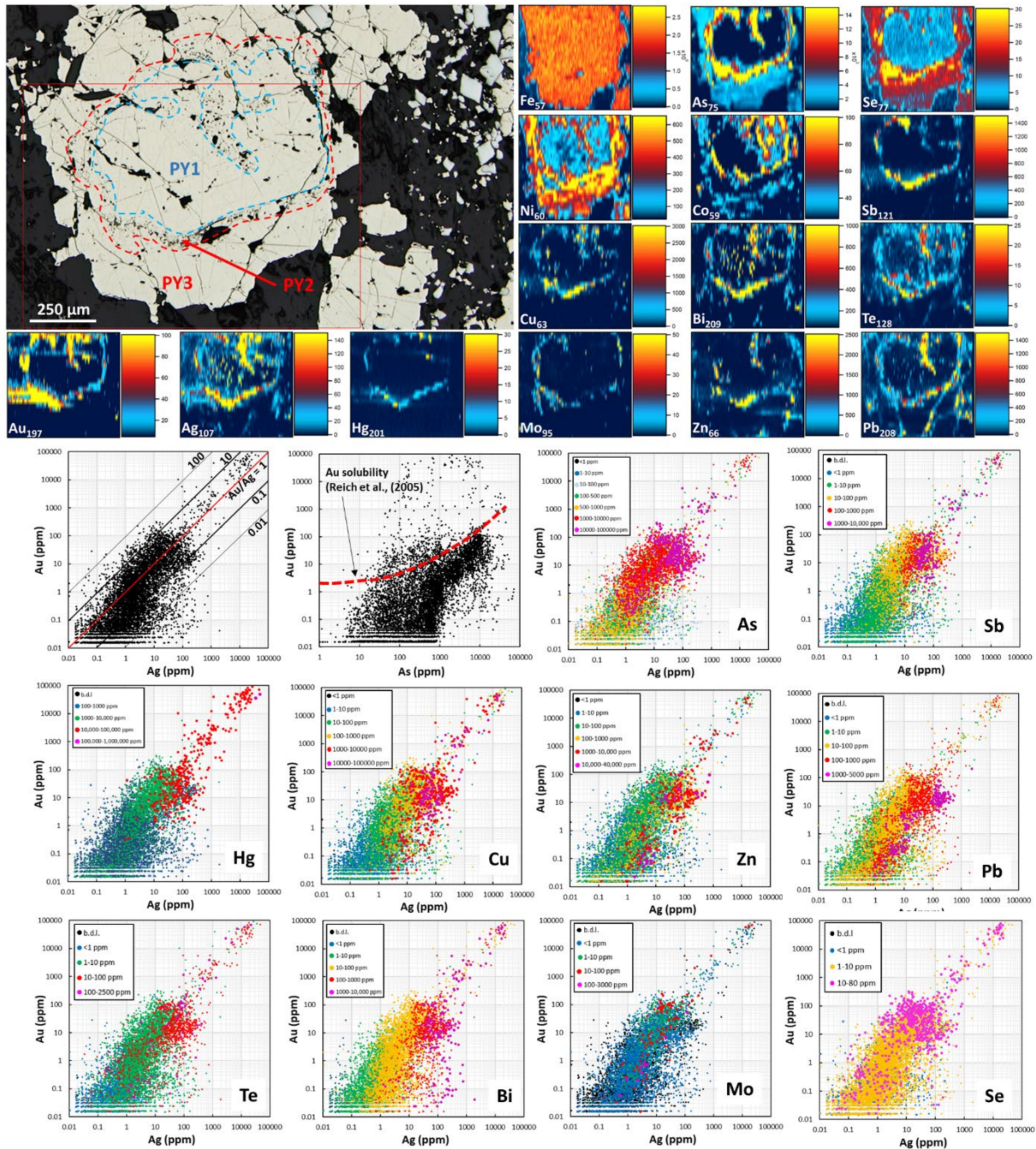


Figure 3.14: Reflected-light image of pyrite grain used for LA-ICP-MS elemental mapping, resultant elemental maps and binary element plots for Ag and As versus Au. Note that the latter plots for Ag versus Au are shown for a third element with its content (in ppm) colour coded from low to high with cold to hot colours, respectively (i.e., blue to red). Note the Au solubility line in the As versus Au plot from (Reich et al., 2005) separates the field for particulate gold (i.e., micron or submicron size as  $\text{Au}^0$ ) versus invisible Au ( $\text{Au}^+$ ).

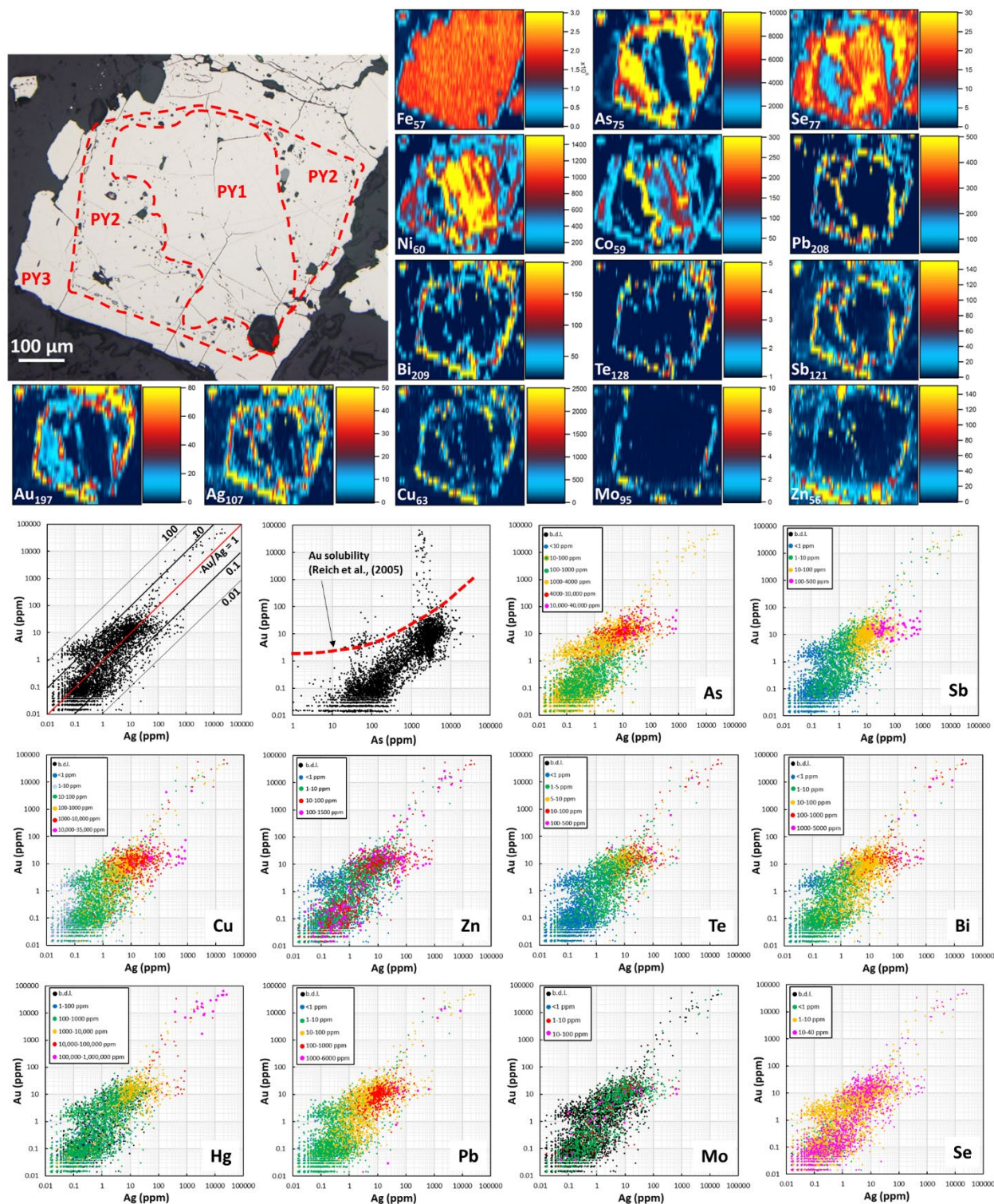


Figure 3.15: Reflected-light image of pyrite grain used for LA-ICP-MS element mapping, resultant elemental maps and binary element plots for Ag and As versus Au. Note that the latter plots for Ag versus Au are shown for a third element with its content (in ppm) colour coded from low to high with cold to hot colours, respectively (i.e., blue to red). Note the Au solubility line in

the As versus Au plot from (Reich et al., 2005) separates the field for particulate gold (i.e., micron or submicron size as  $\text{Au}^0$ ) versus invisible Au ( $\text{Au}^+$ ).

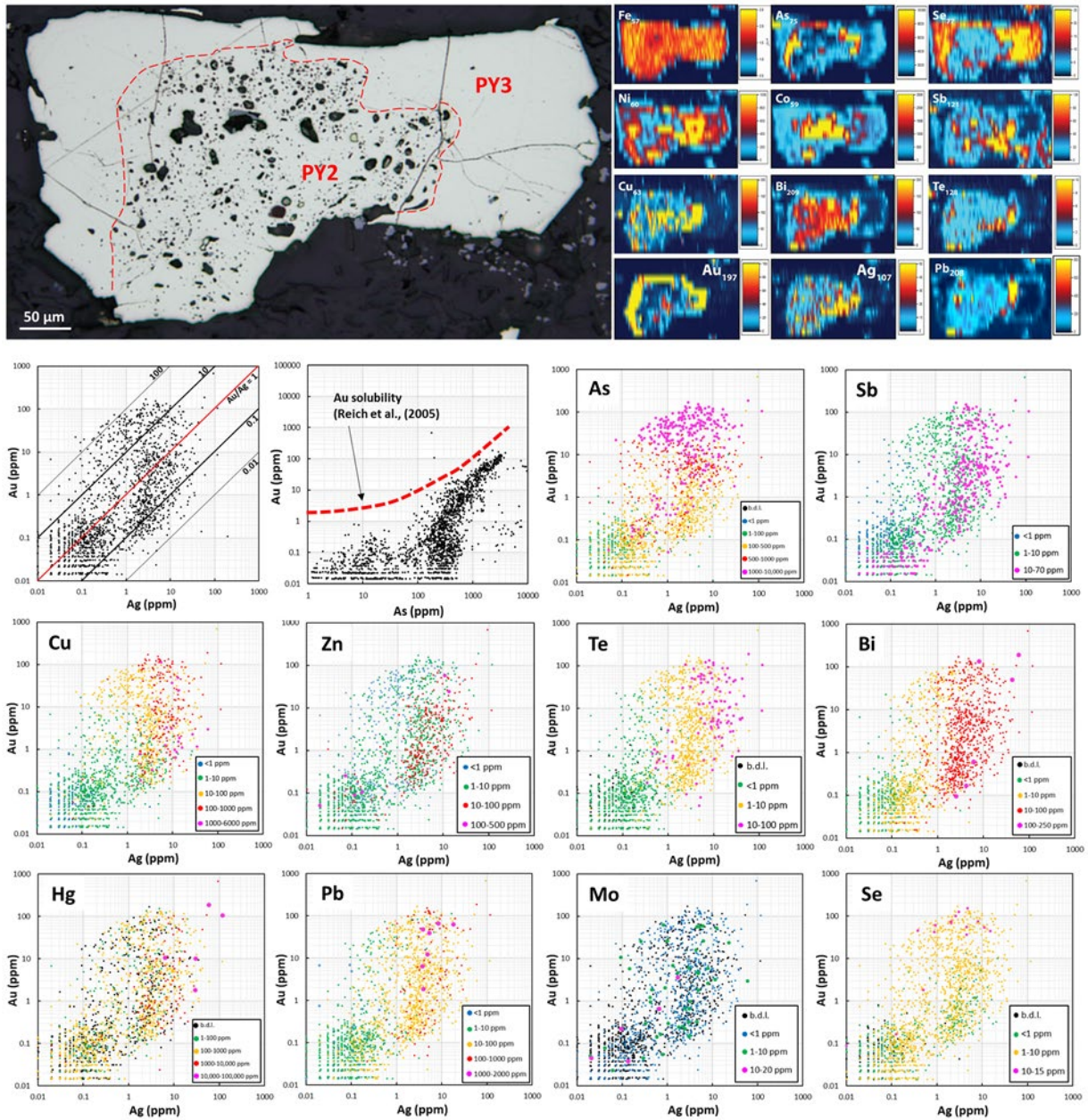


Figure 3.16: Reflected-light image of pyrite grain used for LA-ICP-MS element mapping, resultant elemental maps and binary element plots for Ag and As versus Au. Note that the latter plots for Ag versus Au are shown for a third element with its content (in ppm) colour coded from low to high with cold to hot colours, respectively (i.e., blue to red). Note the Au solubility line in the As versus Au plot from (Reich et al., 2005) separates the field for particulate gold (i.e., micron or submicron size as  $\text{Au}^0$ ) versus invisible Au ( $\text{Au}^+$ ).

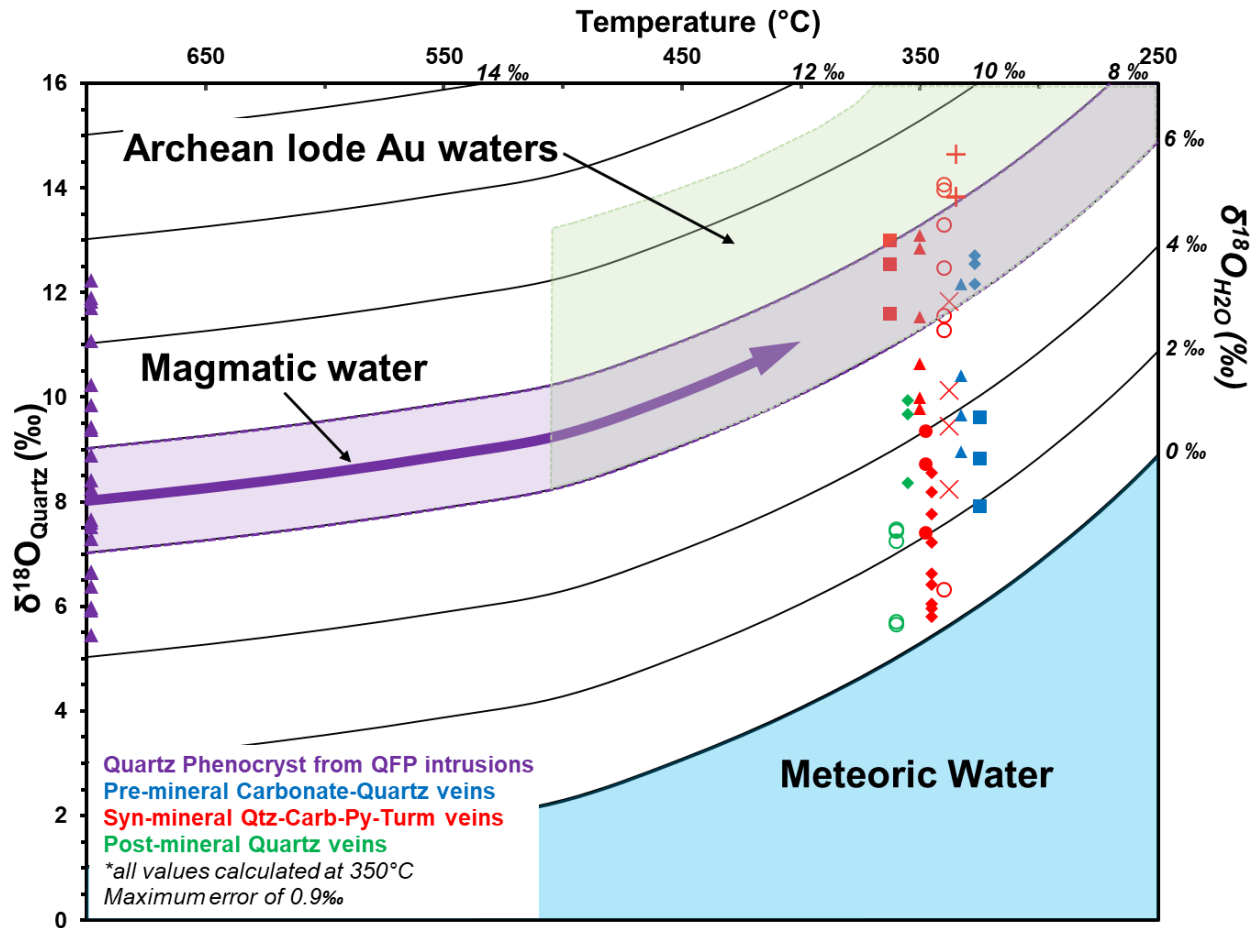


Figure 3.17: Plot of  $\delta^{18}\text{O}_{\text{quartz}}$  values versus temperature with isopleths of  $\delta^{18}\text{O}_{\text{H}_2\text{O}}$  calculated using the quartz-water fractionation equations from Matsuhisa et al. (1979). The  $\delta^{18}\text{O}_{\text{quartz}}$  data for different veins and vein types are represented by varying symbols and colors. Note that all vein quartz is interpreted to have formed at 350°C but are displaced relative to each other for convenience. Also, note that the  $\delta^{18}\text{O}_{\text{quartz}}$  values for phenocrysts are plotted on the y-axis and are used to estimate the primary signature of magmatic  $\text{H}_2\text{O}$ . The fields for  $\delta^{18}\text{O}_{\text{H}_2\text{O}}$  for magmatic water (discussed in text), the fields for meteoric water and Archean lode Au water are from Taylor (1974) and McCuaig and Kerrich (1998), respectively.

### 3.9 Tables

**Table 3.1 - Microthermometry data for type 1a fluid inclusions**

Sample ID	# FIs	Vein Generation	FI Type	P/S/PS/IND	FI Shape	Tm CO <sub>2</sub> (°C)	Th CO <sub>2</sub> (°C) Range	L-V curve	CO <sub>2</sub> Density (avg)	Δdensity
OBM-16-585	5	Carbonate	CO <sub>2</sub>	S	sub-angular	-58	4.5	Liquid	0.90	-
OBM-16-585	4	Carbonate	CO <sub>2</sub>	S	sub-angular	-58	22.0 to 26.0	Liquid	0.72	0.056
OBM-16-585	2	Carbonate	CO <sub>2</sub>	S	sub-angular	-58.6	22.3 to 26.0	Liquid	0.72	0.053
OBM-16-585	2	Carbonate	CO <sub>2</sub>	S	sub-angular	-58	22.0 to 24.3	Liquid	0.74	0.030
OBM-16-585	2	Carbonate	CO <sub>2</sub>	S	sub-angular	-58	23.5	Liquid	0.73	-
OBM-16-585	1	Carbonate	CO <sub>2</sub>	S	irregular	-58	27.5	Liquid	0.67	-
OBM-16-585	5	Carbonate	CO <sub>2</sub>	S	sub-angular	-58	7.0 to 16.0	Liquid	0.85	0.070
OBM-16-585	4	Carbonate	CO <sub>2</sub>	S	sub-angular	-58	27.0	Liquid	0.68	-
OBM-16-585	2	Carbonate	CO <sub>2</sub>	S	sub-rounded	-57.9	22.0	Liquid	0.75	-
OBM-16-585	5	Carbonate	CO <sub>2</sub>	S	sub-angular	-58	22.5	Liquid	0.74	-
NOT-07-150	2	Carbonate	CO <sub>2</sub>	S	angular	-59.4	16.0	Liquid	0.81	-
NOT-07-150	5	Carbonate	CO <sub>2</sub>	S	sub-angular	-59.5	18.9	Liquid	0.78	-
NOT-07-150	10	Carbonate	CO <sub>2</sub>	S	rounded	-58.2	18.0	Liquid	0.79	-
OSK-W-16-760	3	Carbonate	CO <sub>2</sub>	S	rounded	-58.5	21.5	Liquid	0.76	-
OSK-W-16-760	5	Carbonate	CO <sub>2</sub>	S	sub-rounded	-58	13.2 to 19.5	Liquid	0.81	0.058
OSK-W-16-760	5	Carbonate	CO <sub>2</sub>	S	sub-rounded	-58	20.9 to 26.1	Liquid	0.73	0.071
OSK-W-16-760	5	Carbonate	CO <sub>2</sub>	S	sub-rounded	-58	22.9	Liquid	0.74	-
OSK-W-17-792	5	Carbonate	CO <sub>2</sub>	S	irregular	-57.9	22.0 to 27.0	Liquid	0.71	0.074
OSK-W-17-792	2	Carbonate	CO <sub>2</sub>	S	sub-angular	-57.7	29.9	Liquid	0.60	-
OSK-W-17-792	1	Carbonate	CO <sub>2</sub>	S	sub-angular	-58.2	14.2	Liquid	0.83	-
OSK-W-17-792	2	Carbonate	CO <sub>2</sub>	S	rounded	-58.6	-18.5 to -5.8	Liquid	0.99	0.064
OSK-W-17-792	2	Carbonate	CO <sub>2</sub>	S	rounded	-57.8	31.1	Liquid	0.49	-
EAG-12-320	8	Post-Ore Quartz	CO <sub>2</sub>	S	sub-rounded	-57.9	-26 to 5.6	Liquid	0.98	0.167
EAG-12-320	6	Post-Ore Quartz	CO <sub>2</sub>	S	rounded	-57.5	-12.8 to -2.5	Liquid	0.97	0.055
EAG-12-320	3	Post-Ore Quartz	CO <sub>2</sub>	S	rounded	-57.3	-19.3 to -11.5	Liquid	1.01	0.038
BC-WF-001	4	Post-Ore Quartz	CO <sub>2</sub>	S	irregular	-57.7	-33 to -9.4	Liquid	1.03	0.109
BC-WF-001	5	Post-Ore Quartz	CO <sub>2</sub>	S	rounded	-57.4	11.6 to 25.4	Liquid	0.78	0.145
BC-WF-001	4	Post-Ore Quartz	CO <sub>2</sub>	S	rounded	-57.4	-29.2 to -7.7	Liquid	1.02	0.102
BC-WF-001	5	Post-Ore Quartz	CO <sub>2</sub>	S	sub-rounded	-57.5	-42.6 to -14.3	Liquid	1.07	0.122
NOT-07-150	10	Post-Ore Quartz	CO <sub>2</sub>	S	rounded	-58.5	-20.5 to -8.9	Liquid	1.01	0.057
NOT-07-150	10	Post-Ore Quartz	CO <sub>2</sub>	S	sub-rounded	-58.3	-40.0 to -30.0	Liquid	1.10	0.041
NOT-07-150	10	Post-Ore Quartz	CO <sub>2</sub>	S	sub-rounded	-58.5	-35 to -26.4	Liquid	1.08	0.036
NOT-07-150	5	Post-Ore Quartz	CO <sub>2</sub>	S	sub-rounded	-58.2	-28 to -21.7	Liquid	1.05	0.028
OSK-W-17-792	2	Post-Ore Quartz	CO <sub>2</sub>	S	sub-angular	-60.2	-26 to -16	Liquid	1.04	0.046
OSK-W-17-792	15	Post-Ore Quartz	CO <sub>2</sub>	S	rounded	-58.6	-13.3	Liquid	1.00	-
OSK-W-17-792	15	Post-Ore Quartz	CO <sub>2</sub>	S	rounded	-58.6	-31.1 to -16.0	Liquid	1.05	0.068
BC-WF-008	5	Post-Ore Quartz	CO <sub>2</sub>	S	rounded	-57.2	-23.2 to -5	Liquid	1.00	0.090
BC-WF-008	5	Post-Ore Quartz	CO <sub>2</sub>	S	sub-angular	-57.8	-11.2 to 2.8	Liquid	0.95	0.079
BC-WF-008	4	Post-Ore Quartz	CO <sub>2</sub>	S	sub-rounded	-57.8	-19.5 to -9.5	Liquid	1.00	0.049
BC-WF-008	5	Post-Ore Quartz	CO <sub>2</sub>	S	sub-rounded	-57.8	17.8 to 26	Liquid	0.75	0.101
BC-WF-008	7	Post-Ore Quartz	CO <sub>2</sub>	S	sub-rounded	-57.8	-2.4 to 7.0	Liquid	0.91	0.059
BC-WF-008	4	Post-Ore Quartz	CO <sub>2</sub>	S	rounded	-56.9	-2.4 to 4.5	Liquid	0.92	0.042
BC-WF-008	5	Post-Ore Quartz	CO <sub>2</sub>	S	sub-angular	-57.2	-35 to -19.0	Liquid	1.06	0.069
BC-WF-008	2	Post-Ore Quartz	CO <sub>2</sub>	S	irregular	-56.9	4.5	Liquid	0.90	-
BC-WF-008	3	Post-Ore Quartz	CO <sub>2</sub>	S	irregular	-56.9	28.8 to 32.7	Liquid	0.59	0.087
NOT-07-150	5	Post-Ore Quartz	CO <sub>2</sub>	S	sub-angular	-60.1	-15.5 to -9.7	Liquid	1.00	0.029
NOT-07-150	5	Post-Ore Quartz	CO <sub>2</sub>	S	sub-angular	-63	-12	Liquid	0.99	-
OSK-W-17-1315	15	Post-Ore Quartz	CO <sub>2</sub>	S	rounded	-59.8	-12	Liquid	0.99	-
OSK-W-17-1315	10	Post-Ore Quartz	CO <sub>2</sub>	S	sub-rounded	-59	-25 to -2	Liquid	1.00	0.115
OSK-W-17-1315	15	Post-Ore Quartz	CO <sub>2</sub>	S	sub-rounded	-60.2	-14 to 7	Liquid	0.94	0.121
OSK-W-17-1315	25	Post-Ore Quartz	CO <sub>2</sub>	S	rounded	-59.4	-14 to -4	Liquid	0.98	0.052
OSK-W-17-1315	5	Post-Ore Quartz	CO <sub>2</sub>	S	sub-rounded	-60.1	-8 to -3	Liquid	0.96	0.027

**Table 3.1 cont. - Microthermometry data for type 1a fluid inclusions**

Sample ID	# FIs	Vein Generation	FI Type	P/S/PS/IND	FI Shape	Tm CO <sub>2</sub> (°C)	Th CO <sub>2</sub> (°C)	Range	L-V curve	CO <sub>2</sub> Density (avg)	Δdensity
OSK-W-17-1315	3	Post-Ore Quartz	CO <sub>2</sub>	S	sub-rounded	-58.7	-16		Liquid	1.01	-
OSK-W-17-1315	10	Post-Ore Quartz	CO <sub>2</sub>	S	sub-rounded	-59	-20 to -17.5		Liquid	1.03	0.012
OSK-W-17-1315	9	Post-Ore Quartz	CO <sub>2</sub>	S	rounded	-58.7	-25 to -17		Liquid	1.04	0.037
OSK-W-17-1315	15	Post-Ore Quartz	CO <sub>2</sub>	S	rounded	-57.8	-4.2 to 1.6		Liquid	0.93	0.034
EAG-12-355	5	Post-Ore Quartz	CO <sub>2</sub>	S	sub-rounded	-57.9	-12.3 to 29.3		Liquid	0.81	0.375
EAG-12-355	5	Post-Ore Quartz	CO <sub>2</sub>	S	sub-angular	-57.7	-33.8 to -29.8		Liquid	1.08	0.017
EAG-12-355	3	Post-Ore Quartz	CO <sub>2</sub>	S	sub-angular	-57.7	-19.3 to -16.1		Liquid	1.02	0.015
EAG-12-355	7	Post-Ore Quartz	CO <sub>2</sub>	S	sub-angular	-57.8	-37 to 1.3		Liquid	1.01	0.185
EAG-12-355	7	Post-Ore Quartz	CO <sub>2</sub>	S	irregular	-58.6	-19.5 to -2.3		Liquid	0.99	0.088
EAG-12-355	10	Post-Ore Quartz	CO <sub>2</sub>	S	sub-angular	-58.9	-32 to -11.4		Liquid	1.04	0.094
EAG-12-355	5	Post-Ore Quartz	CO <sub>2</sub>	S	sub-angular	-58.8	-8.9		Liquid	0.98	-
EAG-12-355	5	Post-Ore Quartz	CO <sub>2</sub>	S	sub-angular	-58.5	-10.7 to 7.8		Liquid	0.93	0.110
EAG-12-355	10	Post-Ore Quartz	CO <sub>2</sub>	S	sub-rounded	-60.5	-40.8 to 10.5		Liquid	0.99	0.262
EAG-12-320	3	Syn-Ore Quartz	CO <sub>2</sub>	S	sub-rounded	-57.6	-0.8 to 3.0		Liquid	1.02	0.023
EAG-12-320	2	Syn-Ore Quartz	CO <sub>2</sub>	S	sub-rounded	-60	-5 to -3		Liquid	0.95	0.011
EAG-12-320	3	Syn-Ore Quartz	CO <sub>2</sub>	S	sub-rounded	-57.9	-10.2 to 1.2		Liquid	0.95	0.064
OBM-16-584	5	Syn-Ore Quartz	CO <sub>2</sub>	S	irregular	-57.5	-7.2 to 13.6		Liquid	0.90	0.135
OBM-16-584	10	Syn-Ore Quartz	CO <sub>2</sub>	S	rounded	-57.5	-30 to -8		Liquid	1.02	0.103
OBM-16-584	3	Syn-Ore Quartz	CO <sub>2</sub>	S	rounded	-58.3	15.8		Liquid	0.81	-
OBM-16-584	5	Syn-Ore Quartz	CO <sub>2</sub>	S	sub-angular	-59.2	-18 to -16		Liquid	1.02	0.010
OBM-16-584	4	Syn-Ore Quartz	CO <sub>2</sub>	S	sub-angular	-59.2	-34 to -25		Liquid	1.07	0.038
OBM-16-584	2	Syn-Ore Quartz	CO <sub>2</sub>	S	irregular	-57.8	18.2 to 22.1		Liquid	0.77	0.042
OBM-16-584	3	Syn-Ore Quartz	CO <sub>2</sub>	S	sub-rounded	-58.2	-4 to -0.5		Liquid	0.94	0.020
OBM-16-585	5	Syn-Ore Quartz	CO <sub>2</sub>	S	rounded	-60.2	-18.5		Liquid	1.02	0.000
OSK-W-16-760	5	Syn-Ore Quartz	CO <sub>2</sub>	S	irregular	-	-15 to -9		Liquid	0.99	0.030
OSK-W-16-760	3	Syn-Ore Quartz	CO <sub>2</sub>	S	irregular	-59.5	-17 to -12		Liquid	1.01	0.024
OSK-W-16-760	3	Syn-Ore Quartz	CO <sub>2</sub>	S	rounded	-61.1	-37		Liquid	1.10	-
OSK-W-16-760	10	Syn-Ore Quartz	CO <sub>2</sub>	S	sub-rounded	-60.3	-25 to -12		Liquid	1.02	0.061
OSK-W-16-760	5	Syn-Ore Quartz	CO <sub>2</sub>	S	rounded	-61.2	-26.8		Liquid	1.06	-
OSK-W-16-760	5	Syn-Ore Quartz	CO <sub>2</sub>	S	sub-rounded	-61.3	-38.9 to -25.8		Liquid	1.08	0.054
OSK-W-16-760	3	Syn-Ore Quartz	CO <sub>2</sub>	S	rounded	-60.2	-17.7		Liquid	1.02	-
OSK-W-16-760	2	Syn-Ore Quartz	CO <sub>2</sub>	S	rounded	-60.3	-12.5 to -5.9		Liquid	0.98	0.034
OSK-W-17-968	3	Syn-Ore Quartz	CO <sub>2</sub>	S	sub-rounded	-59.5	-18.5 to -6.5		Liquid	0.99	0.060
OSK-W-17-968	2	Syn-Ore Quartz	CO <sub>2</sub>	S	sub-rounded	-57.5	-12 to -4		Liquid	0.97	0.042
OSK-W-17-968	2	Syn-Ore Quartz	CO <sub>2</sub>	S	rounded	-59.8	-21.7		Liquid	1.04	-
OSK-W-17-968	5	Syn-Ore Quartz	CO <sub>2</sub>	S	rounded	-57.9	-23 to 5.0		Liquid	0.97	0.149
EAG-12-311B	2	Syn-Ore Quartz	CO <sub>2</sub>	S	sub-rounded	-60.5	-1		Liquid	0.93	-
EAG-12-311B	3	Syn-Ore Quartz	CO <sub>2</sub>	S	sub-rounded	-59.5	-31.5		Liquid	1.08	-
EAG-12-311B	3	Syn-Ore Quartz	CO <sub>2</sub>	S	sub-rounded	-59.5	10.0 to 20.0		Liquid	0.82	0.088
EAG-12-311B	3	Syn-Ore Quartz	CO <sub>2</sub>	S	sub-rounded	-59.5	-11.7		Liquid	0.99	-
EAG-12-311B	5	Syn-Ore Quartz	CO <sub>2</sub>	S	sub-rounded	-58.4	-26.2		Liquid	1.06	-
EAG-12-311B	5	Syn-Ore Quartz	CO <sub>2</sub>	S	sub-rounded	-	-23.1 to -10		Liquid	1.01	0.063
EAG-12-311B	2	Syn-Ore Quartz	CO <sub>2</sub>	S	sub-rounded	-	-19		Liquid	1.03	-
EAG-12-311B	4	Syn-Ore Quartz	CO <sub>2</sub>	S	sub-rounded	-	-13		Liquid	1.00	-
EAG-12-311B	5	Syn-Ore Quartz	CO <sub>2</sub>	S	sub-rounded	-	-1		Liquid	0.93	-
EAG-12-311B	5	Syn-Ore Quartz	CO <sub>2</sub>	S	sub-rounded	-	-16.5		Liquid	1.02	-
EAG-12-311B	5	Syn-Ore Quartz	CO <sub>2</sub>	S	sub-rounded	-	-31		Liquid	1.08	-
EAG-12-311B	2	Syn-Ore Quartz	CO <sub>2</sub>	S	sub-rounded	-	-25		Liquid	1.05	-
EAG-12-311B	3	Syn-Ore Quartz	CO <sub>2</sub>	S	sub-rounded	-	-17.5		Liquid	1.02	-
EAG-12-311B	5	Syn-Ore Quartz	CO <sub>2</sub>	S	sub-rounded	-60.4	-19.7		Liquid	1.03	-
EAG-12-311B	10	Syn-Ore Quartz	CO <sub>2</sub>	S	sub-rounded	-59.5	-7.5		Liquid	0.97	-
EAG-12-311B	5	Syn-Ore Quartz	CO <sub>2</sub>	S	sub-rounded	-59.8	-17.5 to -11.0		Liquid	1.00	0.032
NOT-07-150	3	Syn-Ore Quartz	CO <sub>2</sub>	S	sub-rounded	-58.5	-10 to -6.1		Liquid	0.97	0.021
NOT-07-150	4	Syn-Ore Quartz	CO <sub>2</sub>	S	sub-rounded	-60.3	-19		Liquid	1.03	-

**Table 3.2 - Microthermometry data for type 1b fluid inclusions**

Sample ID	# FIs	Vein Generation	FI Type	P/S/PS/IND	H <sub>2</sub> O:CO <sub>2</sub>	FI Shape	Tm CO <sub>2</sub> (°C)	Tmelt clath	Th CO <sub>2</sub> (°C)	Th CO <sub>2</sub> L-V Curve	Th final (°C)	L-V Curve	Δdensity
1125-2b	3	Carbonate	H <sub>2</sub> O-CO <sub>2</sub>	S	40:60	sub-angular			31.1	L	265	Liquid	
1125-2b	3	Carbonate	H <sub>2</sub> O-CO <sub>2</sub>	S	40:60	sub-angular			31.1	L	280-309	Liquid	
1125-2b	3	Carbonate	H <sub>2</sub> O-CO <sub>2</sub>	S	80:20	sub-angular			31.1	L	350	Liquid	
EAG-12-320	2	Post-Ore Quartz	H <sub>2</sub> O-CO <sub>2</sub>	S	20:80	irregular	-57		13.1 to 29.3	L	> 320	Liquid	0.73
BC-WF-001	3	Post-Ore Quartz	H <sub>2</sub> O-CO <sub>2</sub>	S	50:50	rounded	-58.4	9.8	-4.8 to 5.0	L	> 250	Liquid	0.93
BC-WF-008	2	Post-Ore Quartz	H <sub>2</sub> O-CO <sub>2</sub>	S	50:50	sub-rounded	-57		26.4 to 32.4	L	> 364	Liquid	
OSK-W-17-1315	3	Post-Ore Quartz	H <sub>2</sub> O-CO <sub>2</sub>	S	50:50	rounded	-57.8		3.1	L	320	Vapor	0.91

**Table 3.3 - Microthermometry data for type 2 fluids inclusions**

Sample ID	# FIs	Vein Generation	FI Type	P/S/PS/IND	L:V	FI Shape	Tfm (1st melting)	Tm <sub>0H</sub>	Tmlce	Tmelt H	Th <sub>0H</sub> (range)	ThTot (avg.)	Salinity
OSK-W-17-792	3	Carbonate	H <sub>2</sub> O	S	95:5	irregular			-2		129b	129	3.4
EAG-12-320	10	Post-Ore Quartz	H <sub>2</sub> O	S	60:40	irregular	-10		-5.8		428d, 453d	441	9.0
EAG-12-320	5	Post-Ore Quartz	H <sub>2</sub> O	S	70:30	sub-rounded			-8		340-400d	370	11.7
EAG-12-320	4	Post-Ore Quartz	H <sub>2</sub> O	S	20:80	rounded			-8.6		430d	430	12.4
EAG-12-320	5	Post-Ore Quartz	H <sub>2</sub> O	S	80:20	irregular	-52	-31	-11		302b, 311b, 336b, 467b	354	15.0
EAG-12-320	4	Post-Ore Quartz	H <sub>2</sub> O	S	20:80	irregular	-52	-29	-22		>475d	475	22.3
OSK-W-17-792	3	Post-Ore Quartz	H <sub>2</sub> O	S	90:10	irregular			-0.2		142b, 175b, 209b	175	0.0
OSK-W-17-1315	5	Post-Ore Quartz	H <sub>2</sub> O	S	95:5	irregular	-46	-36	-21.7	124	170b	170	21.7
EAG-12-320	2	Post-Ore Quartz	H <sub>2</sub> O	S	90:10	irregular	-52	-23	-5.7		273b, 307b	290	9.1
OBM-16-584	2	Syn-Ore Quartz	H <sub>2</sub> O	S	90:10	irregular			-1.7		114b, 170b	142	2.9
OBM-16-584	4	Syn-Ore Quartz	H <sub>2</sub> O	S	95:5	irregular	-56	-28	-11.7		135b, 158b, 188b,	160	27.0
OBM-16-584	2	Syn-Ore Quartz	H <sub>2</sub> O	S	95:5	irregular	-56	-28		178	115b	178	32.0
OBM-16-585	5	Syn-Ore Quartz	H <sub>2</sub> O	S	90:10	irregular					161b-188b	175	
OBM-16-585	5	Syn-Ore Quartz	H <sub>2</sub> O	S	95:5	rounded			-1		150b, 180b, 200b	177	1.7
OSK-W-17-968	10	Syn-Ore Quartz	H <sub>2</sub> O	S	95:5	sub-rounded				230-250	69-95	240	
EAG-12-311B	2	Syn-Ore Quartz	H <sub>2</sub> O	S	70:30	sub-rounded			-26		390b	390	26.2
NOT-07-150	7	Syn-Ore Quartz	H <sub>2</sub> O	S	85:15	sub-angular	-52	-31	-25		326d, >425b	326	23.7
OBM-16-585	1	Carbonate	H <sub>2</sub> O	S	80:20	irregular					242b	242	
OBM-16-585	3	Carbonate	H <sub>2</sub> O	S	90:10	angular					225b	225	
NOT-07-150	3	Carbonate	H <sub>2</sub> O	S	80:20	irregular					361b	361	
EAG-12-355	5	Carbonate	H <sub>2</sub> O	S	90:10	irregular					447b, >460b	447	

**Table 3.4 - <sup>18</sup>O isotope data for quartz**

Sample ID	Material	$\delta^{18}\text{O}_{\text{Quartz}}$ (‰)	1s (‰)	Reproducibility (‰)	T (°C)	$\delta^{18}\text{O}_{\text{H}_2\text{O}}$ (‰)
EAG-13-466	Carbonate vein	12.5	1.2	0.6	350	7.3
EAG-13-466	Carbonate vein	12.2	1.2	0.6	350	6.9
EAG-13-466	Carbonate vein	12.7	1.2	0.6	350	7.4
OBM-15-564	Carbonate vein	10.4	1.2	0.6	350	5.1
OBM-15-564	Carbonate vein	12.2	1.2	0.6	350	6.9
OBM-15-564	Carbonate vein	9.0	1.2	0.6	350	3.7
OBM-15-564	Carbonate vein	9.7	1.2	0.6	350	4.4
OSK-W-17-792	Carbonate vein	7.9	1.2	0.8	350	2.6
OSK-W-17-792	Carbonate vein	8.8	1.2	0.8	350	3.5
OSK-W-17-792	Carbonate vein	9.6	1.2	0.8	350	4.3
OSK-W-16-760	Syn-ore quartz	13.0	1.2	0.6	350	7.7
OSK-W-16-760	Syn-ore quartz	11.6	1.2	0.6	350	6.3
OSK-W-16-760	Syn-ore quartz	12.5	1.2	0.6	350	7.3
OSK-W-18-1546	Syn-ore quartz	13.8	1.2	0.6	350	8.5
OSK-W-18-1546	Syn-ore quartz	13.8	1.2	0.6	350	8.5
OSK-W-18-1546	Syn-ore quartz	14.6	1.2	0.6	350	9.4
OSK-W-17-1145	Syn-ore quartz	9.4	1.2	0.6	350	4.2
OSK-W-17-1145	Syn-ore quartz	10.1	1.2	0.6	350	4.8
OSK-W-17-1145	Syn-ore quartz	11.8	1.2	0.8	350	6.5
OSK-W-17-1145	Syn-ore quartz	8.2	1.2	0.8	350	2.9
OSK-W-17-789	Syn-ore quartz	9.4	1.2	0.6	350	4.1
OSK-W-17-789	Syn-ore quartz	8.7	1.2	0.6	350	3.4
OSK-W-17-789	Syn-ore quartz	7.4	1.2	0.8	350	2.1
EAG-11-311-EXT	Syn-ore quartz	6.0	1.2	0.7	350	0.7
EAG-11-311-EXT	Syn-ore quartz	6.4	1.2	0.7	350	1.1
EAG-11-311-EXT	Syn-ore quartz	6.0	1.2	0.7	350	0.7
EAG-11-311-EXT	Syn-ore quartz	8.2	1.2	0.7	350	2.9
EAG-11-311-EXT	Syn-ore quartz	5.8	1.2	0.7	350	0.5
EAG-11-311-EXT	Syn-ore quartz	8.6	1.2	0.7	350	3.3
EAG-11-311-EXT	Syn-ore quartz	7.8	1.2	0.7	350	2.5
EAG-11-311-EXT	Syn-ore quartz	6.6	1.2	0.7	350	1.3
EAG-11-311-EXT	Syn-ore quartz	7.2	1.2	0.7	350	1.9
OSK-W-17-968	Syn-ore quartz	14.0	1.2	0.7	350	8.7
OSK-W-17-968	Syn-ore quartz	12.5	1.2	0.7	350	7.2
OSK-W-17-968	Syn-ore quartz	13.3	1.2	0.7	350	8.0
OSK-W-17-968	Syn-ore quartz	14.1	1.2	0.7	350	8.8
OSK-W-17-968	Syn-ore quartz	11.6	1.2	0.7	350	6.3
OSK-W-17-968	Syn-ore quartz	11.3	1.2	0.7	350	6.0

**Table 3.4 cont. - <sup>18</sup>O isotope data for quartz**

Sample ID	Material	$\delta^{18}\text{O}_{\text{Quartz}}$ (‰)	1s (‰)	Reproducibility (‰)	T (°C)	$\delta^{18}\text{O}_{\text{H}_2\text{O}}$ (‰)
OSK-W-17-968	Syn-ore quartz	6.3	1.2	0.7	350	1.0
OSK-W-17-792	Syn-ore quartz	9.8	1.2	1.2	350	4.5
OSK-W-17-792	Syn-ore quartz	12.9	1.2	1.2	350	7.6
OSK-W-17-792	Syn-ore quartz	10.0	1.2	1.2	350	4.7
OSK-W-17-792	Syn-ore quartz	13.1	1.2	1.2	350	7.8
OSK-W-17-792	Syn-ore quartz	10.6	1.2	1.2	350	5.3
OSK-W-17-792	Syn-ore quartz	11.5	1.2	1.2	350	6.2
EAG-12-320c	Post-ore quartz	9.7	1.2	0.8	350	4.4
EAG-12-320c	Post-ore quartz	8.4	1.2	0.8	350	3.1
EAG-12-320c	Post-ore quartz	9.9	1.2	0.8	350	4.6
OSK-W-17-1316	Post-ore quartz	7.2	1.2	0.8	350	2.0
OSK-W-17-1316	Post-ore quartz	7.5	1.2	0.8	350	2.2
OSK-W-17-1316	Post-ore quartz	5.7	1.2	0.8	350	0.4
OSK-W-17-1316	Post-ore quartz	7.5	1.2	0.8	350	2.2
OSK-W-17-1316	Post-ore quartz	5.7	1.2	0.8	350	0.4
EAG-12-320	Qtz. Eyes, lg. eye QFP	6.6	1.2	0.8		
EAG-12-320	Qtz. Eyes, lg. eye QFP	6.6	1.2	0.8		
EAG-12-320	Qtz. Eyes, lg. eye QFP	8.1	1.2	0.8		
EAG-12-320	Qtz. Eyes, lg. eye QFP	6.7	1.2	0.8		
EAG-12-320	Qtz. Eyes, lg. eye QFP	6.4	1.2	0.8		
EAG-12-320	Qtz. Eyes, lg. eye QFP	6.0	1.2	0.8		
EAG-12-320	Qtz. Eyes, lg. eye QFP	7.3	1.2	0.8		
EAG-12-320b	Qtz. Eyes, lg. eye QFP	8.9	1.2	0.8		
EAG-12-320b	Qtz. Eyes, lg. eye QFP	5.9	1.2	0.8		
EAG-12-320b	Qtz. Eyes, lg. eye QFP	9.4	1.2	0.8		
EAG-12-320b	Qtz. Eyes, lg. eye QFP	8.1	1.2	0.8		
1048500	Qtz. Eyes, lg. eye QFP	11.1	1.2	0.7		
1048500	Qtz. Eyes, lg. eye QFP	7.5	1.2	0.7		
1090462	Qtz. Eyes, lg. eye QFP	9.4	1.2	0.7		
1090462	Qtz. Eyes, lg. eye QFP	11.7	1.2	0.7		
1090462	Qtz. Eyes, lg. eye QFP	12.2	1.2	0.7		
1090464	Qtz. Eyes, lg. eye QFP	11.9	1.2	0.7		
1090464	Qtz. Eyes, lg. eye QFP	11.8	1.2	0.7		
1090465	Qtz. Eyes, lg. eye QFP	9.8	1.2	0.7		
1090465	Qtz. Eyes, lg. eye QFP	7.7	1.2	0.7		
1090459	Qtz. Eye, late dyke	8.2	1.2	0.7		
1090459	Qtz. Eye, late dyke	8.4	1.2	0.7		
1090459	Qtz. Eye, late dyke	7.6	1.2	0.7		
1090455	Qtz. Eye, late dyke	8.1	1.2	0.7		
1090455	Qtz. Eye, late dyke	7.3	1.2	0.7		
1090456	Qtz. Eye, late dyke	5.4	1.2	0.7		
1090456	Qtz. Eye, late dyke	6.6	1.2	0.7		
1090456	Qtz. Eye, late dyke	10.2	1.2	0.7		

**Table 3.5 -  $\delta^{13}\text{C}$  isotope data for fluid inclusion extracts**

Sample ID	Material	$\delta^{13}\text{C}$ (‰)
OBM-15-564	Pre-Ore Ankerite vein	-0.2
OBM-16-666	Pre-Ore Ankerite vein	-0.6
OSK-W-17-968	Syn-Ore Qtz-Carb-Py-Tur vein	-2.0
OSK-W-16-760	Syn-Ore Qtz-Carb-Py-Tur vein	-5.6
EAG-11-311	Syn-Ore Qtz-Carb-Py-Tur vein	-10.1
OSK-W-17-1316	Post-Ore Quartz vein	-2.0
EAG-12-320	Post-Ore Quartz vein	-3.8

**Table 3.6 -  $^{34}\text{S}$  isotope data for pyrite**

Sample ID	Pyrite Type	$\delta^{34}\text{S}$	1s (‰)
1037-1-G1-01	Py3	1.6	0.3
1037-1-G1-02	Py3	0.8	0.3
1037-1-G1-03	Py3	0.8	0.3
1037-1-G1-04	Py3	2.9	0.3
1037-1-G1-05	Py3	2.6	0.3
1037-1-G1-06	Py2	1.0	0.3
1037-1-G1-07	Py2	1.0	0.3
1037-1-G1-08	Py1	0.9	0.3
1037-1-G1-09	Py2	1.2	0.3
1037-1-G1-10	Py2	0.8	0.3
1037-1-G1-11	Py1	0.9	0.3
1037-1-G1-12	Py1	0.6	0.3
1037-1-G1-13	Py1	0.8	0.3
1037-1-G1-14	Py2	1.6	0.3
1037-1-G1-15	Py3	2.2	0.3
1037-1-G1-16	Py3	1.1	0.3
1037-1-G1-17	Py3	1.1	0.3
1037-1-G1-18	Py3	1.5	0.3
1037-1-G1-19	Py3	1.9	0.3
1037-1-G1-20	Py3	1.6	0.3
1037-1-G2-01	Py3	1.5	0.3
1037-1-G2-05	Py3	1.7	0.3
1037-1-G2-08	Py1	0.9	0.3
1037-1-G2-11	Py1	1.6	0.3
1037-1-G2-14	Py1	0.8	0.3
1037-1-G2-19	Py1	1.0	0.3

Spot-to-spot reproducibility on the pyrite  
reference material = 0.3‰